MICROGRID MULTI-LEVEL CONTROL SYSTEM FOR PHOTOVOLTAIC-WIND HYBRID GENERATION SYSTEM

LINUS ALWAL ALOO

DOCTOR OF PHILOSOPHY

IN

ELECTRICAL ENGINEERING

JOMO KENYATTA UNIVERSITY

OF

AGRICULTURE AND TECHNOLOGY

2024

Microgrid Multi-Level Control System for Photovoltaic-Wind Hybrid Generation System

Linus Alwal Aloo

A Thesis Submitted in Partial Fulfillment of the Requirements for the Degree of Doctor of Philosophy in Electrical Engineering of the Jomo Kenyatta University of Agriculture and Technology

2024

DECLARATION

This thesis is my original work and has not been presented for a degree in any other University

Signature.....Date.....

Linus Alwal Aloo

This thesis has been submitted for examination with our approval as the University Supervisors

Signature.....Date.....

Dr. Peter K. Kihato, PhD

JKUAT, Kenya

Signature.....Date.....

Prof. Stanley I. Kamau, PhD

JKUAT, Kenya

Signature.....Date.....

Dr. (Eng) Roy S. Orenge, PhD

JKUAT, Kenya

DEDICATION

This work is dedicated to my family for their support and patience in the course of my studies.

ACKNOWLEDGMENT

First, is to thank Almighty God for the gift of good health and protection throughout the study period.

Second, I am highly indebted to my supervisors Dr. Peter K. Kihato, Prof. Stanley I. Kamau and Dr. (Eng.) Roy. S. Orenge for the exemplary support and supervision accorded. In particular, their patience, hard work, kindness, availability, continuous support as well as enormous academic experience, has been invaluable to me throughout the period.

My special appreciation goes to the African Development Bank (AfDB) for supporting the work through the Ph.D. scholarship awarded, without which the success of this work would have not been possible. In addition, gratitude to a number of friends and colleagues for the informal support and encouragement including their positive and constructive criticisms.

Finally, yet importantly, I would not have contemplated this road if not for the inspiration and moral support received from my family.

TABLE OF CONTENTS

LIST OF TABLES

LIST OF FIGURES

LIST OF APPENDICES

ACRONYMS AND ABBREVIATIONS

AC	Alternating Current
ANFIS	Adaptive Neuro-Fuzzy Inference System
ANN	Artificial Neural Networks
BESS	Battery Energy Storage System
CCM	Current Control Mode
CCS	Continuous Control Set
CCVSI	Current-Controlled Voltage Source Inverter
CPL	Constant Power Load
DC	Direct Current
DER	Distributed Energy Resources
DFIG	Doubly Fed Induction Generator
DG	Distributed generation/generator
DTSS	Discrete-Time State Space
ECM	Electric Circuit Models

EMS	Energy Management System
ES	Energy Storage
FCS	Finite Control Set
FLC	Fuzzy Logic Control
FOPID	Fractional Order PID
FQB	Frequency-reactive power
GA	Genetic Algorithm
GDC	Generalized Droop Control
GNL	General Non-linear
HMGS	Hybrid Microgrid System
IBC	Interleaved DC-DC Boost Converters
IGBT	Insulated Gate Bipolar Transistor
IHMS	Islanded Hybrid Microgrid System
ISA	Interior Search Algorithm
ITAE	Integral Time Absolute Error

LC	Load Controllers
LPNN	Lagrange programming neural network
MCS	Microgrid Control System
MCC	Microgrid Central Controller
MDSSM	Microgrid Discrete State-Space Model
MMCS	Microgrid Multi-level Control System
MOSFET	Metal Oxide Semi-Conductor Field Effect Transistor
MPC	Model Predictive Control
MPP	Maximum Power Point
MPPT	Maximum Power Point Tracking
MPZC	Model-Based Pole-Zero Cancellation
MTFM	Microgrid Transfer Function Model
NREL	National Renewable Energy Laboratory
NLP	Non-Linear Programming
NPC	Neutral-Point-Clamped

PCC	Point of Common Coupling
PI	Proportional-plus-Integral
PID	Proportional-plus-Integral-plus-Derivative
P&O	Perturb and Observe
PMSG	Permanent Magnet Synchronous Generator
PNGV	New Generation of Vehicles
PSO	Particle Swarm Optimization
PQ	Active/Reactive Power
PV	Photovoltaic
PWM	Pulse Width Modulated
QCQP	Convex Quadratically Constrained Quadratic Program
RBFNN	Radial Basis Function Neural Network
RES	Renewable Energy Source(s)
RDP	Recursive Dynamic Programming
RMS	Root Mean Squared

RMSE	Root Mean Squared Error
SCADA	Supervisory Control and Data Acquisition
SEPIC	Single-Ended Primary Inductance Converter
SISO	Single-Input-Single-Output
SoC	State of Charge
SR	Solar Radiation
SSR	Search Space Restricted
SPWM	Sinusoidal Pulse Width Modulation
STC	Standard Test Conditions
TF	Transfer Function
THD	Total Harmonic Distortion
VCM	Voltage Control Mode
VCVSI	Voltage-Controlled Voltage Source Inverter
VSC/VSI	Voltage Source Converter/Voltage Source Inverter
VPD	Voltage Active Power Droop

WECS Wind Energy Conversion System

WPGS Wind Power Generation System

WT Wind Turbine

WTG Wind Turbine Generator

ZOH Zero-Order Hold

LIST OF NOMENCLATURES

$\boldsymbol{a}$	The ideal constant of the diode
$\boldsymbol{A}$	Area covered by the rotor blades (unit: m^2)
$\boldsymbol{A/A_d}$	$n \times n$ state matrix (continuous/discrete)
$\boldsymbol{AD}$	Number of autonomy days
$\boldsymbol{B/B_d}$	$n \times r$ input or control matrix (continuous/discrete)
$\boldsymbol{C_B(t)}$	Available power in BESS at time slot t
$\boldsymbol{C_B(t-1)}$	Available power in BESS at time slot $t-1$
$\boldsymbol{C_f/L_f/R_f/G_f}$	Filter Capacitance/Inductance/Resistance/Conductance
$\boldsymbol{C/C_d}$	$m \times n$ output matrix (continuous/discrete)
$\boldsymbol{C_p}$	Conversion efficiency/power coefficient of the wind power (unit: %)
$\boldsymbol{C_{Wh}(t)}$	Capacity of the BESS system
$\boldsymbol{D/D_d}$	$m \times r$ direct transition matrix (continuous/discrete)
$\boldsymbol{D_P/D_Q}$	Active/Reactive power droop coefficient
$\boldsymbol{DoD/SoC}$	Allowable Depth of Discharge/State of Charge
$\boldsymbol{E}$ $(\boldsymbol{or\ V})$	Voltage
$\boldsymbol{E^*}$	Primary control reference representing $r.m.s$ output voltage
$\boldsymbol{E_{bat}}$	Nonlinear voltage (unit: V)
$\boldsymbol{E_L}$	Daily energy consumption
$\boldsymbol{E_0}$	Open-circuit voltage (OCV) of the battery at full capacity (unit: V)
$\boldsymbol{E_v/\Delta E_v}$	Voltage prediction error/change in voltage error (unit: V)
$\boldsymbol{F_d}$	Viscous damping (unit: $N.m.s$)
$\boldsymbol{F_r}$	Minimum ripple frequency component in the current (unit: Hz)
$\boldsymbol{F_s}$	Switching frequency for inverter PWM signals (unit: Hz)
$\boldsymbol{f_{switching}}$	Switching frequency (unit: Hz)
$\boldsymbol{G_{SR}}$	Solar radiation (unit:W/m^2)

G_{ING}	The incident irradiance
$G_{PV}/G_{WTG}/$ $G_{BESS}/G_{BC1}/$ $G_{BBC}/G_M/G_L$	Transfer functions of solar PV, Wind, BESS, Boost Converter, Buck-Boost Converter, Inverter/Microgrid system, and Load, respectively
G_{STC}	Solar irradiance at standard test condition (STC) ($= 1000\ W/m^2$)
H	Model horizon
H_m	The equivalent inertia constant of the generator rotor (unit:$Kg.m^2$)
I	Battery current (unit:A)
I^*	Complex conjugate current
i_k	Instantaneous current (unit:A)
I_{mp}	Max Power Current (unit:$A\ dc$)
I_{Ph-STC}	Photovoltaic Current at STC (unit:A)
I_{PV}	PV cell output current (unit: A)
I_{sat1}/I_{sat2}	Saturation currents of the first and second diodes (unit:A)
I_{sc}	Short-circuit Current (unit: $A\ dc$)
i_{sd}, i_{sq}	The d −axis and q −axis currents (unit:A)
J	Objective Function/Cost Function
$J_p(k)$	Predicted output with MPC
K/K_1	Polarization resistance coefficient (unit: Ω)
k_c	Temperature coefficient
$K_p/K_s/K_V$	Max Power/ Voltage/Short-circuit current temperature coefficient (unit: $\%/^0C$)
$K_{PA}, K_{IA}/$ K_{PV}, K_{IV}	Proportional/Integral controller specification of the current/voltage controller
$K_{PV}/K_{WTG}/$ $K_{BESS}/K_{BC1}/$ $K_{BBC}/K_M/K_L$	Amplification factors of solar PV, wind, BESS, Boost Converter, Buck-Boost Converter, Inverter/Microgrid system, and Load, respectively

$\boldsymbol{L_{sd}, L_{sq}}$	The inductance of the PMSG generator (unit:H)
$\boldsymbol{M}$	Control horizon
$\boldsymbol{M_p}$ (%)	Percentage overshoot/undershoot
$\boldsymbol{N}$	Prediction horizon
$\boldsymbol{N_g}$	Generator efficiency
$\boldsymbol{N_m}$	Number of Distributed Generation (DG) units
$\boldsymbol{p}$	The number of pole pairs (unit: dimensionless)
$\boldsymbol{P_{BAT}}$	Battery capacity (Ahr)
$\boldsymbol{PE_v}$	Previous voltage error (unit:V)
$\boldsymbol{P_{gen}(t)}$	Total generated power to cater for load demand
$\boldsymbol{P_m/P_{mp}/P_r/P_s}$	Aerodynamic wind turbine power/Max Power/Rated power of microgrid/ Power stored or drawn from the BESS power (unit:W)
$\boldsymbol{P_{PV-out}(P_{PV})/}$ $\boldsymbol{P_{WT-out}(P_{WT})}$	Power generated from a PV system/Power generated from a wind turbine (WT) unit (unit:W)
$\boldsymbol{P_{ren,dem}(t)}$	The demanded RES energy
$\boldsymbol{P_{STC}}$	Maximum power at standard test condition
$\boldsymbol{Q_i}$	Weighting matrix representing the penalization for control errors
$\boldsymbol{r}$	Radius of the paddle of wind turbine
$\boldsymbol{R}$	Set point/Reference matrix for microgrid dynamic model
$\boldsymbol{R_i}$	Weighting matrix representing the penalization for control increments
$\boldsymbol{R_I/R_s/R_{sh}}$	Internal/Series/Parallel resistance (unit:Ω)
$\boldsymbol{R(k)}$	Discrete reference value for microgrid discrete time model representing the available PV and WT power
$\boldsymbol{S}$	Apparent power/Total power (VA)
$\boldsymbol{t\ or\ t_1}$	Time slot (in hours) over which the microgrid should be operated
$\boldsymbol{T_C/T_{STC}}$	Module Ambient temperature/Temperature at Standard Test Condition (STC) (unit: ^0C)
$\boldsymbol{T_f}$	Static friction (unit:$N.m$)

t_p	Peak time
$T_{PV}/T_{WTG}/$ $T_{BESS}/T_{BC1}/$ T_{BBC}/T_L	Time constants of solar PV, wind, BESS, Boost Converter, Buck-Boost Converter, and Load, respectively
t_r	Rise time
t_s	Settling time
T_s	Sampling time
T_γ	Reference temperature
u	$r-$dimensional control vector or input vector
v	Wind speed of the site (m/s)
V_{ac}/V_{dc}	Inverter output voltage/Input DC voltage (unit:V)
V_{batt}	Terminal voltage (unit:V)
V_{c-out}	DC-DC converter output voltage
V_D/V_T	Diode voltage/Diode thermal (unit:V)
V_{mp}/V_{oc}	Max Power Voltage/ Open-circuit Voltage (unit:Vdc)
v_0^*	VCVSI reference voltage
V_{PCC}	Point of Common Coupling voltage
V_{PV}	PV cell output voltage (unit:V)
V_{ref}	Set microgrid DC voltage (unit:V)
v_{sd} , v_{sq}	The $d-$axis and $q-$axis voltages (unit:V)
x	$n-$ Dimensional state vector
X_{abc}/X_{dqz}	PMSG variables in the stationary/rotating coordinates
y	$m-$dimensional output vector
y_k	Terminal voltage (unit: V)
z_k	Battery's State of Charge (SoC)
ρ	Air density of the power generation site (unit:kg/m^3)
$\eta/\eta_B/\eta_v$	Efficiency/BESS efficiency/Voltage efficiency (unit: %)
λ	Tip speed ratio of the rotor blades (unit:m)

$\boldsymbol{\lambda_b}$	Self-discharge rate of the BESS
$\boldsymbol{\delta}$	Phase difference between converter output voltage & common AC bus
$\boldsymbol{\beta}$	Blade pitch angle (unit:$degrees$)
$\boldsymbol{\tau_1/\tau_2}$	Current control-inner loop/Voltage control-outer loop time constant
$\boldsymbol{\omega}$	Angular frequency (unit:rad/s)
$\boldsymbol{\omega^*}$	Primary control reference representing angular frequency (unit:rad/s)
$\boldsymbol{\omega_s}$	Generator's electrical rotational speed (unit:rad/s)
$\boldsymbol{\psi_p/\psi_{sd}/\psi_{sq}}$	Permanent flux/ The $d-$ and $q-$component of instantaneous stator flux (unit:Wb)
$\boldsymbol{\varepsilon}$	The error between the predicted and actual voltage of PCC (5%)

ABSTRACT

The concept of a microgrid is increasingly attracting interest among researchers and investors. This is because it offers a promising technology for utilizing distributed renewable energy generation resources, notably Photovoltaic (PV) and wind generation systems. However, the off-grid or on-grid utilization of a microgrid with PV and wind generation systems presents power quality challenges due to their intermittency in power outputs and voltage variations. This problem is mainly addressed within the converter section of the microgrid using Maximum Power Point Tracking (MPPT) algorithms and voltage regulation strategies using a Microgrid Control System (MCS). A majority of the existing MCSs still depict some inadequacies in their ability to optimize voltage regulation with intelligence while working for the non-linearities in the microgrid. This research aimed at developing a Microgrid Multi-level Control System (MMCS) for a PV-Wind hybrid microgrid system based on Genetic Algorithm-Adaptive Neuro-Fuzzy Inference System-Model Predictive Control-(GA-ANFIS-MPC). To achieve this, the PV-Wind hybrid microgrid model that incorporates a Battery Energy Storage System (BESS) was first created in MATLAB/SIMULINK. Two microgrid models have been developed: a scalable Simulink Case Study Model from the underlying mathematical equations and a nested voltage-current loop-based Transfer Function model. Next, the GA-ANFIS-MPC-based MCS was designed in two hierarchical levels. The first level is the GA-ANFIS primary controller, which has been used as an MPPT algorithm to optimize the converter outputs and regulate the microgrid output voltage amid power generation variations. The second level of control is the MPC secondary controller, which controls BESS's charging and discharging. In addition, the Proportional plus Integral plus Derivative (PID) regulator control method and the Search Space Restricted-Perturb and Observe (SSR-P&O) were developed to validate the performance of the GA-ANFIS-MPC controller using the simulation model built in MATLAB/SIMULINK. The results and performance obtained indicated that both the GA-ANFIS primary controller and the MPC secondary controller are superior to the SSR-P&O and PID in terms of reduced rise time, settling time, overshoot, and the ability to handle non-linearities in the microgrid. The GA-ANFIS primary controller recorded the best performance followed by the MPC secondary controller. The MPC controller, though with an increased computation time, was seen to have a better response than the GA-ANFIS controller in terms of reduced overshoot in voltage regulation. However, the GA-ANFIS controller has a better response than the MPC controller in terms of reduced rise time and settling time. The main contribution of this study is the designed GA-ANFIS-MPC based MCS that improves voltage responses and also charging and discharging of BESS in the PV-Wind Hybrid microgrid system. Consequently, this improves microgrids' performance in supplying power to targeted remote locations and local communities not connected to the main grid. It also acts as a stepping stone towards realizing the smart grid.

Keywords - BESS, GA-ANFIS-MPC, Microgrid, Perturb and Observe (P&O), Photovoltaic, PV-Wind hybrid system.

CHAPTER ONE

INTRODUCTION

1.1 Background Information

In the recent past, there has been an increasing need to shift focus on power generation from environmentally unfriendly conventional sources such as diesel or coal plants to clean and renewable sources such as Photovoltaic (PV) and wind (Ahmed et al., 2015; Aminu & Solomon, 2016; Bidram et al., 2017). However, the main bottleneck in utilizing these renewable resources has been the proper control and management of their power outputs (Nanda et al., 2021; Sawle et al., 2016). This is mainly attributed to the intermittent nature of PV and wind resources (Badwawi et al., 2015; Borazjani et al., 2014; Palizban & Kauhaniemi, n.d.; Shen, 2017). The scenario is even more challenging when adopting a hybrid of such sources such as the combination of PV and wind generation sources. One solution has been to pool the resources into a microgrid. In its basic form, a microgrid may be viewed as a small local and controllable power system whose main objective is to serve or electrify remote communities (Nanda et al., 2021; Sawle et al., 2016). Microgrids can be operated in grid-connected mode and off-grid mode (Z. Chen et al., 2017; Hossain et al., 2017; Jadav et al., 2017; Ton & Systems, 2015).

Microgrids are known to experience various technical challenges such as errors in the regulation of voltage and frequency, loss in efficient load sharing and improper co-ordination of Distributed Energy Resources (DERs). Further, there are concerns regarding smooth microgrid re-synchronization with the main grid for grid-connected systems, control of power flow between the microgrid and the main grid and optimization of its operating cost. This provides the foundation leading to the study problem in which there is need to develop an appropriate microgrid control system to mitigate against ensuing power quality issues. The main factors leading to the problem include the intermittent nature of PV and wind resources, the power quality issues pertaining to voltage and

frequency and the ability of the control system to act with intelligence as well as dealing with non-linearities in the microgrid.

Several studies have been done on the modeling of hybrid PV-wind energy systems. For instance, M. Jayachandran et al. (Jayachandran & Ravi, 2017) designed and optimized an Islanded Hybrid Microgrid System (IHMS) in which Particle Swarm Optimization (PSO) was used to obtain the lowest cost with a shorter computation time than the Genetic Algorithm (GA). The distributed inverter control strategy is proposed by A. Khalil (Khalil et al., 2016), for load power sharing between PV and Wind, whereas G. Ma'slak and P. Orłowski (Orłowski, 2022) used switched Model Predictive Control (MPC). The MPPT algorithms for a PMSG-based wind energy conversion system (WECS) are reported by P. Sahin et al. (Sahin et al., 2017) using P&O MPPT.

Several authors have applied Artificial Intelligence (AI) techniques in microgrid control. S. Korjani et al. (Korjani et al., 2017) applied a Genetic Algorithm (GA) to solve a microgrid-clustering problem while minimizing power exchanges. K. Abdulhussein et al. (Sumarmad et al., 2022) proposed three algorithms, namely PID, Artificial Neural Networks (ANN), and Fuzzy Logic Control (FLC), for voltage regulation in a hybrid microgrid system. The MPPT controller is based on the P&O method. The results simulated in MATLAB & SIMULINK depicted the FLC to be better than the PID and ANN on account of efficiency and precision. D. Gamage et al. (Gamage et al., 2021) designed an ANFIS controller for an off-grid PV microgrid with a battery and supercapacitor. The simulated results indicated better performance of the ANFIS in voltage regulation compared with other controllers such as FLC and conventional PI.

For efficient performance of a microgrid, a reliable Microgrid Control System (MCS) with suitable control algorithms is required. Over the last decade, several control strategies have been developed for use in microgrid environments. These control strategies and architectures include hierarchical control schemes, conventional and modified droop control methods, Model Predictive Control (MPC), artificial intelligence control methods, and commercial microgrid systems (LI & NEJABATKHAH, 2014; L. Meng et al., 2017;

Minchala-Avila et al., 2015; Reshma Mary Thomas & Deepu Jose, 2015). However, developing specific control strategies and schemes that apply to a hybrid microgrid system is still challenging. It has been attracting the attention of many researchers world-wide to date. This study aimed to bridge the gap by developing a Microgrid Multi-level Control System (MMCS) utilizing Genetic Algorithm-Adaptive Neuro-Fuzzy Inference System-Model Predictive Control (GA-ANFIS-MPC) for a Photovoltaic-Wind hybrid generation microgrid system.

1.2 Problem Statement

The development and utilization of microgrid systems face technical, integration, and sustainability challenges. A Photovoltaic-wind microgrid system may become unstable due to the intermittency of the micro sources as well as when faults and other disturbances occur (Borges et al., 2017; Du et al., 2017; Morstyn et al., 2018; T. Wang et al., 2019). This leads to variations in voltage and power outputs. In addition, for off-grid microgrid systems, there are voltage deviations associated with load changes, low inertia of the microgrid, as well as dynamics of the Battery Energy Storage System (BESS). This means there is always a great challenge in voltage control in off-grid microgrid systems. To address this, appropriate control strategies are required to ensure stability and power quality, especially in the off-grid mode of operation where the microgrid does not receive support from the grid, which comes at an added cost. The literature reviewed and studies conducted have revealed that every control strategy has its merits and demerits and is specific to the needs of the microgrid for which it was designed (ABB Power, 2015; Aminu & Solomon, 2016; GE Digital Energy, 2012; Huang et al., 2011; Jain & Arya, 2015; Jayachandran & Ravi, 2017; Katiraei et al., 2017; Lavanya & Senthil Kumar, 2018; Nanda et al., 2021; Szeidert et al., 2016).

Conventional controllers such as Proportional-plus Integral (PI), Proportional-plus Integral-plus Derivative (PID) and droop-based control methods are simple and easy to implement. However, their performances are degraded in microgrids, characterized by uncertainties leading to a constantly changing structure and configuration. This is because

such controllers have static parameters obtained based on a linear mathematical model of the system and cannot respond favorably to the dynamic changes in a microgrid.

For the Model Predictive Controller (MPC), the computation of the control law is more complex compared with conventional or artificial intelligent based controllers. Further, the success of an MPC controller in microgrids when acting alone mainly depends on the accuracy of the process model which is not easy to obtain. Adaptive Neuro-Fuzzy Inference System (ANFIS), though having the intelligence and learning ability, does not provide optimal results when deployed alone. The Genetic Algorithm (GA) controller provides optimized performance but it's random or unguided mutation may pose challenges to the stability and accuracy of the microgrid controller when used alone.

1.3 Justification

The conventional control methods for regulating microgrid voltage, such as Proportional plus Integral plus Derivative (PID) control, require accurate mathematical models of the microgrid which may be difficult to obtain. Further, such methods exhibit serious struggles with non-linearities, rendering degraded performance under practical conditions. On the other hand, artificial intelligence-based control strategies such as Fuzzy Logic Control (FLC) and Artificial Neural Networks (ANN)-based methods do not require accurate mathematical models of the microgrid. These techniques can also handle the nonlinear dynamics of the microgrid system.

Considering the mentioned challenges, the strategy implemented for control of a microgrid with PV-wind hybrid generation systems is a Microgrid Multi-level Control System (MMCS). The MMCS is based on the GA-ANFIS-MPC algorithms in which a hybrid Genetic Algorithm-Adaptive Neuro-Fuzzy Inference System (GA-ANFIS) acts as the primary controller and the Model Predictive Control (MPC) as the secondary controller, the two hierarchical levels complementing one another. The MPC strengthens model-based prediction to handle BESS voltage dynamics while enforcing requisite

constraints. The GA-ANFIS algorithm on the other hand deploys PV-Wind power generation data-driven predictions to regulate the microgrid voltage.

The designed GA-ANFIS-MPC MMCS offers several advantages over other existing or possible microgrid control schemes. First, it responds better to the changes in the microgrid as the GA-ANFIS-MPC parameters can be adjusted offline and online, and the GA-ANFIS has been trained to offer intelligence to the control system. The result is improved control and voltage regulation, particularly in the off-grid mode. The secondary MPC algorithm prevents over-charging or over-discharging of the Battery Energy Storage System (BESS). It compensates for voltage deviations introduced by implementing the GA-ANFIS primary controller. There is also an efficient load sharing and coordination of distributed PV-wind generation micro sources and prediction of their power outputs. Finally, there is enhanced handling of transients and re-establishing the prescribed microgrid operating point. The research outcome enhances control of microgrid voltage to supply quality power to remote locations and rural areas not connected to the main grid.

From economic and industrial perspectives, the developed Multi-level Control System (MMCS) ensures lower energy costs by efficiently using Solar and Wind energy sources and the charging/discharging of the BESS. With the controller installed, the owner of the microgrid ends up spending the least amount possible on electricity at reduced maintenance costs while enjoying continuity of energy supply. It also predicts both future load and the projected generation which inevitably leads to significant savings while at the same time, increasing energy efficiency and reliability. In addition, the MMCS enhances security and resiliency thereby guaranteeing a consistent energy supply by the smart microgrid which is a key requirement in many industries. 1.4 Objectives

1.4.1 Main Objective

To develop a Microgrid Multi-level Control System (MMCS) for a Photovoltaic-Wind Hybrid generation system based on Genetic Algorithm-Adaptive Neuro-Fuzzy Inference System-Model Predictive Control (GA-ANFIS-MPC).

1.4.2 Specific Objectives

i. To develop a mathematical, simulation, and case study model for a Photovoltaic-Wind hybrid generation microgrid system using state space representation in MATLAB/SIMULINK.
ii. To design a Genetic Algorithm-Adaptive Neuro-Fuzzy Inference System (GA-ANFIS) based MCS to control the voltage supplied by the PV-Wind hybrid generation microgrid system.
iii. To design a Model Predictive Controller (MPC) to regulate and control Battery Energy Storage System (BESS) charging and discharging in the Photovoltaic-Wind hybrid generation microgrid system.
iv. To apply the developed GA-ANFIS-MPC-based multilevel MCS to an off-grid Photovoltaic-Wind Hybrid generation system case study and evaluate the performance compared to the Proportional plus Integral plus Derivative (PID) control method.

1.5 Scope

This study focused on the voltage control problem of an off-grid microgrid containing PV-wind and BESS using the GA-ANFIS-MPC algorithms. Modeling, design, and implementation of the entire microgrid have been done in MATLAB/SIMULINK for the generation side, power electronic interfaces, and the control system. Studies associated with the frequency control problem, load side, and grid-connected systems are beyond the scope of the conducted work.

The Simulink-based Case Study was built around a $10kW$ Solar PV system with peak current of $16A$ and voltage $654V$ simulated at irradiance of $1kW/m^2$ at $25^0\ C$. The Wind Generation System used a West-wind $6.4m$, $10kW$ Wind Turbine with a rated base speed of $12m/s$. The DC-DC converter was a modified Interleaved Boost Converter (IBC) both for the PV and wind sections of the microgrid while the inverters deployed were also two-parallel three-level Voltage Source Converter (VSC) for the PV and wind microgrid.

There is also a Transfer Function (TF) based Simulink Case Study built around the schematic small-signal mathematical TF model of the studied microgrid.

1.6 Organization of Thesis

The thesis is organized into five chapters, including the introduction chapter, which forms Chapter 1. Chapter 2 deals with Literature Review where an overview of related work, microgrid concepts, GA, ANFIS, and MPC basics, and the research gaps are presented.

Chapter 3 handles Methodology. First, it describes the modeling and analysis of the PV-Wind microgrid system and the design of the Perturb and Observe (P&O) and PID controller for the same system for benchmarking. Secondly, the GA-ANFIS primary controller and the MPC BESS charging/discharging controller are designed separately and applied to the system. Finally, the MATLAB/SIMULINK models are created, and the overall simulation setup is developed to test the GA-ANFIS-MPC algorithms' performance.

Chapter 4 presents the Results obtained from the simulation models, and those obtained from the case study developed. The performance of GA-ANFIS and MPC is compared with that of conventional PID controllers and the P&O method. The comparison is done in a MATLAB/SIMULINK environment, and the results are verified.

Chapter 5 concludes the work performed in the study based on the results obtained and highlights the possible limitations. Moreover, further research work that can be carried out to improve the present scenario is mentioned. This section is followed by the reference materials that have been used in the development of the thesis. Finally, appendices outline the supplementary information, relevant to the study.

1.7 Thesis Contribution

The main contribution of this work is the developed Microgrid Multi-level Control System (MMCS) based on GA-ANFIS-MPC algorithm for off-grid Photovoltaic-Wind Hybrid

generation systems. The main areas are the Photovoltaic-wind-based MCS's design, modeling, and analysis. Other contributions of this study include:

- The designed GA-ANFIS primary controller optimizes the converter outputs and performs better than the PID or SSR-P&O algorithms.
- The interleaving of PV and wind micro sources, DC-DC boost converters, the BESS, and the three-phase parallel inverters provided scalability and modularity.
- Modifying the equations and models specified in Table 2.4 under section 2.7 of the Literature Review.
- Presentation of a unique model of the combined $10\ kW$ PV-wind microgrid with interleaving technique and its mathematical transfer function model.
- The designed MPC secondary controller optimizes the BESS charging and discharging and whose performance is better than the PI (D) controller.
- The research outcome enhances control of microgrid voltage to supply quality power to remote locations and rural areas not connected to the main grid.

1.8 Assumptions of the Study

The following assumptions have been made in the study:

1. While it was noted that microgrids have varied capacities and can be operated off-grid or in grid-connected modes, this study considered a microgrid having a power output of $10\ kW$ and is operated in an off-grid mode.
2. The primary GA-ANFIS controller was trained offline with labeled training data while the secondary MPC controller was also designed offline before deployment.
3. The data used in the design of the GA-ANFIS controller was pre-processed using MATLAB codes and converted into a form that the GA-ANFIS required, making the designed GA-ANFIS controller universally acceptable and not limited by the utilized dataset. The study used MATLAB&SIMULINK R2019a. This form of data is available on request.

4. The Solar and Wind raw data before transformation and further modifications was obtained from the National Solar Radiation Database (NSRDB) provided by the National Energy Research Laboratory (NREL). The data is freely and publicly available at https://nsrdb.nrel.gov/data-viewer as well as in the System Advisor Model (SAM) version SAM 2018.11.11 provided freely by NREL (Blair et al., 2018). The site considered was Juja, Kiambu, Kenya with Latitude 1.095161S and Longitude 37.01249E for the period 2017 to 2019 with a spatial resolution of $4km$ by $4km$. Portions of the extracted data set have been provided in Appendix 4.
5. Battery charging and discharging models and processes have been assumed similar so that the response of the BESS has been reported mainly within the discharging framework.

CHAPTER TWO

LITERATURE REVIEW

This chapter presents existing modeling and control techniques for microgrids as well as the research gaps that have been addressed in the study undertaken. It begins with an overview of the emerging power grids followed by the key elements of a hybrid photovoltaic-wind microgrid system. The chapter then proceeds to present microgrid control methods and a detailed review of hybrid controllers and selected existing studies. Finally, it concludes with a summary of research gaps and proposed approach.

2.1 Emerging Power Grids

There has been an increase in small-scale locally generated and distributed power utilization to facilitate rural electrification using distributed sources of clean energy, resulting in power configurations referred to as mini-grid, microgrid, nanogrid, and picogrid. Table 2.1 summarizes these emerging power grids, which have varied definitions among researchers, countries, and industries; thus, the entries made are typically for illustration purposes. In terms of commonly used sizes and the context of Table 2.1, the terminologies are interpreted as follows (Anvari-Moghaddam et al., 2021; Yahyaoui, 2018):

1. A mini-grid refers to a renewable-based small-scale power generation and distribution network with a capacity of 10kW and above (i.e., typically 10kW to 10MW).
2. A microgrid is a smaller system that acts as a single controllable entity concerning the grid with a capacity below 10kW. It can connect to and disconnect from the grid, which allows it to be operated in grid-connected or off-grid mode. Recent studies have depicted different views of a microgrid in terms of capacity, from tens of kilowatts (kW) to a few megawatts (MW). This study

considers a microgrid whose nominal power output is 10 kW and is operated in an off-grid mode.

3. A nano grid is a small electrical domain with a power capacity not exceeding 5kW and is limited to a single building structure, primary load, or a network of isolated loads.
4. A pico grid is even smaller, consisting of a solar home system with a power capacity under 250W meters, providing just enough power for lighting and charging mobile phones.

Table 2.1: Emerging Power Grids

Grid	Function	AC/ DC	Voltage	Power	Connection to Grid	Storage
Mini-grid	Local	AC/ DC	230 $-$ 400V AC, $>$ 60V DC	10kW $-$ 10MW	In principle, no but can be on-grid	Mostly
Micro grid	Distributed	AC/ DC	230 $-$ 400V AC, 24 $-$ 60V DC	$<$ 10kW	Possible	Mostly
Nano grid	Leisure telecom household	AC/ DC	$<$ 24V DC	$<$ 5kW	No, only possible to microgrid	Yes
Pico grid	Telemetry phone charging	DC	$<$ 12V DC	$<$ 0.25kW	Off-grid	Yes

2.2 Hybrid Photovoltaic-Wind Microgrid System

This section presents the key elements that constitute a Hybrid Photovoltaic -Wind Microgrid System. It introduces the general framework of a Microgrid Control System (MCS), Classification of Microgrid and the Generation Sources in a hybrid Photovoltaic and Wind Energy System.

2.2.1 Microgrid Control System (MCS)

A Microgrid Control System (MCS) is a supervisory-based control architecture that enables efficient and cost-effective utilization and integration of Distributed Energy

Resources (DERs), loads, and energy storage in a localized framework (Borges et al., 2017; Du et al., 2017; Morstyn et al., 2018; T. Wang et al., 2019). Figure 2.1 shows a microgrid control system with solar PV and wind as the principal micro sources (Sawle et al., 2016).

If running, the power obtained from the wind turbine and the backup generator is first rectified before being injected into the DC bus. In contrast, power from the PV system is injected directly into the DC bus. The battery storage stores excess power generated to reduce the hours the generator may run. A microgrid control system is required to regulate and optimize the utilization of power generated by these sources, which may be coupled directly to the DC bus at the Point of Common Coupling (PCC) and subsequently to the AC bus via an inverter. The loads, classified as low priority, essential AC, and dump, are connected to the load bus.

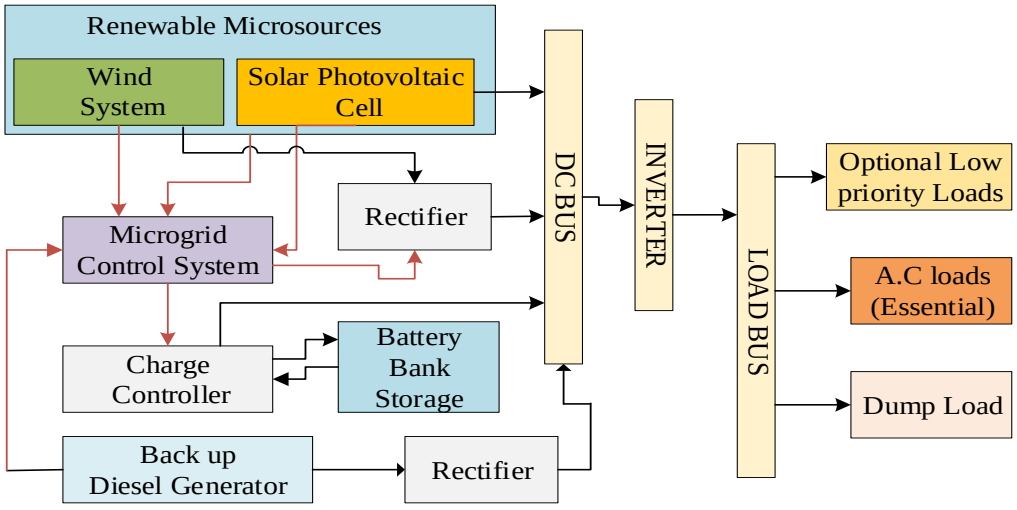

Figure 2.1: Block Diagram of Microgrid Control System

In general, the main roles of a microgrid control system are as follows (Ahmed et al., 2015; Bidram et al., 2017; Nanda et al., 2021; Sawle et al., 2016; Shen, 2017): First is the regulation of voltage and frequency for both grid-connected and off-grid modes. Second, it provides efficient load sharing, co-ordination of DERs, and microgrid re-

synchronization with the main grid for grid-connected systems. Third, it controls power flow between the microgrid and the main grid and optimizes its operating cost by allowing the incorporation of various constraints in the microgrid optimization problem. Finally, it appropriately handles transients and re-establishes prescribed conditions when transitioning between the modes.

2.2.2 Classification of Microgrid

Two broad categories of microgrid based on the type of power handled are AC microgrid and DC microgrid (Bidram et al., 2017; Z. Chen et al., 2017; Jadav et al., 2017; Morstyn et al., 2018). In terms of the operation principle, microgrids can operate in two modes: grid-connected mode and off-grid mode (Lei et al., 2016; LI & NEJABATKHAH, 2014; Minchala-Avila et al., 2015; Reshma Mary Thomas & Deepu Jose, 2015). Based on the grid connection status of a microgrid, it can be categorized into two: permanently isolated microgrid in which stand-alone networks supply all the power demanded by loads in the isolated network. This scenario is typical of remote areas or isolated communities where high transmission costs and losses render connection to the grid uneconomical (Ahmed et al., 2015; Aminu & Solomon, 2016; Bidram et al., 2017). Second is the grid-tied microgrid, which is capable of generating power within its distribution networks and importing and exporting power from and to a utility source.

2.2.3 Generation Sources in Hybrid Photovoltaic and Wind Energy System

The Hybrid Photovoltaic-Wind microgrid architecture of Figure 2.1 can be realized by integrating Photovoltaic (PV) and wind energy systems. However, the sizing of PV modules, wind turbines, and storage systems and determining control settings and operating strategies are interdependent (Sawle et al., 2016).

2.2.3.1 PV System

The power generated from a PV system concerning solar radiation (SR), denoted by P_{PV}, is given by equation (2.1) (T. Wang et al., 2019).

$$P_{PV} = P_{STC}\frac{G_{ING}}{G_{STC}}\left(1 + k_c\left(T_C - T_\gamma\right)\right) \quad (2.1)$$

where P_{PV} is the power generated from a PV system, G_{ING}, is the incident irradiance, P_{STC}, is maximum power at standard test conditions, G_{STC}, is irradiance at standard test conditions, k_c, is the temperature coefficient, T_C, is the module temperature, and T_γ, is the reference temperature (T. Wang et al., 2019).

2.2.3.2 Wind Turbine Generator System

The electrical power generated from a Wind Turbine (WT) unit, P_{WT}, can be specified as a cubic polynomial concerning the wind speed at the monitoring station according to equation (2.2) (T. Wang et al., 2019).

$$P_{WT} = \frac{1}{2}\rho\pi R^2 v^3 C_p \quad (2.2)$$

where P_{WT}, is the power generated from a WT system, R is the radius of the paddle of the wind turbine, ρ is the air density of the monitoring area, v is the wind speed of power generation area, and $C_{p,}$ is the conversion efficiency of the wind power (T. Wang et al., 2019).

The Permanent Magnet Synchronous Generator (PMSG) WT with a Voltage Source Converter (VSC) is preferred by most manufacturers as it is more efficient and reliable. Its advantages over a Doubly Fed Induction Generator (DFIG) include gearless construction, no need for a DC excitation system, and the ability to extract maximum wind power. A simplified PMSG equivalent circuit dq-coordinate frame model is represented in Figure 2.2 (Amara et al., 2020; C. N. Wang et al., 2014).

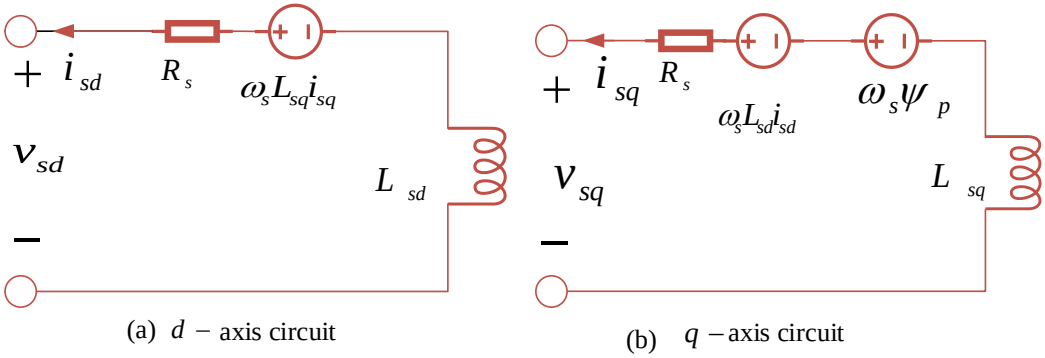

Figure 2.2: Simplified $d-q$ Coordinate Frame PMSG Model

The generator is modeled in dq-coordinates in which the current equations for the d −axis and q −axis are given by equations (2.3) and (2.4), whereas equation (2.5) defines the electromagnetic torque in the rotor, T_e (Amara et al., 2020; C. N. Wang et al., 2014).

$$\frac{di_{sd}}{dt} = -\frac{R_s}{L_{sd}} i_{sd} + \omega_s \frac{L_{sq}}{L_{sd}} i_{sq} + \frac{1}{L_{sd}} v_{sd} \tag{2.3}$$

$$\frac{di_{sq}}{dt} = -\frac{R_s}{L_{sq}} i_{sq} - \omega_s \left(\frac{L_{sd}}{L_{sq}} i_{sd} + \frac{1}{L_{sq}} \psi_p \right) + \frac{1}{L_{sq}} v_{sq} \tag{2.4}$$

$$T_e = 1.5p\left[\psi_p i_{sq} + i_{sd} i_{sq} (L_{sd} - L_{sq})\right] \tag{2.5}$$

where, v_{sd} , v_{sq} and i_{sd}, i_{sq} are the d −axis and q −axis voltages and currents, respectively, ω_s is the generator's electrical rotational speed, L_{sd} and L_{sq} are the generator inductance, ψ_p is permanent flux, R_s is the stator's resistance, and p is the number of pole pairs.

Using the PMSG transient model, which is the Park model, the stator voltage equation is defined by equation (2.6) (Sumathi et al., 2015; Yahyaoui, 2018):

$$\begin{pmatrix} v_{sd} \\ v_{sq} \end{pmatrix} = -R_s \begin{pmatrix} i_{sd} \\ i_{sq} \end{pmatrix} - \frac{d}{dt} \begin{pmatrix} \psi_{sd} \\ \psi_{sq} \end{pmatrix} + \omega_s \begin{pmatrix} 0 & -1 \\ 1 & 0 \end{pmatrix} \begin{pmatrix} \psi_{sd} \\ \psi_{sq} \end{pmatrix} \tag{2.6}$$

where, $v_{sd}, v_{sq,}\ i_{sd}, i_{sq}, \psi_{sd}$, and ψ_{sq} are, respectively, $d-q$ instantaneous stator voltage, current, and flux.

The stator flux linkages are defined as equation (2.7)

$$\begin{pmatrix}\psi_{sd}\\ \psi_{sq}\end{pmatrix} = \begin{pmatrix}L_{ls}+L_{dm} & 0\\ 0 & L_{ls}+L_{qm}\end{pmatrix}\begin{pmatrix}i_{sd}\\ i_{sq}\end{pmatrix} + \begin{pmatrix}\psi_p\\ 0\end{pmatrix} \tag{2.7}$$

where L_{dm} and L_{qm} are respectively the stator and rotor $d-$ and $q-$axis mutual inductances, L_{ls} is the leakage inductance of stator winding, ψ_p is the flux linkage produced by the permanent magnet. The electromagnetic torque now becomes equation (2.8) (Grzegorz Ma´slak and Przemysław Orłowski, 2022; Jayachandran & Ravi, 2017):

$$T_e = 2p\left(\psi_{sd}i_{sq} - \psi_{sq}i_{sd}\right) = p\left(\psi_p i_{sq} + \left(L_d - L_q\right)i_{sd}i_{sq}\right) \tag{2.8}$$

where, $L_d = L_{ls} + L_{dm},\ L_q = L_{ls} + L_{qm}$.

In the case of a directly coupled multipole PMSG, the stator resistance is much smaller than the synchronous reactance. Moreover, the difference between the $d-$ and $q-$ axis mutual inductance is small. With these considerations, equation (2.8) reduces to equation (2.9) (Grzegorz Ma´slak and Przemysław Orłowski, 2022; Jayachandran & Ravi, 2017; C. N. Wang et al., 2014):

$$T_e = 2p\left(\psi_f i_{sq}\right) \tag{2.9}$$

For a PMSG, the mechanical torque (T_m) and electrical torque (T_e) can be given by equations (2.10) and (2.11), respectively (C. N. Wang et al., 2014):

$$T_m = \frac{P_m}{\omega_m} \tag{2.10}$$

$$T_e = \frac{P_e}{\omega_e} = \frac{1}{p}\frac{P_e}{\omega_m} \tag{2.11}$$

where ω_m, ω_e, P_e, P_m and p are the rotor mechanical speed, rotor electrical speed, the electrical power of the PMSG, the mechanical power of the PMSG, and the number of pole pairs, respectively.

Considering a gearless small wind turbine PMSG system, the rotor mechanical speed is assumed to equal the rotor electrical speed. Therefore, the mechanical power of the PMSG is expressed as equation (2.12):

$$P_m = T_m\omega_m = \frac{T_e\omega_e}{P} \tag{2.12}$$

The generator equation of motion can be used to compute variations in the generator speed arising from a difference in electrical and mechanical torque as given by equation (2.13):

$$\frac{d\omega_m}{dt} = \frac{1}{2H_m}(T_m - T_e) \tag{2.13}$$

where H_m represents the equivalent inertia constant of the generator rotor.

The generator output active power delivered to the load P_L can be determined from equation (2.14):

$$P_L = P_m - P_{Cu,s} = 1.5\left[v_{sd}i_{sd} + v_{sq}i_{sq}\right] \tag{2.14}$$

where the stator winding loss $P_{Cu,s}$ is given by equation (2.15):

$$P_{Cu,s} = 3{I_s}^2 R_s \tag{2.15}$$

The generator output reactive power delivered to the load P_Q is given by equation (2.16):

$$P_Q = 1.5\left[v_{sq} i_{sd} + v_{sd} i_{sq}\right] \tag{2.16}$$

The R.M.S stator current and voltage I_s and V_s respectively, can be computed from equations (2.17) and (2.18):

$$I_s = \sqrt{\frac{(i_{sd}{}^2 + i_{sq}{}^2)}{\sqrt{2}}} \tag{2.17}$$

$$V_s = \sqrt{\frac{(v_{sd}{}^2 + v_{sq}{}^2)}{\sqrt{2}}} \tag{2.18}$$

2.3 Microgrid Control Methods

Existing microgrid architectures and control strategies include: hierarchical control schemes, conventional and modified droop control methods, Model Predictive Control, nonlinear programming algorithms, artificial intelligence control methods, and commercial microgrid systems.

2.3.1 Hierarchical Control Architecture

The control objectives of microgrids can be considered in terms of a hierarchical control structure, as shown in Figure 2.3 (Ahmed et al., 2015; Bidram et al., 2017). This view leads to a multilevel control structure to address a microgrid system's different design and performance goals. The primary control level operates at the fastest timescale and encompasses the distributed PV-wind micro sources' internal voltage and current control loops. It is responsible for stabilizing the voltage and frequency within the microgrid.

Consequently, it deals with local measurements and does not need a communication system. It also curtails the occurrence of circulating currents representing harmonics and provides for the reconfiguration capability of the DERs. It is also necessary for active and

reactive power regulation, usually achieved by droop-based controls (Ahmed et al., 2015; Aminu & Solomon, 2016; Bidram et al., 2017; Nanda et al., 2021).

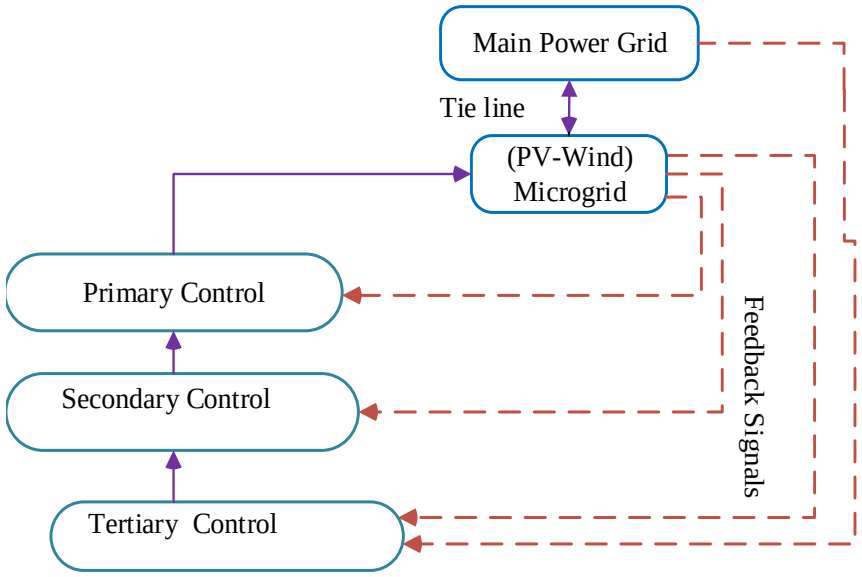

Figure 2.3: Hierarchical Control Levels of a Microgrid

The secondary control, also known as the microgrid Energy Management System (EMS), is utilized to compensate for the variations in voltage and frequency due to actions by the primary controls. It ensures reliable, secure, and efficient operation of microgrids in either grid-connected or off-grid mode (Nanda et al., 2021; Sawle et al., 2016). The secondary control is the highest level for a microgrid operating in off-grid mode. It can be realized using two main approaches: centralized and decentralized architectures (Borazjani et al., 2014; Nanda et al., 2021; Palizban & Kauhaniemi, n.d.). Centralized control uses a communication system with a Microgrid Central Controller (MCC) located far from the micro sources. The central system collects data from all sensors, computes the control variable for various control equipment, and then sends them to each controller, thereby managing the entire system. An example is Microgrid Supervisory Control And Data Acquisition (MicroSCADA) (Borazjani et al., 2014; Ton & Systems, 2015). It is recommended for certain small microgrids and those with shared goals and thus should cooperate. However, with growth in source data, the centralized approach is not fast

enough, hinders up-scaling, is uneconomical, and creates a single point of failure for the microgrid system.

Decentralized control is preferred for interconnected microgrids from different vendors, which should make independent decisions about their operating conditions. The microgrid control system incorporates intelligent control for each micro source. It reduces the network complexity, allows easy scalability (future extension), improves power supply reliability, is more economical, and offers bi-directional power flow. However, a disadvantage of this approach is the load-dependent frequency and amplitude deviations due to the utilization of the droop control method to adjust the active and reactive power in primary control [8], [9]. Finally, the tertiary control is at the highest level and operates at the slowest timescale. It manages the bidirectional power flow between the microgrid and the main grid. This facilitates an economical and optimal operation of the hierarchical control structure (Bidram et al., 2017).

Several control techniques, as shown in Figure 2.4, (Bidram et al., 2017), have been proposed in the literature for the inner-loop control and primary control and are deployed according to the characteristics of the microgrid (Borges et al., 2017; Du et al., 2017; GE Digital Energy, 2012; Jayachandran & Ravi, 2017; Lavanya & Senthil Kumar, 2018; Morstyn et al., 2018; T. Wang et al., 2019). The aim is to improve the power quality, disturbance rejection, and voltage or current tracking of the inverter output (ABB Power, 2015; Hossain et al., 2017). Conventional (active power control/frequency droop characteristic and reactive power control/voltage droop characteristic) and modified droop control methods have been widely utilized in microgrid systems, particularly for inner control loops/primary control [1]-[4], [8]–[11], [13]–[16], (Lavanya & Senthil Kumar, 2018). Droop control methods do not require communication links between the converters and, hence, are considered autonomous and wireless control strategies [2].

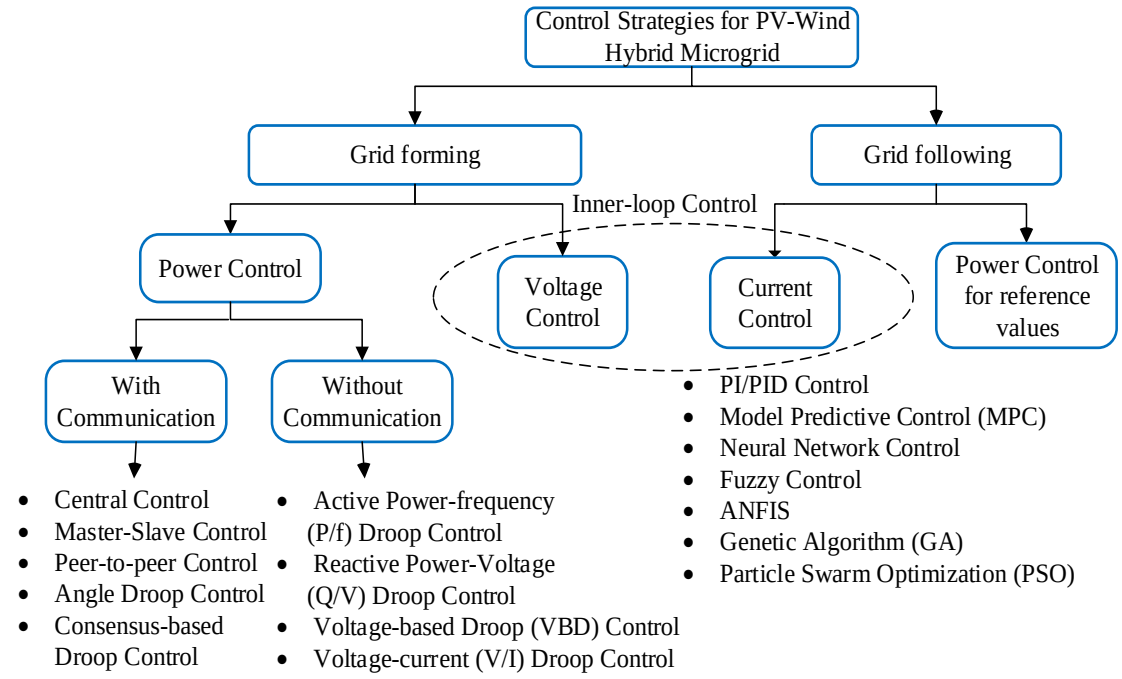

Figure 2.4: Inner-Loop Control and Primary Control Techniques

2.3.2 Droop Control Methods

A typical conventional droop control method is shown in Figure 2.5 (Bidram et al., 2017).

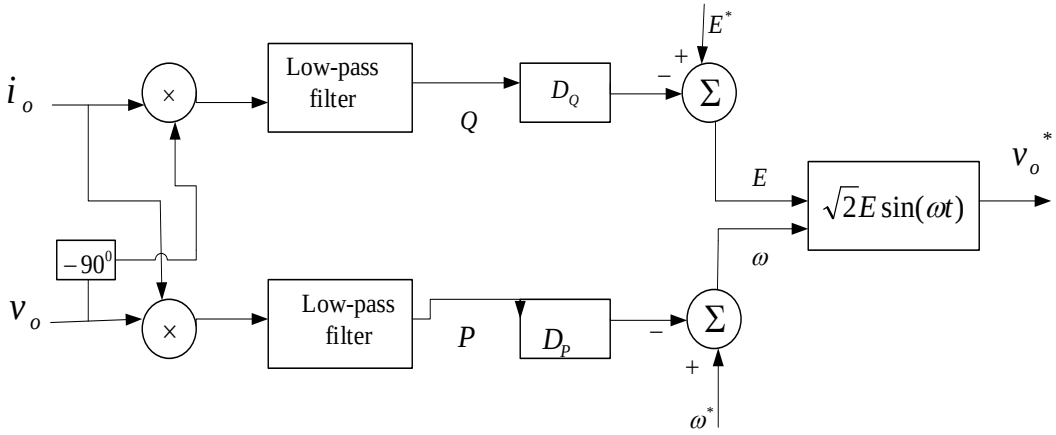

Figure 2.5: Conventional Droop Method

The primary control techniques are mostly implemented in active/reactive power (PQ) or voltage control modes.

i. PQ Control Mode: Here, the DG active and reactive power supply is regulated based on predetermined reference points. A current-controlled voltage source inverter (CCVSI) is used for its implementation (Bidram et al., 2017). The power source supplies stable power output irrespective of any variations in voltage, frequency, or load (Shen, 2017).

ii. Voltage Control Mode (VCM): The DG functions as a voltage-controlled voltage source inverter (VCVSI), implying that the reference voltage $v_0{}^*$, is obtained through droop characteristics using the primary control. Li and Nejabatkhah (LI & NEJABATKHAH, 2014) reported that VCM-based techniques are acquiring more attention as they can emulate a synchronous generator's behavior. The VCM nested voltage and current control loops are shown in Figure 2.6 (Bidram et al., 2017). It is seen that such a control strategy injects the current signal as feedback.

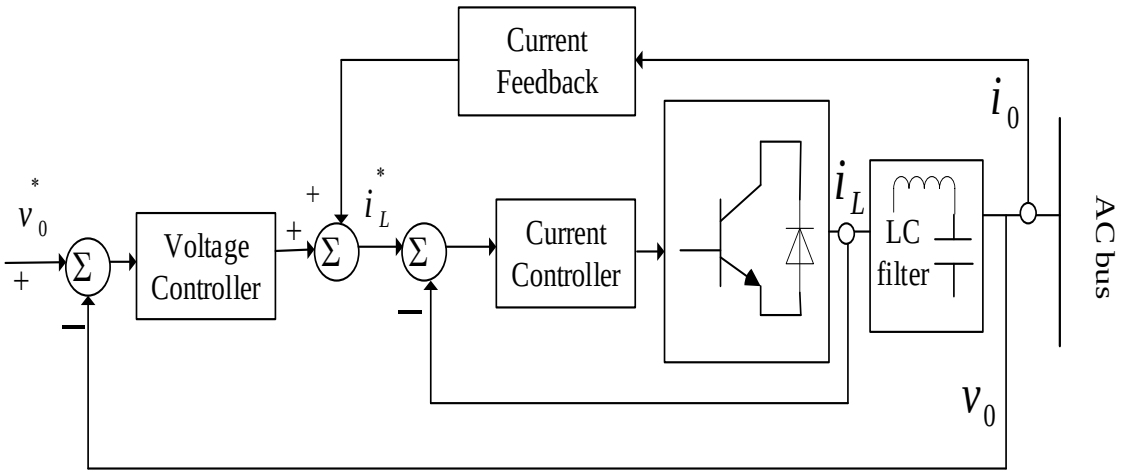

Figure 2.6: Voltage and Current Control Loops in Voltage Control Mode

If this model were to be applied in small-scale off-grid systems with PV-wind sources, the major concern would be how to improve the power quality in the presence of non-linear and single-phase loads and due to the low inertia presented by the microgrid. One direct

way to improve the power quality suggested in (Bidram et al., 2017) and (Hossain et al., 2017) is to modify the control structure by adopting a low pass filter both in the feed-forward inner current loop and the feedback outer voltage loop.

Consider an equivalent circuit of a VCVSI coupled to an AC bus as shown in Figure 2.7, where the VCVSI is modeled as an AC source, with a voltage of $E\angle\delta$, the common AC bus voltage is $V_{com}\angle 0$, and the $Z\angle\theta$ is the combined impedance of the line and the converter output.

With this, the complex power delivered to the common AC bus is given by equation (2.19):

$$S = P + jQ = V_{com}I^{*} = \frac{V_{com}E\angle\theta - \delta}{Z} - \frac{V^{2}{}_{com}E\angle\theta}{Z} \tag{2.19}$$

where δ is the phase difference between the converter output voltage and the common AC bus.

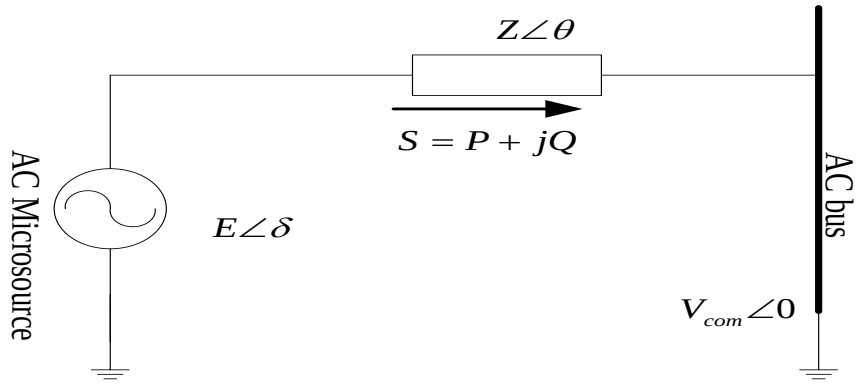

Figure 2.7: Simplified Diagram of a Converter Connected to the Microgrid

From equation (2.19), the real and reactive powers are calculated as:

$$\begin{cases} P = \dfrac{V_{com}E}{Z}cos(\theta - \delta) - \dfrac{V^2{}_{com}}{Z}cos\,\theta, \\ Q = \dfrac{V_{com}E}{Z}sin(\theta - \delta) - \dfrac{V^2{}_{com}}{Z}sin\,\theta \end{cases} \tag{2.20}$$

Assuming that the effective line impedance, $Z\angle\theta$, is purely inductive, $\theta = 90^0$ Equation (2.20) yields equation (2.21):

$$\begin{cases} P = \dfrac{V_{com}E}{Z}sin\ \delta, \\ Q = \dfrac{V_{com}E\,cos\ \delta - V^2{}_{com}}{Z} \end{cases} \tag{2.21a}$$

Equation (2.21a) can be simplified further into equation (2.21b) when δ, is considered small enough such that, $sin\,\delta \approx \delta$ and $cos\,\delta \approx 1$.

$$\begin{cases} P = \dfrac{V_{com}E}{Z}\delta, \\ Q = \dfrac{V_{com}E - V^2{}_{com}}{Z} \end{cases} \tag{2.21b}$$

These assumptions are very important as they enable the application of frequency and voltage droop characteristics to fine-tune the reference voltage of the VCVSI, as depicted earlier in Figure 2.5, which is based on

$$\begin{cases} \omega = \omega^* - D_P P, \\ E = E^* - D_Q Q, \end{cases} \tag{2.22}$$

where ω^* and E^*, are the primary control references representing angular frequency and r.m.s output voltage, respectively, of the DG at the no-load condition.

Modifications of the droop coefficients, D_P and D_Q, is mostly achieved by using heuristic or tuning algorithms (such as particle swarm optimization (PSO), Genetic Algorithms (GA), Interior Search Algorithm (ISA), etc.). In the heuristic approach, D_P and D_Q Are

obtained based on the converter power rating and the maximum allowable deviations in voltage and frequency. For example, in a microgrid with N_m DGs, constraints put on the determination of D_P and D_Q, are as given in equation (2.23):

$$\begin{cases} D_{P1}P_{n1} = D_{P2}P_{n2} = \cdots = D_{PN_m}P_{nN_m} = \Delta\omega_{max}, \\ D_{Q1}Q_{n1} = D_{Q2}Q_{n2} = \cdots = D_{QN_m}Q_{nN_m} = \Delta E_{max}, \end{cases} \tag{2.23}$$

where $\Delta\omega_{max}$ and ΔE_{max}, designate the maximum allowable angular frequency and voltage deviations, respectively, while P_{ni} and Q_{ni}, represent the nominal active and reactive powers of the i^{th} DG (Bidram et al., 2017). Contrary to the active load-sharing technique, the conventional droop method can be implemented without any communication links; hence, it is more reliable.

However, some of its drawbacks include (Bidram et al., 2017), (Hossain et al., 2017; LI & NEJABATKHAH, 2014; L. Meng et al., 2017; Reshma Mary Thomas & Deepu Jose, 2015).

i. The approach handles only one control variable for each droop characteristic thus, it is impossible to achieve multiple control objectives simultaneously. For instance, a design trade-off must be considered between the control system's time constant and the voltage and frequency regulation.
ii. Development of the conventional droop method assumes that the effective impedance between the VCVSI and the AC bus is highly inductive. However, this assumption does not hold in microgrid applications where the low-voltage transmission lines are majorly resistive. This renders equation (2.21a) and (2.21b) invalid in microgrid systems.
iii. In a microgrid, frequency is a global quantity, whereas the voltage is not. Consequently, the reactive power control in equation (2.22) may adversely affect the voltage regulation for critical loads.

Further, the conventional droop method cannot distinguish the load current harmonics from the circulating current for non-linear loads. This leads to distortion of the DG output voltage by the current harmonics. These challenges may be addressed by adjusting the conventional droop method to minimize the total harmonic distortion (THD).

The following techniques have been proposed for adjusting the conventional droop method (Bidram et al., 2017), (Hossain et al., 2017; LI & NEJABATKHAH, 2014; L. Meng et al., 2017; Reshma Mary Thomas & Deepu Jose, 2015).

a) Adjustable load sharing method-in which the time constant of the active and reactive controllers can be altered without affecting the DG voltage and frequency.
b) VPD/FQB Droop method-The voltage active power droop and frequency-reactive power boost (VPD/FQB) characteristics approach is proposed for tackling the challenges of low-voltage microgrids with highly resistive transmission lines. Assuming resistive effective line impedance (i.e., $\theta = 0^0$) as is the case in low-voltage transmission lines and also considering δ being small enough, making $sin\ \delta \approx \delta$, then equation (2.20) can be reduced into equation (2.24):

$$\begin{cases} P \approx \dfrac{V_{com}E - V^2{}_{com}}{Z}, \\ Q \approx -\dfrac{V_{com}E}{Z}\delta \end{cases} \tag{2.24}$$

The VPD/FQB technique can also be altered to vary the controller time constant without changing voltage and frequency based on equation (2.25) and Figure 2.8 (Bidram et al., 2017), (Hossain et al., 2017; LI & NEJABATKHAH, 2014; L. Meng et al., 2017; Reshma Mary Thomas & Deepu Jose, 2015).

$$\begin{cases} E = E^* - D_P P, \\ \omega = \omega^* + D_Q Q, \end{cases} \tag{2.25}$$

However, it is highly dependent on system parameters, thereby restricting its application. Moreover, the VPD/FQB technique may malfunction when subjected to non-linear loads and hence cannot assure sustained voltage regulation. The regulation of voltage and frequency in a microgrid is such that in the grid-connected mode, PQ control is preferred. In contrast, a constant voltage and frequency control strategy is favored in the islanded mode.

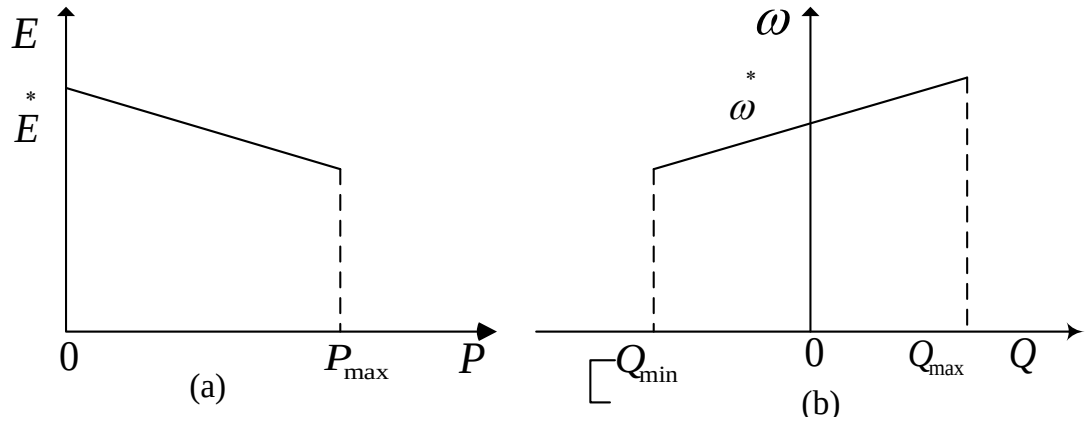

Figure 2.8: Droop/Boost Characteristics For Low-Voltage Microgrids: a) VPD and b) FQB Characteristic

2.3.3 Model Predictive Control

The Model Predictive Control (MPC) is presented in (Du et al., 2017; Morstyn et al., 2018; Nanda et al., 2021; Shen, 2017). The MPC method uses a prediction model based on existing system knowledge and future predictions to determine the control variables in real time (online) for every sampling period. From this, the optimal value of the control variable in the predictive function is selected for the next sampling period (time step) [6], [19]. Thus, an optimization model covering a finite horizon is deployed at every discrete time step to generate a control action sequence, from which the first action is often utilized.

Using the renewed system state and future information, the system then moves to the next time step, and the above computation is repeated [20].

Figure 2.9 shows the MPC block diagram, which can be viewed as a closed-loop system due to the continuous modulation of control variables to compensate for prediction inaccuracies (Seborg E. Dale, 2003).

The present values of the output variables are predicted using the process model. The residuals, denoting deviations of the actual outputs from the predicted outputs, form the feedback signal to a prediction block. The predictions are fed into two types of MPC calculations executed at every sampling instant: set-point and control calculations. The set points are typically computed each time the control calculations are performed.

However, set-points may also be known in advance and thus may need not to be calculated. Inequality constraints on the input and output variables, e.g., upper and lower limits, can be incorporated in either type of calculation.

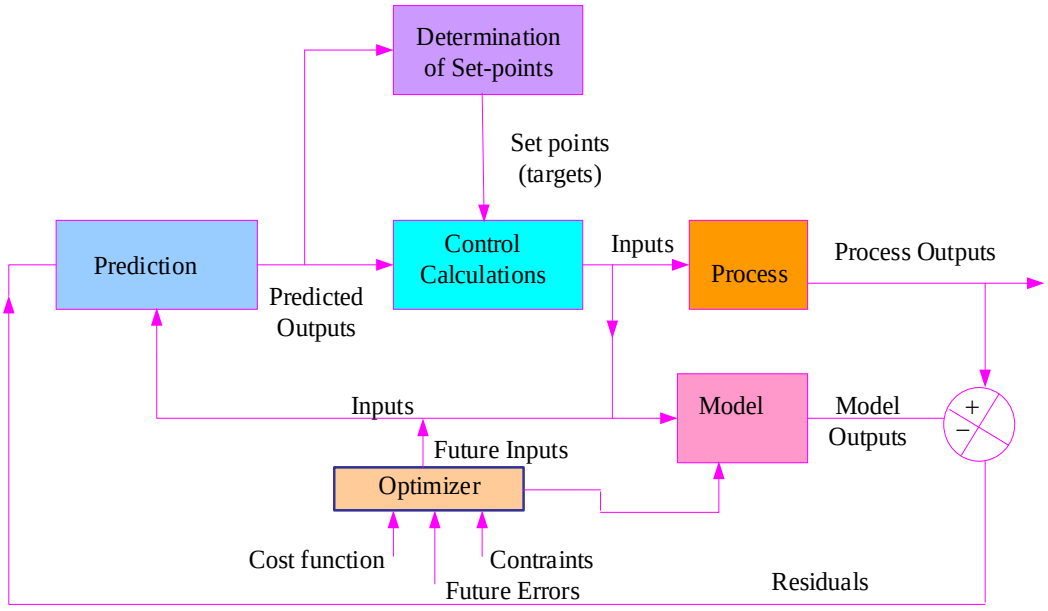

Figure 2.9: Block Diagram for Model Predictive Control

The MPC makes calculations based on present measurements and predicted future output values. The basic formulation of the MPC control problem or algorithms requires five major elements: process model, performance index, constraints, optimization method, and receding horizon principle. Figure 2.10 shows the principle of MPC, where y is the actual output, $\hat{y}$, is the predicted output, and u is the control input (Seborg E. Dale, 2003).

Taking the current sampling instant as k, the MPC strategy calculates a set of M values of the input. $\{\hat{u}(k+i-1|k), i = 1, 2, \dots, M\}$, where M is the control horizon. This set comprises the current input $\hat{u}(k)$ and $M-1$ future inputs. The input is kept constant after the M-control moves. The outputs are calculated so that a set of predicted outputs $\hat{y}(k+i), i = 1,2, \dots, N\}$, where N is the prediction horizon, optimally achieves the set point. The control calculations are based on optimizing an objective function (performance index), which penalizes the deviations of the predicted outputs, $\hat{y}(k+i|k)$ from the reference trajectory $r(k+i|k)$ and the variations in the control input $\Delta u(k+i|k)$ (Kerdphol et al., 2017; Seborg E. Dale, 2003).

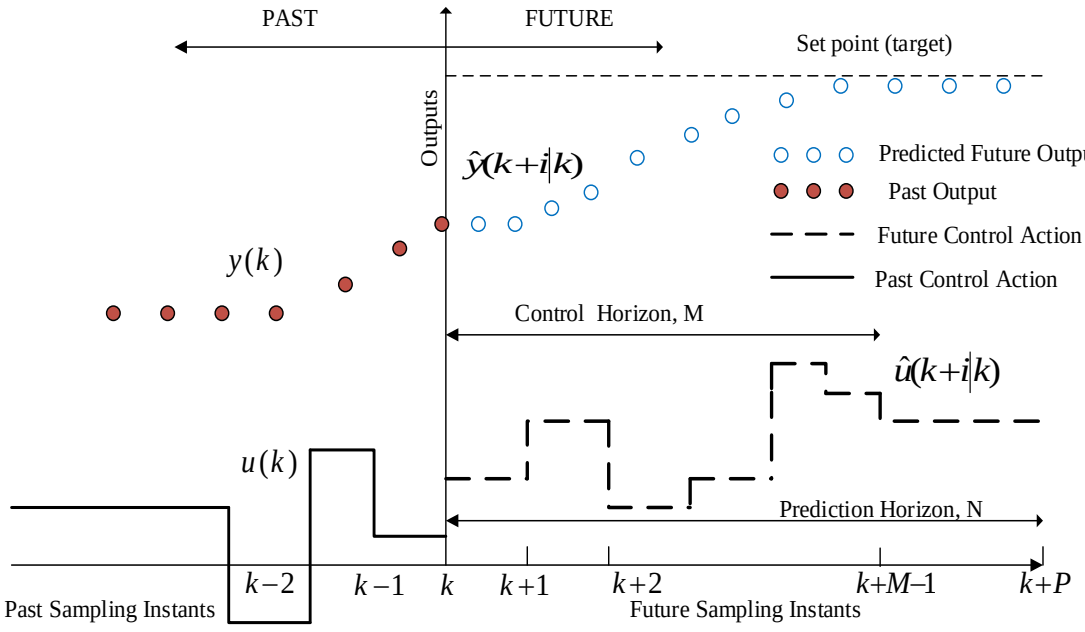

Figure 2.10: Basic Principle of the MPC

For example, for a linear system, the cost function can be formulated as a sum of quadratic functions and is given as in equation (2.26):

$$J = \sum_{i=1}^{N} [\hat{y}(k+i|k) - r(k+i|k)]^T \boldsymbol{Q}_i [\hat{y}(k+i|k) - r(k+i|k)] + \sum_{i=0}^{M-1} [\Delta u(k+i|k)]^T \boldsymbol{R}_i [\Delta u(k+i|k)] \quad (2.26)$$

where y is the controlled variable, r is the set point, Δu is the manipulated variable increment, $\boldsymbol{Q}_i$ is a weighting matrix representing the penalization parameters for control errors and $\boldsymbol{R}_i$, is a weighting matrix representing the penalization parameters for control increments. N is known as the prediction horizon, and M is known as the control horizon (such that after M control changes, the control action is maintained constant). Matrices $\boldsymbol{Q}_i$ and $\boldsymbol{R}_i$, are real, symmetric, positive, semi-definite matrices. The general simplified cost function expressed in matrix notation becomes equation (2.27):

$$J = [\boldsymbol{Y} - \boldsymbol{R}]^T \boldsymbol{Q}_i [\boldsymbol{Y} - \boldsymbol{R}] + \boldsymbol{U}^T \boldsymbol{R}_i \boldsymbol{U} \quad (2.27)$$

The MPC method can be realized in centralized or decentralized schemes and has been widely used as an inverter control strategy (Shen, 2017) and to solve the problem of real-time economic dispatch and power exchange between the microgrid and the Energy Storage (ES) or utility system (Du et al., 2017; Morstyn et al., 2018). With the cost function at hand, the next step is getting predictions based on a prediction model. Various MPC prediction models can be adopted, including Impulse Response Models, Step Response Models, Transfer Function Models, and State Space Models.

The state space algorithm has been adopted in the undertaken study. The discrete-time form of the state space model is as highlighted in equations (2.28) and (2.29):

$$\boldsymbol{x}(k+1) = \boldsymbol{A}\boldsymbol{x}(k) + \boldsymbol{B}u(k) \quad (2.28)$$

$$y(k) = \boldsymbol{C}x(k) \tag{2.29}$$

which is converted into incremental form as given in equations (2.30) and (2.31):

$$\underbrace{\begin{bmatrix} \boldsymbol{x}(k+1) \\ \boldsymbol{u}(\boldsymbol{k}) \end{bmatrix}}_{x_p(k+1)} = \underbrace{\begin{bmatrix} \boldsymbol{A} & \boldsymbol{B} \\ \boldsymbol{0} & \boldsymbol{I} \end{bmatrix}}_{\boldsymbol{F}} \underbrace{\begin{bmatrix} \boldsymbol{x}(k) \\ \boldsymbol{u}(\boldsymbol{k}-\boldsymbol{1}) \end{bmatrix}}_{x_p(k)} + \underbrace{\begin{bmatrix} \boldsymbol{B} \\ \boldsymbol{I} \end{bmatrix}}_{\boldsymbol{G}} \Delta u(k) \tag{2.30}$$

$$\boldsymbol{y}(k) = \underbrace{[\boldsymbol{C} \quad \boldsymbol{0}]}_{\boldsymbol{H}} \underbrace{\begin{bmatrix} \boldsymbol{x}(k) \\ \boldsymbol{u}(\boldsymbol{k}-\boldsymbol{1}) \end{bmatrix}}_{x_p(k)} \tag{2.31}$$

These equations can be written as in equation (2.32) and (2.33):

$$\tilde{\boldsymbol{x}}(k+1) = \boldsymbol{F}\tilde{\boldsymbol{x}}(k) + \boldsymbol{G}\Delta u(k) \tag{2.32}$$

$$\boldsymbol{y}(k) = \boldsymbol{H}\tilde{\boldsymbol{x}}(k) \tag{2.33}$$

where $\boldsymbol{F}, \boldsymbol{G}$ and $\boldsymbol{H}$ are as defined in equation (2.34):

$$\boldsymbol{F} = \begin{bmatrix} \boldsymbol{A} & \boldsymbol{B} \\ \boldsymbol{0} & \boldsymbol{I} \end{bmatrix}, \boldsymbol{G} = \begin{bmatrix} \boldsymbol{B} \\ \boldsymbol{I} \end{bmatrix}, \boldsymbol{H} = [\boldsymbol{C} \quad \boldsymbol{0}] \tag{2.34}$$

The incremental form model reduces steady-state errors. The design of MPC may incorporate constraints, which are broadly classified as hard and soft constraints as well as input, output or state constraints. Typically, the input, output and state constraints are specified as in equation (2.35) (Kerdphol et al., 2017; Seborg E. Dale, 2003).

$$\left.\begin{array}{ll} u_{min} \le u(i) \le u_{max}, & i \in \{k, k+N_u-1\} \\ y_{min} \le y(i) \le y_{max}, & i \in \{k+1, k+N_2\} \\ \boldsymbol{X}_{min} \le \boldsymbol{x_p}(\boldsymbol{i}) \le \boldsymbol{X}_{max}, & i \in \{k+1, k+N_2\} \end{array}\right\} \tag{2.35}$$

In the study undertaken the constraints are necessary to cater for limits in voltages, currents, frequencies, power and state of charge of batteries. The flowchart in Figure 2.11 summarizes the seven steps undertaken in the MPC calculations, in the order they are performed at each control implementation time.

Step 1 acquires new process data via the regulatory control system that is linked to the process. In Step 2, the new output predictions are calculated based on the process model and the new data whereas Step 3 determines the current control structure.

The control structure should not change from one control execution time to another. If this happens, then the control calculations can become ill-conditioned, meaning that the available control inputs have very similar effects on two or more outputs. Such scenarios must be identified and rectified prior to executing the MPC calculations in Steps 5 and 6. Step 7 implements the calculated control actions, usually as set points to regulatory PI or PID control loops. Finally, decision is made by checking the tracking consensus against constraints and specified MPC requirements. If satisfactory, the MPC computation is terminated else if not, then the process is repeatedly incrementally.

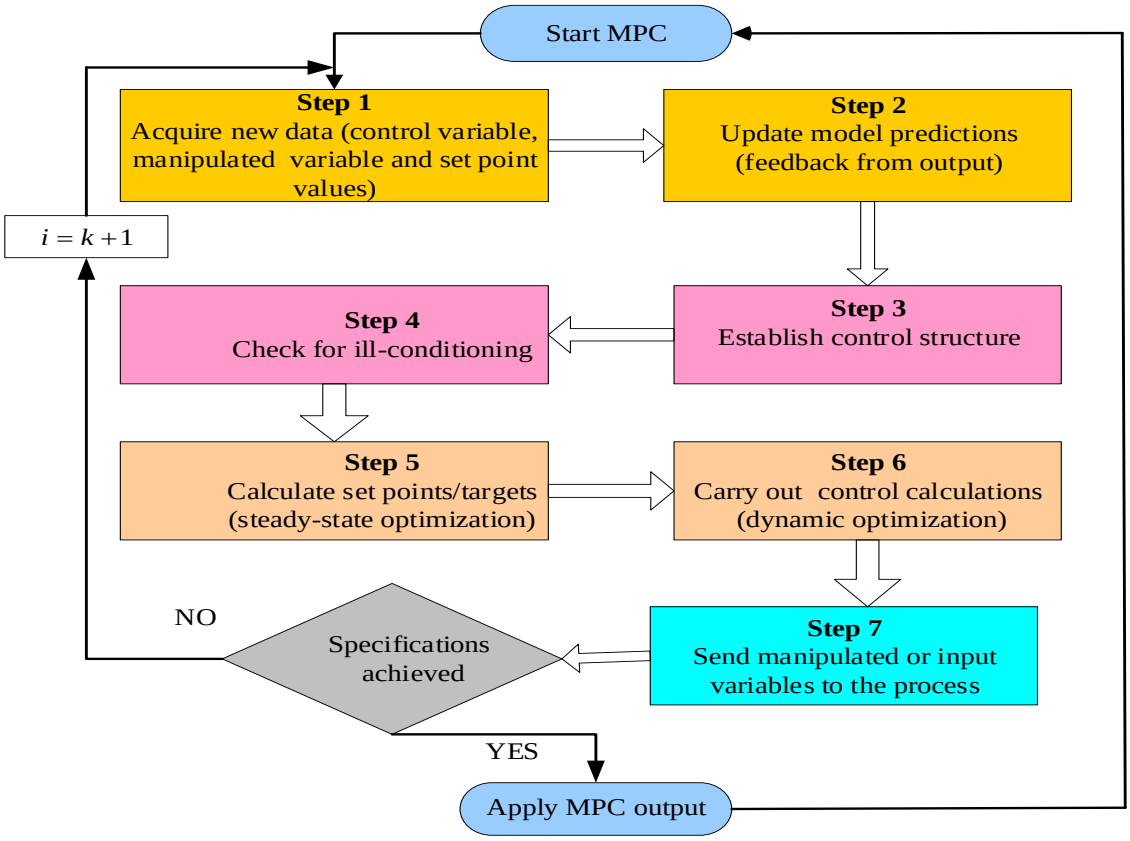

Figure 2.11: Flow chart of MPC Algorithm

The advantages of MPC as a tool include:

1. The method can handle Single-Input-Single-Output (SISO) and multivariable systems,
2. The process model takes care of both dynamic and static interactions between input, output, and disturbance variables,
3. The formulation of MPC enables it to handle constraints on inputs and outputs in a systematic manner,
4. The computations of control actions can be coordinated with the calculation of optimum set points,

5. Accurate model predictions can provide early and timely warnings of potential problems or system malfunctions and
6. MPC formulation allows for closer operation of the system to the constraints and this contributes to higher profits.
7. However, the principal disadvantages of MPC are:
8. The computation of the control law is more complex compared to conventional controllers such as PID.
9. Its success depends on the accuracy of process model, which may not be easy to realize.
10. MPC requires hardware with a high computational ability and this is more expensive.

One of the existing MPC methods for microgrids with distributed ES involves strategies considering only one ES system or aggregated multiple ES systems such as the two BESS used in (Nguyen et al., 2015). This does not account for the power flows between various ES systems. The other category involves strategies based on non-convex optimization. For example, MPC-based on non-linear programming (NLP) in unbalanced microgrids (Morstyn et al., 2018; Nanda et al., 2021). However, if the problem is non-convex, scalability is limited and the available solvers are capable of only providing locally optimal solutions (Morstyn et al., 2018). Recursive dynamic programming (RDP), which produces a globally optimal solution, may be an alternative for the ES system optimal power flow problem. However, its numerical complexity increases with the number of ES systems (Morstyn et al., 2018).

Morstyn et al. (Morstyn et al., 2018), proposed a new convex MPC strategy for solving the dynamic optimal power flow problem between battery energy storage systems distributed in an AC microgrid. The problem formulation is based on a linear $d-q$ reference frame VCM and linearized power flow approximations. The performance of the strategy was evaluated from the real-time digital simulations conducted for an islanded microgrid based on the IEEE 13 bus prototypical feeder. The system had distributed battery energy storage system (BESS) and intermittent PV generation. The results

indicated that the proposed control strategy approaches the performance of a strategy based on non-convex optimization, while minimizing the required computation time by a factor of 1000.

Since the problem was solved as a convex Quadratically Constrained Quadratic Program (QCQP), for which fast and robust solvers exist, it is recommended for a real-time receding horizon MPC implementation (Morstyn et al., 2018). The method does not assume real and reactive power flows are decoupled, allowing line losses, voltage constraints and converter current constraints to be considered in the optimization. The implementation of MPC for solving nonlinear optimization problems at each time-step is called nonlinear MPC (NMPC) and is presented in (Nanda et al., 2021) for microgrids.

The performance of a DC microgrid with a hybrid energy storage system having battery-supercapacitor combination is improved using Filtration-based Model Predictive Controller (FB-MPC) by Abadi et al. (Ghorashi Khalil Abadi et al., 2022). The FB-MPC strategy has been used to carry out the sharing of power/current between the BESS and the supercapacitor, enabling the microgrid voltage controller to operate with higher gain values.

Zhao et al. (Zhao et al., 2022) proposed an adaptive intelligent MPC for load frequency control in a microgrid. The results showed that the performance of the MPC based on a type-2 fuzzy system has the best performance followed closely with type-1 fuzzy MPC but both of which recorded a better performance than the traditional MPC.

A consensus-based energy management in a DC microgrid is performed using MPC by Ali et al. (S. U. Ali et al., 2023). The MPC controller assists the individual controllers for the distributed renewable energy sources and BESS to operate as grid forming or grid feeding based on the power flow mode selection. It was observed that the MPC method exhibited settling time of less than 1 μs and 5% overshoot in comparison with the PI and Sliding Mode Control (SMC) strategies.

2.3.4 Artificial Intelligence Control Methods

When PV-wind hybrid microgrid systems are to be implemented in remote areas, which are ideal for stand-alone operation, it becomes challenging to acquire long-term weather data such as solar irradiation and wind speed to aid in generation sizing by matching actual generation to the load demand. Consequently, artificial intelligence techniques such as Artificial Neural Networks (ANN), Fuzzy Logic (FL), Genetic Algorithms (GA) and particle swarm optimization (PSO) become very useful in sizing stand-alone systems as compared with the conventional sizing method, which is highly dependent on long-term weather data (Badwawi et al., 2015; Borges et al., 2017; Jayachandran & Ravi, 2017; Sawle et al., 2016; T. Wang et al., 2019).

2.3.4.1 Genetic Algorithm Method

Genetic Algorithm (GA) method is a search technique and is suitable for a complex problem such as a PV-wind hybrid system when other techniques do not offer acceptable solutions. In this case, the weather conditions are varying hourly and daily and thus will be different for different seasons in a year. The GA method can be deployed to aid in obtaining the optimum number of facilities to use based on the hourly average metrological and load data collected say over a few years for simulation purposes (Sawle et al., 2016). Figure 2.12 shows breakdown of the GA algorithm (Korjani et al., 2017; Sawle et al., 2016).

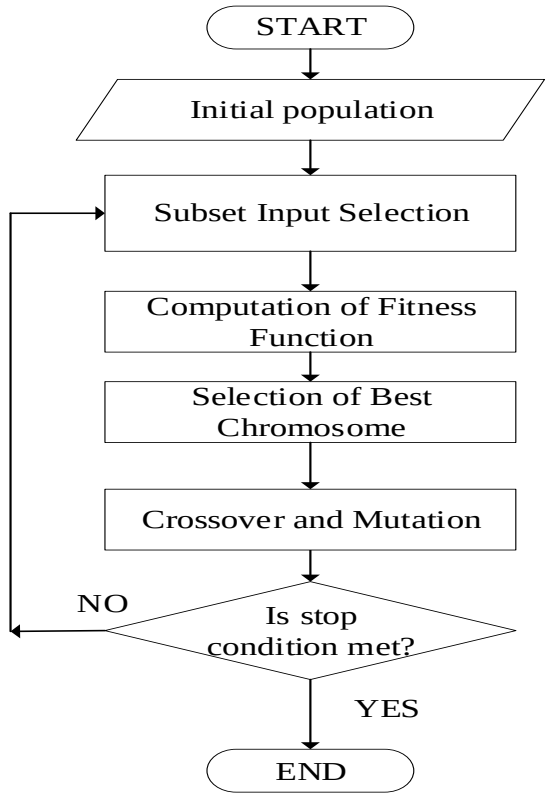

Figure 2.12: Flow chart of GA Algorithm

Most researchers using GA in microgrid problems such as in (Korjani et al., 2017) create initial population based on weather and load data sets. The data is manipulated iteratively using selection, crossover and mutation until a preset condition is attained. The implementation of GA algorithm requires that the following important parameters are specified: population size, maximum number of generations, number of elite chromosomes, selection method, crossover function and fraction, mutation function, and mutation rate.

2.3.4.2 Artificial Neural Networks (ANN)

Artificial Neural Network (ANN) mimics how the central nervous system of the human body functions. The basic structure of an ANN is composed of three layers, namely: input layer, hidden layer and output layer. The ANN has a self-learning feature, which enables

the algorithm to be easily designed for different operating conditions and grid disturbances (Hossain et al., 2017). However, it lacks performance in off-line training technique. Wang et al (T. Wang et al., 2019) used the Lagrange programming neural network (LPNN) in a hybrid microgrid to achieve optimal scheduling and management. The objective function includes power generation cost, fuel cost, operating and maintenance cost and emission-control cost. It is solved so as to minimize total cost and maximize the power generated by the DERs subject to some defined equality and inequality constraints. Through combination of the variable neurons with Lagrange neurons, the LPNN minimized the cost function and maximized the energy generated by the Wind Turbines (WTs) and Photovoltaic cells (PVs) as confirmed from the results simulated in MATLAB.

In addition, the energy stored into and supplied from the storage system was optimized too. Further, the Radial Basis Function Neural Network (RBFNN) achieved day-ahead prediction of load demand and renewable resources. When the results of LPNN were compared with those of the basic PSO it was observed that the LPNN was better than the PSO method. For instance, when LPNN cost is $\$274.64$ and PSO cost is $\$476.84$, and defining LTP as the ratio of PSO to LPNN then the LTP becomes 1.74, indicating clearly that the PSO is weaker in dealing with constrained problem (T. Wang et al., 2019).

2.3.4.3 Particle Swarm Optimization

The Particle Swarm Optimization method (PSO), introduced in 1995, is reported in (Borges et al., 2017; Jayachandran & Ravi, 2017; Sawle et al., 2016; T. Wang et al., 2019) which can be used in optimal sizing of the hybrid energy systems. The algorithm treats the generation units as if they are selected particles from a swarm of particles, say p, within a design space, say D. The discrimination within D is carried out based on the position and speed of a particle such that in every iterative process, each particle continuously records the best solution thus far during its flight (Sawle et al., 2016). The position and speed may be assigned different variables in a PV-wind microgrid optimization problem. Borges et al (Borges et al., 2017) applied the PSO method to solve a day-ahead microgrid dispatch problem taking into account uncertainties which are

associated with energy production by the PV and wind sources. The stated uncertainties were modeled by incorporating a robust approach in PSO and the method tested on 21-bus microgrid (MG) of a university campus located in Portugal. From the test results, it was observed that the robust optimization approach (PSO) was more advantageous (17%) compared to the deterministic optimization, including worst case scenario. Although the execution time of PSO (2360 seconds) is comparatively high, it was acceptable for the day-ahead decision time.

The success of PSO scheme is also reported by Jayachandran et al. (Jayachandran & Ravi, 2017), where it is used in the design and optimization of a Hybrid Microgrid System (HMGS) using site specific solar and wind meteorological data. Specifically, in this study, PSO was applied in determination of the sizing of wind turbines (WT), photovoltaic (PV) module, battery energy storage system (BESS) and diesel generator. The contribution of solar PV energy was higher than the wind. Based on the simulation results obtained in MATLAB and evaluated in the worst-case scenario and the sensitivity analysis conducted, it is observed that the PSO technique achieved the best size and configuration of PV-wind based HMGS. In the microgrid considered in this study, the GA has been selected over PSO as it can improve solution through mutation (Exploration) and crossover (Exploitation) operators (Korjani et al., 2017; Sawle et al., 2016).

2.3.4.4 Fuzzy Based Controllers

The Fuzzy Control Methods possess the ability to manage the non-linear behavior of complex control structures since they take advantage of heuristics and expert knowledge of the process under control. It is also insensitive to variations in system parameters. However, the strategy is relatively slow. Lavanya et al. (Lavanya & Senthil Kumar, 2018), refer to a Fuzzy Logic Controller (FLC) used in the non-linear DG interface for voltage regulation, control of real and reactive power as well as an Adaptive Linear Neuron (ADALINE) utilized to eliminate harmonics and unbalance compensation. The FLC is also implemented together with the conventional Proportional plus Integral (PI) controller

to regulate voltage and frequency in AC microgrid. In addition, a new intelligent droop control deploying adaptive neuro-fuzzy inference system (ANFIS) is mentioned in (Lavanya & Senthil Kumar, 2018). This is used to provide a solution for intelligent model-free based Generalized Droop Control (GDC) and achieves desired voltage and frequency regulation in an islanded microgrid.

2.3.4.5 Adaptive Neuro-Fuzzy Inference System (ANFIS) Controller

Adaptive Neuro-Fuzzy Inference System (ANFIS) method is used as a teaching method for Sugeno-type fuzzy systems and was proposed by Jang in 1993 (A. Alwal et al., 2016; Jang, 1993).

The method is more efficient because it combines the advantages of FLC and ANN approach to construct a nonlinear self-tuning controller. In addition, since the rules are in linguistic format, intermediate results can be analyzed and interpreted easily. A typical architecture of the ANFIS control structure is shown in Figure 2.13, in which a circle indicates a fixed node, whereas a square indicates an adaptive node.

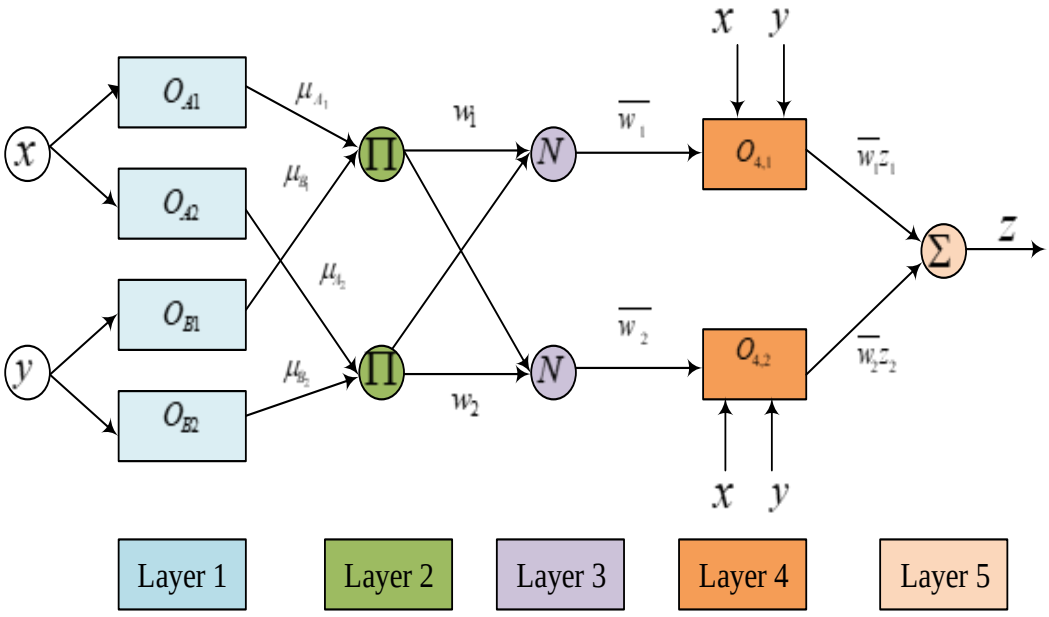

Figure 2.13: Typical ANFIS architecture

For simplicity, two inputs x, y, and one output z structure is considered. A common rule set can be expressed as in equations (2.36) and (2.37) for a first-order Sugeno fuzzy model with two fuzzy if-then rules.

Rule 1: If x is A_1 and y is B_1, then:

$$z_1 = p_1 x + q_1 y + r_1 \tag{2.36}$$

Rule 2: If x is A_2 and y is B_2, then:

$$z_2 = p_2 x + q_2 y + r_2 \tag{2.37}$$

where A_i and B_i, are the fuzzy sets in the antecedent, and p_i, q_i, and r_i, are the design parameters that are determined during the training process. The ANFIS network structure is made up of a set of units (and connections) organized into five connected network layers, 1 to 5, as shown in Figure 2.13 (A. Alwal et al., 2016; Jang, 1993). The significance of each layer and detailed operation of the 2-input-1-output ANFIS structure is presented in (A. Alwal et al., 2016; Jang, 1993).

The PSO acting alone depicted increased computation time and can't improve the solution through mutation and crossover as does the GA. However, the GA on its own, may yield random mutation that may pose challenges to the stable and accurate operation of the microgrid when used alone. The FLC utilized alone, though depicting the ability to manage non-linearities while exploiting heuristics and expert knowledge, is comparatively slow. Therefore, in this study, a hybrid combination of GA and ANFIS has been chosen as the primary microgrid controller to borrow from the strengths of each controller. This is because the ANFIS, though possessing the intelligence and learning ability, it does not provide optimal results when acting alone. The Genetic Algorithm (GA) controller has been used to optimize the ANFIS and further reducing the settling time and rise time.

2.3.5 Software for Optimization of Microgrid Systems

Several software tools have been developed to aid in designing and optimizing hybrid microgrid systems. They also offer a means of assessing the performance of renewable energy systems. Most of these tools are commercial (ABB Power, 2015; GE Digital Energy, 2012; Katiraei et al., 2017; Sawle et al., 2016). Reference (Sawle et al., 2016) presents a detailed coverage of the software tools for optimizing hybrid systems with predefined system configurations. The results' advantages, disadvantages, achievable tasks, and validity are captured. The software tools include SOMES, HOMER, HYBRID 2, INSEL, SOLSIM, WATSUN-PV, PVSYST, PV-DESIGN PRO, RAPSIM, PHOTO, RAPSYS, RETScreen, ARES and PVF-chart. From these, only the first two (SOMES and HOMER) are recommended for PV-wind hybrid system since both have the ability to provide optimal design of the hybrid system. For instance, HOMER can be used to model both conventional and renewable energy technologies: including PV, wind turbine, diesel generator, fuel cell, utility grid, run-of-river hydropower, micro turbine, battery bank and hydrogen storage. It conducts simulation for all of the possible system configurations, including whether off-grid or on-grid and determines a feasible one. Next, HOMER estimates the installation and operation cost of the system and displays a list of configurations arranged according to their life cycle cost. The tool also offers a powerful user interface, accurate sizing and detail analysis of the system (Badwawi et al., 2015; Sawle et al., 2016).

In (GE Digital Energy, 2012), the Grid IQ Microgrid Control System (MCS) developed by General Electric (GE) Company in 2012 is presented. This commercial supervisory control architecture based on U90PLUS Generation Optimizer provides optimization solutions for permanently islanded or grid-connected microgrids. The software can forecast load, renewables, and electricity prices; carry out microgrid generator unit commitment integration, energy storage integration, intelligent local controllers, and a suite of security features.

In (ABB Power, 2015), the “Microgrid Plus” control system based on the MGC600 series of controllers, developed by ABB Australia Pvt. Ltd, is introduced. This commercial modular, networked, and easily configured power flow and energy storage control system is suitable for stabilizing intermittent renewable generation such as PV and wind into microgrids. The system is designed for use in isolated microgrids, remote communities and research centers, and predominantly grid-connected microgrids, such as commercial and industrial complexes and education campuses.

Katiraei et al. (Katiraei et al., 2017) capture the state of commercial microgrid controllers, exposing the strengths and weaknesses of adopting such microgrid control strategies. It is reported that currently, most suppliers offer a microgrid control solution instead of a set of microgrid control products that can be accessed off-the-shelf and utilized directly in a project by the system owner’s engineers. This situation denies the system investors some flexibility, scalability, and accessibility in implementing controls. In addition, although the proprietary approaches offer a high level of security and reliability, there are challenges regarding the long-run sustainability and maintainability of the proprietary aspects of the control system.

Any change in the microgrid system characteristics raises maintenance costs due to continued vendor involvement. For example, there may be a need to incorporate a new generation unit such as a PV system, wind turbine, or load (due to increased demand) or a new component (due to technological changes). The needs to be addressed include standardization of the core microgrid control functions and formulation of common development and verification procedures for microgrid control systems. Furthermore, a provision should be made for interoperability regarding communication and data exchange among devices, remote access and control by the operator, and the interrelationship between protection functions and controls.

2.4 Other Control Strategies and Emerging Issues

Jain et al. (Jain & Arya, 2015) point to ANFIS-based Generalized Droop Control (GDC), which is used to overcome the drawbacks of GDC-based frequency and voltage control in microgrids utilizing more than one DG. The ANFIS-based GDC deploys the training ability of the ANN to the FL to create a new hybrid technique, termed ANFIS. The ANFIS is trained using input-output (I/O) data saved from the GDC approach. Once a valid model is achieved, the ANFIS-based controller is used instead of the GDC in the inverter-interfaced DG control structure. This approach applies to a wide range of MGs and does not require knowledge about the MG structure or the line parameters (Jain & Arya, 2015).

Microgrid islanding control can be achieved through peer-to-peer or master-slave strategies (Huang et al., 2011; Shen, 2017). The peer-to-peer strategy allows microsources to be added to the microgrid without adjusting the existing control and protection set up. It can be implemented by droop control. The master-slave strategy is shown in Figure 2.14 [6].

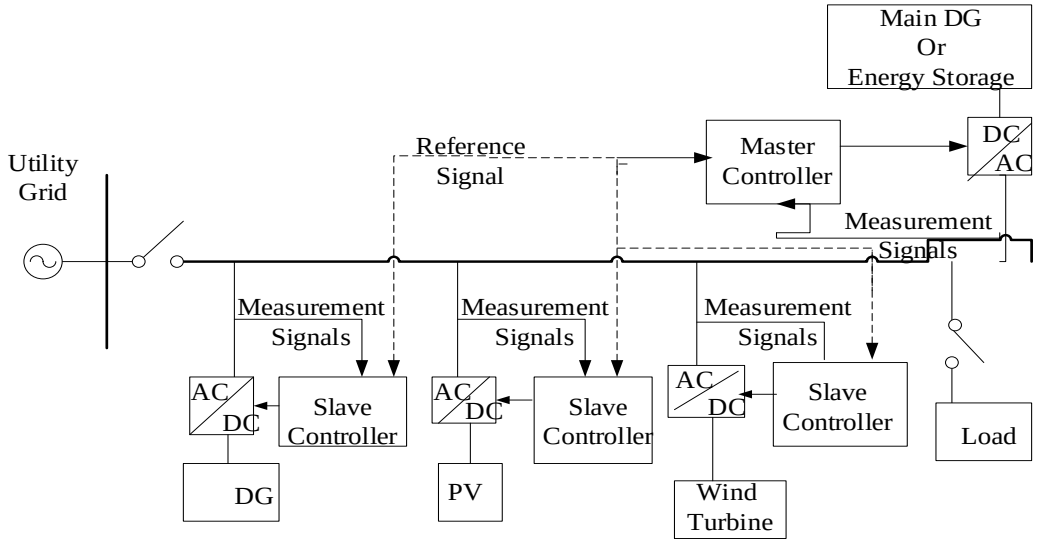

Figure 2.14: The Master-Slave Control Structure

Here, there is a master controller, while the others are slave controllers that receive instructions from the master controller via a communication link. In islanded mode, the master controller in the microgrid maintains the system frequency and power balance separately using a suitable algorithm.

Shen (Shen, 2017) adopted the droop control based on Model Predictive Control (MPC) in a peer-to-peer control structure. It is highlighted that when operating in the grid-connected model, the utility grid will ensure that the microgrid has a stable voltage and frequency. On the other hand, when operating in islanded mode, the microgrid is required to sustain its stable voltage and frequency, hence droop control.

This study considered only PV micro-source in the simulation model. However, a real microgrid system may incorporate additional micro-sources such as wind turbines and battery storage. Furthermore, the MPC controller proposed in (Shen, 2017) is developed for the limit step system.

2.5 A Review of Hybrid Controllers and Selected Existing Studies

Several studies have been done on the modeling of hybrid PV-wind energy systems. For instance, Jayachandran et al. (Jayachandran & Ravi, 2017) designed and optimized an Islanded Hybrid Microgrid System (IHMS) in which Particle Swarm Optimization (PSO) was used to obtain the lowest cost with a shorter computation time than the Genetic Algorithm (GA). Samrat et al. (Samrat et al., 2015) also studied the IHMS using a bidirectional DC-DC buck-boost converter controller for battery charging. At the same time, a three-phase voltage source inverter regulates the load voltage and frequency using a complex vector control scheme. Sawle et al. (Sawle et al., 2016) present several PV-wind hybrid system combinations alongside modeling parameters of the components and software tools for sizing. The distributed inverter control strategy is proposed by (Khalil et al., 2016) for load power sharing between PV and Wind, whereas authors in (Orłowski, 2022) used switched Model Predictive Control (MPC).

Some studies have presented modeling and simulation of the generic renewable energy-based systems, which are not specific to a microgrid, with a Permanent Magnet Synchronous Generator (PMSG) Wind Turbine used in studies such as (Elbeji et al., 2014; Kokate et al., 2019; C. N. Wang et al., 2014). The microgrid system is considered, for instance, in (Amara et al., 2020; Jayachandran & Ravi, 2017; Khalil et al., 2016; Orłowski, 2022; Samrat et al., 2015). The modeling of a Battery Energy Storage System (BESS) using mathematical and circuit-oriented techniques is provided by authors in (Li & Ke, 2011), while (J. Meng et al., 2018) presents the modeling of a Lithium-Ion battery with state of charge approximation.

The concepts concerning the DC-DC boost converter modeling are introduced in (Abdel-Rahim, 2020), where a high step-up DC-DC boost converter with an MPC-based MPPT algorithm is applied to a PV system. However, the variable switching frequencies created problems of optimum design, and no interleaving was used. A comparison between interleaved DC-DC boost converters (IBC) and the conventional boost DC-DC converter is presented in a general case in (Faraj & Hussain, 2020a) and IBC compared with Cuk Converter for PV system in (R.D Tayade & S. & Mopari, 2017), both of which reinforced the benefits of IBC.

In addition, (Prabhakaran & Agarwal, 2020) applies a Single-Ended Primary Inductance Converter (SEPIC) type interleaved DC-DC boost converter to a bipolar DC microgrid, while the three-phase parallel IBC of (Hisar, 2020) demonstrates how output ripples decrease with an increase in the number of parallel converters. The System Advisor Model (Blair et al., 2018) presented a platform to access technical details of actual microgrid components and data for building case studies.

Various MPPT algorithms are presented for PV systems, namely P&O for the standalone PV system (ÖZEL & KARAARSLAN, 2020), P&O with confined search space in (Kamran et al., 2020), and P&O for the grid-connected PV system in (Mohamed & Abd El Sattar, 2019). The MPPT algorithms for a PMSG-based wind energy conversion system (WECS) are reported by authors in (Sahin et al., 2017) using P&O MPPT and in (Tounsi

et al., 2018) using Proportional plus Integral (PI) MPPT. Moreover, authors in (Zebraoui & Bouzi, 2018) compared various MPPT methods for WECS. The researchers in (Fouad et al., 2017) used MATLAB & SIMULINK to model microgrid system components. However, it has not presented the mathematical equations and equivalent circuit models used to create the SIMULINK models, nor has the interleaving technique been applied.

The hybrid PV-wind system model in (Sawle et al., 2016) has a diesel generator based on a single diode. However, detailed equations for modeling the PV system, the WECS, and the SIMULINK models have not been presented and are not specific to the microgrid. Further, a hybrid PV-wind with storage and a diesel generator is given in (Grzegorz Ma´slak and Przemysław Orłowski, 2022; Samrat et al., 2015; Sawle et al., 2016; Sumathi et al., 2015) and without the diesel generator in (Amara et al., 2020; Fouad et al., 2017; Khalil et al., 2016; Kokate et al., 2019; Prabhakaran & Agarwal, 2020). Most studies, such as (Amara et al., 2020; Khalil et al., 2016; Mohamed & Abd El Sattar, 2019; Samrat et al., 2015; Sawle et al., 2016), used single-diode equivalent circuits in modeling off-grid PV systems owing to their simplicity and acceptable accuracy. In contrast, a few others, like (Priyadarshi et al., 2018; Yahyaoui, 2018), used the double diode equivalent circuit model, which is very accurate but requires intensive mathematical manipulation.

Several authors have applied Artificial Intelligence (AI) techniques in microgrid control. Korjani et al. (Korjani et al., 2017) used a Genetic Algorithm (GA) to solve a microgrid-clustering problem while minimizing power exchanges. The results from the IEEE 69-bus network showed better convergence than the Tabu Search (TS). Abdulhussein et al. (Hizam, 2022) proposed three algorithms, namely PID, Artificial Neural Networks (ANN), and Fuzzy Logic Control (FLC), for voltage regulation in a hybrid microgrid system. The MPPT controller is based on the P&O method. The results simulated in MATLAB & SIMULINK depicted the FLC to be better than the PID and ANN on account of efficiency and precision.

Gamage et al. (Gamage et al., 2021) designed an ANFIS controller for an off-grid PV microgrid with a battery and super capacitor. The simulated results indicated better

performance of the ANFIS in voltage regulation (Root Mean Squared Error (RMSE) value $= 0.137$, settling time of $0.055\ s$) compared with other controllers such as FLC (RMSE value $= 0.357$, settling time of $0.076\ s$) and conventional PI (RMSE value $= 1.373$, settling time of $0.25\ s$). Truong et al. (Truong et al., 2021) controlled the inverter DC voltage in a hybrid solar and wind grid-tie system using an ANFIS controller. Like (Hizam, 2022), the MPPT controller deployed the P&O method. ANFIS controller performed better than the traditional PI controller in reducing overshoot and settling time. Bogaraj et al.(Bogaraj & Kanakaraj, 2016) report the successful utilization of ANFIS controller in energy prediction for an HRES and a PV system by Pawar et al. (Pawar & Nema, 2020).

Bilgundi et al. (Bilgundi et al., 2022) introduced an ANFIS-optimized PI current controller to address the impact of frequency variations, voltage distortion, and nonlinear load simultaneously. The ANFIS-PI controller performed better than FLC and PI controllers by recording a Total Harmonic Distortion (THD) of $4.5\ \%$ compared to $12.4\ \%$ and $22.6\ \%$ for FLC and PI controllers, respectively.

Elsisi et al. (Elsisi et al., 2021) designed an ANFIS controller for battery charging that was trained using data generated by a GA-based PI controller in MATLAB & SIMULINK. The GA-based ANFIS controller performed better than the conventional PI controller and the GA-based PI controller regarding reduced overshoot and settling time.

2.6 A Review of Techniques Involved in Battery Energy Storage System

2.6.1 The Role of Battery Energy Storage System (BESS) in Microgrids

The Battery Energy Storage System (BESS) is necessary for a microgrid to serve various functions such as (Chatzigeorgiou et al., 2024; Hannan et al., 2021):

1. Off-grid support in which the BESS is used for energy storage in standalone energy systems or standalone micro-grid systems,
2. Seasonal storage such as the ability to store energy for a longer period,

3. Frequency regulation and stability control where the BESS facilitates the maintenance of a constant frequency in the system,
4. Reliability enhancement by improving microgrid quality of service
5. Power quality and voltage control in which a constant voltage is maintained through reactive power injection,
6. Load leveling and peak shaving where demand is transferred elsewhere and the peaks are minimized.

Nikolas et al. (Chatzigeorgiou et al., 2024) conducted a detailed review of BESS-based solutions, focusing on applications, developments, and research trends for hybrid installations. Some of the studies reported capture the BESS utilization based on techno-economic analysis, others focus on the operational control, the other category on system sizing, and the last group focus on demand response.

The operation of a BESS can be deployed in any of the following six distinct modes, each dependent on factors such as energy capacity, irradiance availability, grid status, and energy demand (Anwar et al., 2024): Mode A1 (Charge and Export), Mode A2 (Export only), Mode A3 (Charge only), Mode B1 (Discharge and Import) Mode B2 (Import only) and Mode B3 (Discharge only). Kumar, (S. Kumar, 2022) introduced battery charging and discharging dynamics by mainly focusing on the Lead-acid and Lithium-ion BESS in MATLAB&SIMULINK environment.

2.6.2 Battery Energy Storage System Types and Technologies

BESS technologies based on electrochemical reactions are broadly classified into primary and secondary BESS. Primary BESS are non-rechargeable hence used only once and discarded such as the Zinc carbon dry cells and Alkaline cells. Secondary BESS are rechargeable batteries that are reusable and include Lead-acid, Nickel Cadmium (NiCd) Nickel Metal Hydride (NiMH), and Lithium-ion (Li-ion) batteries (Anvari-Moghaddam et al., 2021; Yahyaoui, 2018), (Chatzigeorgiou et al., 2024; Hannan et al., 2021). A detailed overview of different BESS technologies considering life cycle, efficiency, power

and energy density, advantages, limitations, and applications is provided in (Hannan et al., 2021). Table 2.2 shows the comparison of various BESS technologies (Anvari-Moghaddam et al., 2021; Yahyaoui, 2018), (Hannan et al., 2021).

Table 2.2: Battery Technologies Comparison

	Units	Lead-acid	Lithium-ion	Sodium-ion	Sodium-sulphur	Va-redox flow
Life time	years	Not good	Very good	Very good	Good	Good
Cycles	number	Not good	Good	Good	Good	Very good
Depth of Discharge	%	Not good	Good	Very good	Very good	Very good
Efficiency	%	Not good	Very good	Good	Not good	Not good
Self-discharge	$\%/day$	Good	Good	Good	Very good	Good
Response (Charge/ Discharge)	s	Very good	Very good	Very good	Good	Good

Linking with the information from Table 2.2, it is clear that the Lead-acid batteries possess lower energy density, has lower efficiency (80 to 85%) and charges ten times slower than the Lithium-ion batteries. The later possesses a higher energy density, higher efficiency of 95% and above and charges ten times faster than the Lead-acid BESS (S. Kumar, 2022; Tan, 2021). Table 2.3 compares vital parameters for the two types of batteries considered.

2.6.3 Types of battery Energy Models

The three main classical empirical models are the Shepherd model, the Unnewehr Universal model, and the Nernst model. The Shepherd model is known to perform well in the case of a continuously discharging current, whereas the Nernst model achieves the best accuracy. Electric Circuit Models (ECM) are battery models based on electrical equivalent circuits constructed using combinations of resistors, capacitors, voltage sources, and current sources.

Table 2.3: Comparison of Vital Parameters for the Lead Acid and Li-Ion Batteries

Parameter	Lead Acid Batteries	Lithium Ion Batteries
Life Cycle	Lower life cycle (400-1500 cycles).	Higher life cycle (2000-4000 cycles).
Deep cycle charging	1. Can only handle a charge rate 0.2 times its capacity. 2. Charges ten times slower 3. Can handle over-charging.	1. Li-Ion can handle a charge rate 5 times its capacity. 2. Ten times faster charging time. 3. Can't handle over-charging
Energy density/ Effective battery capacity/ power density	1. Lower energy density-stores less energy for the same physical space. 2. Lower power density-BESS created in this study using a nominal power density of 930 kWh. 3. Weigh 30% more for equivalent Li-ion capacity.	1. Higher energy density-Stores more energy using the same physical space. 2. Higher power density-BESS of 2713 kWh in this study. 3. Weigh 30% less for equivalent lead acid capacity.
Discharge curve	Their voltage drops significantly throughout the discharge rate.	Has a nearly flat discharge curve (battery voltage falls very little until almost fully discharged).
Efficiency	Offer 80 to 85% efficiencies (Amara et al., 2020).	They are at least 95% efficient.

Examples: the Rint model, Thevenin model, Impedance-based models, Run time-based models, Partnership for a New Generation of Vehicles (PNGV), and the General Non-linear (GNL) model (Li & Ke, 2011; J. Meng et al., 2018).

According to the Shepherd model, which is considered a voltage-current classical empirical battery energy model, the constant-current discharge equation is given by equation (2.38) (Li & Ke, 2011; J. Meng et al., 2018):

$$V_{batt} = E_0 - K\left[\frac{Q}{(Q - it)}\right]i - Ri = E_0 - \left[\frac{K}{SoC}\right]i - Ri \qquad (2.38)$$

where V_{batt} is the terminal voltage, E_0 is the Full capacity battery open-circuit voltage (OCV), R is the internal resistance, K is the polarization resistance coefficient (Ω), P_{BAT} is the battery capacity (Ahr), i is the battery current (A), $it = \int i.dt$ (Ahr) = Charge and SoC is the State of Charge.

The State of Charge (SoC), is defined as in equation (2.39):

$$SoC = \frac{(P_{BAT} - it)}{P_{BAT}} \tag{2.39}$$

2.7. Summary of Research Gaps and Proposed Approach

Based on the literature reviewed, every control strategy has its merits and demerits as well as levels of efficiency and cost [1]-[14]. Consequently, every approach should be assessed based on the needs of the microgrid for which it was designed. From the reviewed literature on microgrid modeling and control, it is clear that a microgrid control system's success relies on the accuracy and dependency of the microgrid model and controller, which is still being improved through research.

Conventional control methods for regulating microgrid voltage and frequency, such as PI control, require accurate mathematical models of the microgrid and exhibit serious struggles with non-linearities. On the other hand, artificial intelligence-based control strategies such as FLC and ANN-based methods do not require accurate mathematical models of the microgrid. They can handle the nonlinear dynamics of the system. This study addresses challenges in hybrid PV-wind microgrid modeling and control using the interleaving technique and the GA-ANFIS-MPC controller.

The contribution of this work is the developed reliable and intelligent multilevel microgrid control scheme based on a Genetic Algorithm-Adaptive Neuro-Fuzzy Inference System-Model Predictive Control (GA-ANFIS-MPC) controller for a PV-Wind generation system. Utilizing the GA-ANFIS-MPC algorithms is meant to draw from their strengths while shunning their weaknesses; compensating for the inadequacies of each algorithm is used alone.

In terms of interleaving technique, some existing models have not used the DC-DC converter interleaving technique, such as [4], [5], while in (Samrat et al., 2015), only

inverters are interleaved. From the perspective of control (MPPT) algorithms, some existing models only have MPPT on the PV side, while some have neither used the interleaving technique nor the GA-ANFIS-MPC. Apart from using the interleaving technique for micro sources, converters, and storage, the proposed model has a GA-ANFIS controller for both PV and wind-side DC-DC boost converters and an MPC controller for the BESS converter. The DC-DC boost converter was modified by incorporating an RC circuit parallel to the output capacitor.

A unique approach was taken in designing, modeling, and analyzing the proposed PV-wind-based MCS by deploying mathematical and software tools to formulate a dynamic model of the microgrid and its case study. The application of the intelligent GA-ANFIS-MPC microgrid control system was then conducted. The research outcome significantly enhances the performance of microgrids in supplying quality power to off-grid locations and rural areas by improving the control and tracking of voltage to $\pm 5\%$ of the desired output voltage. Table 2.4 compares the proposed and the existing hybrid microgrid models.

Table 2.4: The Proposed Versus the Existing Hybrid Microgrid Models

Description	Existing Hybrid Microgrid Models	Proposed Hybrid Microgrid Model
Interleaving Technique	1. Some existing models have not used the DC-DC Converter interleaving technique, such as (Jayachandran & Ravi, 2017), (Samrat et al., 2015). In (Khalil et al., 2016), only inverters are interleaved. 2. Few studies reviewed used interleaved DC-DC converters in microgrids.	1. Used interleaving technique for micro sources, converters, and storage. 2. Used the modified DC-DC boost converter by incorporating an RC circuit in parallel with the output capacitor.
Mathematical/Simulation modeling	1. Most existing models used the single diode model in the PV cell for simplicity (Alzahrani et al., 2017; Amara et al., 2020; Khalil et al., 2016; Sahin et al., 2017; Samrat et al., 2015; Sawle et al., 2016), except (Priyadarshi et al., 2018; Yahyaoui, 2018). 2. Some authors have not presented a SIMULINK model.	1. Used the double-diode model in PV cells, which is more complex but has increased accuracy. 2. A detailed, complete SIMULINK model has been presented.
Control (MPPT) Algorithms	Some existing models have MPPT on the PV side only and not on the wind side, such as (Korjani et al., 2017), while some with both have not used the interleaving technique nor the GA-ANFIS.	The proposed model has a GA-ANFIS controller and modified P&O MPPT with a 15% SSR for both PV and Wind side DC-DC converters.
Hybridization Framework	Hybridization has been done at selected levels, mainly at the micro source level and less at the power converter, storage, and microgrid levels (Sawle et al., 2016), thereby limiting future scalability.	Hybridization has been done at four levels: micro source level, power converter level, storage level, and microgrid level, thus supporting future expansion,
Microsources/Components	1. Some existing hybrid models include diesel generators (Grzegorz Ma´slak and Przemysław Orłowski, 2022; Samrat et al., 2015; Sawle et al., 2016; Sumathi et al., 2015). 2. Most of the reviewed work uses standard components.	1. No generator, but instead, parallel storage is included. 2. Used modified models of micro sources and converters.

CHAPTER THREE

METHODOLOGY

This chapter presents the approach adopted in developing the Microgrid Multilevel Control System (MMCS) to solve the problem of power supply to communities and households in off-grid areas. The design task begins with problem formulation and system modeling followed by the development of control algorithms, which include GA-ANFIS and MPC for the microgrid primary and secondary control systems respectively. The algorithms have been tested on a microgrid case study model within a MATLAB/SIMULINK environment. The developed microgrid system is split into three sections, i.e. PV-Wind Hybrid Microgrid System Modeling and Case Study, Control Methods, and Simulation Models, as shown in Figure 3.1.

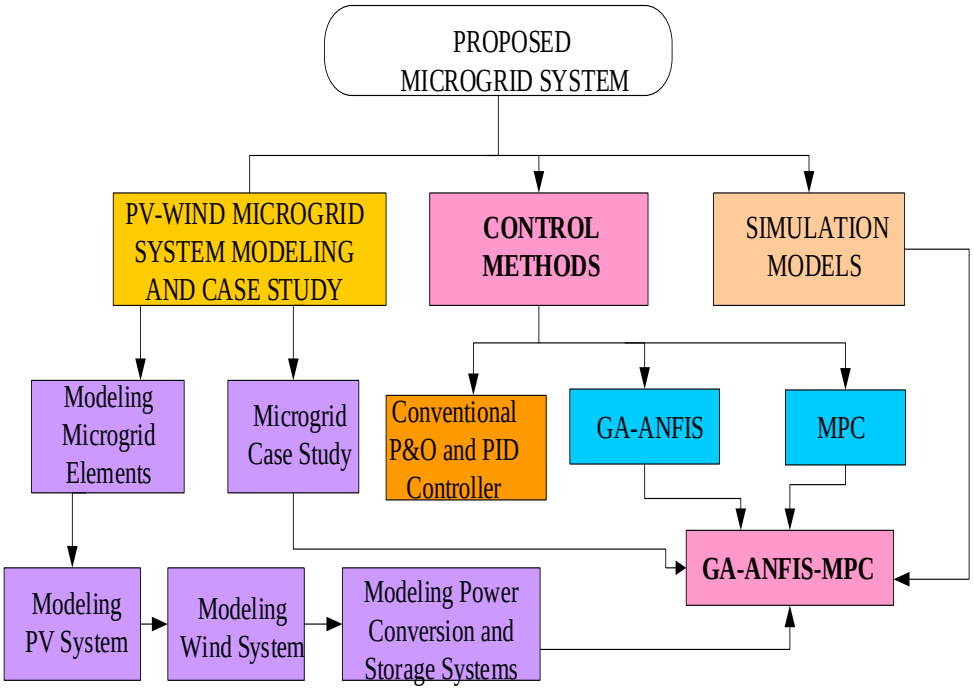

Figure 3.1: Structure of Methodology

3.1 PV-Wind Microgrid System, Case Study Description and Problem Formulation

3.1.1 Elements of Proposed PV-Wind Microgrid System

Figure 3.2 shows block diagram set-up of the proposed PV-Wind microgrid system.

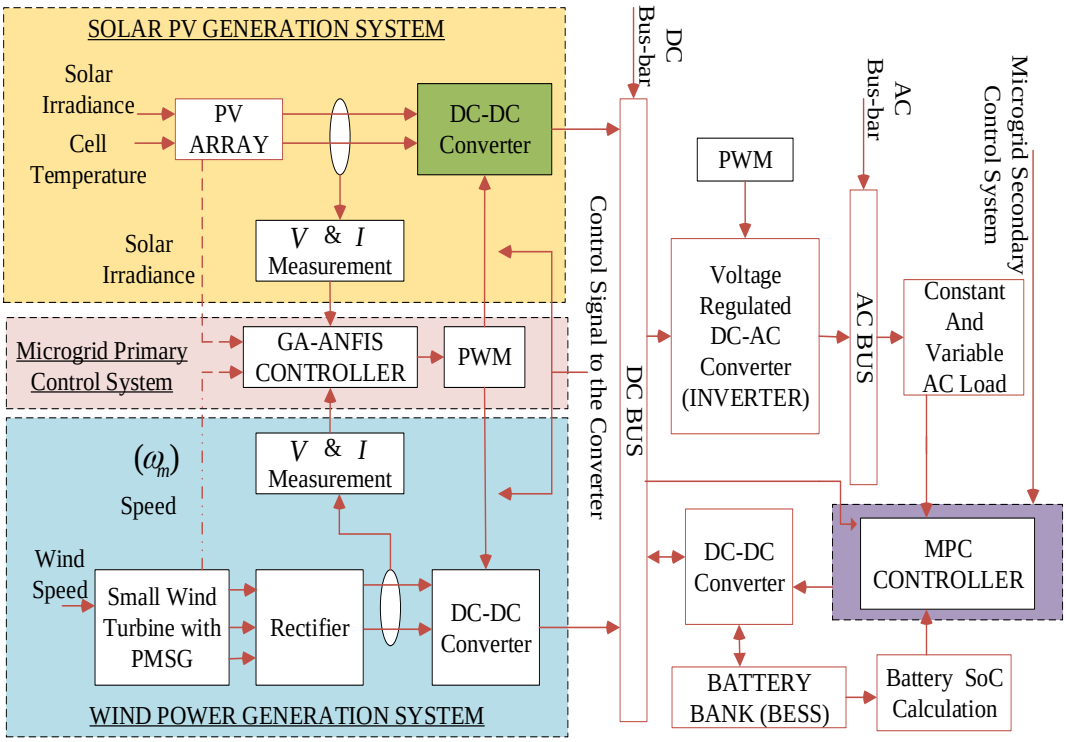

Figure 3.2: Block Diagram of Proposed Microgrid and its Control System

The key elements of the proposed PV-Wind microgrid system with the MMCS are discussed as follows.

3.1.1.1 Solar PV and Wind Power Generation System

The microgrid system has two principal sources of power. The first source is Solar PV array system, which generates direct current (DC) power based on the amount of received solar irradiance as well as the cell temperature. This power is fed directly into a DC-DC converter after its voltage and current have been measured for use by the GA-ANFIS

controller. The solar PV power is highly intermittent owing to variations of levels of received solar irradiance and is only available during the day when there is sunshine. The second source of power is a $10kW$ Wind Turbine (WT) based on a Permanent Magnet Synchronous Generator (PMSG) which generates Alternating Current (AC) power by utilizing wind speed. This power can be produced any time of the day as long as the wind speed exceeds the cut-in speed of the wind turbine. The generated AC power is first fed into an uncontrolled AC-DC converter whose output voltage and current are measured for channeling to the GA-ANFIS controller while at the same time injecting into the DC-DC converter.

3.1.1.2 Microgrid Multilevel Control System

The focus of this study is on the Microgrid Control System, which is made up of three different control algorithms organized into a multi-level control structure. Figure 3.3 shows the hierarchical structure of the designed Microgrid Multi-level Control System (MMCS) strategy for control of a scalable microgrid with PV-wind hybrid generation systems. The multilevel approach addresses several demands of a microgrid system and its controller (Mathew et al., 2019). As presented in Figure 3.3, the MMCS uses a decentralized GA-ANFIS controller supported with a centralized MPC to achieve primary control and secondary control respectively based on voltage/current control loops and feedback signals.

The first control system is the microgrid primary controller, which operates at the fastest time scale and is made up of the hybrid combination of Genetic Algorithm (GA) and the Adaptive Neuro-Fuzzy Inference System (ANFIS) to create a GA-ANFIS controller. The GA is used to capture the highly variable meteorological data and utilizes this information to automatically tune and optimize the ANFIS controller, which is trained, based on the required performance of the microgrid system.

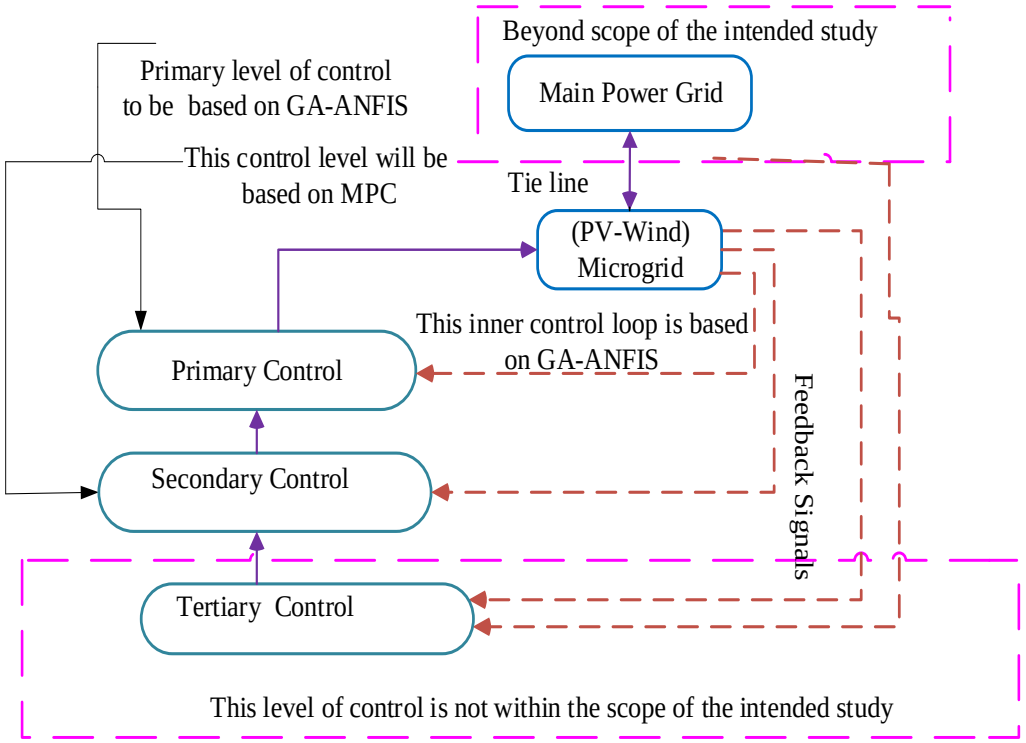

Figure 3.3: Microgrid Multi-Level Control System

Thus, the ANFIS controller takes in as its inputs the measured voltage and current as well as the GA output signal based on the intermittent solar and wind meteorological data and uses this information to generate a Pulse Width Modulated (PWM) signal. The PWM block then generates the control signal to drive the DC-DC converters. Under control of the combined intelligent GA-ANFIS controller, these DC-DC converters supply a stabilized DC output voltage and current to the DC-bus bar.

The second part of the Microgrid Multilevel Control System (MMCS) is made up of the Model Predictive Controller (MPC). It operates at a slower time scale and is used as a secondary controller in the microgrid system. The MPC controller controls the charging and discharging of the battery bank by regulating the voltage and current supplied to the storage system via the DC-DC converters. Under this role, key input to the MPC is the State of Charge (SoC) of the battery bank, which must be calculated or measured directly. One of the key challenges of off-grid microgrids is the variations in voltage owing to its

low-inertia, changes in the loads as well as the dynamics of exchange of stored energy between the battery bank and the DC bus. The MPC controller also requires a suitable discrete time state-space model of the microgrid system as well as the performance indices and or constraints associated with the charging and discharging of the battery bank and the stabilization of the system voltage.

3.1.2 Case Study Description and Data Used in the Study

This study focused on the voltage control problem of an off-grid microgrid containing PV-wind and BESS using the GA-ANFIS-MPC algorithms. Modeling, design, and implementation of the entire microgrid have been done in MATLAB/SIMULINK for the generation side, power electronic interfaces, and the control system. The Simulink based Case Study was built around a $10kW$ Solar PV system with peak current of $16A$ and voltage $654V$ simulated at irradiance of $1kW/m^2$ at $25^0\ C$. The Wind Generation System used a West-wind $6.4m$, $10kW$ Wind Turbine with a rated base speed of $12m/s$. The DC-DC converter was a modified Interleaved Boost Converter (IBC) both for PV and wind sections of the microgrid while the inverters deployed were also two-parallel three-level Voltage Source Converter (VSC) for the PV and wind microgrid. There is also a Transfer Function (TF) based Simulink Case Study built around the schematic small-signal mathematical TF model of the studied microgrid. While it was noted that microgrids have varied capacities and can be operated off-grid or in grid-connected modes, this study considered a microgrid having a power output of $10\ kW$ and is operated in an off-grid mode. The primary GA-ANFIS controller was trained offline with labeled training data while the secondary MPC controller was also designed offline before deployment. The data used in the design of the GA-ANFIS controller was pre-processed using MATLAB codes and converted into a form that the GA-ANFIS required, making the designed GA-ANFIS controller universally acceptable and not limited by utilized dataset. The Study used MATLAB&SIMULINK R2019a. This form of data is available on request. The Solar and Wind raw data before transformation and further modifications was obtained from the National Solar Radiation Database (NSRDB) provided by the National Energy Research

Laboratory (NREL). The data is freely and publicly available at https://nsrdb.nrel.gov/data-viewer as well as in the System Advisor Model (SAM) version SAM 2018.11.11 provided freely by NREL (Blair et al., 2018). The site considered was Juja, Kiambu, Kenya with Latitude 1.095161S and Longitude 37.01249E for the period 2017 to 2019 with a spatial resolution of $4km$ by $4km$. Extracted portions of the data have been presented in Appendix 4. Battery charging and discharging models and processes have been assumed to be similar so that the response of the BESS has been reported mainly within the discharging framework.

3.1.3 Problem Formulation and Performance Criterion

The development of the proposed microgrid control system involves optimization of objective functions, both with the GA-ANFIS and the MPC. In general, the main objective function involves the maximization of power generated by the PV and wind generation system and the surplus power to be stored in the Battery Energy Storage System (BESS). It is defined as in equations (3.1) and (3.2):

$$J = max\ P\ (\int_0^t (P_{PV-out}, P_{WT-out}, P_s)\ dt\ ) \tag{3.1}$$

subject to

$$P_{PV-out} \geq 1 - P_{WT-out}\ or\ \left((P_{PV-out} + P_{wT-out}) \geq 1\right) \tag{3.2a}$$

$$P_{BATmin} \leq\ P_s\ \leq P_{BATmax}, t \leq t_1 \tag{3.2b}$$

where P_{PV-out}, and P_{WT-out} are respectively the power generated from a PV system and Wind Turbine (WT) unit, t is the time variable in hours whose ceiling is at $t_1 = 24\ hours$.

The electrical power generated from a PV system (P_{PV-out}) is given by equation (2.1) whereas the instantaneous electrical power generated from a WT unit (P_{WT}) is defined according to equation (2.2) as given under Chapter 2.

The t or t_1 in equations (3.1) and (3.2) represents the time window (in hours) over which the microgrid should generate and supply power. Typically, the time window is set to 24hrs (1day). P_s is the power stored into or drawn from the BESS in time slot t given by equation (3.3):

$$P_s = \frac{C_{Wh}(t)}{t} = \frac{E_L \times AD}{(\eta_V \times \eta_B \times DoD)t} \tag{3.3}$$

where $C_{Wh}(t)$ is Capacity of the BESS, E_L is Daily energy consumption, AD is Number of autonomy days, η_V is Voltage efficiency, η_B is BESS efficiency and DoD is Allowable depth of discharge.

The stored or drawn power should not exceed BESS power capacity (P_{BAT}), given by equation (3.4).

$$P_{BAT}(t) = C_B(t) - (1-\lambda)(C_B(t-1)) \tag{3.4}$$

Where, $P_{BAT}(t) \geq P_s$, $C_B(t)$ and $C_B(t-1)$ represent the available power in BESS at time slot t and $t-1$ while λ denotes the self-discharge rate of the BESS. During charging operation of the BESS, $C_B(t)$ must be kept between C_{Bmin} and C_{Bmax} as in equation (3.5)

$$C_{Bmin} \leq C_B(t) \leq C_{Bmax} \tag{3.5}$$

The performance of the proposed GA-ANFIS-MPC algorithm in controlling output voltage is measured using three performance indicators: percentage overshoot/undershoot (% M_p), rise time (t_r), and settling time (t_s). The goal of the GA-ANFIS-MPC controller is to keep a majority or all the three indicators at a minimum.

The percentage overshoot is given by equation (3.6):

$$\%\, M_p = \frac{\left|C(t_p) - C(t_{sp})\right|}{C(t_{sp})} \times 100\% \tag{3.6}$$

with t_p being the time to reach first overshoot/undershoot (Peak time), $C(t_p)$ and $C(t_{sp})$ are the maximum and the set point values of the system, respectively.

The rise time is the time interval over which the response gets from 10% to 90% of its final value. The settling time is the time interval necessary for the response to fall within $\pm 5\%$ of its final value. Thus, the designed Microgrid Multi-level Control System based on GA-ANFIS-MPC when incorporated into the PV-Wind microgrid system is required to regulate the voltage to within $\pm 5\%$ of desired output voltage and prevent BESS from over-charging or over-discharging.

3.2 PV-Wind Microgrid System Modeling and Case Study

This section of the methodology mainly corresponds to the specific objective number one on modeling of the proposed PV-Mind Microgrid System, including the Case Study for deploying the GA-ANFIS-MPC controller. However, section 3.2.8 on the Transfer Function Model of PV-Wind hybrid Microgrid also supports the methodology for specific objectives two and three.

3.2.1 Mathematical Modeling of PV Generation System

The PV system has been modeled in terms of an equivalent circuit using the two-diode model of a PV cell (the smallest unit of solar photovoltaic (PV) power generation that is rated at about 0.5V) as shown in Figure 3.4. The model has two diodes as well as a series (R_s) and shunt resistance (R_{sh},). It is used because it provides better accuracy and increased power extraction compared to the other two models: the one-diode model and the $R_s - R_{sh}$ model (Priyadarshi et al., 2018; Yahyaoui, 2018).

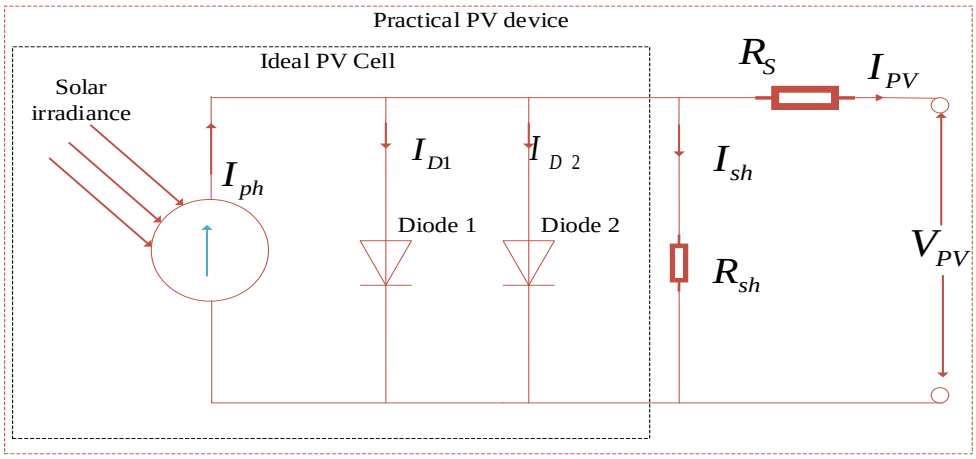

Figure 3.4: Two-diode PV Model Equivalent Circuit

The PV cell output current I_{PV}, in the two-diode model of Figure 3.4 is represented by a nonlinear mathematical exponential expression given in Equation (3.7) (Amara et al., 2020; Yahyaoui, 2018):

$$I_{PV} = I_{Ph} - I_{D1} - I_{D2} - I_{sh} = I_{Ph} - I_{D1} - I_{D2} - \frac{(V_{PV} + I_{PV}R_s)}{R_{sh}} \tag{3.7}$$

where V_{PV}, is the PV cell output voltage, R_s is the Series resistance, R_{sh} is the Parallel resistance, I_{D1} and I_{D2} are, respectively, the first and second diode currents.

The Photovoltaic Current due to irradiation I_{Ph} is given by equation (3.8):

$$I_{Ph} = [I_{Ph-STC} + K_s(T_C - T_{STC})] \times (\frac{G}{G_{STC}}) \tag{3.8}$$

where T_{STC} is the STC Temperature (Standard Test Condition = 298 K), I_{Ph-STC} is the STC Photovoltaic Current T_C is the Ambient temperature, K_s is the Short-circuit current coefficient, G is the Solar radiation, and G_{STC} is the Solar irradiance at STC (= 1000 W/m^2).

The diode currents I_{D1} and I_{D2} are obtained based on the standard diode current equation as follows in equations (3.9), (3.10) and (3.11):

$$I_{D1} = I_{sat1}\left[exp\left(\frac{V_D}{a_1 V_T}\right) - 1\right] \tag{3.9}$$

$$I_{D2} = I_{sat2}[exp\left(\frac{V_D}{a_2 V_T}\right) - 1] \tag{3.10}$$

$$I_{Ph-STC} = \frac{(R_{sh} + R_s)}{R_{sh}} I_{short-STC} \tag{3.11}$$

The PV cell output current I_{PV}, in the two-diode model thus becomes equation (3.12) (Amara et al., 2020; Jayachandran & Ravi, 2017):

$$I_{PV} = I_{Ph} - I_{sat1}\left[exp\left(\frac{V_D}{a_1 V_T}\right) - 1\right] - I_{sat2}\left[exp\left(\frac{V_D}{a_2 V_T}\right) - 1\right] - \frac{(V_{PV} + I_{PV} R_s)}{R_{sh}} \tag{3.12}$$

The ideality factor a, is ideally 1 for germanium and 2 for silicon, but in practice varies between 1 and 2. The ideality factor of the first diode is taken to be $a_1 = 1$ and for the second diode, $a_2 = 2$. The model is simplified by assuming that the diode resistance is negligible and that the two reverse saturation currents I_{sat1} and I_{sat2} are equal in magnitude as given in equation (3.13) (Amara et al., 2020; Jayachandran & Ravi, 2017) :

$$I_{sat1} = I_{sat2} = I_{D1} = I_{D2} = I_0 = \frac{(I_{Ph-STC} - \left(\frac{V_{open-STC}}{R_{sh}}\right))}{(exp\left(\frac{V_{open-STC}}{V_T}\right) - 1)} \tag{3.13}$$

where I_0, is the Dark Saturation Current, which indicates the leakage current density flowing through the diode without light. Assuming that a_1=1 and $a_2 \leq 2$ gives equation (3.14):

$$I_{PV} = I_{Ph} - I_0 \left[exp\left(\frac{V_D}{V_T}\right) + exp\left(\frac{V_D}{a_2 V_T}\right) - 2 \right] - \frac{(V_{PV} + I_{PV} R_s)}{R_{sh}} \quad (3.14)$$

It can also be shown that the diode saturation current for the two diodes, I_{D1} and I_{D2}, can be expressed as in equation (3.15) (Hizam, 2022):

$$I_{D1} = I_{D2} = \frac{I_{short-STC} + K_s(T_C - T_{STC})}{exp\dfrac{\left[\left(V_{open-STC} + K_V(T_C - T_{STC})\right)\right] - 1}{aV_T}} \quad (3.15)$$

Where $I_{short-STC}$ is the Short-circuit current at STC, $V_{open-STC}$ is the Open-circuit voltage at STC, V_T is the Diode thermal voltage, K_V is the Voltage temperature coefficient and a is the Ideal constant of the diode.

Alternatively, the saturation current I_D, which depends on the temperature, can be determined by the expression in equation (3.16):

$$I_D = (I_{D1})\left(\frac{T_{STC}}{T_C}\right)^3 exp\left[\frac{qE_g}{a_1 K}\left(\frac{1}{T_{STC}} - \frac{1}{T_C}\right)\right] + (I_{D2})\left(\frac{T_{STC}}{T_C}\right)^3 exp\left[\frac{qE_g}{a_2 K}\left(\frac{1}{T_{STC}} - \frac{1}{T_C}\right)\right] \quad (3.16)$$

where E_g, is the energy band gap of the semiconductor and is $\approx 1.12eV$ for multicrystalline silicon panels. For thin-film cadmium telluride ($CdTe$) solar cells, $E_g \approx 1.44eV$ (Jayachandran & Ravi, 2017).

The photovoltaic current generated at STC is given by equation (3.17)

$$I_{Ph-STC} = \frac{R_{sh} + R_s}{R_{sh}} \times I_{short-STC} \quad (3.17)$$

The thermal potential of the panel $V_{Thermal}$, is given by equation (3.18).

$$V_{Thermal} = \frac{N_s \times K \times T_C}{q} \tag{3.18}$$

N_s is the number of cells in series, K is the Boltzmann constant [$= 1.3806503 \times 10^{-23}\, J/K$], q is the charge of an electron [$= 1.6 \times 10^{-19}$C].

If a panel is made up of N_p cells connected in parallel, then the photovoltaic current due to irradiation, I_{Ph} is given by equation (3.19).

$$I_{Ph} = N_p \times\ I_{Ph-cell} \tag{3.19}$$

where $I_{Ph-cell}$, is the photovoltaic current for one cell.

The saturation current I_D, of the panel, is given by equation (3.20)

$$I_D = N_p \times (I_{D1} + I_{D2}) = N_p \times I_{D0} \tag{3.20}$$

where I_{D0}, is the saturation current for the two diodes in a single-cell model.

A PV array is created when several cells are wired in series and parallel. Since the N_p cells in the panel are connected in parallel, the voltage across the panel is still V_{PV}.

The values of R_s and R_{sh} are usually not supplied by the manufacturers in the datasheet. One way of determining these values is to extract them from the maximum power output formula (Sumathi et al., 2015; Yahyaoui, 2018), or a System Advisor Model (Blair et al., 2018). To extract these values from the maximum power output formula, equations (3.21) and (3.22) are solved simultaneously (Jayachandran & Ravi, 2017; Sumathi et al., 2015).

$$P_{mp,m} = V_{mp}\left\{I_{Ph} + I_{D1}\left[exp\left(\frac{V_{mp} + R_s I_{mp}}{a_1 V_T}\right) - 1\right] + I_{D2}\left[exp\left(\frac{V_{mp} + R_s I_{mp}}{a_2 V_T}\right) - 1\right] - \frac{V_{mp} + R_s I_{mp}}{R_{sh}}\right\}$$

$$= P_{mp,e} \qquad (3.21)$$

$$R_{sh} = \frac{V_{mp}\{V_{mp} + R_s I_{mp}\}}{\left\{V_{mp} I_{Ph} - V_{mp} I_{D1} exp\left[\frac{(V_{mp} + R_s I_{mp})}{a_1 V_T}\right] + V_{mp} I_{D1} - V_{mp} I_{D2} exp\left[\frac{(V_{mp} + R_s I_{mp})}{a_2 V_T}\right] + V_{mp} I_{D2} - P_{mp,e}\right\}} \qquad (3.22)$$

where V_{mp} and I_{mp}, are respectively maximum voltage and current. $P_{mp,m}$, represents the maximum power obtained from a model identification approach while $P_{mp,e}$, is the nominal experimental maximum power that the panel manufacturer supplies.

3.2.2 Wind Turbine Model

The mechanical power of the wind turbine P_m, in watts, is related to equation (2.2) excluding the generator efficiency term and is given by the cubic relationship equation (3.23):

$$P_m = \frac{1}{2}\rho A v^3 C_p(\lambda, \beta) \qquad (3.23)$$

where ρ, is the air density of the power generation site (kg/m^3), A is the area covered by the rotor blades, v is the wind speed of the site (m/s), C_p, is the conversion efficiency of the wind power defined by the rotor blades' tip speed ratio λ and the blade pitch angle β (Elbeji et al., 2014; C. N. Wang et al., 2014).

The tip speed ratio (TSR) specifies the relation between the wind speed and the rotor speed as in equation (3.24) [40]:

$$\lambda = \frac{R\omega}{v \times \eta_{gear}} \tag{3.24}$$

where ω is the angular velocity of the blades and $\eta_{gear,}$ is the gear efficiency assumed to be unity for a PMSG directly coupled to the turbine shaft (Elbeji et al., 2014; Tounsi et al., 2018).

According to Betz, (Sahin et al., 2017; Tounsi et al., 2018) C_p, is limited to 0.59. The power coefficient $C_p(\lambda, \beta)$ can be computed from equation (3.25) (Zebraoui & Bouzi, 2018):

$$C_p(\lambda, \beta) = C_1 \left(C_2 \frac{1}{\lambda_i} - C_3\beta - C_4 \right) exp\left(\frac{-C_5}{\lambda_i} \right) + C_6\,\lambda \tag{3.25}$$

where C_1, C_2, C_3, C_4, C_5, and C_6, are coefficients to be specified for a given wind turbine, and the parameter λ_i, is defined as equation (3.26) (Kokate et al., 2019; Tounsi et al., 2018; Yahyaoui, 2018; Zebraoui & Bouzi, 2018):

$$\frac{1}{\lambda_i} = \frac{1}{(\lambda + 0.08\beta)} - \frac{0.035}{\beta^3 + 1} \tag{3.26}$$

Typical values of the factors are as follows: $C_1 = 0.5176$, $C_2 = 116$, $C_3 = 0.4$, $C_4 = 5$, $C_5 = 21$ and $C_6 = 0.0068$ (Zebraoui & Bouzi, 2018).

3.2.3 Mathematical Modeling and Design of Interleaved DC-DC Boost Converter

For a microgrid containing a photovoltaic (PV) system and wind energy, which are known to have the least voltage output, the boost converter circuit is suitable to give a sufficient voltage at the output side (Abdel-Rahim, 2020; Faraj & Hussain, 2020b). The advantages of boost converters include high efficiency, ease of control, and integration (R.D Tayade & S. & Mopari, 2017). In this study, an Interleaved Boost Converter (IBC) has been

adopted. A more accurate boost converter circuit was modified by incorporating an RC circuit in parallel with the output capacitor, as shown in Figure 3.5.

The interleaving technique entails realizing a converter by paralleling two or more converters, thus dividing the input current among the inductors. The I^2R losses and the current stress are minimized. It significantly reduces the output current and voltage ripples, increasing the overall efficiency (Prabhakaran & Agarwal, 2020). The boost converter is modeled using the averaging method. The switching frequency is 20 kHz, which is high enough to guarantee small voltage and current ripples.

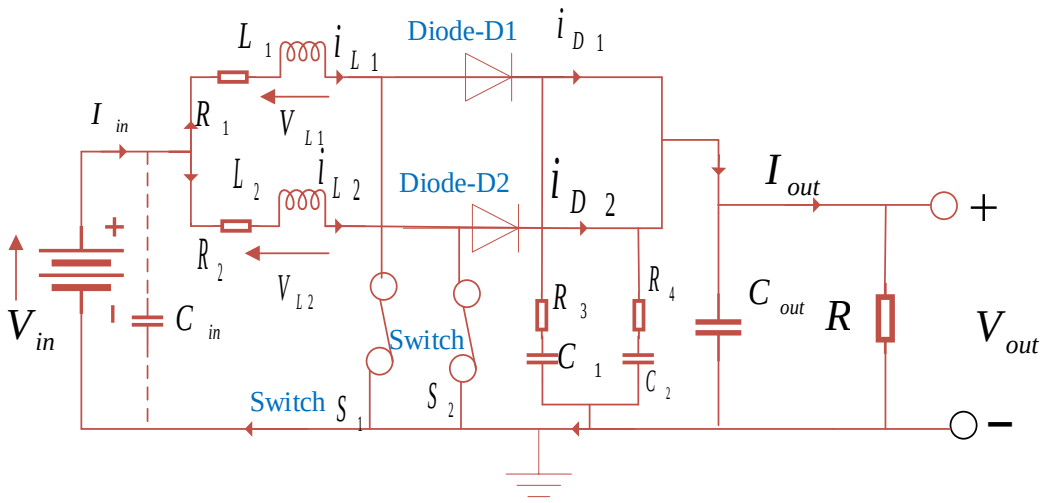

Figure 3.5: Modified Interleaved DC-DC Boost Converter with Two Phases

Using the averaging method, the state space equations for each of the interleaved converters become equations (3.27) and (3.28):

$$\begin{bmatrix} \dot{x_1} \\ \dot{x_2} \end{bmatrix} = \begin{bmatrix} -\frac{R_L}{L} & \frac{-(1-D)}{L} \\ \frac{(1-D)}{C} & -\frac{1}{RC} \end{bmatrix} \begin{bmatrix} x_1 \\ x_2 \end{bmatrix} + \begin{bmatrix} \frac{1}{L} \\ 0 \end{bmatrix} V_{in} + \begin{bmatrix} \frac{-(1-D)}{L} \\ 0 \end{bmatrix} V_d$$

$$= \bar{A} \begin{bmatrix} x_1 \\ x_2 \end{bmatrix} + \bar{B} V_{in} + \begin{bmatrix} \frac{-(1-D)}{L} \\ 0 \end{bmatrix} V_d \qquad (3.27)$$

where

$$\bar{A} = \begin{bmatrix} 0 & \frac{-(1-D)}{L} \\ \frac{(1-D)}{C} & -\frac{1}{RC} \end{bmatrix} = A_1 D + A_2(1-D), \qquad \bar{B} = \begin{bmatrix} \frac{1}{L} \\ 0 \end{bmatrix} = B_1 D + B_2(1-D) \qquad (3.28)$$

The revised average model (considering V_d and R_L) is an excellent approximation of the switch model with reduced steady-state errors.

Table 3.1 summarizes the complete parameters of the proposed IBC converter.

Table 3.1: Parameters of the IBC Converter

S/No.	Parameters	Value
1	Inductors ($L_1 = L_2$)	$6\ mH$
2	Capacitor ($C_1 = C_2$)	$1\ \mu F$
3	Capacitor (C_{out})	$220\ \mu F$
4	Resistor ($R_1 = R_2$)	$10\ m\Omega$
5	Resistor ($R_3 = R_4$)	$1\ m\Omega$
6	Resistor (R)	$36\ \Omega$
7	Current ripple ($\Delta I_{L_1} = \Delta I_{L_2}$)	$0.7308\ A$
8	Voltage ripple (ΔV_0)	$41.7\ V$
9	Switching frequency ($f_{switching}$)	$20\ kHz$

The design calculations for the various parameters of the IBC are given next (Faraj & Hussain, 2020b; R.D Tayade & S. & Mopari, 2017).

- Duty Cycle. The voltage of the PV array V_{PV} is $561V$ and the DC link voltage of the inverter V_{DC}, is taken to be $695V$ hence the duty cycle of the IBC was calculated using equation (3.29) as 0.1928:

$$D = \frac{V_{DC} - V_{PV}}{V_{DC}} \tag{3.29}$$

- Inductor L_1 and L_2. Taking the IBC switching frequency as $20\ kHz$ to reduce the ripple current (ΔI_L), the inductor current the I_L is calculated as $16.58\ A$ using equation (3.30):

$$I_L = N_P \times I_m \tag{3.30}$$

where N_P, is the number of paralleled modules, taken as 2 and I_m, is the PV peak/maximum current, taken as $8.29\ A$, all obtained from the PV system case study designed. The values of the two inductors L_1 and L_2 are obtained as $5.43\ mH \approx 6\ mH$ using equation (3.31):

$$L_1 = \ L_2 \ = \frac{V_{PV} D}{f \Delta i_L} \tag{3.31}$$

where Δi_L is the ripple current set at 6% of I_L, D is the duty ratio set at 0.1928, f is the converter switching frequency taken to be $20\ kHz$ and V_{PV} is the PV system voltage taken as $561\ V$, all the parameters having been obtained from the case study built and literature.

-DC Link Capacitor C. The minimum value of the DC Link Capacitor C_{min}, is calculated as $4.463\ \mu F$ using equation (3.32):

$$C_{min} = \frac{D}{R(\left(\frac{\Delta V_{out}}{V_{out}}\right))f} = \frac{0.1928}{\frac{36(0.06 \times 695)}{695}(20 \times 10^3)} = \ 4.463\ \mu F \tag{3.32}$$

where D is set at 0.1928, f is taken to be $20\ kHz$, R is the load resistance taken to be $36\Omega, V_{out}$ is the maximum PV system output voltage taken as $695\ V$, and ΔV_{out} is the voltage ripple taken to be 6% V_{out} of all the parameters having been obtained from the case study built, best industry practice and literature.

Taking $f = 50\ Hz$, the angular frequency, ω, is obtained using equation (3.33) as $314.1592\ rad/sec$.

$$\omega = 2\pi f \tag{3.33}$$

The value of the DC Link Capacitor C is calculated as $216.3\ \mu F \approx 220\ \mu F$ using equation (3.34):

$$C = \frac{I_{DC}}{6 \times \omega \times \Delta V_{DC}} \tag{3.34}$$

where I_{DC} is the Input DC current taken to be $17\ A$ from the PV array, ΔV_{DC} is the dc voltage ripple taken to be 6% V_{DC} and of 6 is a constant factor, all the parameters having been obtained from the case study built, best industry practice and literature.

3.2.4 Mathematical Modeling of Two Parallel Inverters for Microgrid Application

The voltage-controlled voltage source inverter (VCVSI) is preferred for interfacing renewables in a stand-alone microgrid to the load on the grid. A VCVSI comprises four main elements: a DC link, an R-L-C filter, three-leg inverters, and an RL coupling inductor.

The switching averaging method is used to derive the average model of a phase leg (lead). The variables of the stationary coordinates X_{abc} are transformed into the corresponding rotating coordinates X_{dqz}, and this simplifies the average model according to $i_z = i_{z1} = -i_{z2} \approx 0$ (Khalil et al., 2016). If the input DC power sources are assumed ideal, it gives equations (3.35), (3.36), and (3.37):

$$\frac{d}{dt}\begin{bmatrix}\hat{\imath}_{d1}\\ \hat{\imath}_{q1}\end{bmatrix} = \frac{1}{L_1}\begin{bmatrix}\hat{d}_{d1}\\ \hat{d}_{q1}\end{bmatrix} V_{dc1} - \frac{1}{L_1}\begin{bmatrix}\hat{V}_d\\ \hat{V}_q\end{bmatrix} - \begin{bmatrix}0 & -\omega\\ \omega & 0\end{bmatrix}\begin{bmatrix}\hat{\imath}_{d1}\\ \hat{\imath}_{q1}\end{bmatrix} \tag{3.35}$$

$$\frac{d}{dt}\begin{bmatrix}\hat{\imath}_{d2}\\ \hat{\imath}_{q2}\end{bmatrix} = \frac{1}{L_2}\begin{bmatrix}\hat{d}_{d2}\\ \hat{d}_{q2}\end{bmatrix} V_{dc2} - \frac{1}{L_2}\begin{bmatrix}\hat{V}_d\\ \hat{V}_q\end{bmatrix} - \begin{bmatrix}0 & -\omega\\ \omega & 0\end{bmatrix}\begin{bmatrix}\hat{\imath}_{d2}\\ \hat{\imath}_{q2}\end{bmatrix} \tag{3.36}$$

$$\frac{d}{dt}\begin{bmatrix}\hat{V}_d\\ \hat{V}_q\end{bmatrix} = \frac{1}{2C}\left(\begin{bmatrix}\hat{\imath}_{d1}\\ \hat{\imath}_{q1}\end{bmatrix} + \begin{bmatrix}\hat{\imath}_{d2}\\ \hat{\imath}_{q2}\end{bmatrix}\right) - \begin{bmatrix}\frac{1}{RC} & -\omega\\ \omega & \frac{1}{RC}\end{bmatrix}\begin{bmatrix}\hat{V}_d\\ \hat{V}_q\end{bmatrix} \tag{3.37}$$

Equations (3.35) to (3.37) can be represented in the general state space form as in equations (3.38) to (3.41) (Korjani et al., 2017):

$$\dot{\hat{x}} = \boldsymbol{A}\hat{x} + \boldsymbol{B}\hat{u} \tag{3.38}$$

$$\hat{y} = \boldsymbol{C}\hat{x} \tag{3.39}$$

where the state vector is

$$\hat{x} = \begin{bmatrix}\hat{V}_d & \hat{V}_q & \hat{\imath}_{d1} & \hat{\imath}_{q1} & \hat{\imath}_{d2} & \hat{\imath}_{q2}\end{bmatrix}^T \tag{3.40}$$

and the control variables are

$$\hat{u} = \begin{bmatrix}\hat{d}_{d1} & \hat{d}_{q1} & \hat{d}_{d2} & \hat{d}_{q2}\end{bmatrix}^T \tag{3.41}$$

and

$$\boldsymbol{C} = \boldsymbol{I}.$$

The matrices *A* and *B* are given by equations (3.42) and (3.43) (Korjani et al., 2017):

$$\boldsymbol{A} = \begin{bmatrix} -\frac{1}{RC} & \omega & \frac{1}{2C} & 0 & \frac{1}{2C} & 0 \\ -\omega & \frac{1}{RC} & 0 & \frac{1}{2C} & 0 & \frac{1}{2C} \\ -\frac{1}{L_1} & 0 & 0 & \omega & 0 & 0 \\ 0 & -\frac{1}{L_1} & -\omega & & & \\ -\frac{1}{L_2} & 0 & 0 & 0 & 0 & 0 \\ & & & 0 & 0 & \omega \\ 0 & -\frac{1}{L_1} & 0 & 0 & -\omega & 0 \end{bmatrix} \tag{3.42}$$

$$\boldsymbol{B} = \begin{bmatrix} 0 & 0 & 0 \\ 0 & 0 & 0 \\ \frac{Vdc_1}{L_1} & 0 & 0 \\ 0 & \frac{Vdc_1}{L_1} & 0 \\ 0 & 0 & \frac{Vdc_2}{L_2} \\ 0 & 0 & 0 \end{bmatrix} \begin{matrix} 0 \\ 0 \\ 0 \\ 0 \\ 0 \\ \frac{Vdc_2}{L_2} \end{matrix} \tag{3.43}$$

3.2.5 Battery Energy Storage System Modeling

The Battery Energy Storage System (BESS) is a crucial component of the proposed PV-wind hybrid microgrid. It improves the reliability and efficiency of the system through energy storage (Li & Ke, 2011; Sumathi et al., 2015).

The three traditional mathematical models (Shepherd model, Unnewehr Universal model and the Nernst model) can be improved in terms of accuracy by combining them into a single mathematical expression in equation (3.44) (Krishnan, 2021; J. Meng et al., 2018; S. Kumar, 2022; Tan, 2021):

$$y_k = E_0 - R.i_k - \frac{K_1}{z_k} - K_2.z_k + K_3.ln(z_k) + K_4.ln(1 - z_k) \tag{3.44}$$

Where y_k is the terminal voltage, E_0 is the open-circuit voltage (OCV) at full battery charge, R is the internal resistance, K_1 is the polarization resistance, i_k is the instantaneous current, z_k is the battery State of Charge (SoC).

The modified empirical battery energy model was created from the Shepherd relation and SimPower system battery model. Using the Shepherd relation and SimPower system battery model, the modified battery model representing the discharge and charge of lead-acid batteries, respectively, are given by equations (3.45) and (3.46) (Bogaraj & Kanakaraj, 2016; J. Meng et al., 2018; Pawar & Nema, 2020; Truong et al., 2021).

$$V_{dis} = E_0 - K_{dr}\frac{1}{SoC}i^* - Ri - K_{dv}\left[\frac{1}{SoC} - 1\right] + exp\,(t) \tag{3.45}$$

$$V_{ch} = E_0 - K_{cr}\frac{P_{BAT}}{it + \lambda.P_{BAT}}i^* - Ri - K_{cv}\left[\frac{1}{SoC}it\right] + exp\,(t) \tag{3.46}$$

where K_{dr} is polarization resistance coefficient (Ω), K_{dv} is polarization overvoltage coefficient (V/Ah), λ is the coefficient to account for the shift in polarization resistance as the battery gets charged, i^* is the filtered battery current used to modify the polarization ohmic voltage drop, R is the internal resistance, whose value is different for charge and discharge, $exp\,(t)$ represents an exponential dynamic voltage, which accounts for the nonlinear hysteresis phenomenon between discharge and charge and is defined for lead-acid batteries as equation (3.47):

$$Exp\,(t) = B.i.(exp\,(t) + A.u(t)) \tag{3.47}$$

where $(t) = 0$ for discharge and (t) =1 for charge.

The simplified General Non-linear (GNL) model, which better emulates the dynamics concerning the SoC operation mode, is shown in Figure 3.6.

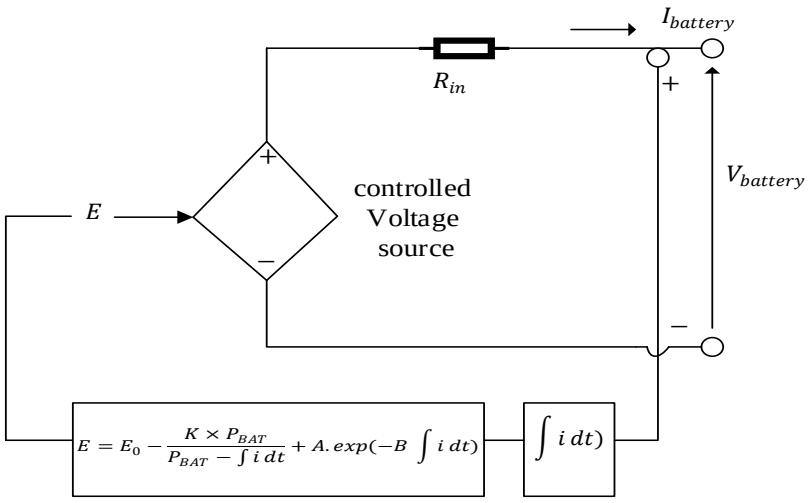

Figure 3.6: Electrical Equivalent Circuit-Based Battery Model

This consists of a (ideal) voltage source in a cascade with an internal resistance to evaluate the battery behavior. The mathematical expression for the final controlled voltage is given by equations (3.48) and (3.49):

$$E = E_0 - \frac{K \times P_{BAT}}{P_{BAT} - \int i\,dt} + A.exp\left(-B \int i\,dt\right) \quad (3.48)$$

$$V_{Battery} = E - R_{in}\, I_{Battery} \quad (3.49)$$

3.2.6 Design of the Baseline Controllers

This section presents the design of the two base line controllers i.e. Modified Search Space Restricted Perturb and Observe (SSR-P&O) and the Proportional plus Integral plus Derivative (PID) controllers. These two controllers have been selected because they are the industry standards when it comes to simpler, less expensive, computationally light and linear controllers that are applicable to Maximum Power point tracking and voltage regulation in microgrids. The controllers perform very well under linear conditions and

are widely applied in Literature to validate more complex modern controllers such as the GA-ANFIS-MPC controller developed in this study.

3.2.6.1 PV System MPPT Using Modified Perturb and Observe (P&O)

The proposed modified P&O algorithm is based on restricting the search area within the PV array power curve, where the search space here has been confined to 15% instead of the 10% used in (Mohamed & Abd El Sattar, 2019). This is to allow for PV shading and due to fact that the PV system is in parallel with WT which requires a larger search area to accommodate the dynamics of the WT. The voltage at maximum power point, V_{MPP} is approximately 76% of the open circuit voltage, V_{oc} i.e. $V_{MPP} = 0.76V_{oc}$. Therefore, the power curve can be partitioned into three zones called Zone 1, Zone 2, and Zone 3 as depicted in Figure 3.7 and whose specifications are presented in Table 3.2. The partitioning is done with reference to published literature (Mohamed & Abd El Sattar, 2019) and the profile of the PV power curve.

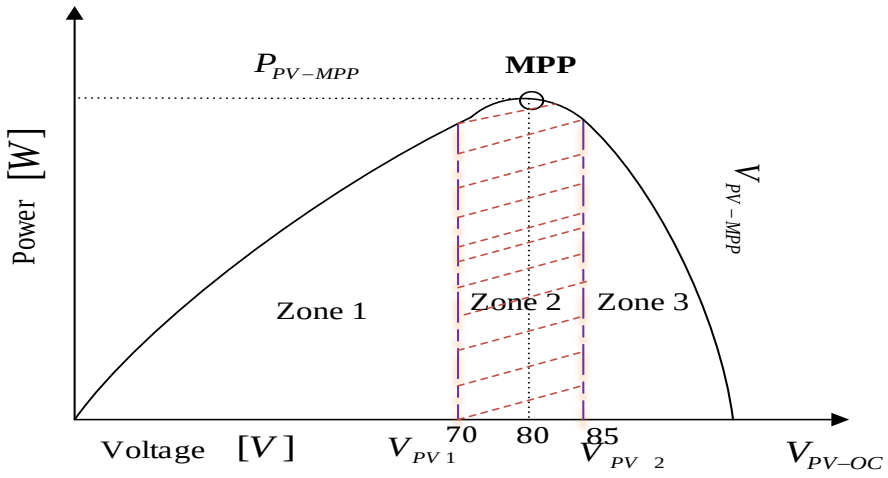

Figure 3.7: Search Space Restriction of the PV System Power Curve

Figure 3.8 shows the restricted search space P&O algorithm. In this case, the P&O algorithm, which has been developed using a MATLAB script/code, is implemented by

first measuring the voltages V_{PV1} and V_{PV2} which restricts the region containing the MPP within Zone 2 representing only 15% of the power curve.

Table 3.2: Power Curve Partitioning into Zones

Zone/Area	Starting (% of V_{oc})	Ending (% of V_{oc})	Total zone/area (% of V_{oc})
Zone 1	0	70	70
Zone 2	70	85	15
Zone 3	85	100	15

Next, perturbation and observation is initiated which ends only after a few perturbation steps have been executed, which means that the MPP is achieved early and maintained at the desired point. If there is a change in the irradiance level, a new local maximum is obtained just as is done with constant irradiance and is then maintained.

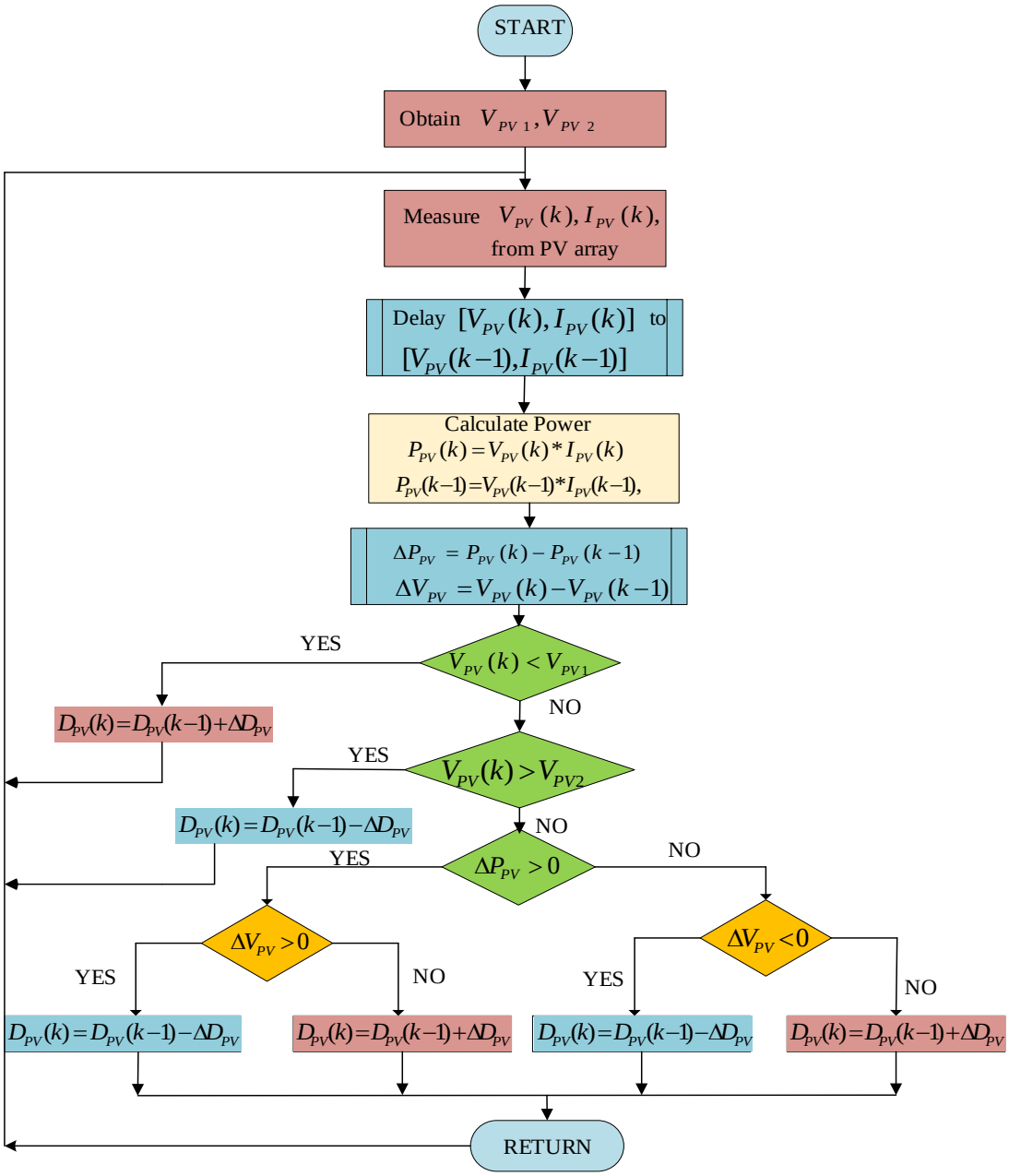

Figure 3.8: Flowchart of Improved P&O Algorithm for PV Power

3.2.6.2 Proposed Improved P & O MPPT Algorithm for WECS

In a wind energy conversion system (WECS), MPPT algorithms are necessary to optimize the energy efficiency of the system by tracking the optimum operating point/maintaining

the MPP. In this study, the improved P & O algorithm has been obtained by introducing three zones (Zones 1, 2, and 3 corresponding to V_{w1}, $V_{w2,}$ and V_{w3}) as shown in Table 3.3 within the WECS power curve and restricting the search to only 15% of the power curve as shown in Figure 3.9 and Figure 3.10. This is because the WT requires a larger search area to accommodate the dynamics of the WT especially around the PMSG and variations in wind speeds, which broaden the power curve.

Table 3.3: WECS Power Curve Partitioning into Zones

Zone/ Area	Starting (% of V_m)	Ending (% of V_m)	Total zone/area (% of V_m)
Zone 1	0	70	70
Zone 2	70	85	15
Zone 3	85	100	15

Figure 3.11 shows the improved restricted search space WECS P&O algorithm. In this case, the P&O algorithm is implemented by first measuring the voltages V_{WT1} and V_{WT2} which restricts the region containing the MPP to Zone 2. Next, perturbation and observation is initiated which ends only after a few perturbation steps have been executed $\omega_{step} \leq 10$ which means that the MPP is achieved early and maintained at the desired point.

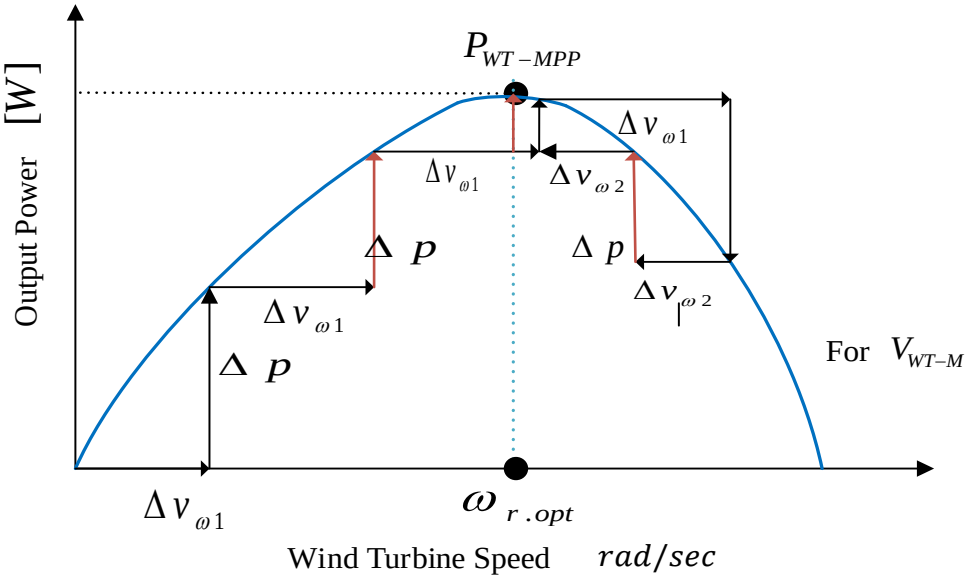

Figure 3.9: P&O MPPT Controller Methodology

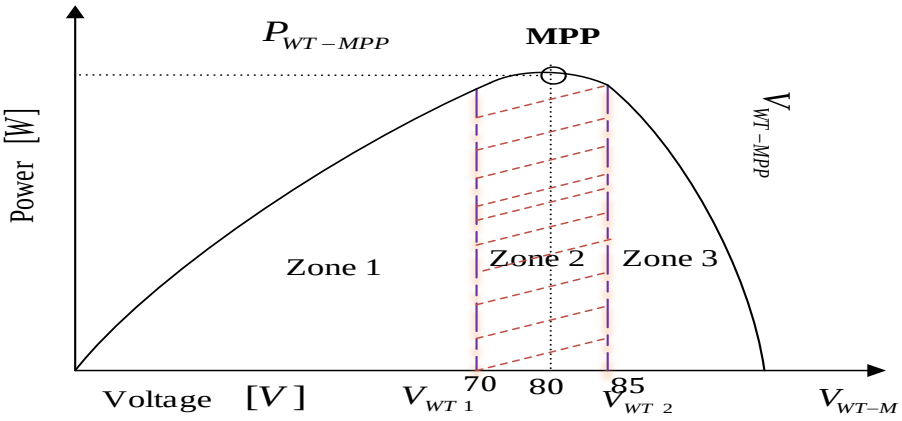

Figure 3.10: Modified P&O MPPT with Search Space Restriction of the WECS Power Curve

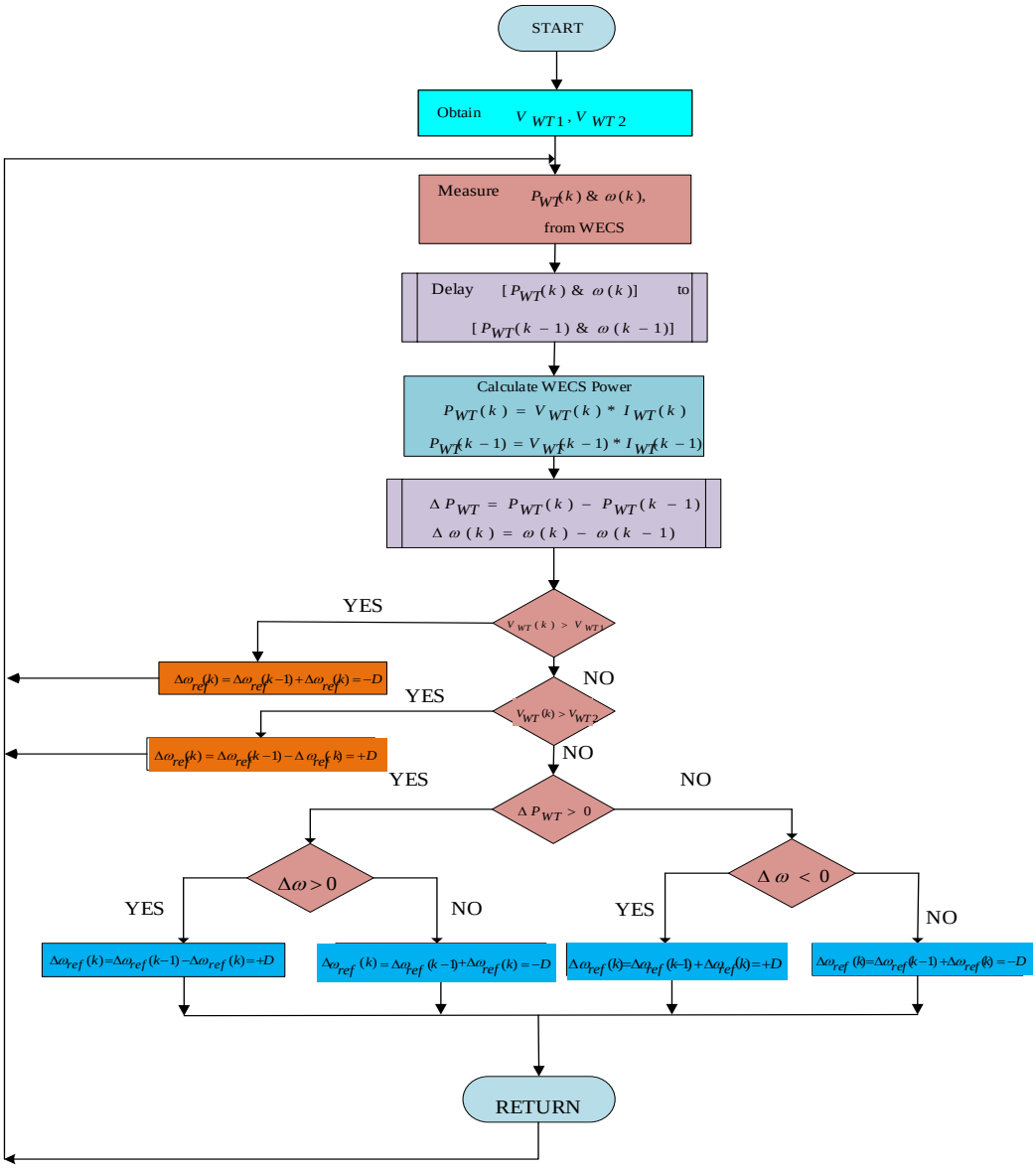

Figure 3.11: Proposed Improved Restricted Search Space WECS P&O Algorithm

3.2.6.3 PI/PID Controller for Benchmarking with GA-ANFIS and MPC.

The Proportional-plus-Integral (PI) and Proportional-plus-Integral-plus-Derivative (PID) controller optimum gains were obtained by applying the Ziegler-Nichols ultimate cycle tuning method (and improved using the MATLAB PID auto-tuning tool) as $K_p = 1.77$, $K_I = 31.74$, $K_D = 0.016$ and filter coefficient $N = 2558.64$. The contribution of the

derivative term of the PID controller was minimal; hence, the controller action was very close to PI.

3.2.7 SIMULINK Case Study Models

3.2.7.1 Case Study SIMULINK Model of a 10 kW PV System

The PV modules, each 310 W having 72 cells of peak voltage 37.4 V and a peak current of 8.29 A are wired in series/parallel arrangements to realize the desired voltage. Figure 3.12 shows the SIMULINK diagram of the designed 310W PV module.

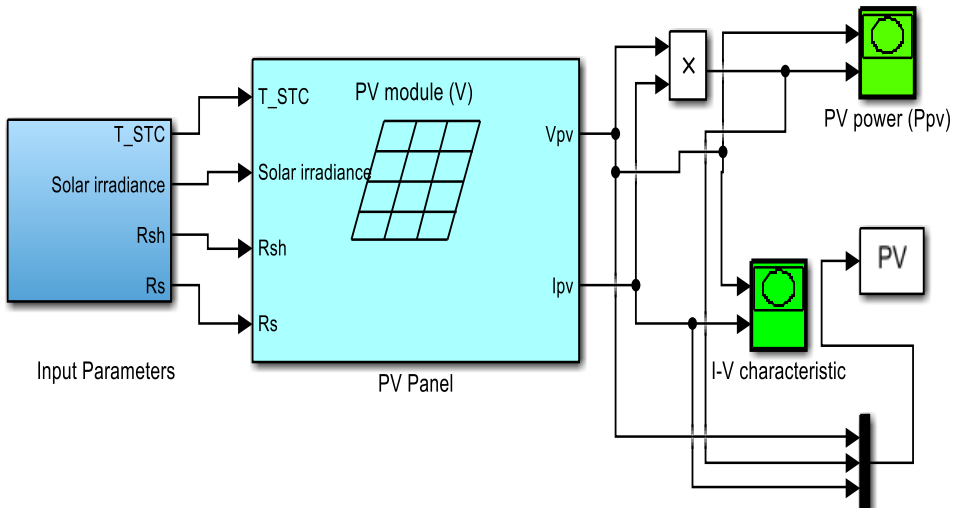

Figure 3.12: Simulink Diagram of a 310W PV Module

The photovoltaic generator used in the case study is a Type A panel (Jinko Solar JKM310M -72 panel) based on monocrystalline technology. Table 3.4 shows the technical specifications obtained from a System Advisor Model (SAM 2018.11.11) (Blair et al., 2018).

Table 3.4: Technical Specifications of the Type a Panel and PV Array

For PV Panel (Jinko Solar JKM310M-72 panel)		
Electrical Characteristics	**Parameter**	**Value**
	Max Power-P_{mp}	$310\ W$
	Open-circuit Voltage -V_{oc}	$45.9\ Vdc$
	Short-circuit Current-I_{sc}	$8.8\ Adc$
	Max Power Voltage-V_{mp}	$37.4\ Vdc$
	Max Power Current-I_{mp}	$8.29\ Adc$
	Efficiency-η	15.98%
Temperature Coefficients	Temperature coefficient at MPP-K_p	$-0.40\%/^0C$
	Temperature coefficient of Voltage-K_V	$-0.29\%/^0C$
	Short-circuit current coefficient-K_s	$0.05\ \%/^0C$
Physical Characteristics	Material	Monocrystalline
	Length by width	$1.956\ \times\ 0.992\ m$
	Module Area	$1.940\ m^2$
	Number of cells	72
Additional Parameters	Series resistance-R_s	$0.30353\ \Omega$
	Parallel resistance-R_{sh}	$96.1505\ \Omega$
PV Array System		
$\boldsymbol{V_{mpp} = V_{pv}}$	$654.5\ V$	
$\boldsymbol{P_{mpp} = P_{pv}}$	$10.537\ kW$	
$\boldsymbol{I_{mpp} = I_{pv}}$	$\frac{P_{mpp}}{V_{mpp}} = \frac{10537}{654.5} = 16.1\ A$	
No. of modules in series	$\frac{V_{mpp}}{V_m} = \frac{654.5}{37.4} = 17$	
No. of modules in parallel	$\frac{I_{mpp}}{I_m} = \frac{17.8}{8.29} = 2$	

The designed PV array system voltage at Maximum Power Point (MPP) is injected into a DC-DC boost converter with PID, SSR-P & O MPPT algorithm, and GA-ANFIS-MPC controllers in MATLAB/SIMULINK. Figure 3.13 shows the case Study Model of a $10kW$ PV System Microgrid created in MATLAB/SIMULINK. There are two section of the PV array modules, the first one called PV Array is for linking with the MATLAB &

SIMULINK Array design area and the subsequent three blocks containing 5 modules each are marked as a 5-module PV Array 1, 2 and 3.

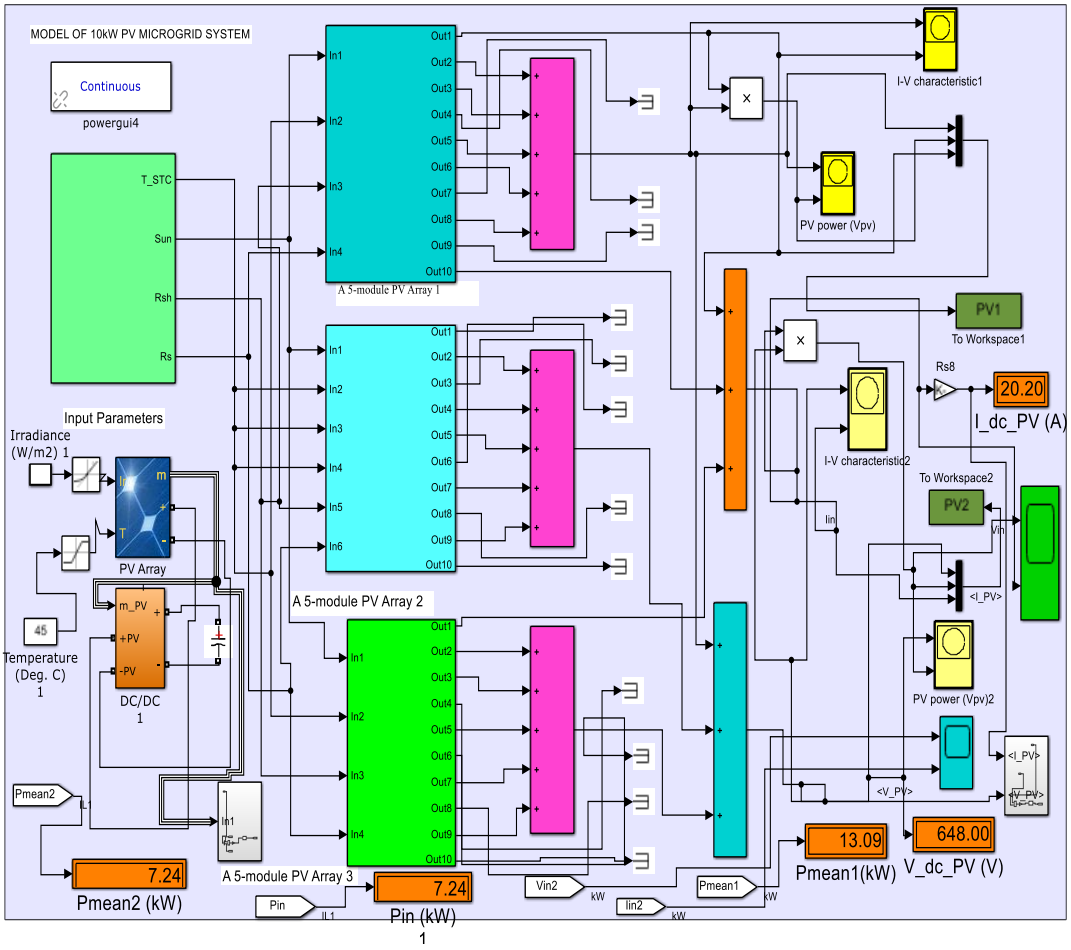

Figure 3.13: Model of a Practical 10kW PV System Microgrid

3.2.7.2. Simulink Model of PMSG Wind Generation System

Electrical power is generated from a WTG in a two-stage process involving the PMSG for the electrical part of the system and a wind turbine model to extract the mechanical power from the wind (Elbeji et al., 2014; C. N. Wang et al., 2014). The Wind Power Generation System (WPGS) has been modeled using the PMSG. The case study version was created around a type A wind turbine (Westwind 6.4 m,10 kW) whose kW rating is 11.48 kW.

The WPGS model consists of two main sections i.e. Wind Turbine Model (WTM) and the Electrical Generator Model (EGM). Table 3.5 summarizes the parameters of the WTM and PMSG models.

Table 3.5: WTM Parameters and PMSG Model

PARAMETER	VALUE	UNITS/REMARKS
Nominal Mechanical Output Power	10,000	Watts (W)
Electrical Generator Base Power	11,111	Volt-amperes (VA)
Base Wind Speed	12	Meters per second (m/s)
Maximum power	0.73	Pu of Nominal Mechanical Power
Base Rotational Speed	1.2	Pu of base generator speed
Pitch angle beta	0^0 or 5^0	Deg (max power at 0^0)
Stator Phase Resistance (R_s)	0.18	Ohms (Ω)
Armature Inductance	0.000835	Henrys (H)
Machine Constant	0.0714394	Volt-second ($V.s$)
Inertia (H_m)	0.0006214	$Kg.m^2$
Viscous damping (F_d)	0.00030345	$N.m.s$
Pole pairs (p)	4	($dimensionless$)
Static friction (T_f)	0	$N.m$
Initial Conditions: ω_m (rad/s), $theta_m$ (deg) and (i_a, i_b, i_c) in (A)	0	Initial conditions $= 0$, units as indicated against parameters.

The Wind Turbine Model (WTM) has three inputs; which are the generator speed per unit of the base speed (synchronous speed), the blade pitch angle (deg), and the wind speed (m/s). The pitch angle either can be set manually or obtained from the pitch angle controller for a variable pitch WTM. The input to the pitch controller is the PMSG rotor speed, $\omega_m rad/s$. The WTM has a single output, T_m (pu), which is the wind turbine mechanical output (pu). This represents the torque applied to the generator shaft in per unit of the generator rating.

The Electrical Generator Model (EGM) used is based on a PMSG with three phases, a sinusoidal back EMF waveform and a round rotor. In the case of a preset model, which is only available for the sinusoidal back EMF machine, the $26.13Nm, 560Vdc\ 3000rpm - 27.3Nm$ machine model can be used as it closely mimics the case study. The mechanical

input is set to Torque (T_m) since the WTM has been modeled to output T_m. After setting the configuration aspects (namely, number of phases, back EMF waveform, rotor type, mechanical input, and preset model); the machine parameters were computed from standard manufacturer specifications using the advanced area functionality of the PMSG block.

The parameters were generated based on the modified Park model, i.e., the rotor flux position when $\theta = 0^0$ is determined based on 90^0 behind phase A axis (modified Park). The generator output included:

i. Rotor speed ω_m (rad/s)
ii. Electromagnetic torque T_e(N*m)
iii. Stator currents for each of the three phases labeled as in equation (3.50):

$$i_{-a}(A),\ i_{-b}(A),\ i_{-c}(A) \tag{3.50}$$

Figure 3.14 shows Simulink diagram of the 10kW wind power generation Case Study System.

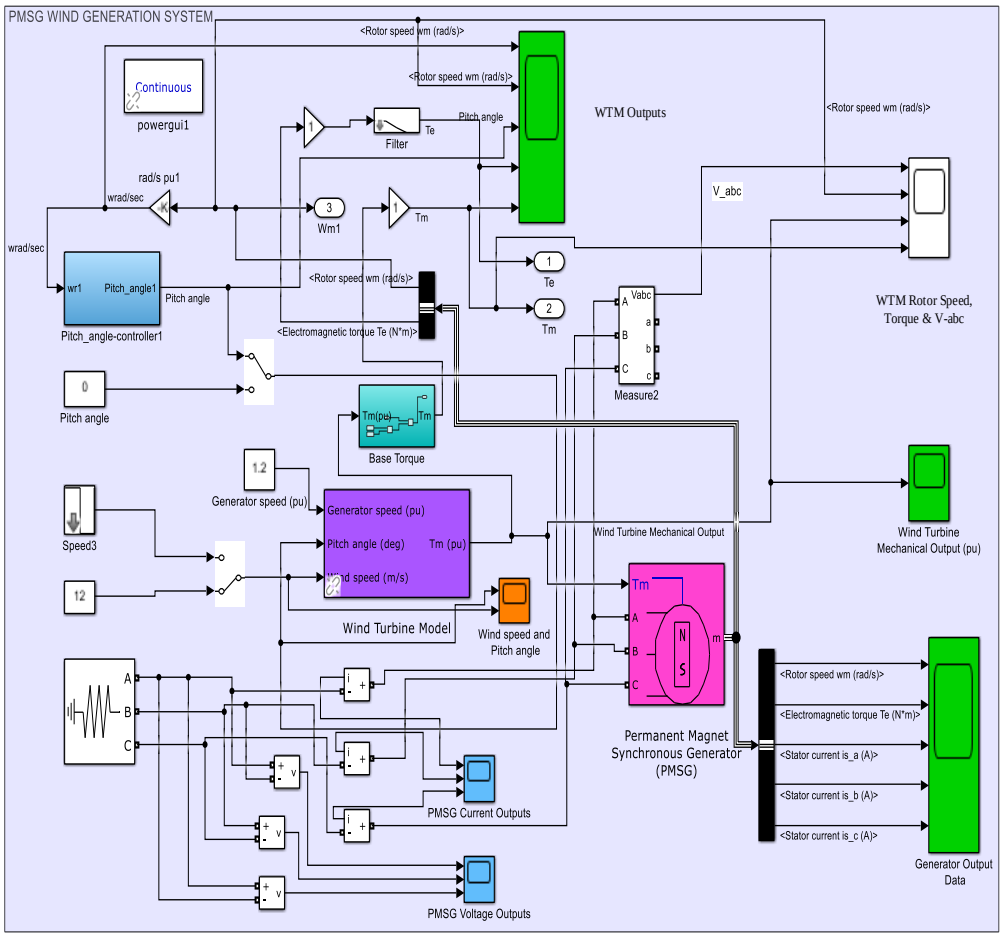

Figure 3.14: Simulink Diagram of a 10kW Wind Power Generation Case Study

3.2.7.3 SIMULINK Design for the Interleaved DC-DC Boost Converter

Figure 3.15 shows the simulation diagram of the suggested IBC built within MATLAB & SIMULINK environment with the improved MPPT algorithms for both Solar PV and WECS within the microgrid. Only the code implementing the MPPT and the values fed to the MPPT are changed in each case (Hisar, 2020). The input voltage is taken to be $V_{in} = 561V$, the switching frequency is $20kHz$, the duty ratio is $D = 0.1928$ (which can be varied using the P & O algorithm), and a resistive load $R = 36\,\Omega$.

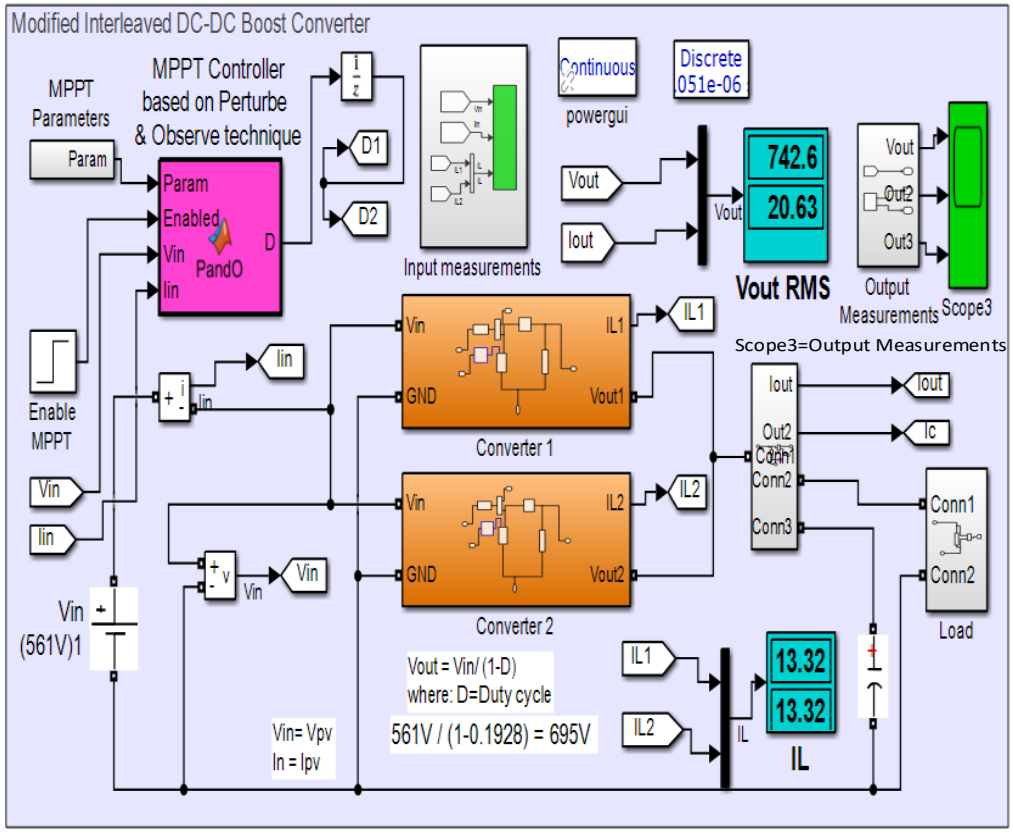

Figure 3.15: Designed Modified IBC

3.2.7.4 Two-Parallel Three-Level VSC for PV-Wind Microgrid Simulink Diagram

The SIMULINK model designed in this study involves a parallel connection of two, three-phase, three-level Neutral-Point-Clamped (NPC) Voltage Source Inverters (VSIs).

Figure 3.16 shows the Simulink Model of the designed Two-Parallel Three-Level VSC for PV and Wind Microgrid. The inverter, which is connected to the PV system DC-DC boost converter, utilizes IGBT as switching device with neutral clamped diodes (Priyadarshi et al., 2018). The other inverter of the parallel pair is connected to the wind turbine DC-DC boost converter and is designed using MOSFETs and neutral point clamped diodes.

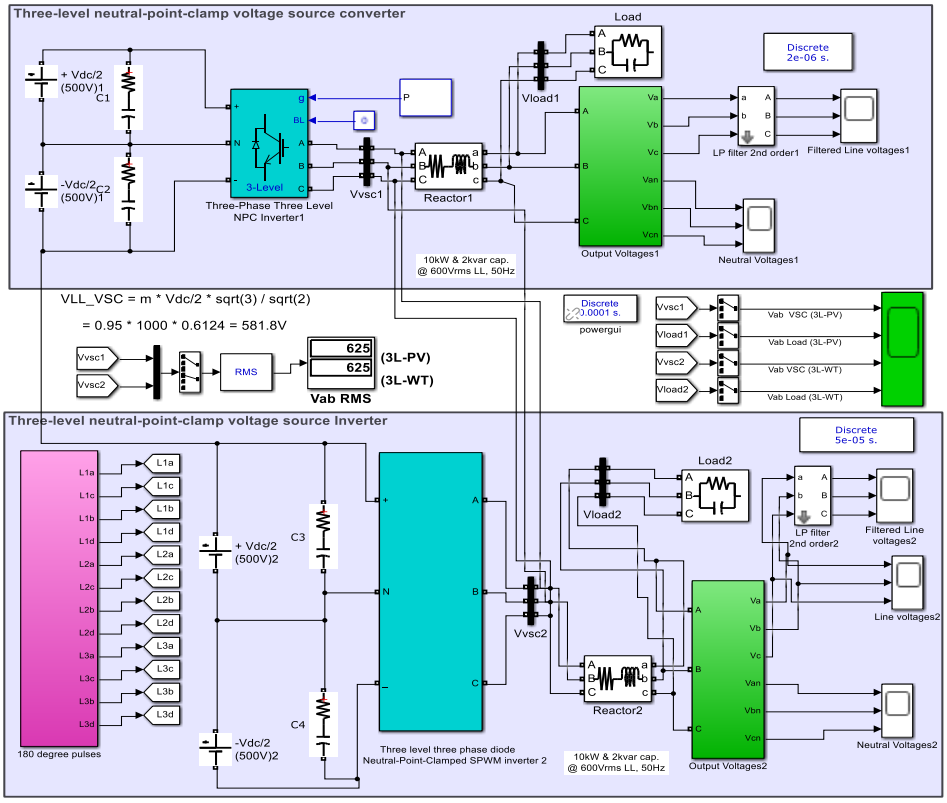

Figure 3.16: Two-Parallel Three-Level VSC for PV and Wind Microgrid Simulink Diagram

MOSFETs are preferred for breakdown voltages less than $250V$, are cheaper and also operate at a higher switching frequency (above $20kHz$). On the other hand, the IGBT is used at frequencies below $20kHz$ with a higher breakdown voltage of more than $400V$ and is costlier than the MOSFETs. For these reasons, the two devices have been chosen for use in the two inverters. Both inverters use the Sinusoidal Pulse Width Modulation (SPWM) modulation strategy (S. A. Rahman Kashif, 2021). To run the model, the (unbounded) variables T_s (e.g. $T_s = 0.01s$) and frequency f (.e.g. $f = 50Hz$) were first declared. The discrete powergui's are set typically at 10^{-6} s for the two inverters and at 10^{-6} s for the voltage measurement scopes.

3.2.7.5 BESS Case Study Model

The BESS model has been created in MATLAB/SIMULINK using equations (3.51) to (3.54) (derived from equations (3.45 and 3.46)), in addition to information gathered from literature, particularly (Krishnan, 2021; S. Kumar, 2022). The values of SoC vary as the value of the DC Voltage source of around $600\ V$. If the DC voltage exceeds the battery's nominal voltage, then SoC will remain the same, i.e., 1. If the battery's nominal voltage exceeds the DC Voltage, then SoC will decrease. A load profile can be established to discharge the battery while simultaneously it is charged by a DC Voltage source.

Table 3.6 shows the charge/discharge parameters used in the simulated case for the two types of batteries considered. All parameters were verified against the existing manufacturer's data sheets and literature (Hisar, 2020; S. Kumar, 2022; Tan, 2021). For the lead-acid battery type, the model uses equations (3.51) and (3.52) (S. Kumar, 2022; Tan, 2021):

Discharge model ($i^* > 0$):

$$f_1(it, i^*, i, Exp) = E_0 - K.\frac{P_{BAT}}{P_{BAT} - it}.i^* - K.\frac{P_{BAT}}{P_{BAT} - it}.it + Laplace^{-1}\left(\frac{Exp(s)}{Sel\ (s)}.0\right) \quad (3.51)$$

Table 3.6: Charge/Discharge Parameters for the Two Types of Batteries Considered

S/No.	Parameter	Lead Acid	Lithium-Ion
Charge parameters			
1	Battery Nominal Voltage (V)	600	600
2	Battery Rated Capacity (Ah)	5000	5000
3	Battery Initial State of Charge (%)	100	100
4	Battery Response Time (s)	30	30
Discharge parameters			
1	Maximum Capacity (Ah)	5208.33	5000
2	Cut-off Voltage (V)	450	450
3	Fully-Charged Voltage (V)	653.29	698.39
4	Nominal discharge current (A)	1000	2173.91
5	Internal Resistance (Ω)	0.0012	0.0012
6	Capacity (Ah) at Nominal Voltage	1551.39	4521.74
7	Exponential Zone [Voltage (V), Capacity (Ah)]	[610.86, 16.67]	[648.23, 245.65]
8	Discharge current [$[i_1, i_2, i_3, \dots]$][A]	50	50

Charge model ($i^* < 0$):

$$f_2\,(it, i^*, i, Exp) = E_0 - K.\frac{P_{BAT}}{|it| + 0.1.P_{BAT}}.i^* - K.\frac{P_{BAT}}{P_{BAT} - it}.it + Laplace^{-1}\left(\frac{Exp(s)}{Sel\,(s)}.1s\right) \quad (3.52)$$

For the Lithium-Ion battery type, the model uses equations (3.53) and (3.54) (J. Meng et al., 2018; S. Kumar, 2022):

Discharge model ($i^* > 0$):

$$f_1\,(it, i^*, i,) = E_0 - K.\frac{P_{BAT}}{P_{BAT} - it}.i^* - K.\frac{P_{BAT}}{P_{BAT} - it}.it + A.exp(-B.it) \quad (3.53)$$

Charge model ($i^* < 0$) (Krishnan, 2021; S. Kumar, 2022):

$$f_2(it, i^*, i,) = E_0 - K.\frac{P_{BAT}}{|it| + 0.1.P_{BAT}}.i^* - K.\frac{P_{BAT}}{P_{BAT} - it}.it + A.exp(-B.it) \qquad (3.54)$$

where A is the Exponential voltage (V), B is the Exponential capacity, (Ah^{-1}) and E_{bat} is the nonlinear voltage (V).

The performance of the BESS is tested with the output of a modified interleaved DC-DC Boost Converter (DBC) developed earlier via a controlled voltage source as shown in Figure 3.17.

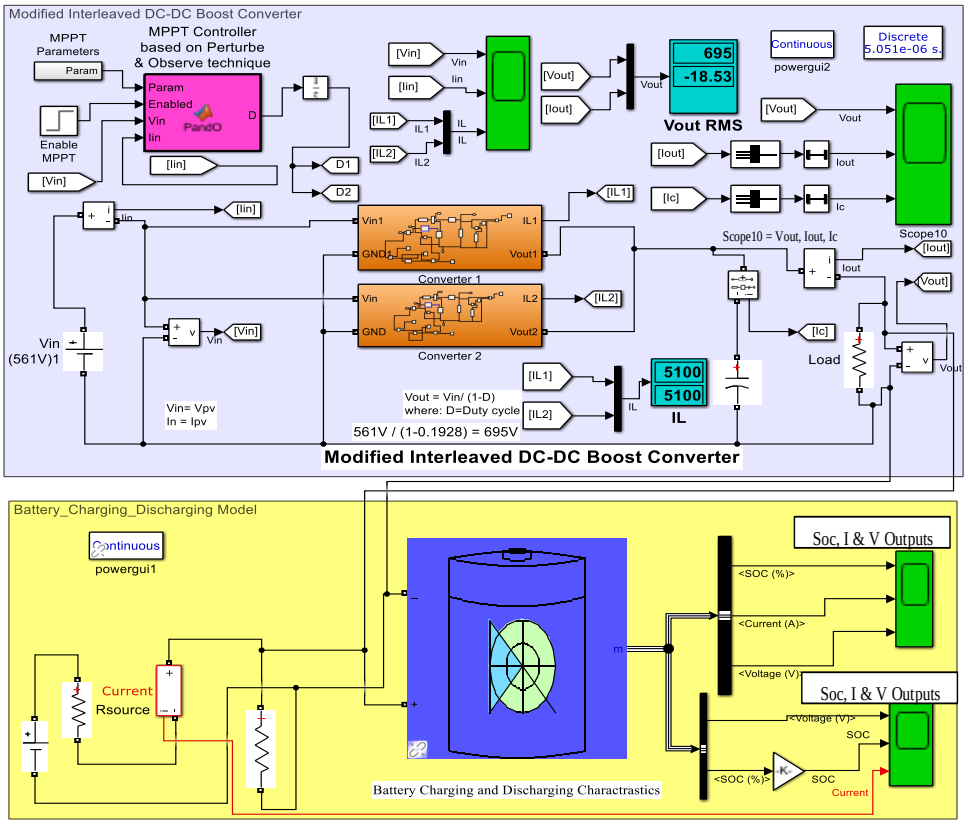

Figure 3.17: The BESS Model Connected with the Modified IBC in MATLAB & SIMULINK

3.2.8 Transfer Function Model of PV-Wind Hybrid Microgrid

3.2.8.1 Overall Transfer Function Model of the PV-Wind Hybrid Microgrid

The microgrid's mathematical transfer function model has been created to study the working of the proposed GA-ANFIS-MPC controller in regulating the microgrid's voltage within the context of transient response. The derivation of the proposed PV-Wind Microgrid mathematical model using the Transfer Function is challenging due to the nonlinear components in the microgrid, such as the solar PV, PMSG-wind turbine, BESS, IBCs, and the VSI inverters (Kumar et al., 2020; Pavan Kumar & Bhimasingu, 2021). The microgrid is generally a multi-input, multi-output (MIMO) system with dual control loops, namely, outer voltage and inner current control loops (Kumar et al., 2020; Pavan Kumar & Bhimasingu, 2021).

Researchers have modeled the RES components in microgrids by assuming a transfer function model with a time lag under small-signal considerations (M. Ali et al., 2021; c et al., 2019; Kumar et al., 2020; Pavan Kumar & Bhimasingu, 2021).

As reported by (Kumar et al., 2020), the output power (in watts) of the PV system given in equation (3.55) indicates that power is linearly proportional to solar radiation G_{SR} (W/m^2), assuming ambient temperature (T_c), surface area (A), and efficiency (η_{PV}) are constant.

$$P_{PV} = \eta_{PV} A G_{SR} \{1 - (0.005(T_c + 25))\} \tag{3.55}$$

In the Transfer Function modeling of the hybrid microgrid under study, the following assumptions have been made, which also form the limitations of the study:

i. The PV & WTG are operating at their MPP.
ii. The ambient temperature, irradiance, insolation, wind speed, etc., do not vary with time; thereby, the MPP of the PV array & WTG are also fixed.

iii. The voltage and current output of the inverter are in phase. Therefore, the system works at a unity power factor, and no reactive power is supplied to the load.

iv. When the change in the voltage (ΔV) is positive, BESS status is charging, or else it is discharging.

In this study, the mathematical transfer function models for a solar PV plant, wind turbine generator, and BESS have been portrayed as first-order lagging systems of gains ($K_{PV}, K_{WTG}, K_{BESS}$) and time constants ($T_{PV}, T_{WTG}, T_{BESS}$) as given in equations (3.56), (3.57), and (3.58), respectively (M. Ali et al., 2021; c et al., 2019; Kumar et al., 2020; Mohanty et al., 2017).

$$G_{PV} = \frac{K_{PV}}{sT_{PV} + 1} \tag{3.56}$$

$$G_{WTG} = \frac{K_{WTG}}{sT_{WTG} + 1} \tag{3.57}$$

$$G_{BESS} = \frac{K_{BESS}}{sT_{BESS} + 1} \tag{3.58}$$

Similarly, the transfer function of the boost converter assuming any resistive load is considered as a first-order system given by equation (3.59):

$$G_{BC} = \frac{\Delta V_{out}(s)}{\Delta V_{in}(s} = \frac{K_{BC}}{sT_{BC} + 1} \tag{3.59}$$

where K_{BC} and T_{BC}, represent the amplification factor and time constant, respectively.

The Transfer Function (TF) of the 6-switch three-phase two-level inverter without any Low Pass Passive filter circuit is approximately defined as a first-order lagging system by equation (3.60) (Mohanty et al., 2017).

$$G_{Inv} = \frac{V_o(s)}{V_{ref}(s} = \frac{K_{inv}}{sT_{inv} + 1} \tag{3.60}$$

Figure 3.18 shows the complete mathematical transfer function model of the PV-wind hybrid microgrid based on small-signal low-order dynamic models of the individual components. The PMSG's output is rectified and measured for channeling to the GA-ANFIS-MPC controller while simultaneously injecting it into the DC-DC converter. The PV system has been modeled using an equivalent circuit at the cell level based on the two-diode model to achieve better accuracy and increased power extraction (Abdel-Rahim, 2020).

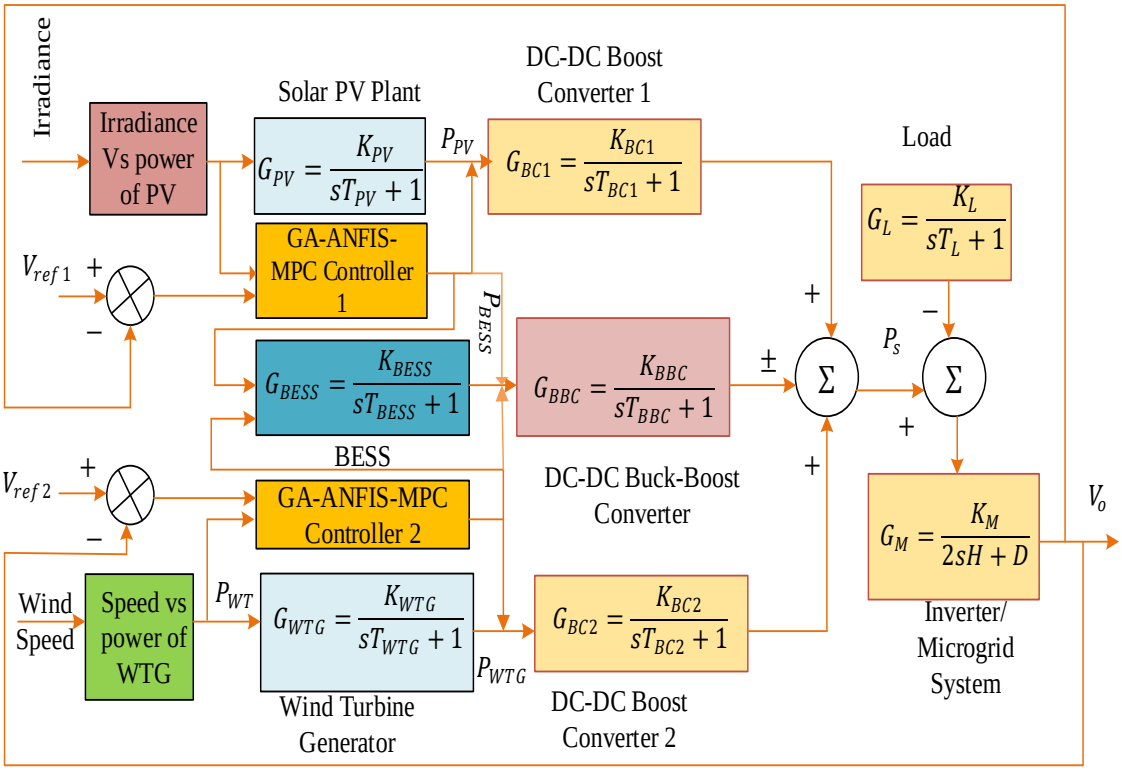

Figure 3.18: Schematic Small-Signal Mathematical Transfer Function Model of the PV-Wind Hybrid Microgrid with GA-ANFIS-MPC

The PV array system's Maximum Power Point (MPP) voltage is fed to the IBC with the GA-ANFIS-MPC algorithm. The schematic diagram of the microgrid in Figure 3.18 was transformed into a controlled equivalent transfer function model viewed in terms of a small-signal-based dual voltage-current (V/I) controller TF model, as shown in Figure 3.19 (Pavan Kumar & Bhimasingu, 2021).

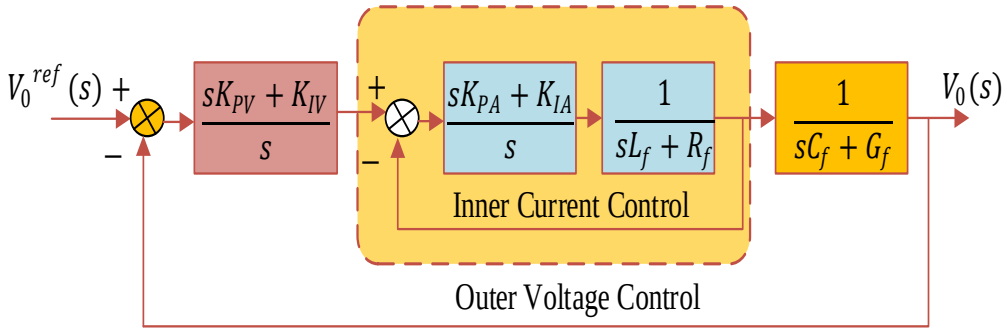

Figure 3.19: Reduced Dual-Loop V/I Controlled Microgrid

Table 3.7 depicts each subsystem's transfer functions and corresponding parameters (M. Ali et al., 2021; Pavan Kumar & Bhimasingu, 2021).

Table 3.7: The transfer Functions and Related Parameters Used in Each Subsystem

Subsystem	Transfer Function	Parameters
Solar PV plant	$G_{PV} = \frac{K_{PV}}{sT_{PV} + 1}$	$K_{PV} = 1, T_{PV} = 0.03s$
Wind Turbine Generator (WTG)	$G_{WTG} = \frac{K_{WTG}}{sT_{WTG} + 1}$	$K_{WTG} = 1, T_{WTG} = 1.5s$
BESS	$G_{BESS} = \frac{K_{BESS}}{sT_{BESS} + 1}$	$K_{BESS} = 1.8, T_{BESS} = 0.001s$
DC-DC Boost Converter	$G_{BC1} = \frac{K_{BC1}}{sT_{BC1} + 1}$	$K_{BC1} = 2.5, T_{BC1} = 0.01s$
DC-DC Buck-Boost Converter	$G_{BBC} = \frac{K_{BBC}}{sT_{BBC} + 1}$	$K_{BBC} = 1.5, T_{BBC} = 0.1s$
Inverter/Microgrid system	$G_M = \frac{K_M}{2sH + D}$	$K_M = 1.8, H = 2, D = 0.015pu/Hz,$ $H = 0.085\ pu.s$
Load	$G_L = \frac{K_L}{sT_L + 1}$	$K_L = 2, T_L = 0.04s$

The overall TF was obtained using the block diagram reduction procedure, the small signal model pole-zero cancellation (MPZC), and the power quality requirements specified by IEEE-1547 and IEEE-519 standards. The TF relating the output to input for the system is given by equations (3.61), (3.62) and (3.62) (Pavan Kumar & Bhimasingu, 2021):

$$\frac{V_0(s)}{{V_0}^{ref}(s)} = Closedloopof\big(F_1(s) \times F_2(s) \times F_3(s)\big) \tag{3.61}$$

where

$$\begin{cases} F_1(s) = \dfrac{K_{IV} + sK_{PV}}{s} \\ F_2(s) = CI.loop\left(\dfrac{K_{IA} + sK_{PA}}{s\big(sL_f + R_f\big)}\right) = \dfrac{K_{IA} + sK_{PA}}{s^2L_f + \big(R_f + K_{PA}\big)s + K_{IA}} \\ F_3(s) = \dfrac{1}{G_f + C_f s} \end{cases} \tag{3.62}$$

$$\begin{cases} \therefore \dfrac{V_0(s)}{{V_0}^{ref}(s)} = \dfrac{(K_{PA}K_{PV})s^2 + (K_{IV}K_{PA} + K_{PV}K_{IA})s + K_{IA}K_{IV}}{\left(\begin{matrix}(L_fC_f)S^4+(R_fC_f+G_fL_f+K_{PA}C_f)s^3+(G_fR_f+K_{PA}G_f+K_{PA}K_{PV}+C_fK_{IA})s^2 \\ (K_{IA}K_{PA}+G_fK_{IA}+K_{IV}K_{PA})s+K_{IA}K_{IV}\end{matrix}\right)} \end{cases} \quad (3.63)$$

To obtain one of the simulated scenarios, the model-based pole-zero cancellation (MPZC) technique was applied by setting $G_f = 0$, $K_{IV} = 0$, and the filter parameter (C_f) specified in Table 3.8 alongside the resultant computed values presented in Table 3.8. With these, the ultimate equations are given in equation (3.64) for the conventional best (CC) and equation (3.65) for MPZC (Pavan Kumar & Bhimasingu, 2021).

$$\left\{\frac{V_0(s)}{{V_0}^{ref}(s)}\right|^{CC} = \frac{1.99s^2 + 68.72s + 190.17}{0.001s^4 + 0.18s^3 + 5.47s^2 + 68.72s + 190.17} \quad (3.64)$$

$$\left\{\frac{V_0(s)}{{V_0}^{ref}(s)}\right|^{MPZC} = \frac{s + 56.08}{0.001s^3 + 0.163s^2 + 5.97s + 56.08} \quad (3.65)$$

Table 3.8: Parameters Used for the V/I Controller Equivalent Transfer Function

Parameter	Description	Specification
P_r	Microgrid rated power	$25\ kW$
V_{dc}	Inverter Input DC voltage	$540\ V$
ΔV_{ac}	The maximum deviation in the inverter output voltage	$\pm 62\ V$
F_s	Inverter switching frequency for PWM signals	$15\ kHz$
F_r	Minimum current ripple frequency	$600\ Hz$
C_f	Filter capacitance	$50\ \mu F$
L_f	Filter inductance	$1.35\ mH$
R_f	Filter resistance	$0.1\ \Omega$
G_f	Filter conductance	$0\ mho$
τ_1	Inner current control loop time constant	$15\ ms$
τ_2	Outer voltage control loop's time constant	$90\ ms$
K_{PA}	Proportional controller specification of the current controller	0.12
K_{IA}	Integral controller specification of the current controller	6.7
K_{PV}	Proportional controller specification of the voltage controller	$5.65e^{-4}$
K_{IV}	Integral controller specification of the voltage controller	0

3.2.8.2 TF Model of the Microgrid System with Hybrid GA-ANFIS Controllers

The schematic model of the studied PV-wind hybrid microgrid and the individual components' transfer function (TF) based on small-signal low-order dynamic models with the GA-ANFIS controller has been shown in Figure 3.20. The PMSG's output is rectified and measured for channeling to the GA-ANFIS controller while simultaneously injecting it into the DC-DC converter. The PV system has been modeled using an equivalent circuit at the cell level based on the two-diode model to achieve better accuracy and increased power extraction (Abdel-Rahim, 2020). The PV array system's maximum power point (MPP) voltage is fed to the IBC with the GA-ANFIS controller algorithms.

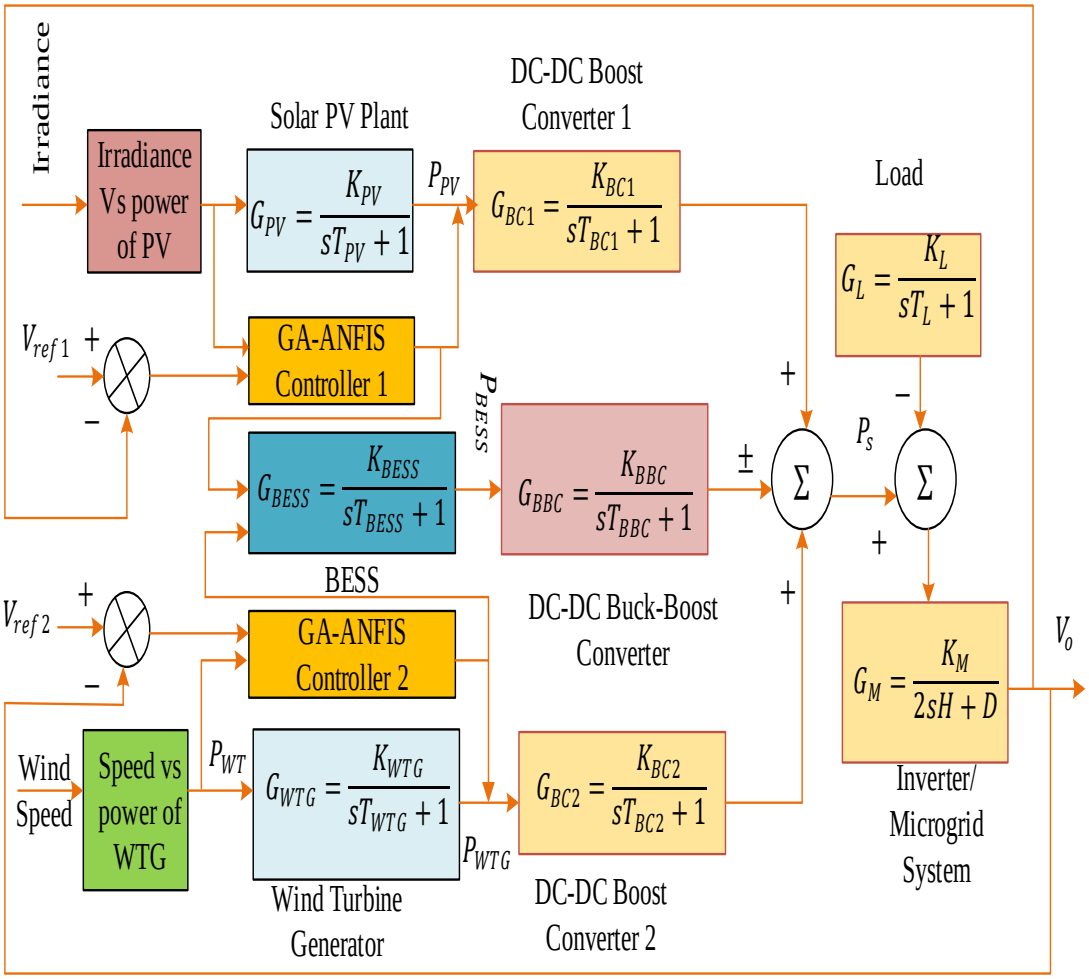

Figure 3.20: Schematic Mathematical Transfer Function Model of the PV-Wind Hybrid Microgrid with Hybrid GA-ANFIS Controller

3.2.8.3 TF Model of the Photovoltaic-Wind Microgrid System with MPC Controller

The schematic model of the studied PV-wind hybrid microgrid and the individual components' transfer function (TF) based on small-signal low-order dynamic models with MPC controller is shown in Figure 3.21.

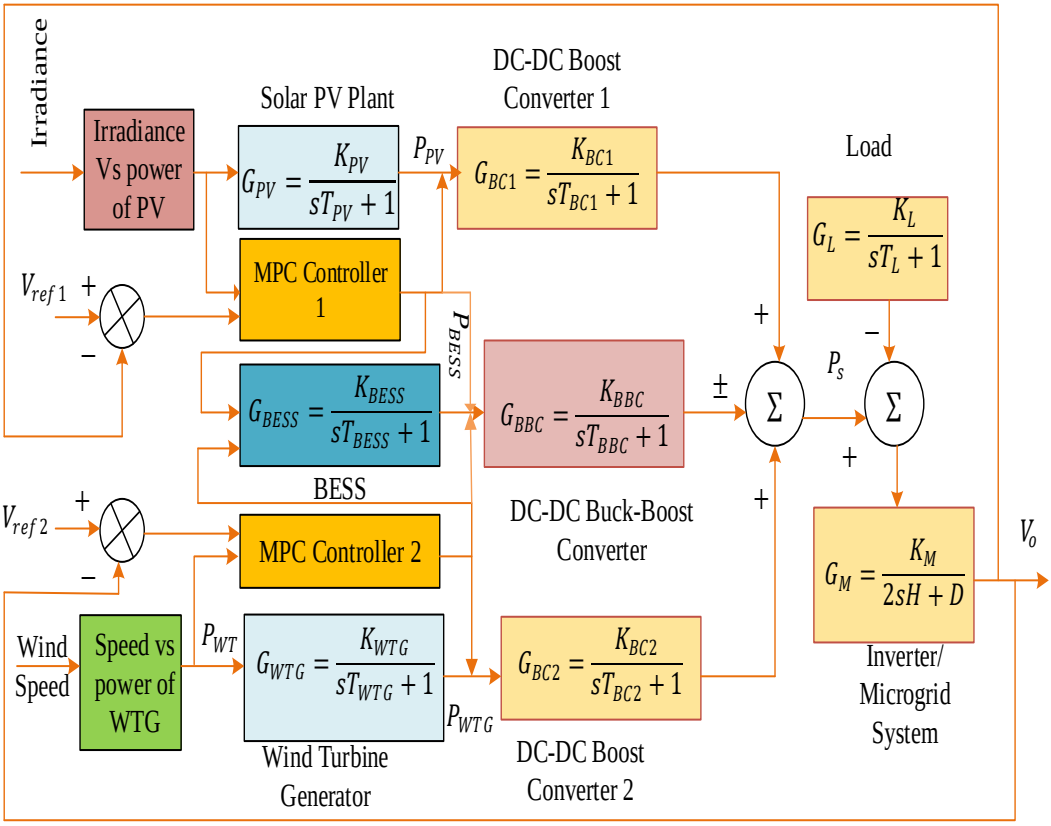

Figure 3.21: Schematic Small-Signal Mathematical Transfer Function Model of the PV-Wind Hybrid Microgrid with MPC Controller

3.3. Design of the Proposed GA-ANFIS Controller

The control method presented in this section (i.e. GA-ANFIS) supports the realization of specific objective number two. The first step in choosing a control strategy is to determine whether the microgrid will be grid- connected off-grid, or making transitions between the two. If grid-connected, the microgrid control strategy is dictated by the utility. On the other hand, in off-grid mode of operation, the control strategy is determined by a set of factors including type of micro sources and net capacity, capacity of available energy storage, type of load and ownership. This study focused on off-grid mode of operation.

3.3.1 GA-ANFIS Primary Microgrid Control System

This section corresponds to the specific objective two and presents the design of the Genetic Algorithm-Adaptive Neuro-Fuzzy Inference System (GA-ANFIS) controller. The GA-ANFIS controller has been used as a Maximum Power Point Tracking (MPPT) algorithm to optimize the converter outputs and provide voltage regulation amid power generation variations. The performance of the GA-ANFIS algorithm was compared with the Search Space Restricted-Perturb and Observe (SSR-P&O) and the Proportional-plus-Integral-plus-Derivative (PID) controllers using a simulation model built in MATLAB/SIMULINK.

3.3.2 Adaptive Neuro-Fuzzy Inference System (ANFIS) Control Structure

The Adaptive Neuro-Fuzzy Inference System (ANFIS) is the training tool for Sugeno-type fuzzy systems (Gamage et al., 2021). ANFIS is more efficient because it infuses the merits of the FLC and ANN techniques to create a robust nonlinear self-tuning controller. The ANFIS rules are in linguistic format, making it easier to analyze and interpret intermediate results (Aloo et al., n.d.). The ANFIS control structure consists of a network of units and connections forming a five-layer connected network with layers 1 to 5, as depicted earlier in Figure 2.13 under Literature Review (Bogaraj & Kanakaraj, 2016; Truong et al., 2021). The significance of each layer and detailed operation of the 2-input-1-output ANFIS structure are presented in (Gamage et al., 2021). The hybrid-learning algorithm automatically achieves the ANFIS controller's tuning. The algorithm uses a combination of the least-square estimation (for output membership functions) and a backpropagation algorithm (for output and input membership functions) to generate the teaching signal (Pawar & Nema, 2020).

Assuming two inputs $x, y,$ and one output z structure for simplicity, a rule set can be expressed in equations (3.66) to (3.69) for a first-order Sugeno fuzzy model with 49 fuzzy if-then rules.

Rule 1: If x is A_1 and y is B_1, then:

$$z_1 = p_1x + q_1y + r_1 \tag{3.66}$$

Rule 2: If x is A_2 and y is B_2, then:

$$z_2 = p_2x + q_2y + r_2 \tag{3.67}$$

Rule 3: If x is A_3 and y is B_3, then:

$$z_3 = p_3x + q_3y + r_3 \tag{3.68}$$

$$\vdots$$

Rule 49: If x is A_{49} and y is B_{49}, then:

$$z_{49} = p_{49}x + q_{49}y + r_{49} \tag{3.69}$$

where A_i and B_i denote the fuzzy sets in the antecedent, and p_i, q_i, and r_i, are the design parameters computed while executing the training. The parameters that were trained are A_i and B_i of the premise parameters and p_i, q_i, and r_i, of the consequent parameters. Here, $x = A_i$ represents the PV-wind Power Generation Error, $y = B_i$ the change in PV-wind Power Generation Error and z represents the GA-ANFIS Output. Part of the data used for the GA-ANFIS training and overall design is presented in Appendix 4, such as Table A4.5.

3.3.3 Flow chart of Proposed Genetic Algorithm (GA)

The GA-ANFIS primary controller is required to generate appropriate pulse width modulated (PWM) control signals necessary to regulate and stabilize the converter voltage and is made up of two parts. Figure 3.22 presents the flow chart of the GA part of the control system.

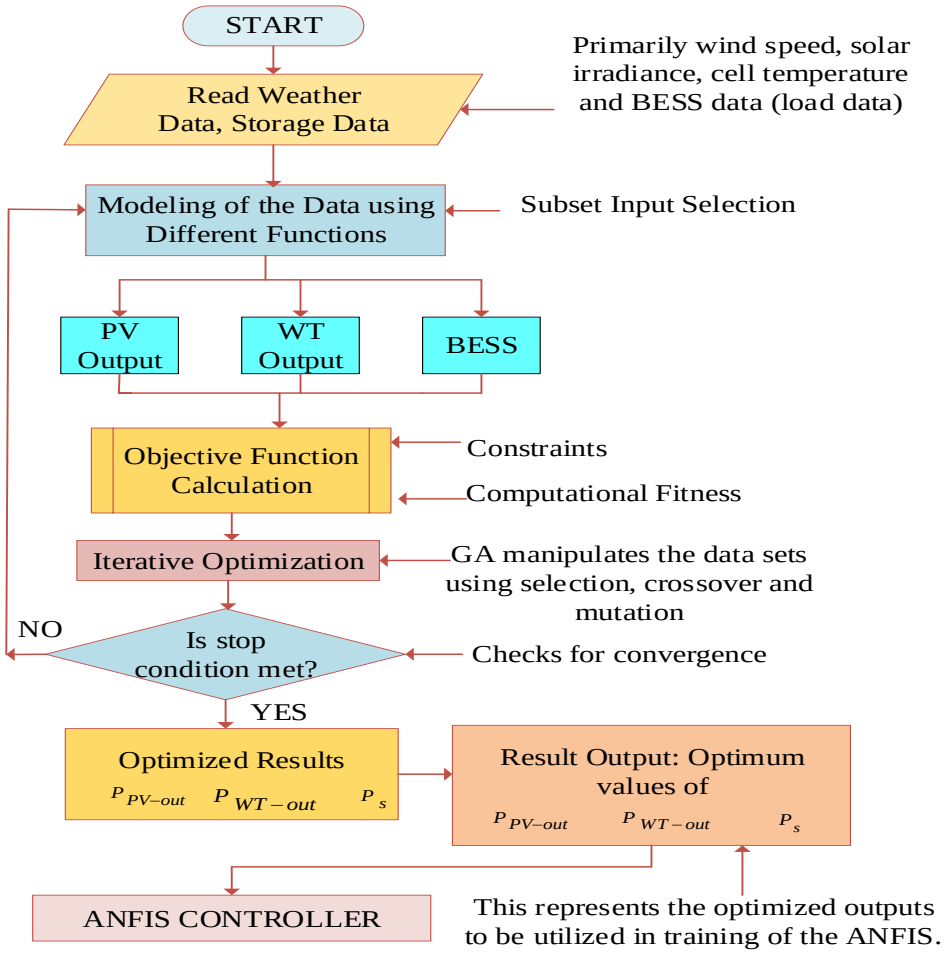

Figure 3.22: Flow Chart of Proposed Genetic Algorithm (GA)

The first portion is the GA unit used to obtain optimal generation outputs of PV and WT of the microgrid system based on the available meteorological data. The rest of the steps are as follows:

1. In step 1, the inputs to the GA, primarily the wind speed, solar irradiance, cell temperature, and BESS data representing the initial population, are specified.
2. The captured data is modeled in step 2 using different functions to create clusters denoting average seasonal variations in the weather and storage performance corresponding to subset input selection. The outputs of this step include data about

PV output (P_{PV-out}), wind turbine (P_{WT-out}), and the BESS stored/drawn power (P_s).

3. Step three, corresponds to the determination of computational fitness and represents the calculation of the objective function, which is done according to the objective function in equation (3.1) guided by the power balance equation (3.70) and the constraints defined by equation (3.2):

$$P_T = P_{WTG} + P_{PV} \mp P_s \tag{3.70}$$

where P_T, is the total power generated in the microgrid.

4. In step four, the GA is taken through iterative optimization where it manipulates the prescribed data sets using selection, crossover, and mutation processes of the standard GA algorithm. If the stop condition has not been reached, it jumps to the modeling step; else, it proceeds to the optimized results, i.e., optimum P_{PV-out}, P_{WT-out}, and P_s.
5. In the last step, this data is applied in the training of ANFIS in the second part of the proposed GA-ANFIS controller.

The GA algorithm was implemented using a program written in MATLAB in which all the important parameters were specified, including population size, the maximum number of generations, the number of elite individuals, selection method, crossover function and fraction, mutation function, and mutation rate.

3.3.4 Flow Chart of Proposed GA-Optimized ANFIS Controller

The flowchart of Figure 3.23 shows the GA-optimized ANFIS algorithm (Aloo et al., 2023).

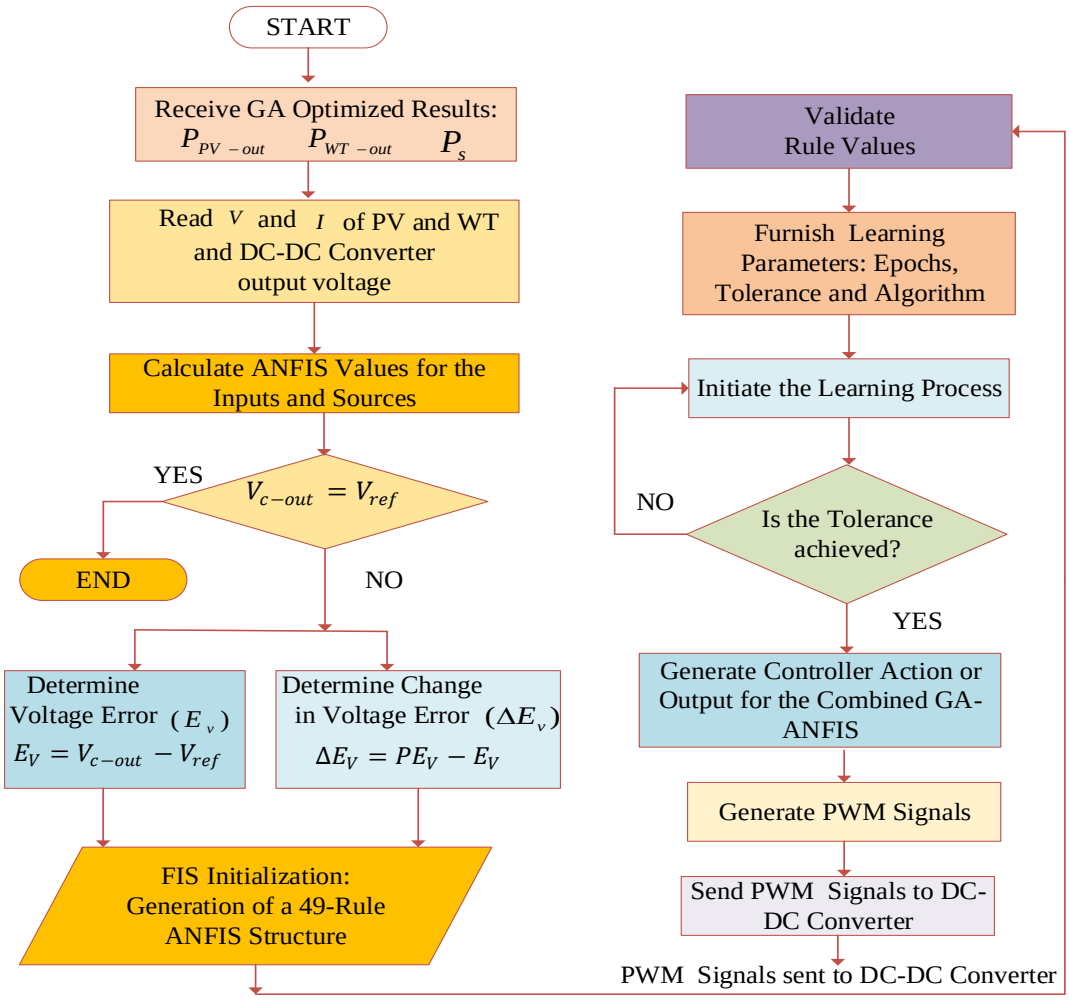

Figure 3.23: Steps for GA-Optimized ANFIS Controller Design

The GA-optimized results (P_{PV-out}, P_{WT-out}, and P_s) are presented to the ANFIS alongside the measured values of V and I and the expected DC-DC converter output voltage (V_{ref}). The reference voltage is computed using predetermined conditions according to the power balance equation. The generated output voltage (V_{c-out}) is compared with the set reference voltage (V_{ref}) to generate the voltage error (E_v) and change in the voltage error (ΔE_v) which form the final inputs to the ANFIS part of the

GA-optimized ANFIS controller. The output is a control output voltage signal used to fire the PWM operator that runs the DC-DC converter.

Once a new set of training data is created, the same is used to compute the ANFIS values in terms of reference microgrid DC voltage (V_{ref}) and DC-DC converter output voltage (V_{c-out}) for each input. A comparison is made between V_{c-out} and V_{ref}, and if equal, no action is taken. If the two are not equal, the voltage error (E_v) and change in voltage error (ΔE_v) are obtained using V_{c-out}, $V_{ref,}$ and PE_v, where PE_v, is the previous voltage error. All the ANFIS values are checked, and its learning parameters are supplied.

A hybrid algorithm of the least squares method and the backpropagation gradient descent method is used to train the ANFIS. The training parameters of the ANFIS controller specified during its design are the number of fuzzy rules, the number of linear and nonlinear parameters, the number of nodes, and the number of training, checking, and testing data pairs. Once trained according to the tolerance or criteria set, the GA-ANFIS controller generates a suitable output control signal. This control signal is sent to the PWM module that produces PWM signals fed to the DC-DC converter to regulate the converter output voltage.

Supervised learning was used in the ANFIS design because labeled training data was available. The data was obtained from the designed model run with the SSR-P&O and a MATLAB code, according to the generation data available at the National Renewable Energy Laboratory (NREL) site (Blair et al., 2018). The data used in the design of the GA-ANFIS controller was pre-processed using MATLAB codes and converted into a form that the GA-ANFIS required, making the designed GA-ANFIS controller universally acceptable and not limited by utilized dataset. This form of data is available on request.

The Solar and Wind raw data before transformation and further modifications was obtained from the National Solar Radiation Database (NSRDB) provided by the National Energy Research Laboratory (NREL). The data is freely and publicly available at https://nsrdb.nrel.gov/data-viewer as well as through the System Advisor Model (SAM)

version SAM 2018.11.11 provided freely by NREL (Blair et al., 2018). The site considered was Juja, Kiambu, Kenya with Latitude 1.095161S and Longitude 37.01249E for the period 2017 to 2019 with a spatial resolution of $4km$ by $4km$. The parameters of the designed integrated GA and ANFIS system are captured in Table 3.9.

Table 3.9: GA-ANFIS System Parameters

GA Parameters	
PopulationType	Double Vector
PopulationSize	50
Elite Count (0.05*PopulationSize)	Adapted in simulations
Crossover Fraction (0.8)	Adapted in simulations
Migration Interval	20
Migration Fraction	0.2
Generations (100*number of variables)	300
PenaltyFactor (InitialPenalty = 10)	100
StallGenLimit	50
ANFIS Parameters	
Number of nodes	115
Number of linear parameters	147
Number of nonlinear parameters	224
Total number of parameters	371 (premise=28, consequent =349)
Number of training data pairs	54 (57.4%)
Number of checking data pairs	20 (21.3%)
Number of testing data pairs	20 (21.3%)
Number of fuzzy rules	49
Training method	Hybrid learning algorithm
Designated epoch number	50
ANFIS training error tolerance	0.001

Figure 3.24 shows the surface plots capturing the inputs and output of the designed ANFIS at a particular instant of simulation. Input 1 represents the voltage error (E_v) and input 2 the change in the voltage error (ΔE_v) whereas the output is the control output voltage signal for generating the PWM signals for the DC-DC Converter.

In Figure 3.25, the structure of the designed ANFIS controller is shown, where a total of 49 rules are generated from the 7x7 input membership functions. It has 115 nodes, 147 linear parameters and 224 nonlinear parameters.

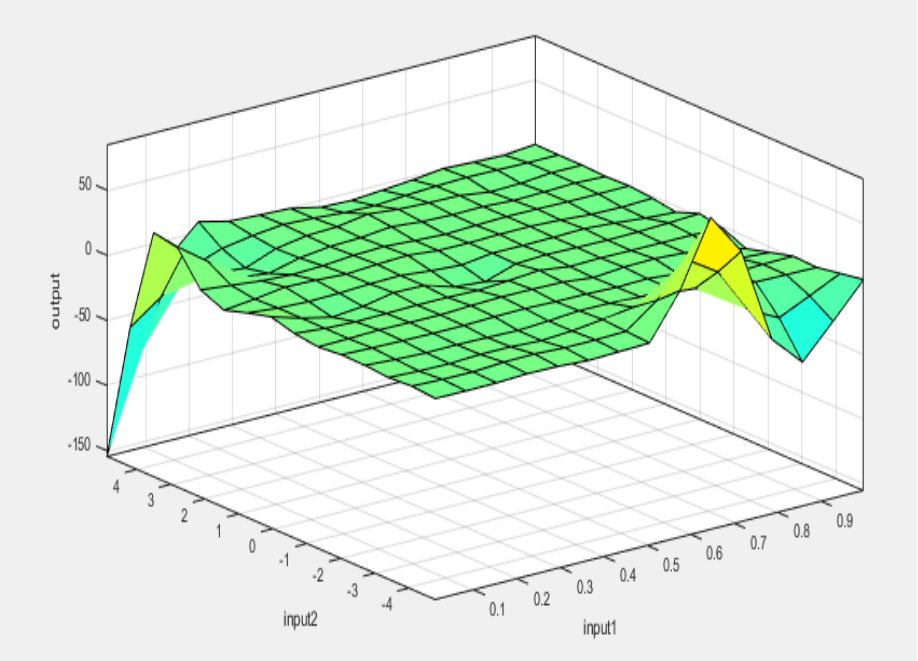

Figure 3.24: The Inputs and Output of the Designed ANFIS

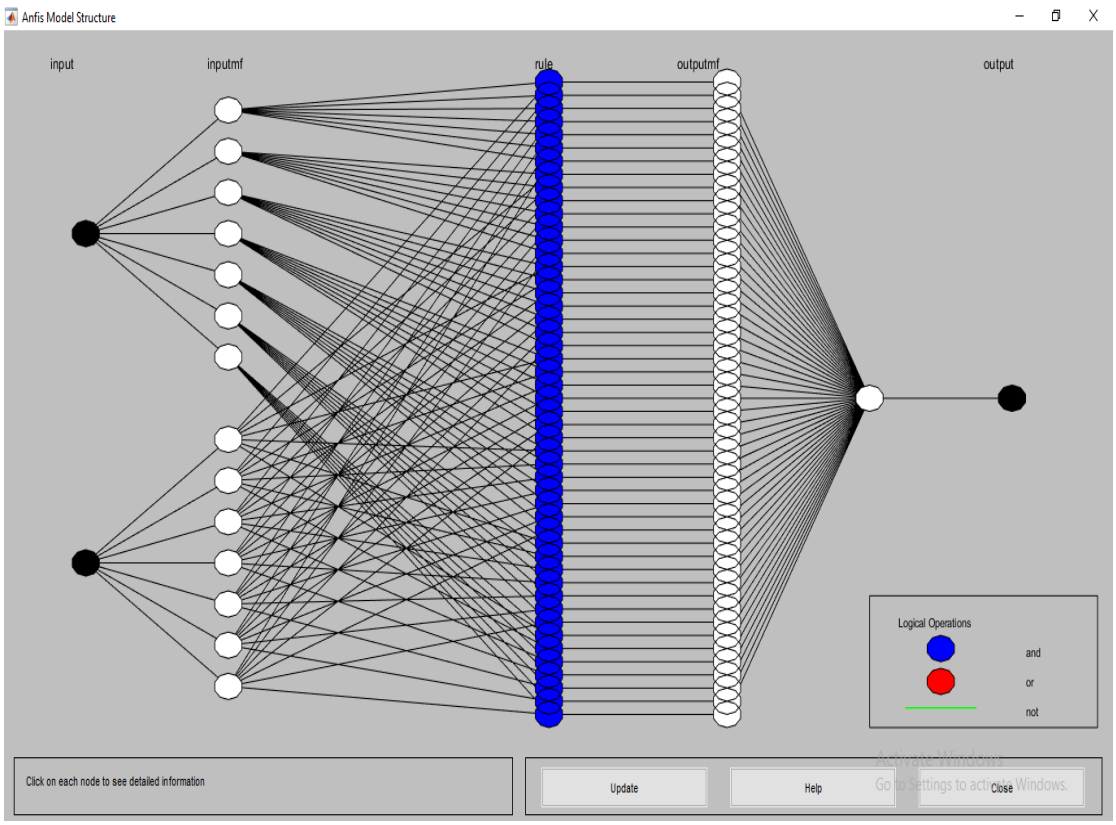

Figure 3.25: The Structure of the Designed ANFIS

3.3.5 Combined SIMULINK Model with a Case Study for the PID, and GA-ANFIS Controllers

The consolidated 10 kW microgrid SIMULINK case study model of Figure 3.26 with the GA-ANFIS Controller was obtained by integrating the individual models for the 10 kW solar PV system, the 10 kW wind energy system, the designed IBCs, and the BESS. Figure 3.27 shows the MATLAB/SIMULINK Transfer Function (TF) Model of the proposed PV-Wind hybrid microgrid to test the SSR-P&O, PID, ANFIS performance, and GA-ANFIS controllers.

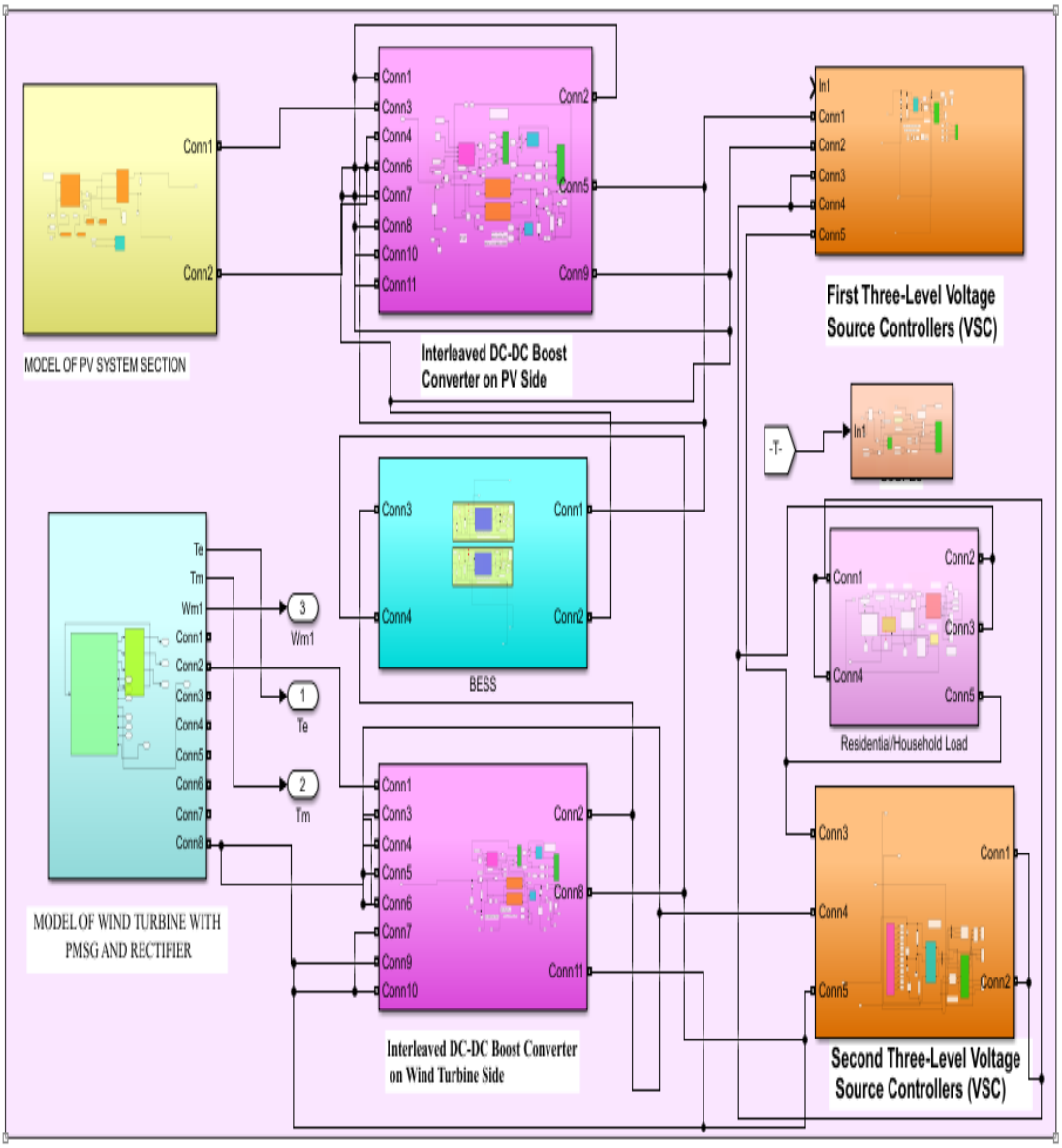

Figure 3.26: GA-ANFIS Controller in the SIMULINK Model of the Microgrid Case Study with IBC

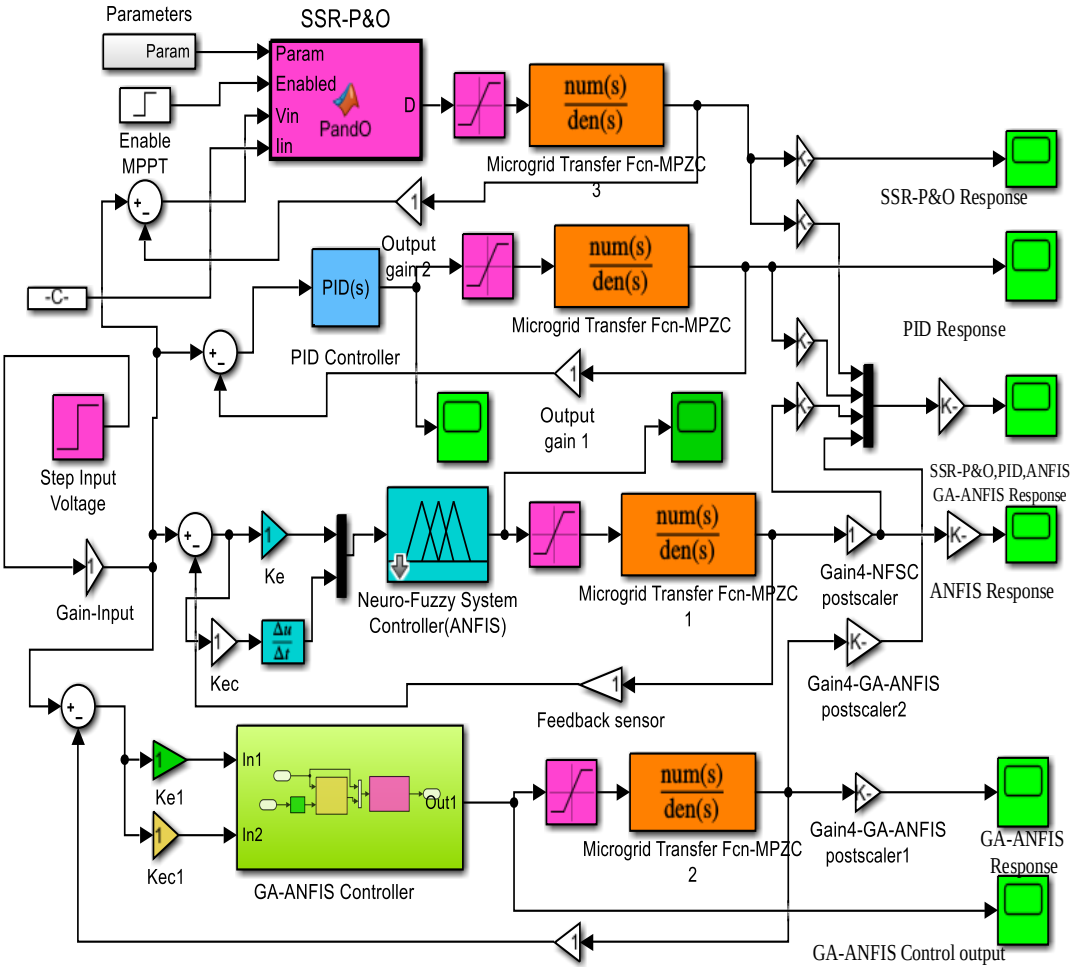

Figure 3.27: Simulink Transfer Function Model of Proposed PV-Wind Hybrid Microgrid with PID and GA-ANFIS Controllers

3.4 Design of the MPC Secondary Microgrid Control System for BESS

This section corresponds to the specific objective three and presents the design of the Model Predictive Controller (MPC). The MPC controller has been realized using codes and MATLAB & SIMULINK MPC controller Toolbox.

3.4.1 Structural aspects of the Model Predictive Controller (MPC)

Figure 3.28 is a generalized block diagram depicting the structural aspects of the Model Predictive Controller (MPC), which are useful in the development of this type of control strategy for the proposed system. As can be seen, the MPC is a discrete-time controller, which takes in discrete reference value, $R(k)$ representing the available PV and WT power and compares it with the predicted value $\hat{y}(k)$. In case of discrepancies between the two, the error generated, $e(k)$ is adjusted according to an objective function within stipulated constraints (Aloo et al., n.d.).

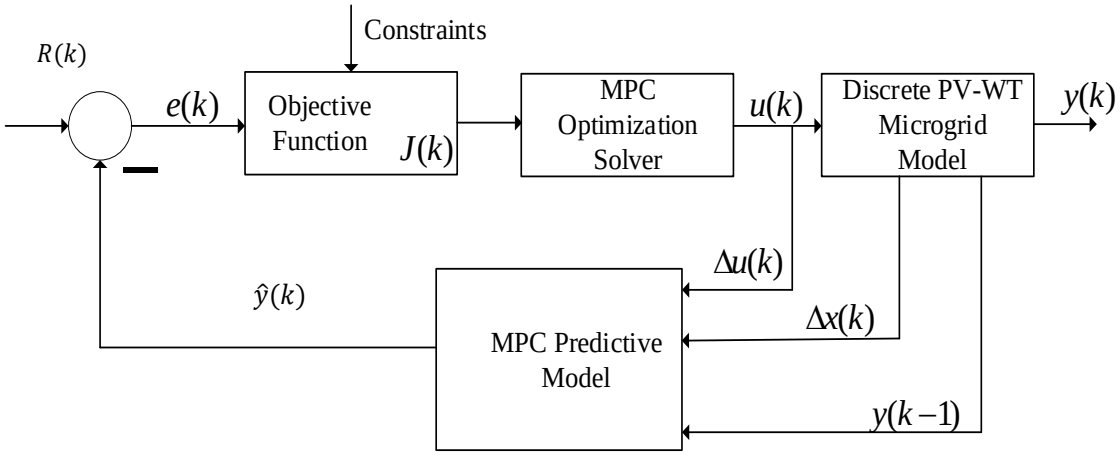

Figure 3.28: Block Diagram Structure of the MPC Controller

An optimization solver is then used to solve an optimization problem and its output, $u(k)$, is applied to a discrete linear model of the PV-WT model of the proposed microgrid system. The actual output $y(k)$, the changes in the controller output $\Delta u(k)$, state variables $\Delta x(k)$, and the output at a previous sampling instant $y(k-1)$ are used by the MPC predictive model to generate the predicted output $\hat{y}(k)$ (M. R. Chen et al., 2019; Dongol et al., 2018).

3.4.2 Microgrid State-Space Models for MPC Controller Design

The state-space model of the PV-Wind hybrid microgrid has been obtained from equation (3.65), repeated here in equation (3.71) but in a reorganized form for convenience:

$$\frac{V_0(s)}{V_0{}^{ref}(s)} = \left\{\left(\frac{1000}{s^3 + 163s^2 + 5970s + 56080}\right)\right\} \times \{(s + 56080)\} \qquad (3.71)$$

From the equation (3.71), the microgrid system transfer function has been separated into two cascaded blocks as shown in Figure 3.29. The first block contains a denominator and a gain of 1000 whereas the second block contains the numerator term $(s + 56080)$.

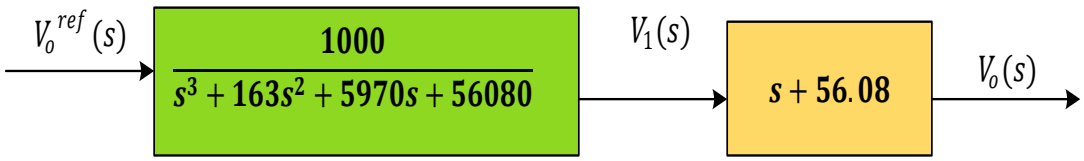

Figure 3.29: Cascaded Block Diagram Structure of PV-Wind microgrid TF

Using the Bush form or companion form or controllable canonical form of state space representation, the state variables for the first block have been selected as successive derivatives to get equation (3.72):

$$x_1 = v_1(t),\ x_2 = \dot{v}_1(t), x_3 = \ddot{v}_1(t) \qquad (3.72)$$

Then defining state variables by differentiating both sides of equation (3.72), gives equation (3.73):

$$\dot{x}_1 = \dot{v}_1(t) = x_2 \quad \dot{x}_2 = \ddot{v}_1(t) = x_3, \dot{x}_3 = \dddot{v}_1(t)$$

$$= -56080x_1 - 5970x_2 - 163x_3$$

$$+ 1000v_0{}^{ref} \qquad (3.73)$$

By taking the output as $x_1 = v_1(t)$, and using the vector-matrix notation, the state space representation of the system in continuous-time form is given as in equation (3.74):

$$\begin{bmatrix} \dot{x}_1 \\ \dot{x}_2 \\ \dot{x}_3 \end{bmatrix} = \begin{bmatrix} 0 & 1 & 0 \\ 0 & 0 & 1 \\ -56080 & -5970 & -163 \end{bmatrix} \begin{bmatrix} x_1 \\ x_2 \\ x_3 \end{bmatrix} + \begin{bmatrix} 0 \\ 0 \\ 1000 \end{bmatrix} {v_0}^{ref} \tag{3.74}$$

The output $v_1(t)$ is given by equation (3.75)

$$v_1(t) = [1 \quad 0 \quad 0] \begin{bmatrix} x_1 \\ x_2 \\ x_3 \end{bmatrix} \tag{3.75}$$

The second transfer function with just the numerator yields equation (3.76):

$$V_0(s) = (s + 56.08)V_1(s) \tag{3.76}$$

Incorporating the definitions of the phase variables utilized in the first block and writing the terms in the reverse order to conform to an output equation gives equation (3.77):

$$v_0(t) = 56.08x_1(t) + x_2(t) \tag{3.77}$$

Therefore, the second block creates a linear combination of the state variables formulated in the first block. In other words, the denominator (and the gain of 1000 representing the input reference voltage) yields the state equations while the numerator produces the output equation. The complete state-space representation of the microgrid system is as given in equations (3.74) and (3.78):

$$v_0(t) = [56.08 \quad 1 \quad 0] \begin{bmatrix} x_1 \\ x_2 \\ x_3 \end{bmatrix} \tag{3.78}$$

Now, the general state space model equations of a time invariant system (linear or nonlinear) are defined by equations (3.79 and 3.80):

$$\dot{x}(t) = \boldsymbol{A}x(t) + \boldsymbol{B}u(t) \quad (3.79)$$

$$y(t) = \boldsymbol{C}x(t) + \boldsymbol{D}u(t) \quad (3.80)$$

where

$x = n -$ Dimensional state vector, $u = r -$dimensional control vector or input vector, $y = m -$dimensional output vector, $\boldsymbol{A}$ – $n \times n$ state matrix, $\boldsymbol{B}$– $n \times r$ input or control matrix, $\boldsymbol{C}$ – $m \times n$ output matrix and $\boldsymbol{D}$ – $m \times r$ direct transition matrix.

Comparing equations (3.74 and 3.78) with equations (3.79 and 3.80) respectively, we obtain equation (3.81) and (3.82):

$$\boldsymbol{A} = \begin{bmatrix} 0 & 1 & 0 \\ 0 & 0 & 1 \\ -56080 & -5970 & -163 \end{bmatrix}, \quad \boldsymbol{B} = \begin{bmatrix} 0 \\ 0 \\ 1000 \end{bmatrix} \quad (3.81)$$

$$\boldsymbol{C} = [56.08 \quad 1 \quad 0], \boldsymbol{D} = [0] \quad (3.82)$$

Figure 3.30 shows an equivalent block diagram that vividly captures the state space model of the PV-Wind microgrid system.

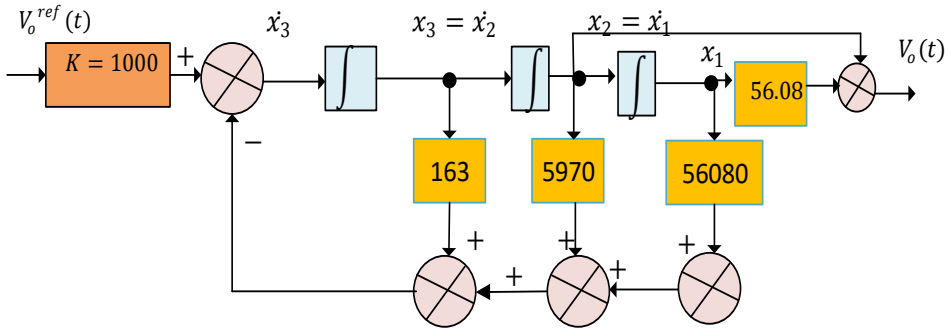

Figure 3.30: State Variable Diagram of PV-Wind Microgrid System

The discrete-time state-space model of the microgrid was obtained from the continuous-time state space using MATLAB functions and scripts based on a Zero-Order Hold (ZOH) with appropriate sample times as given in Figure A3.1.

For instance, the discrete-time transfer function with a sample time of $0.2\ seconds$ and no fractional delays in the input yields equation (3.83) and that with the input delayed by two samples is given by equation (3.84):

$$hd1 = \frac{V_0(z)}{{V_0}^{ref}(z)} = \frac{0.9219z^2 + 0.02599z - 4.637e-06}{z^3 - 0.05224z^2 + 7.522e-05z - 6.95e-15} \tag{3.83}$$

$$hd2 = \frac{V_0(z)}{{V_0}^{ref}(z)} = z^{-2} * \frac{0.8375z^3 + 0.1103z^2 + 1.773e-05z - 1.398e-13}{z^3 - 0.05224z^2 + 7.522e-05z - 6.95e-15} \tag{3.84}$$

It is noted that the discretization algorithm absorbs the residual half-period delay into the coefficients of hd1 in equation (3.83).

The discrete-time state-space model can be obtained directly from the continuous-time transfer function based on ZOH with a sample time, T_s of $0.2\ seconds$ and sampling instant k using the MATLAB script as given in Figure A3.2 as in equations (3.85) and (3.86):

$$\begin{bmatrix} x_1(k+1) \\ x_2(k+1) \\ x_3(k+1) \end{bmatrix}$$

$$= \begin{bmatrix} 0.005269 & 0.01249 & 0.01075 \\ -0.02512 & -0.05872 & -0.04826 \\ 0.0564 & 0.1311 & 0.1057 \end{bmatrix} \begin{bmatrix} x_1(k) \\ x_2(k) \\ x_3(k) \end{bmatrix}$$

$$+ \begin{bmatrix} -0.003141 \\ 0.0141 \\ 0.2613 \end{bmatrix} {v_0}^{ref}(k) \tag{3.85}$$

$$v_0(k) = [0 \quad 1.953 \quad 3.423] \begin{bmatrix} x_1(k) \\ x_2(k) \\ x_3(k) \end{bmatrix} \tag{3.86}$$

Now, for time-invariant (linear or nonlinear) discrete-time systems, the general state equation may be written as defined by equations (3.87 and 3.88):

$$x(k+1) = \boldsymbol{A_d} x(k) + \boldsymbol{B_d} u(k) \tag{3.87}$$

$$y(k) = \boldsymbol{C_d} x(k) + \boldsymbol{D_d} u(k) \tag{3.88}$$

Where x is $n-$ Dimensional state vector, u is $r-$dimensional control vector or input vector, y is $m-$dimensional output vector, $\boldsymbol{A_d}$ is $-n \times n$ state matrix, $\boldsymbol{B_d}$ is $n \times r$ input or control matrix, $\boldsymbol{C_d}$ is $m \times n$ output matrix and $\boldsymbol{D_d}$ is $m \times r$ direct transition matrix.

Comparing equations (3.85 and 3.86) with equations (3.87 and 3.88) respectively, we obtain equation (3.89):

$$\boldsymbol{A_d} = \begin{bmatrix} 0.005269 & 0.01249 & 0.01075 \\ -0.02512 & -0.05872 & -0.04826 \\ 0.0564 & 0.1311 & 0.1057 \end{bmatrix}, \boldsymbol{B_d} = \begin{bmatrix} -0.003141 \\ 0.0141 \\ 0.2613 \end{bmatrix},$$

$$\boldsymbol{C_d} = [0 \quad 1.953 \quad 3.423], \boldsymbol{D_d} = [0] \tag{3.89}$$

Also, the discrete-time state space matrices $\boldsymbol{A_d}$, $\boldsymbol{B_d}$, and $\boldsymbol{C_d}$ can be obtained as defined in equations (3.90), (3.91) and (3.92) (Ghiasi et al., 2022):

$$\boldsymbol{A_d} = e^{AT_s} \tag{3.90}$$

$$\boldsymbol{B_d} = \int_0^{T_s} e^{A\tau} \boldsymbol{B} d\tau \tag{3.91}$$

$$\boldsymbol{C_d} = [0 \quad 1.953 \quad 3.423] \tag{3.92}$$

The equations given in (3.90)-(3.92) are used as the predictive model in the proposed MPC.

In the simulated microgrid case study SIMULINK model, the parameters defined in equations (3.74) and (3.78) for the continuous-time state space model and equations (3.85) and (3.86) for the discrete-time state space change dynamically according to equations (3.93, 3.94 and 3.96):

$$\boldsymbol{A} = \begin{bmatrix} -\frac{1}{T_{BESS}} & 0 & 0 & 0 & 0 \\ 0 & -\frac{1}{T_{PV}} & 0 & \frac{1}{T_{BC1}} & 0 \\ 0 & 0 & -\frac{1}{T_{WTG}} & 0 & \frac{1}{T_{BBC}} \\ 0 & 0 & \frac{1}{T_{WTG}} & \frac{1}{T_{WTG}} & 0 \\ -\frac{1}{2H} & \frac{1}{2H} & 0 & -\frac{1}{2H} & -\frac{D}{2H} \end{bmatrix} \tag{3.93}$$

$$\boldsymbol{B} = [\frac{1}{T_{BESS}} \quad \frac{1}{T_{WTG}} \quad 0 \quad 0 \quad -\frac{1}{2\square}]^T \tag{3.94}$$

$$\boldsymbol{C} = [0 \quad 0 \quad 0 \quad 0 \quad 1]^T \tag{3.96}$$

Now, referring back to equations (3.85) and (3.86), the subsequent set of equations describe the microgrid with emphasis on the BESS. In this context, the states of the system $x(t)$ is a vector whose elements are SoC of the BESS (SoC(t)), $P_{PV}(t)$, $P_{WTG}(t)$ and the total generated power to cater to load demand, $P_{gen}(t)$. The input vector of the system $u(t)$ is constituted of BESS power, $P_S(t)$, the demanded RES energy, $P_{ren,dem}(t)$ and the generated renewable power injected into the BESS, $P_{bCi}(t)$. The definitions of the state

vector, the input vector, and the output vector of the system are as expressed in equations (3.97), (3.98), and (3.99):

$$x\,(t) = [SOC(t) \quad \left(P_{PV}(t) + P_{WTG}(t)\right) \quad P_{gen}(t)]^T \tag{3.97}$$

$$u\,(t) = [P_s(t) \quad P_{ren,dem}(t) \quad P_{bCi}(t)]^T \tag{3.98}$$

$$y\,(t) = [SOC(t) \quad \left(P_{PV}(t) + P_{WTG}(t)\right) \quad P_{gen}(t)]^T \tag{3.99}$$

Now, the proposed MPC utilizes the performance index to regulate microgrid voltage and guarantee BESS's smooth charging and discharging.

The BESS-based microgrid relations are as defined in equations (3.100), (3.101), and (3.102), which are expressed in state space form in equation (3.103), and the output of the system is as given in equation (3.104):

$$SOC(t+1) = SOC(t) - K_{BESS}\,T_{BESS}\,(P_s(t) - P_{bCi}(t)) \tag{3.100}$$

$$\left(P_{PV}(t) + P_{WTG}(t)\right)(t+1) = P_{ren,dem}(t) + P_{bCi}(t) \tag{3.101}$$

$$P_{gen}(t+1) = P_s(t) + P_{ren,dem}(t) \tag{3.102}$$

$$\begin{bmatrix} SOC(t+1) \\ \left(P_{PV}(t) + P_{WTG}(t)\right)(t+1) \\ P_{gen}(t+1) \end{bmatrix} = \begin{bmatrix} 1 & 0 & 0 \\ 0 & 0 & 0 \\ 0 & 0 & 0 \end{bmatrix} \begin{bmatrix} SOC(t) \\ \left(P_{PV}(t) + P_{WTG}(t)\right)(t) \\ P_{gen}(t) \end{bmatrix} +$$

$$\begin{bmatrix} -K_{BESS}\,T_{BESS} & 0 & K_{BESS}\,T_{BESS} \\ 0 & 1 & 1 \\ 1 & 1 & 0 \end{bmatrix} \begin{bmatrix} P_s(t) \\ P_{bCi}(t) \\ P_{gen}(t) \end{bmatrix} \tag{3.103}$$

$$y(t) = \begin{bmatrix} 1 & 0 & 0 \\ 0 & 1 & 0 \\ 0 & 0 & 1 \end{bmatrix} \begin{bmatrix} SOC(t) \\ \left(P_{PV}(t) + P_{WTG}(t)\right)(t) \\ P_{gen}(t) \end{bmatrix} \quad (3.104)$$

From equations (3.103) and (3.104), the BESS matrix dynamics on the microgrid, represented by the matrices $\boldsymbol{A}$, $\boldsymbol{B}$, and $\boldsymbol{C}$ have the form defined in equations (3.105):

$$\boldsymbol{A} = \begin{bmatrix} 1 & 0 & 0 \\ 0 & 0 & 0 \\ 0 & 0 & 0 \end{bmatrix}, \boldsymbol{B} = \begin{bmatrix} -K_{BESS}\, T_{BESS} & 0 & K_{BESS}\, T_{BESS} \\ 0 & 1 & 1 \\ 1 & 1 & 0 \end{bmatrix} \boldsymbol{C} = \begin{bmatrix} 1 & 0 & 0 \\ 0 & 1 & 0 \\ 0 & 0 & 1 \end{bmatrix} \quad (3.105)$$

3.4.3 The Model Predictive Controller (MPC) Design for BESS

The initial energy stored in BESS and the energy of the BESS at any instant of time is given respectively by equations (3.106) and (3.107) (Basantes et al., 2023):

$$E\,(t) = E_0 + \eta_{BESS,C} \times P_{bCi}(t) \frac{P_{bdci}(t)}{\eta_{BESS,D}} \quad (3.106)$$

$$E\,(t) = E(t-1) + \eta_{BESS,C} \times P_{bCi}(t) \frac{P_{bdci}(t)}{\eta_{BESS,D}} \quad (3.107)$$

where E_0 is the initial energy of the BESS, $E\,(t)$ is instantaneous of the BESS power, discharging mode, $E(t-1)$ represents BESS energy at the previous instant, $\eta_{BESS,C}$ and $\eta_{BESS,D}$, respectively represent the battery performance in the charging and discharging modes of operation.

The percentage of energy stored in the BESS is a function of the BESS SoC, as shown in equation (3.108) (Topa Gavilema et al., 2023):

$$SOC\ (t+1) = SOC(t) - \frac{\eta_{BESS} T_s}{P_{BAT,max}} P_s(t) \tag{3.108}$$

where $SoC(t)$ is defined as the ratio between the present BESS capacity, $P_s(t,)$ and the maximum BESS capacity, $P_{BAT,max}$, expressed in $kWh,$ for each sampling instant T_s. To simplify the optimization problem with the MPC controller, it is assumed the performance of the BESS during charging and discharging is the same as introduced with the BESS performance factor, η_{BESS}.

Using SoC, the boundary constraint of the BESS to ensure it is operated within safe operating zones and prolong its life span is defined according to equation (3.109):

$$SoC_{\ min} \leq SoC(t) \leq SoC_{\ max} \tag{3.109}$$

The constraint defined in equation (3.110) is necessary to prevent the BESS from simultaneous charging and discharging and those of equations (3.111), (3.112) and (3.113) are capacity constraints associated with the power limits of the BESS (Basantes et al., 2023):

$$X_{BESS,C}(t) + X_{BESS,D}(t) \leq 1 \tag{3.110}$$

$$0 \geq P_{b\ Ci}(t) \geq -(P_{BAT,max}) \times X_{BESS,C}(t) \tag{3.111}$$

$$0 \leq P_{bdci}(t) \leq (P_{BAT,max}) \times X_{BESS,C}(t) \tag{3.112}$$

$$P_s(t) \leq (P_{BAT,max}) \tag{3.113}$$

3.4.5 MPC Controller Objective Function for the Microgrid

The formulation of an objective function for an MPC controller in a microgrid control problem requires knowledge of the control set, plant dynamics, and constraints. There are two main categories of MPC controllers based on the control set, i.e., the Finite Control Set (FCS) (Ghiasi et al., 2022) and the Continuous Control Set (CCS) MPC. Implementing the former requires a modulator with a variable switching frequency, whereas the latter deploys a modulator and a constant switching frequency. Further, the response of CCS MPC can be easily compared with that of the PI and PID controllers.

The MPC controller is a multivariable control algorithm utilizing a family of controllers. Therefore, the computation of optimal control moves entails solving a multi-faceted optimization problem specified by a cost or objective function. The quadratic cost function for a general optimal control problem has been given in equation (2.10) under the Literature Review. On this basis, a general optimization problem for the microgrid problem can be defined as in equation (3.114) (Ghorashi Khalil Abadi et al., 2022),(L. Wang, 2016),(Syed & Khalid, 2023):

$$J = \sum_{i=1}^{N} [\boldsymbol{Q_i}(Y - R)]^2 + \sum_{i=0}^{M-1} \boldsymbol{R}_i [\Delta U]^2 \tag{3.114}$$

where Y is the output vector of the system, $\boldsymbol{Q_i}$, a weighting factor to penalize variations in the predictions, R is the reference representing the desired microgrid operating point, $\boldsymbol{R}_i$, is the weighting factor to scale the increments in the microgrid input signal (ΔU), N is the prediction horizon, and M the control horizon.

The output vector of the system Y and the optimal control vector ΔU (which contains the increments of the microgrid input signal $\Delta u(k), \Delta u(k+1), \Delta u(k+2), \ldots\ldots\ldots \Delta u(k+M-1)$ are related in a more compact form through equation (3.115):

$$Y = \boldsymbol{F}x(t) + \boldsymbol{G}\Delta U \tag{3.115}$$

where matrices $\boldsymbol{F}$ and $\boldsymbol{G}$ are defined in equations (3.116) and (3.117) linked to equation (3.105) (Elmouatamid et al., 2019),(Akpolat et al., 2022):

$$\boldsymbol{F} = \begin{bmatrix} \boldsymbol{CA} \\ \boldsymbol{CA^2} \\ \boldsymbol{CA^3} \\ . \\ \boldsymbol{CA^P} \end{bmatrix} = \begin{bmatrix} \boldsymbol{CA} \\ \boldsymbol{CA^2} \\ \boldsymbol{CA^3} \end{bmatrix} \tag{3.116}$$

$$\boldsymbol{G} = \begin{bmatrix} \boldsymbol{CB} & \mathbf{0} & \mathbf{0} & . & . & \square \\ \square\square\square & \boldsymbol{CB} & \mathbf{0} & . & . & \square \\ \boldsymbol{CA^2B} & \boldsymbol{CAB} & \square\square\square & . & . & \square \\ . & . & . & . & . & . \\ . & . & . & . & . & . \\ \boldsymbol{CA^{P-1}B} & \boldsymbol{CA^{P-2}B} & \boldsymbol{CA^{P-3}B} & . & . & \boldsymbol{CA^{P-M}B} \end{bmatrix}$$

$$= \begin{bmatrix} \boldsymbol{CB} & \mathbf{0} & \mathbf{0} \\ \square\square\square & \boldsymbol{CB} & \mathbf{0} \\ \boldsymbol{CA^2B} & \boldsymbol{CAB} & \square\square\square \end{bmatrix} \tag{3.117}$$

The vector $U(k)$ is computed so that it is used to minimize the predicted errors over the prediction horizon, N and the size of the control move over the control horizon, M. The objective function for the proposed MPC controller has two augmented parts to cater for BESS control and for voltage regulation in the microgrid, respectively and is as defined in equation (3.118):

$$J = \sum_{i=1}^{N} [\ [c_{ch}\big(P_{bCi}(k) - P_{bdci}(k)\big) + c_{dis}\big(P_{bdci}(k) - P_{bci}(k)\big)$$

$$+ c_{soc}\left(SOC(k) - SOC_{ref}(k)\right)^2 + [V(k) - V_{ref}(k)]^2\ ]$$

$$+ \sum_{i=0}^{M-1} \boldsymbol{R_i}[U(k)]^2 \tag{3.118}$$

subject to the following constraints equations (3.119) to (3.123) and equation (3.70) (Félix Garcia-Torres, Carlos Bordons, 2020):

1. Battery power limits in equations (3.119) and (3.120):

$$P_{bci,min} \leq P_{bCi}(k) \leq P_{bci,max} \tag{3.119}$$

$$P_{bdci,min} \leq P_{bdci}(k) \leq P_{bdci,max} \tag{3.120}$$

2. State of charge (SoC) limits given in equation (3.121):

$$SoC_{min} \leq SoC(k) \leq SoC_{,max} \tag{3.121}$$

3. Voltage limits defined in equation (3.122):

$$V_{min} \leq V(k) \leq V_{max} \tag{3.122}$$

4. Control input limits as given in equation (3.123):

$$U_{min} \leq U(k) \leq U_{max} \tag{3.123}$$

5. The power balance equation (3.70).

In equation (3.118), c_{ch} and c_{dis} are respectively the cost of charging and discharging the BESS per unit of power (usually taken as positive values). $P_{bCi}(k)$ and $P_{bdCi}(k)$ represent the charging and discharging power of the BESS, at time step k, respectively. J is the total performance index or cost function to be minimized, N is the prediction horizon (number of control intervals), M is the number of control moves, and R a positive definite weighting factor or penalty term used to balance deviations in voltage and also to control the input effort. $V(k)$ and $V_{ref}(k)$, respectively denote the microgrid voltage and the desired

reference voltage at time step k, $U(k)$ represents the control input at time step k and equals to $(P_{WTG} + P_{PV} \mp P_s)$.

The first component of the objective function is introduced to aid in optimizing the BESS charging and discharging in the PV-Wind hybrid microgrid subject to the stipulated constraints. Its parameters involve: $P_{bci}(k)$, $P_{bdci}(k)$, $SOC(k)$ and $SOC_{ref}(k)$.

The goal of the second portion of the objective function is to perform voltage regulation by minimizing the variation of the microgrid converter voltage from the desired reference subject to the stipulated constraints and has the terms: $V(k)$, $V_{ref}(k)$ and $U(k) = (P_{WTG} + P_{PV})$. The MPC controller designed is a linear finite-horizon MPC controller. The BESS is kept as much as possible near its maximum SoC by adhering to the constraints, while avoiding discharging it below a set threshold to avert a deep discharge of the BESS. The SoC, one of the input parameters to the MPC controller, is acquired by predicting the BESS charge/discharge current.

3.4.6 The Proposed Model Predictive Controller (MPC) for BESS

Figure 3.31 shows the flow chart of the proposed MPC algorithm. The role of the Model Predictive Controller (MPC) in the proposed microgrid control system is to perform power control of the Battery Energy Storage System (BESS). This is necessary to avoid over-charging or over-discharging the BESS. To achieve this, the MPC controller takes in predicted PV and WT power and sampled State of Charge (SoC) values of the BESS, which are applied as feedback signals. Next, an initial prediction model is obtained.

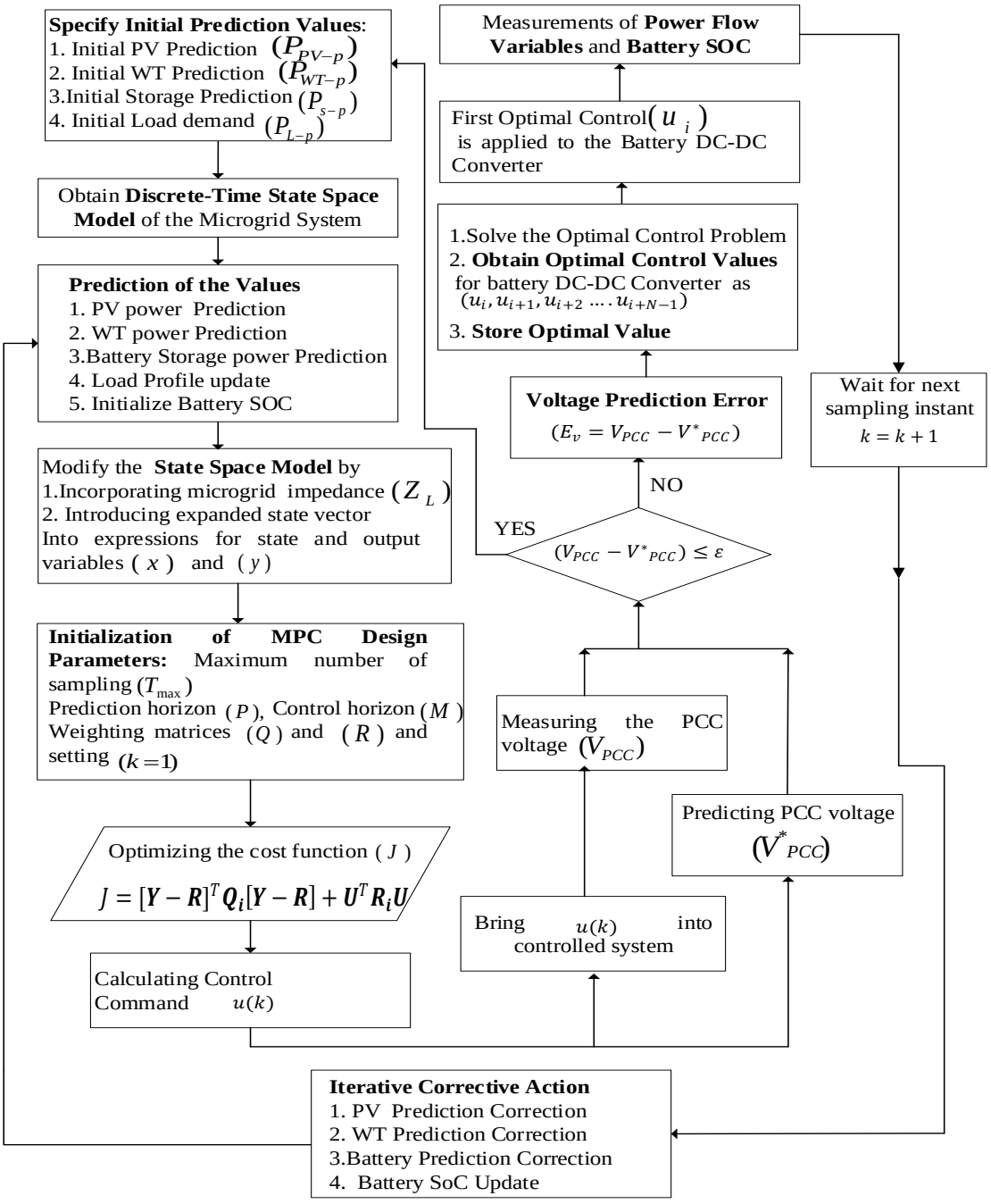

Figure 3.31: Steps for Proposed MPC Controller Design

The power flow within the PV, WT, and BESS system is required to satisfy the power-flow balance relationship of equation (3.70) which has been re-organized for convenience when designing the MPC controller and its code development to equation (3.124):

$$P_{PV-out\,i} + P_{WT-out\,i} - P_{L\,i} = P_{bc\,i} + P_{bdc\,i} + P_{L\,oss\ i} \quad (3.124)$$

where $P_{PV-out\,i}$ and $P_{WT-out\,i}$ are the available power from PV and WT, $P_{L\,i}$ is the load power demand, $P_{bc\,i}$ and $P_{bdc\,i}$, are the charging and discharging power of the BESS while $P_{L\,oss\ i}$ denotes power losses in the microgrid, all considered at the i^{th} sampling instant.

The model of the system is then obtained. Using the DTSS model of the system, the initial values and constraints, if any, of the model are predicted. An expanded state space model discrete-time state space (DTSS) is then obtained, for instance, by introducing an expanded state vector or, the microgrid impedance, Z_L into expressions for state variable x and the output variable y. This is followed by initializing key parameters of the MPC design namely, maximum number of sampling instants (T_{max}), prediction horizon (N), control horizon (M), weighting vectors $\boldsymbol{Q_i}$ and $\boldsymbol{R_i}$ and setting $k = 1$.

Next, the cost function J is defined and this forms the basis for calculating the control command$u(k+1)$,, which represents the change value of the BESS value. The calculated value of control command $u(k)$ is then incorporated into the system to be controlled, and the voltage at the common point of coupling P_{CC}, $V_{PCC,}$ measured. At the same time, the predicted value of the voltage at P_{CC}, V^*_{PCC}, is obtained, and the two values of voltages are then compared. If they are equal, the algorithm joins the initial prediction model.

On the other hand, if they are not equal, it means there is a voltage prediction error. This prompts the need to solve the optimal control problem whose outcome is the optimal control values for the battery-connected DC-DC converter obtained as $u_i, u_{i+1}, u_{i+2}, \dots, u_{i+N-1}$. Out of these values, the optimal value or vector, usually the first value u_i, is stored. The stored optimal value is sent to the battery DC-DC converter. Again, the power variables and battery SoC are measured. These values are used at the next sampling instant to generate PV and WT prediction corrections and battery SoC updates. In the proposed system, $x(k)$ represents the total power of PV, WT, and BESS,

while $y(k)$ denotes the voltage at the PCC. $P_{PV-out}(k)$, $P_{WT-out}(k)$ and $P_{bat}(k)$, are the measured PV, WT, and BESS power, respectively. $P_{PV-out}(k+1)$, $P_{WT-out}(k+1)$ and $P_{bat}(k+1)$ are the predicted values of PV, WT, and BESS power, respectively.

The microgrid impedance parameters, $Z_{L,}$ is usually unknown and varies from one system to another. This value can be corrected per the error between the predicted and actual voltage of PCC, set at $\varepsilon \leq 0.05$. The prediction error obtained at every sampling instant is used to correct the model, and this happens repeatedly as long as the proposed MPC secondary controller is running. With this, in addition to managing the charging and discharging of BESS, the MPC algorithm also compensates for deviations in voltages created because of the implementation of the primary GA-ANFIS controller.

The proposed MPC has been selected over the conventional charging control methods and other commercial devices because it offers a better performance in charging and discharging batteries, which is complex and nonlinear. This is in terms of improved regulation of charging and discharging voltages, State of Charge (SoC), energy management, charging time, and charging efficiency. The MPC uses a precise mathematical model of the microgrid system to enforce required constraints and has a high flexibility contrary to the traditional charging control methods (Banguero et al., 2018; Dongol et al., 2018). The upper and lower voltage thresholds in charging and discharging of the BESS can be incorporated as constraints in the MPC objective function.

3.4.7 Application Framework of the MPC Controller to the Microgrid Model

The proposed linear finite-horizon MPC controller utilizes the receding horizon control approach in which only the first step of the M-step control framework, $U(k)$, generated in equation (3.135) is implemented. Since not all the states may be available to realize the MPC controller strategy, the state estimation was carried out using the Kalman filter, whose parameters have been tuned and adapted from the MATLAB MPC controller Toolbox (Bemporad et al., 2019).

The selection of the MPC design parameters used in the simulations was made per the following guidelines:

1. Model Horizon (H) and sampling period (T_s).

   These parameters have been selected so that $NT_s \geq$ open-loop settling time. Typical values of H being $30 \leq H \leq 120$. In the proposed MPC, $H = 30$ has been used, and $T_s = 0.2s$.

2. Prediction Horizon (number of predictions) (N).

   Increasing N yields a less aggressive control action; thus, the choice of it is guided by $N = H + M$. In the proposed MPC, $N = 40$ has been used.

3. Control Horizon (number of control moves) (M):

   Normally, $M < N$ to reduce the complexity of the optimization problem. Moreover, the number of decision variables in the optimization problem, though not dependent on N, increases with M. Consequently, increasing M results in a more aggressive controller and increases computational effort. Typically, M is taken in the range $5 \leq M \leq 20$. In the simulations, M was set to a maximum of value of $M = 10$.

4. Weighting matrices $\boldsymbol{Q}$ and $\boldsymbol{R}$.

   The Weighting matrix for predicted errors is a positive definite matrix ($\boldsymbol{Q} > 0$), and the weighting matrix for control moves is a positive semi-definite matrix ($\boldsymbol{R} \geq 0$). These elements were adapted in the simulation, mainly as the diagonal matrices containing the largest elements match the most important variables in the microgrid. Table 3.10 summarizes the parameters of the designed MPC controller.

Table 3.10: Designed MPC Controller Parameters

Parameter	Symbol	Value	Comments
Plant input signal sizes	Defined in corresponding equations.	[1,1,1]	No. of manipulated variables/measured disturbance/unmeasured disturbance = 1/1/1. Updated values adapted in simulation.
Plant output signal sizes	Defined in corresponding equations.	[1,0]	No. of measured outputs = 1, No. of unmeasured outputs = 0
Output variables weight	$\boldsymbol{Q_i}$	1.8	Value is given as a starting point and then adapted in simulation.
Manipulated variables rate weight.	$\boldsymbol{R}$	1	Weighting Factor for Voltage Deviation, adapted in simulation
Model horizon	H	30	$30 \leq H \leq 120$ Adapted in simulation
Prediction horizon	N	40	The choice is guided by: $N = H + M$
Control horizon	M	10	Typically, M is taken in the range: $5 \leq M \leq 20$
Sampling time	T_s	$1s$	The value selected based on microgrid dynamics and desired controller performance
State estimation	$x[k\|k]$	Adapted in simulation	Used the MPC built-in Kalman filter
Other parameters	$c_{ch}, c_{dis}, c_{soc},$ $P_{bCi}(k),$ $P_{bdCi}(k), SOC_m$ SOC_{max}, v_{ref}	$1, 1, 1, 50,$ $-50, 0.2,$ $0.8, 600V$	Some values given are starting points. Custom constraints and plant limits adapted in simulation (Equation (3.135)).

The MPC controller was designed and implemented using a series of MATLAB codes written following the created model and implemented alongside the tools based on the MATLAB and SIMULINK MPC Controller Toolbox.

3.4.8 SIMULINK Design of the MPC Controller for BESS

The MPC controller applied to the consolidated $10\,kW$ microgrid case study model is given in Figure 3.32**.** The action of the MPC controller has been compared with that of

the GA-ANFIS and PID controllers in terms of rise time, settling time, and maximum overshoot.

3.5 Combined Simulink Models and Performance Comparison

This section presents the Simulink Models for Transfer Function and Case Study that support specific objectives two, three, and four and on whose basis the results to validate the performance of the GA-ANFIS-MPC controller have been conducted. The consolidated microgrid case study SIMULINK model was obtained by integrating the individual models for the PV system, WT system, IBCs, Two parallel Inverters, BESS, and the Load Model. It significantly altered the response time by increasing the computation and dynamic response time.

3.5.1 SIMULINK Microgrid Transfer Function (TF) Model

Figure 3.33 shows the MATLAB/SIMULINK microgrid Transfer Function (TF) of the proposed PV-Wind hybrid microgrid used to test the performance of the designed MPC controller. The MPC controller performance has been compared with that of the PID controller and G

A-ANFIS controller in the same simulation context regarding rise time, settling time, and maximum overshoot. Further, MPC controller action is also tested on the Microgrid State Space Model.

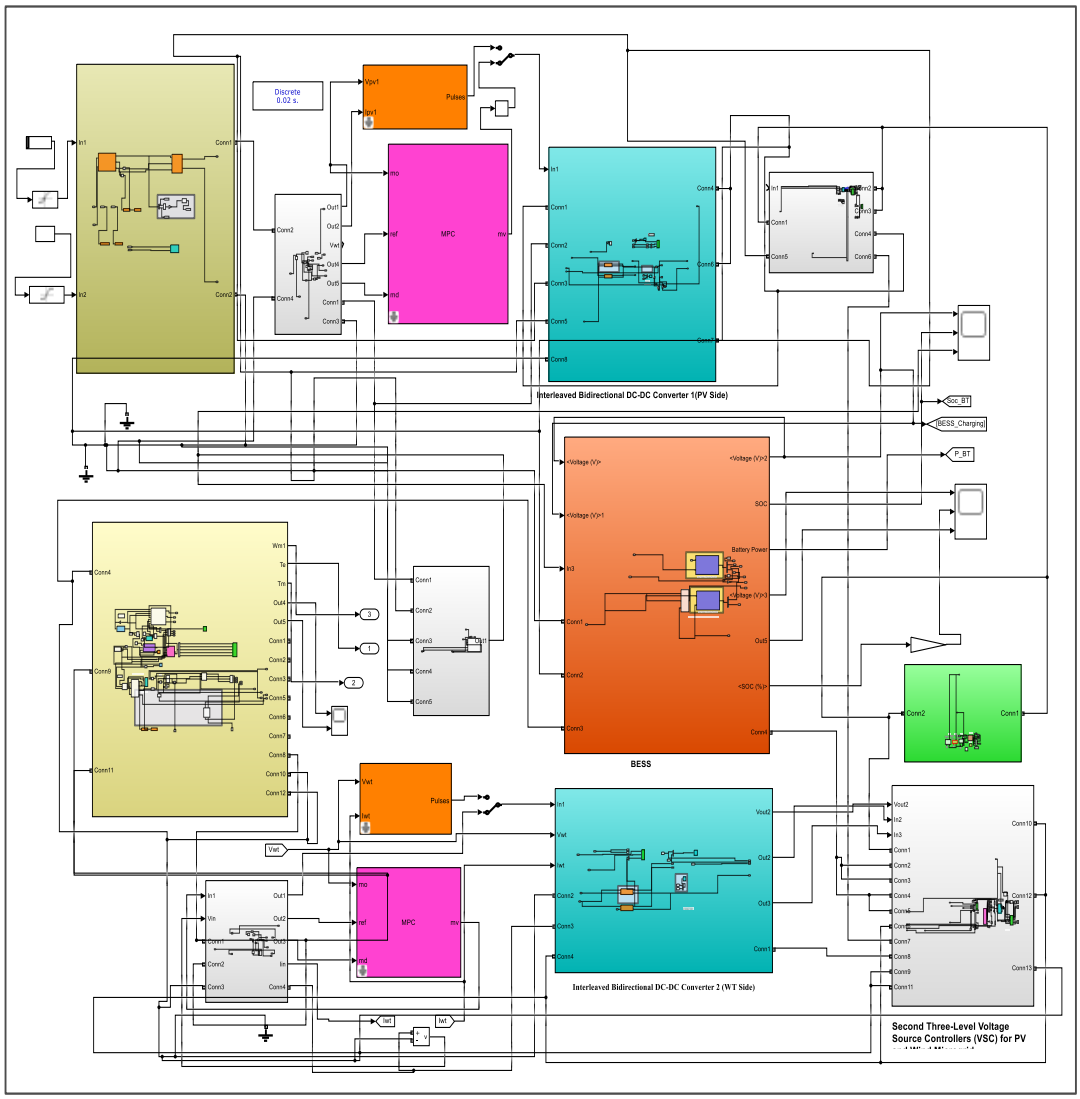

Figure 3.32: MPC Performance in the SIMULINK Model of the Microgrid Case

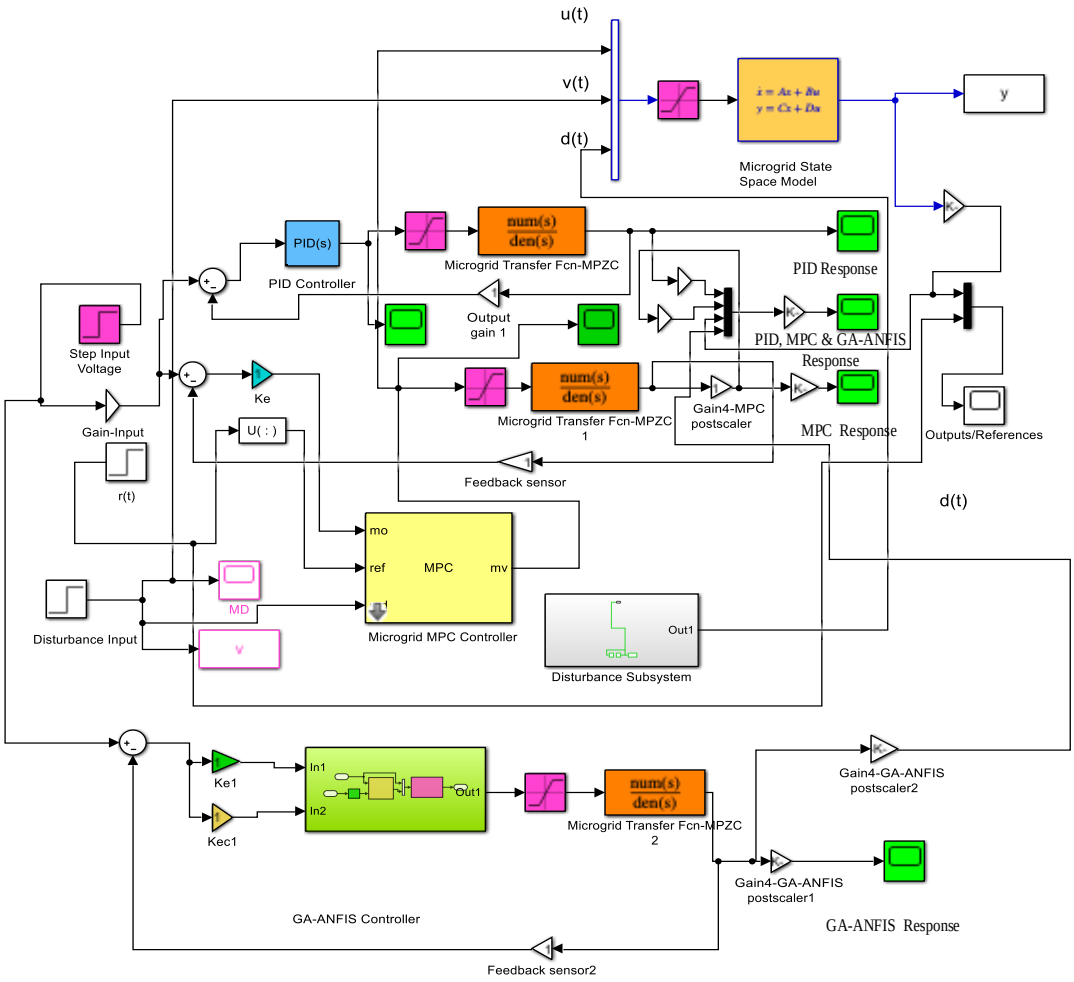

Figure 3.33: Simulink Transfer Function Model of Proposed PV-Wind Hybrid Microgrid with MPC, GA-ANFIS and PID Controllers

3.5.2 SIMULINK Microgrid Case Study Model

The consolidated microgrid case study SIMULINK model with the GA-ANFIS-MPC controller is shown in Figure 3.34 and a detailed version is depicted in Figure A2.1 in Appendix 2. In essence, the developed microgrid model is a nonlinear model in which the nonlinearities have been handled as follows. First, the zone restriction technique was applied to the PV and wind power curve to eliminate 85% of the curve and only focus on the 15% section. The restriction kept the operating points of PV and WT close to the

equilibrium points around the MPP and had a higher chance of exhibiting local stability if subjected to the Jacobian linearization of the state-space model equations. Second, the form of the TF was used after the model pole-zero cancellation, which simulates a nearly linear microgrid. Finally, the designed GA-ANFIS-MPC controller was used to withstand the impact of nonlinear dynamics on the model response.

The GA-ANFIS controller has been applied as the primary controller to regulate the generated microgrid voltage whereas the MPC controller regulates the battery charging and discharging. The MPC controller can reinforce the BESS charging/discharging constraints alongside other microgrid constraints (Ghorashi Khalil Abadi et al., 2022), (Félix Garcia-Torres, Carlos Bordons, 2020).

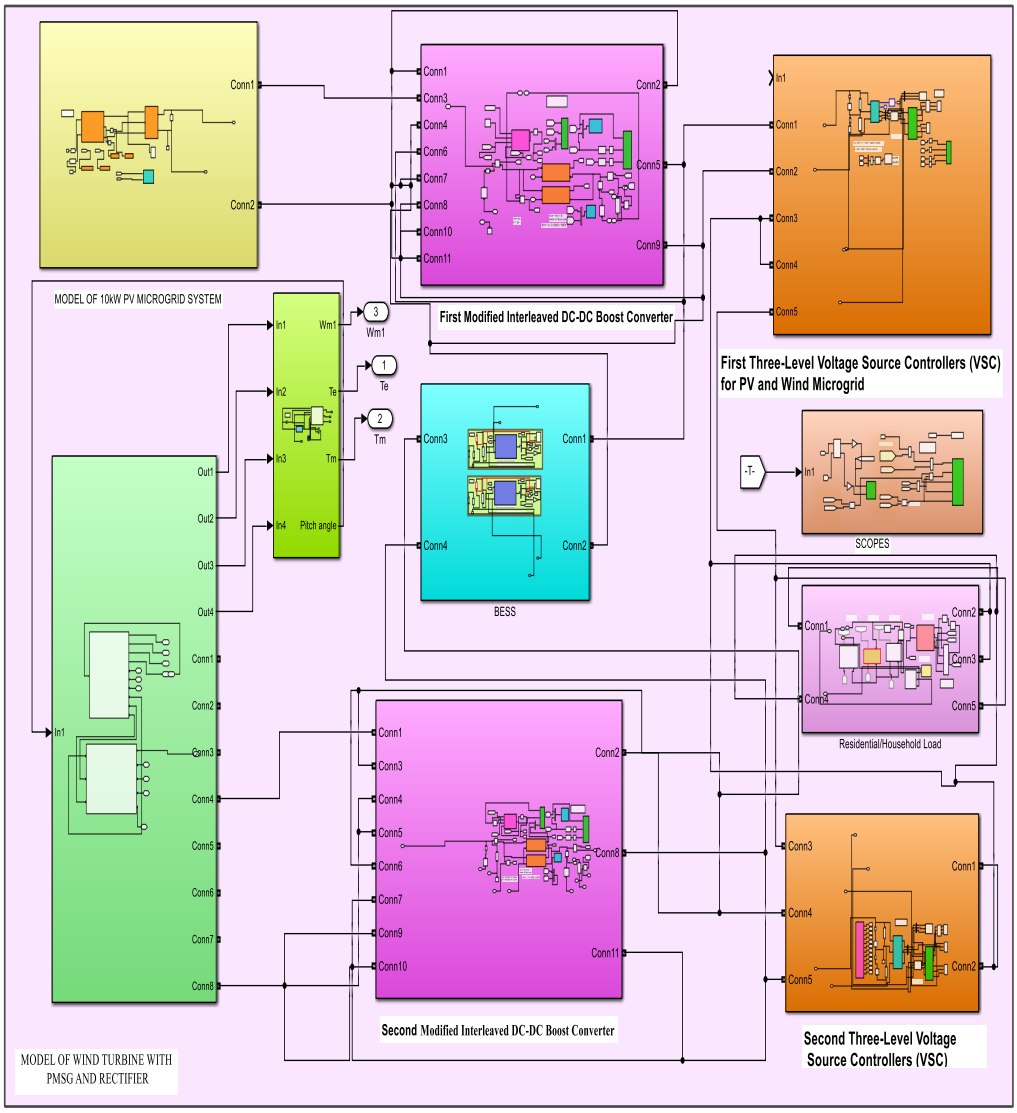

Figure 3.34: Combined Simulink Model of the Proposed Microgrid with Case Study with PID, GA-ANFIS and MPC Controllers

CHAPTER FOUR

RESULTS AND DISCUSSIONS

4.1 Results from the Modeling of the PV-Wind Microgrid System

This section (i.e. section 4.1) corresponds to the results of specific objective number one. After building the model of the PV-Wind microgrid system in MATLAB & SIMULINK, the current and voltage as well as the power outputs were plotted at various points within the microgrid without deploying any control strategy. This was necessary to ensure that the microgrid model is operational before deploying the proposed control strategies.

4.1.1 PMSG Output Phase Voltages

Simulation results of the PMSG Wind Generation System connected to an uncontrolled three-phase diode rectifier and an Interleaved Boost Converter (IBC) were carried out to ascertain its performance. It was noted that the maximum power extraction happens when the Wind Turbine, which is connected directly to the PMSG, is subjected to a wind speed of $12\ m/s$ and pitch angle of 0^0. Figure 4.1 shows the non-normalized PMSG output phase voltages between $-900\ V$ and $+900\ V$ for the Red, Yellow and Blue phases as given, respectively. The phase voltage profiles are similar, considering it is a balanced three phase PMSG system. However, the Red phase, being the reference phase, has been plotted separately for convenience.

The utilized simulation conditions were a constant pitch angle of 0^0 and constant mechanical torque of $35\ Nm$. The variation in voltage and frequency are evident, which calls for further improvement such as via smoothing or stabilizing to obtain a constant outcome of $561\ V$. It is also clear from the PMSG three phase voltage outputs of Figure 4.1 that similarly, the PMSG three phase out currents will adopt a similar profile.

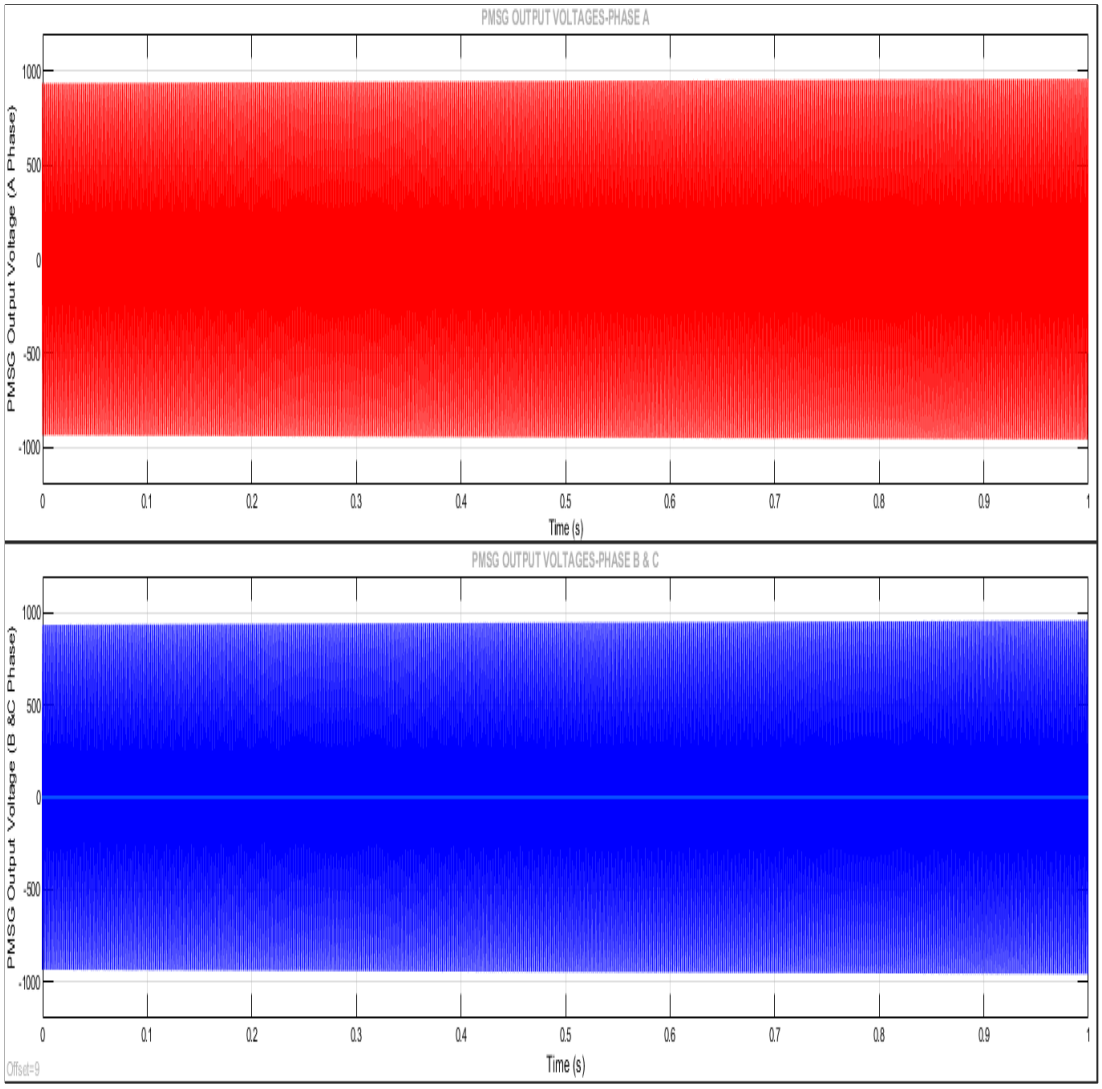

Figure 4.1: Turbine Output Power for Various Turbine Speeds

4.1.2 Results from the IBC section of the Microgrid with MPPT

Figure 4.2 shows the inputs to the designed IBC in terms of voltage $V_{in} = 561\,V$ and current, $I_{in} = 26\,A$. The DC input voltage remains nearly constant at $561V$ throughout the simulation time frame of $10\,s$. This is because at this point, the functionality of the IBC needed to be tested using the DC input voltage that represents the near ideal scenario.

However, the input current experiences some ripples at the beginning which falls to within $\pm 15\%$ of the nominal input current i.e. $26 \pm 4\ A$ within $0.5\ s$. The inductor current plot follows a similar profile as for the input current, representing the impact of energy storage elements such as inductors in the performance IBC.

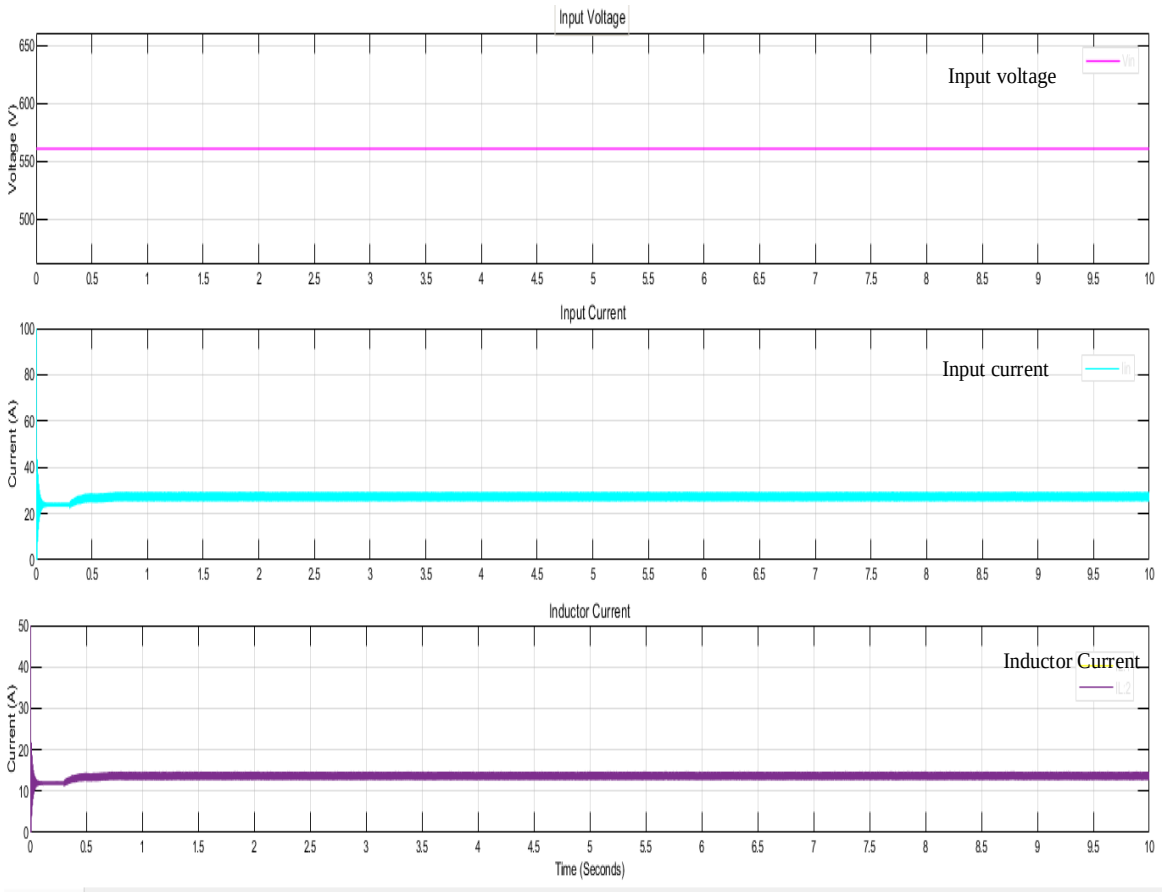

Figure 4.2: Designed Modified IBC Input

The IBC output voltage of $742.6\ V$ and current of $20.63\ A$ obtained at a switching frequency of $20\ kHz$ and the duty ratio is $D = 0.1928$ are presented in Figure 4.3.

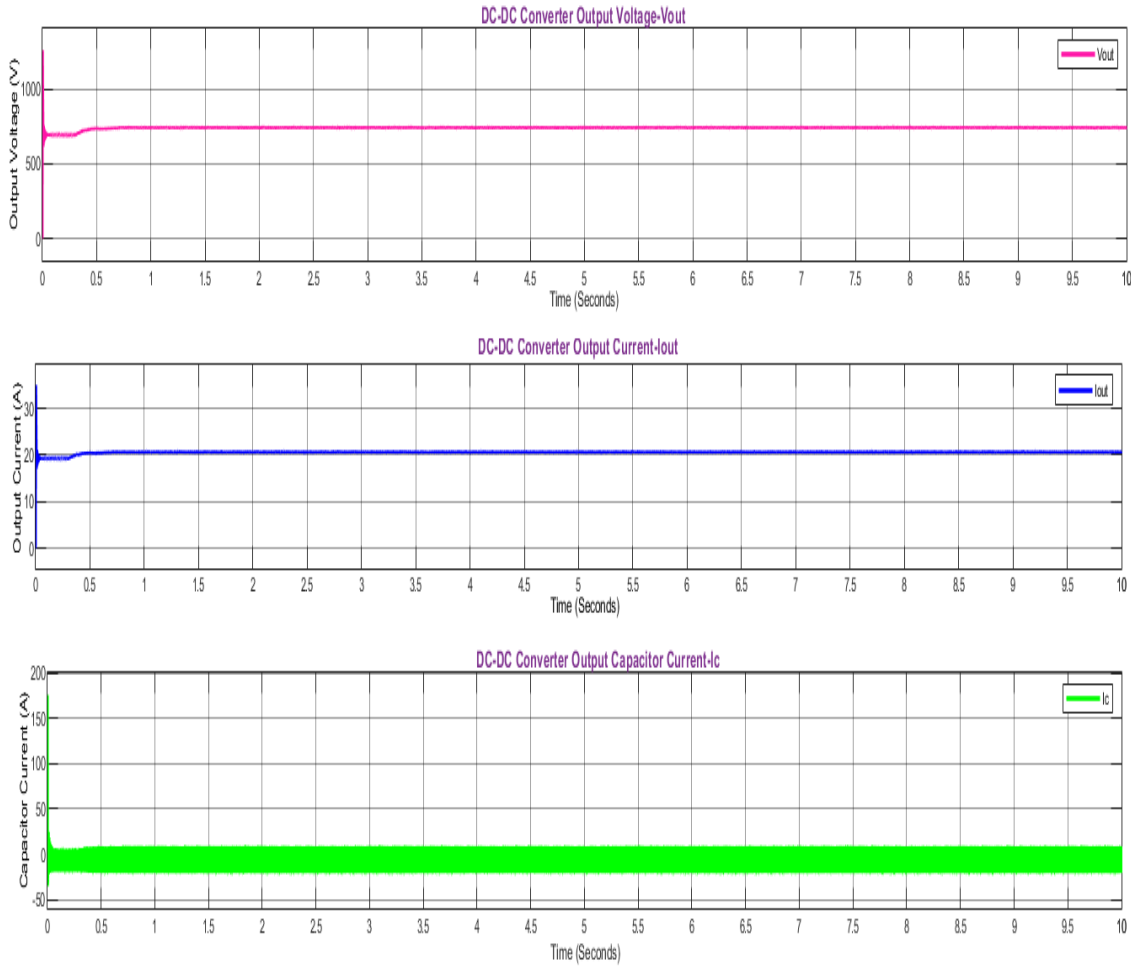

Figure 4.3: Designed Modified IBC Output

Both the input voltage and current depict some ripples at the beginning which falls to within $\pm 6.7\%$ of the nominal input voltage and current i.e. $742.6 \pm 50\ V$ and $26 \pm 1.4\ A$ respectively within $0.4\ s$. The inductor current follows a similar profile as for the input current.

The ripples are indicating that the IBC faces challenges during the transient period before attaining the desired voltage and current levels at steady-state conditions. There are notable improvements in the profiles with the P&O MPPT, particularly under linear conditions of operation.

4.1.3 Outputs of Two Parallel Inverters for Microgrid Application

The output voltage profiles of the proposed Two Parallel Inverters on PV side and Wind Turbine without inverter control strategy are shown in Figure 4.4 and Figure 4.5, respectively.

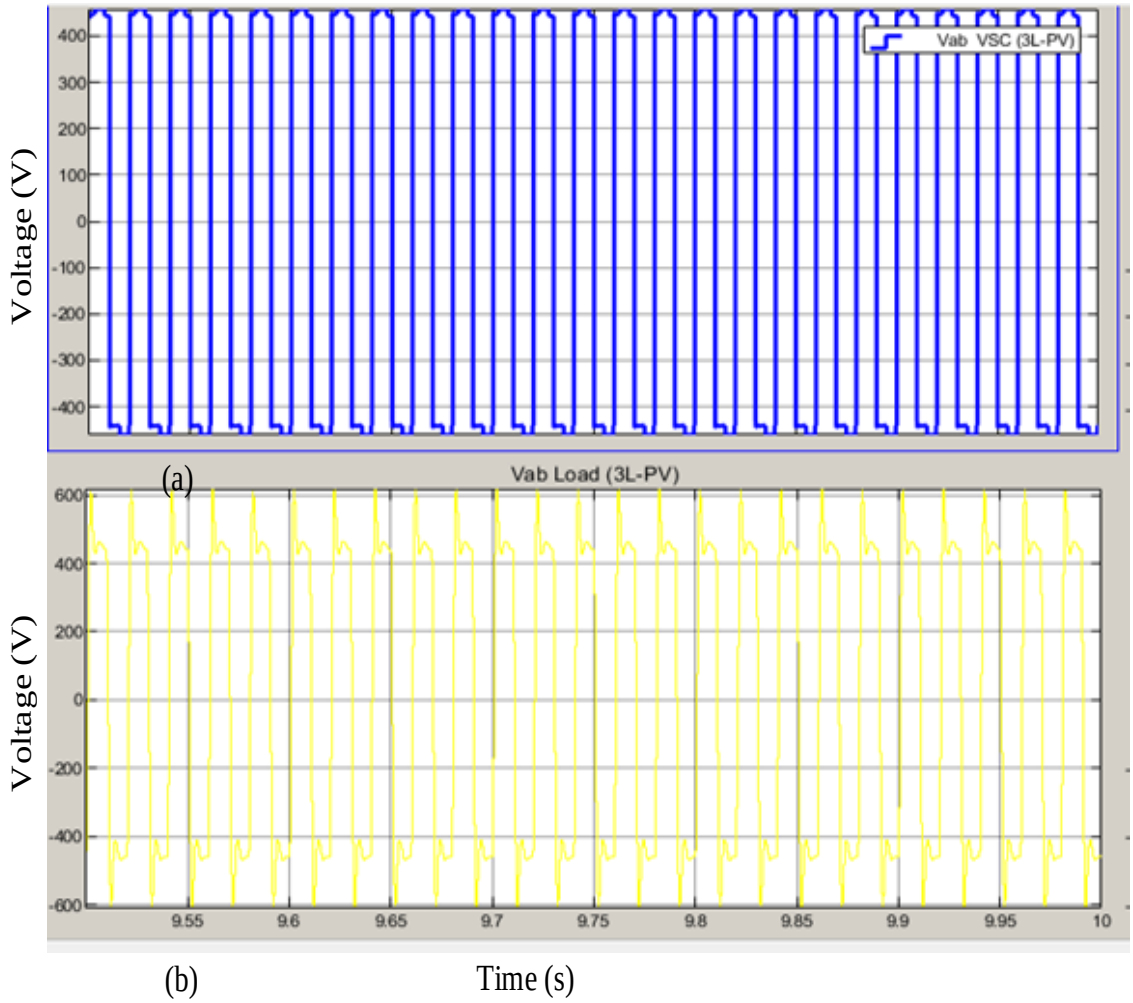

Figure 4.4: Proposed Inverter output on PV Side without Inverter Control Strategy: (a) VSC Voltage (b) Load Voltage

The upper plots (i.e. (a)) indicate a modified sinusoidal output ranging between $-500\,V$ and $500V$ fed to the load while the lower plots (i.e. (b)) depict the deformations or spikes

introduced in the voltage by connecting a nonlinear three-phase load to the inverter output, which is at $-600\ V$ and $600\ V$. The variations in the inverter outputs are within the limit of $\pm 10\%$.

Two inverters have been used to achieve the desired inverter paralleling: one inverter is connected to the PV side and the other to the WT side. The inverter connected to the PV side comprises the IGBT switches while the one attached to the WT side has been designed using MOSFETs. This partly explains the reason the two profiles differ. These results are consistent with those obtained in the literature regarding the near-perfect sinusoidal voltage outputs expected from inverters.

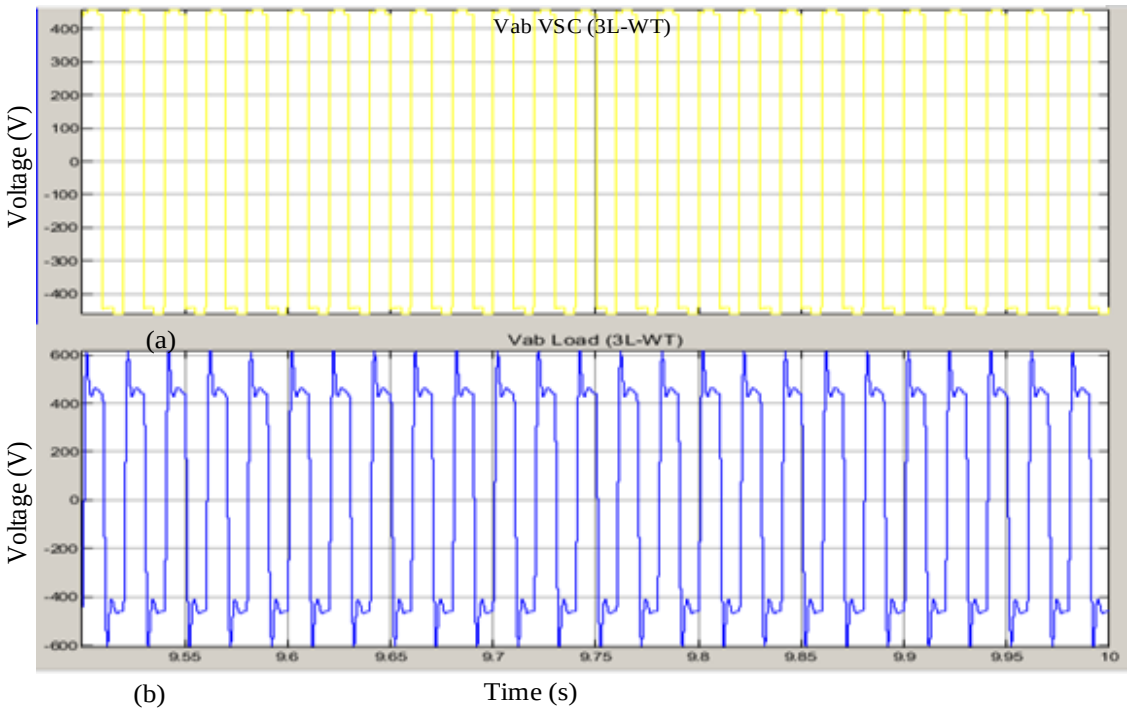

Figure 4.5: Proposed Inverter output on Wind Turbine side without Inverter Control Strategy: (a) VSC Voltage (b) Load Voltage

Figure 4.6 present the unfiltered three-phase voltage outputs of the proposed inverter without inverter control strategy.

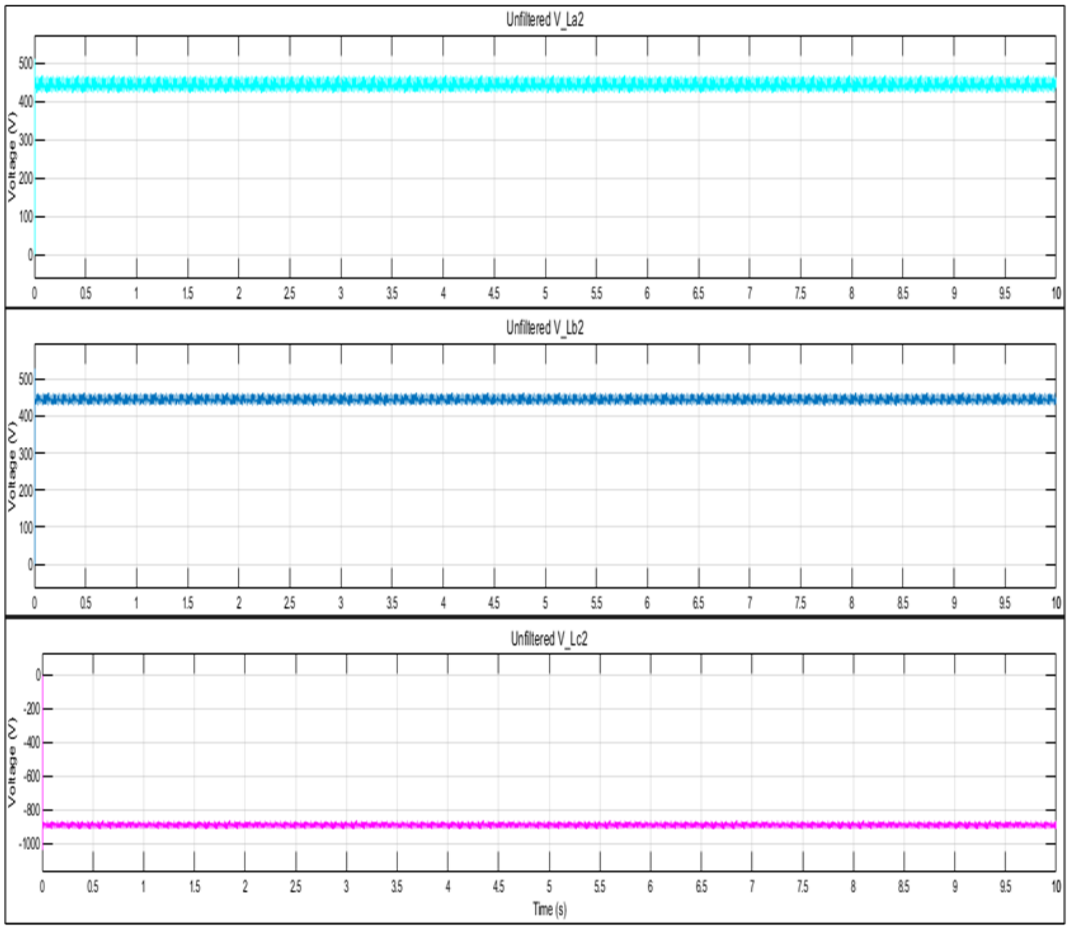

Figure 4.6: Proposed Inverter Unfiltered Output Voltages

From Figure 4.6, for each of the phases, without the inverter control strategy, the variations in the inverter output voltages are clearly evident, though the rise time is still fast enough. These ripples in the inverter outputs may lead to power quality issues if unchecked. The absence of filters and inverter control strategy suggests the degraded performance and this can be addressed by incorporating appropriate controllers as deployed in this study.

Figure 4.7 depicts the zoomed views of the unfiltered three-phase voltage outputs of the proposed inverter without inverter control strategy within simulation time frame of 9.55 s to 10 s.

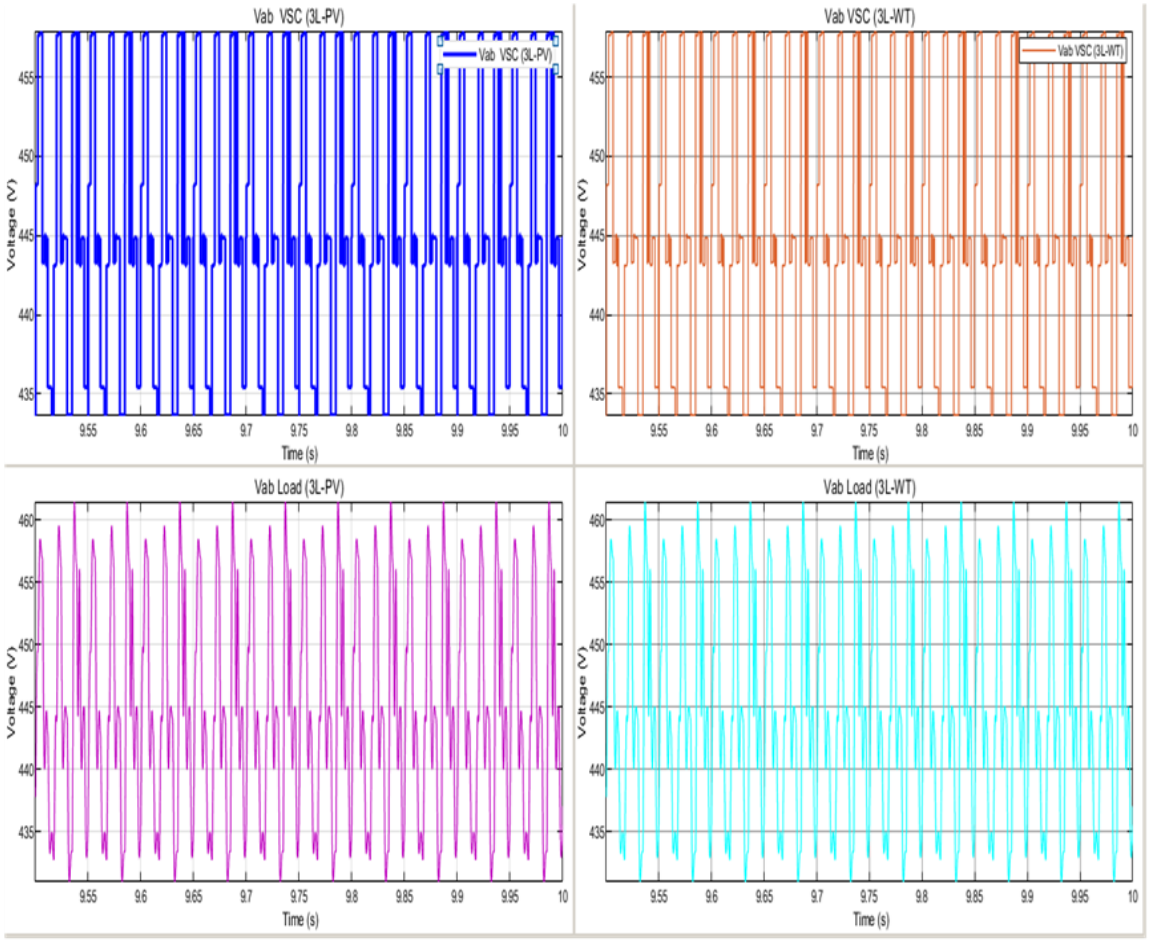

Figure 4.7: Proposed Inverter Unfiltered Zoomed Output Line without Inverter Control Strategy

It can be seen from Figure 4.7 that the voltages for both the PV and wind turbine sides are varying within $\pm 10\%$ of the nominal value i.e. $445 \pm 45\ V$. This is attributed to the non-linear occurrences in the microgrid particularly those attributed to the intermittency in PV and WT generation as well as the power electronic converter components. Figure 4.8 shows the filtered forms of the inverter output voltages on the PV side.

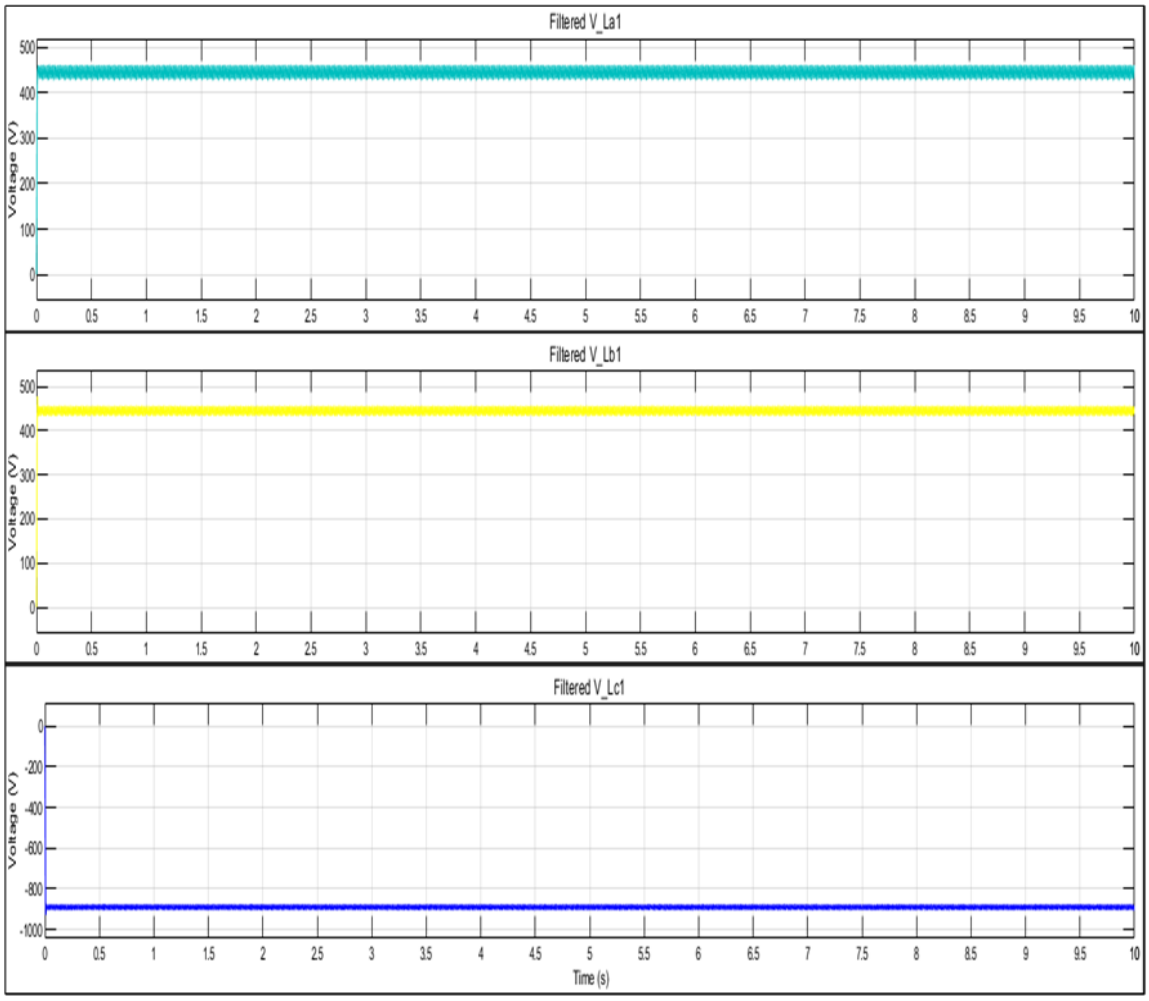

Figure 4.8: Proposed Inverter 1 Filtered Output Line Voltages (for Solar PV Side)

The filtered forms of the inverter output voltages on the Wind Turbine side are shown in Figure 4.9. From Figure 4.8 and Figure 4.9, it can be observed that with the introduction of the filter, the inverter output voltage profiles are slightly better due to some reduction in ripple content. The variations in the inverter output voltages on both the PV and wind turbine sides have also improved slightly to fall within $\pm 8.5\%$ of the nominal value i.e. $445 \pm 40\ V$.

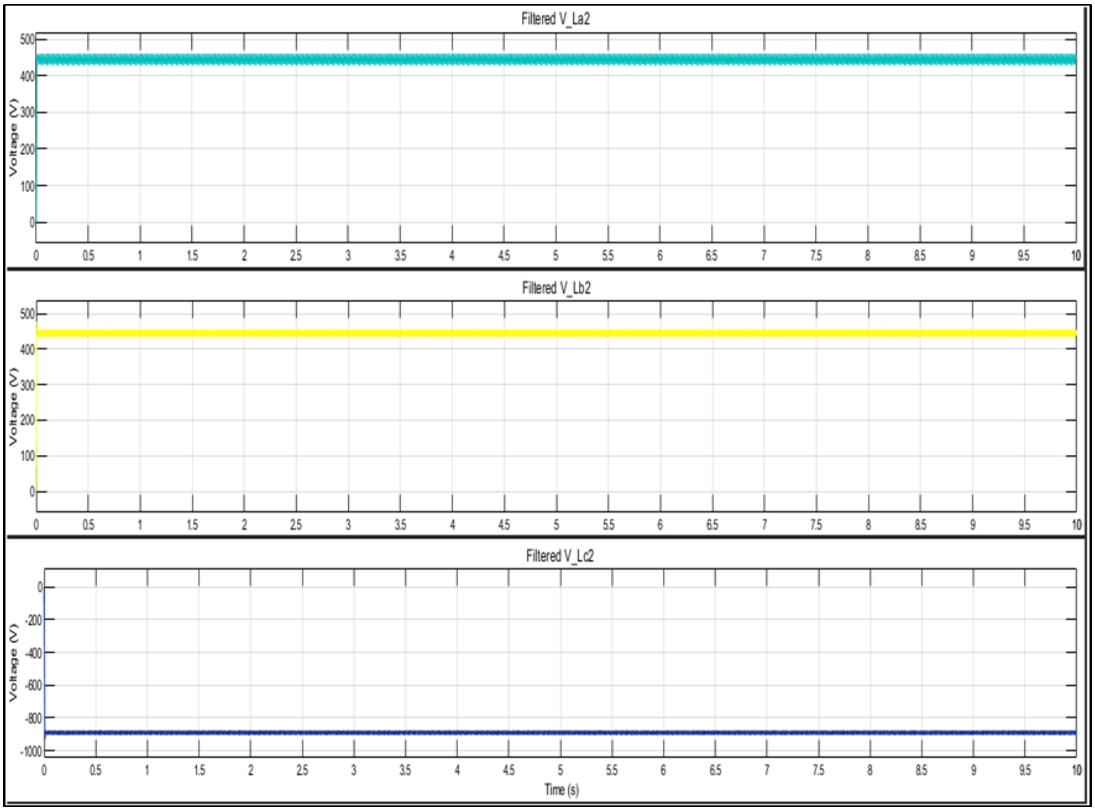

Figure 4.9: Proposed Inverter 2 Filtered output Line voltages (for WT side)

4.1.4 Response Characteristics of the Battery Energy Model

The nominal current discharge characteristics of a 5000 Ah capacity of the Lead-Acid BESS model and Lithium-Ion BESS model, respectively, are shown in the plots of Figure 4.10 and Figure 4.11. It was observed that for the same storage capacity, the discharge rate is faster in Lead-Acid BESS compared to Lithium-Ion BESS. For this reason, the Lithium-Ion BESS is the preferred choice for use in the proposed microgrid.

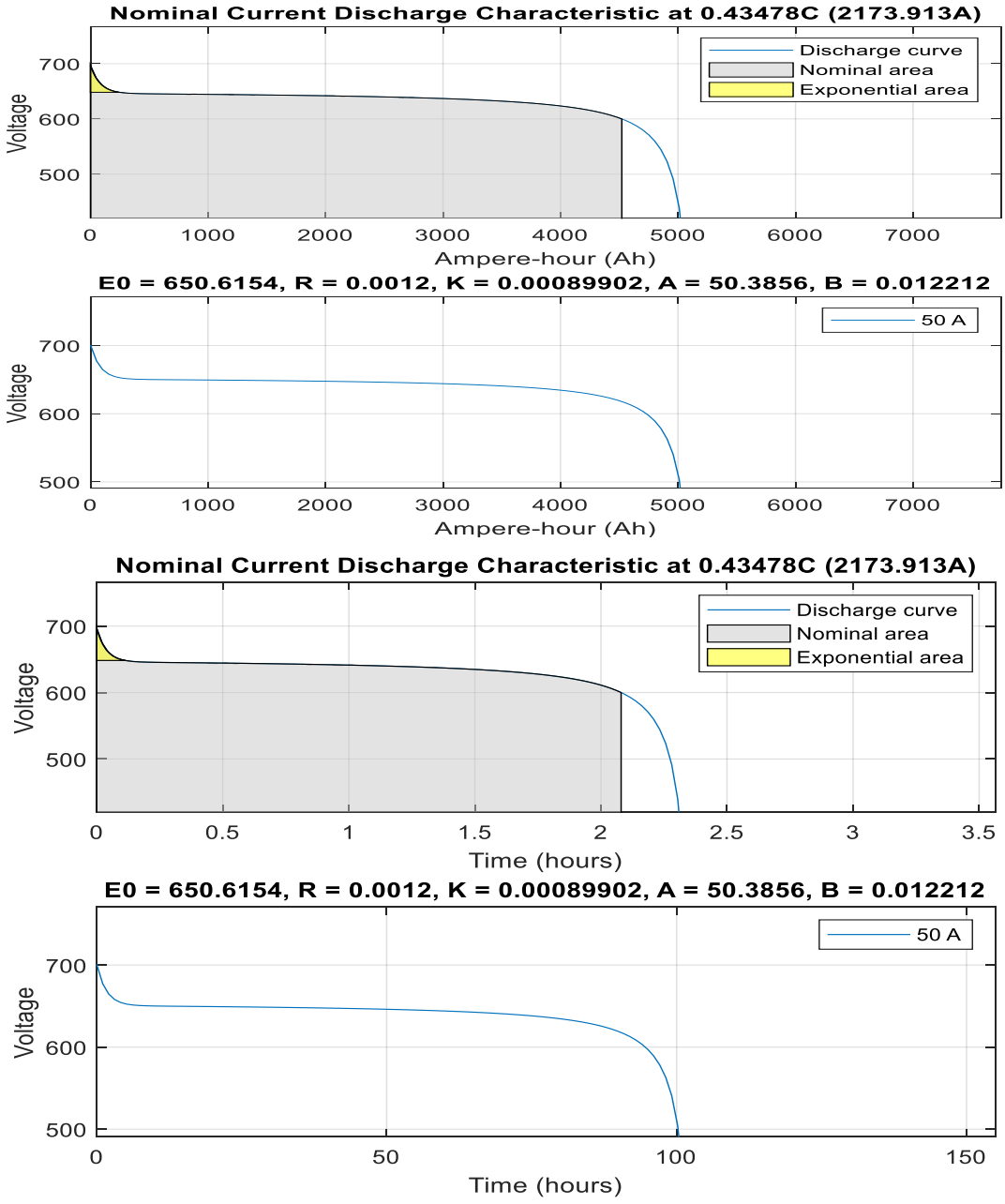

Figure 4.10: Lead-Acid Response Characteristics

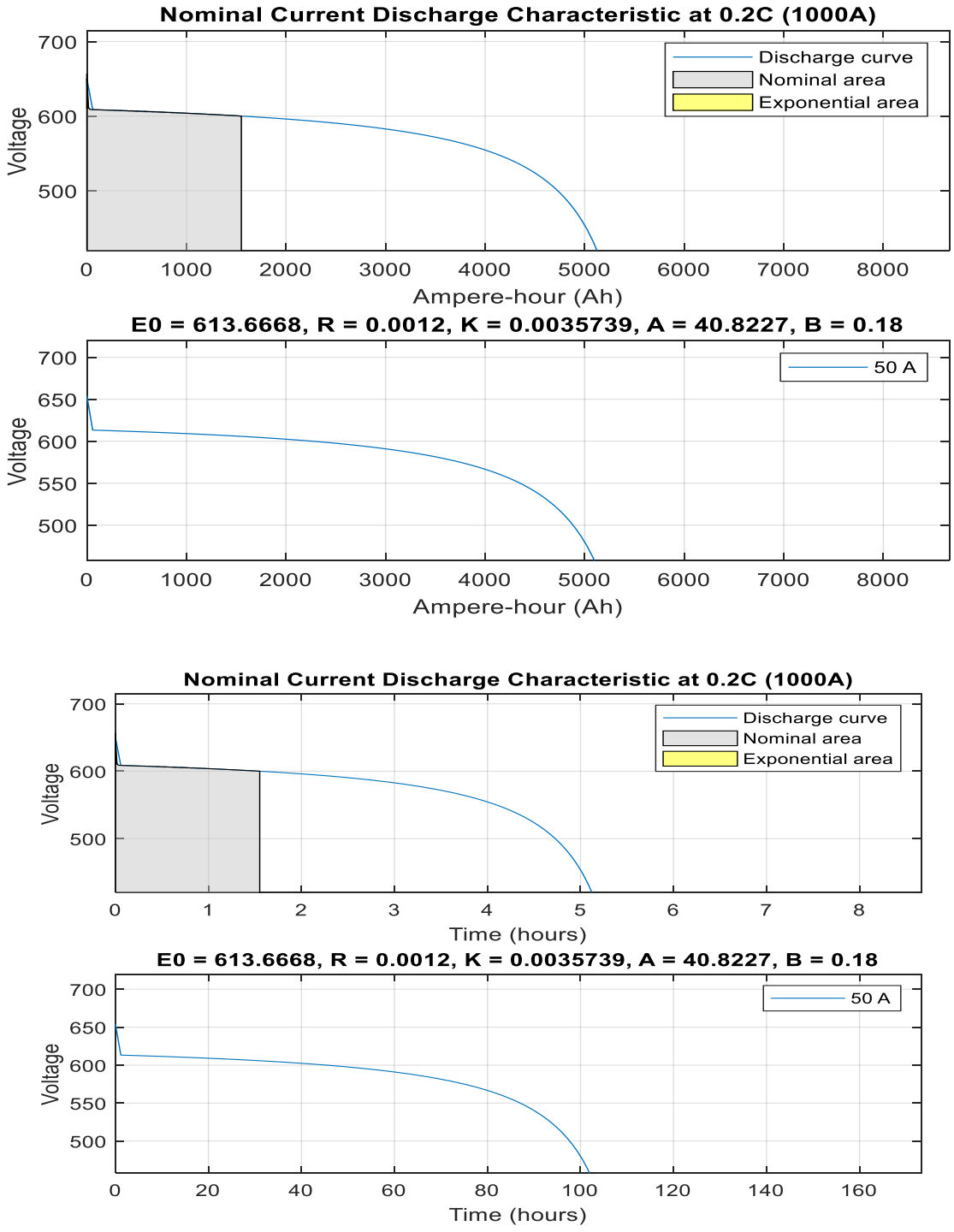

Figure 4.11: Lithium-Ion Response Characteristics

4.1.5 Combined Simulink Model Test Results

4.1.5.1 Solar PV System Output Voltage and Output Current in the Proposed Microgrid

Figure 4.12 shows the Solar PV System output voltage (V_{out}) and output current (I_{out}) in the proposed Microgrid. The PV System output voltage (V_{out}) starts from zero and the generation begins immediately after sufficient solar irradiance has been received. As such, the PV voltage is noted to vary from a low of $30\ V$ to a high of $561\ V$, settling to within $322.23\ V$ at steady state after $0.2\ s$. The PV system output current does not oscillate as much as the voltage does and for this, a steady state current value of $17.53\ A$ is attained after $0.01\ s$ for the simulation instant captured.

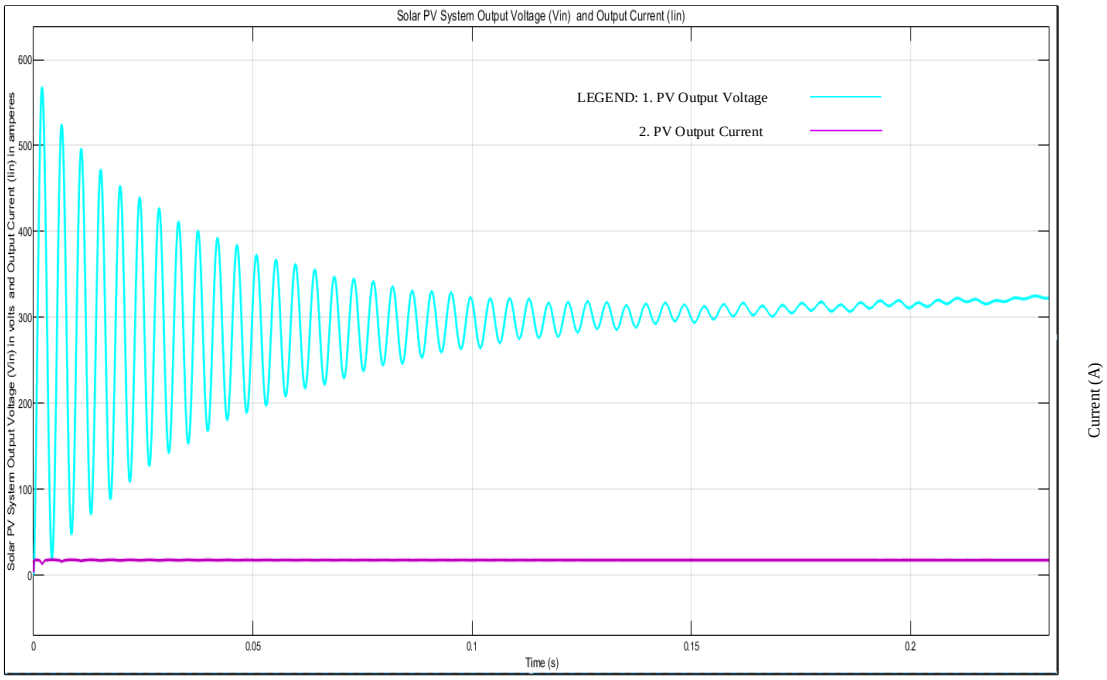

Figure 4.12: Solar PV System Output Voltage (Vout) and Output Current (Iout) in the proposed Microgrid

4.1.5.2 PV System IBC Input and Output Voltage and Current in the proposed Microgrid

Figure 4.13 indicate the PV System IBC input voltage (V_{in}) and current (I_{in}) in the proposed Microgrid with PID controller. From Figure 4.13, the PV system side IBC input voltage depicts a maximum value of $565\,V$ and a minimum voltage $530\,V$. There are some ripples in the voltage profile which falls to $540 \pm 5\,V$ within $0.05\,s$.

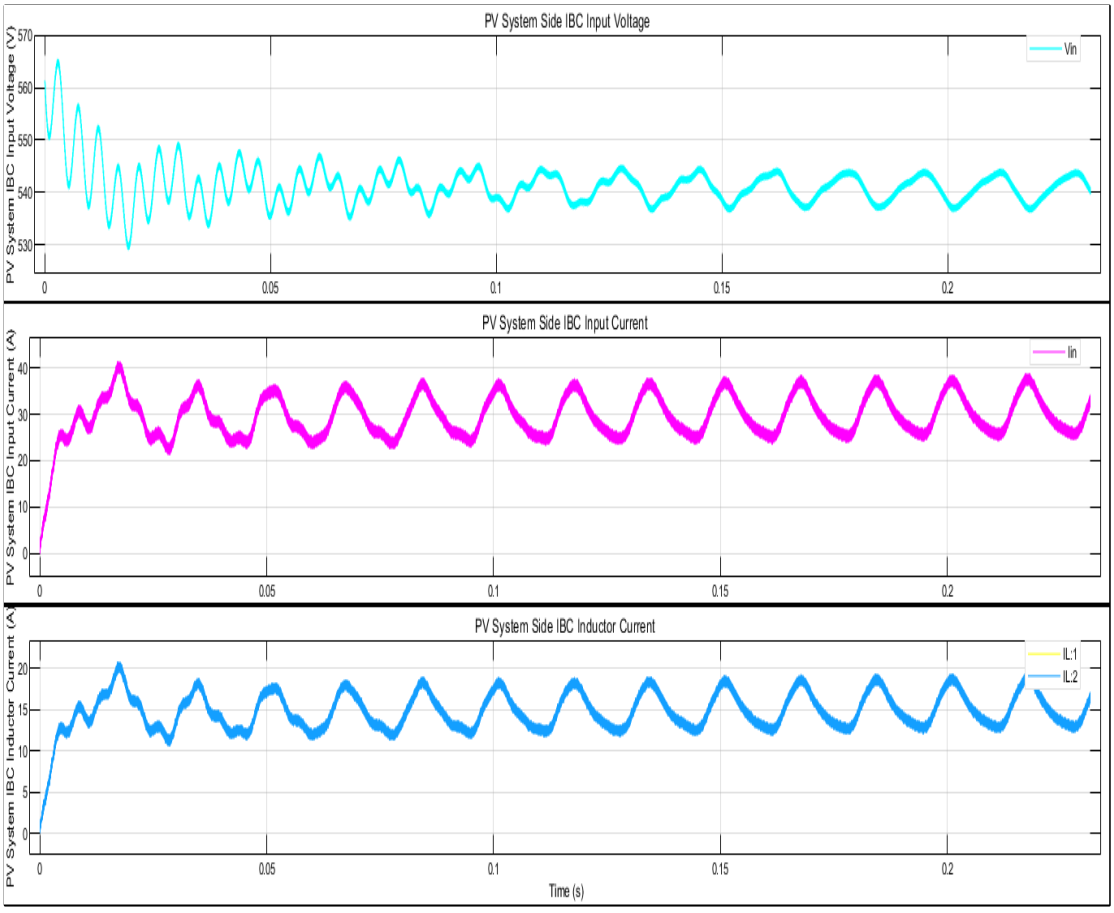

Figure 4.13: PV System IBC Input Voltage (V_{in}) and Current (I_{in}) in the Proposed Microgrid with PID Controller

The PV side IBC input current experiences some ripples at the beginning which falls to the range of $30 \pm 4\ A$ within $0.05\ s$. The PV side IBC inductor current plot followed a similar profile as for the input current, range of $15 \pm 8\ A$ within $0.05\ s$, representing the impact of the energy storage elements such as inductors in the operation of IBC.

Figure 4.14 shows the PV System IBC output voltage (V_{out}) and current (I_{out}) in the proposed Microgrid with PID Controller.

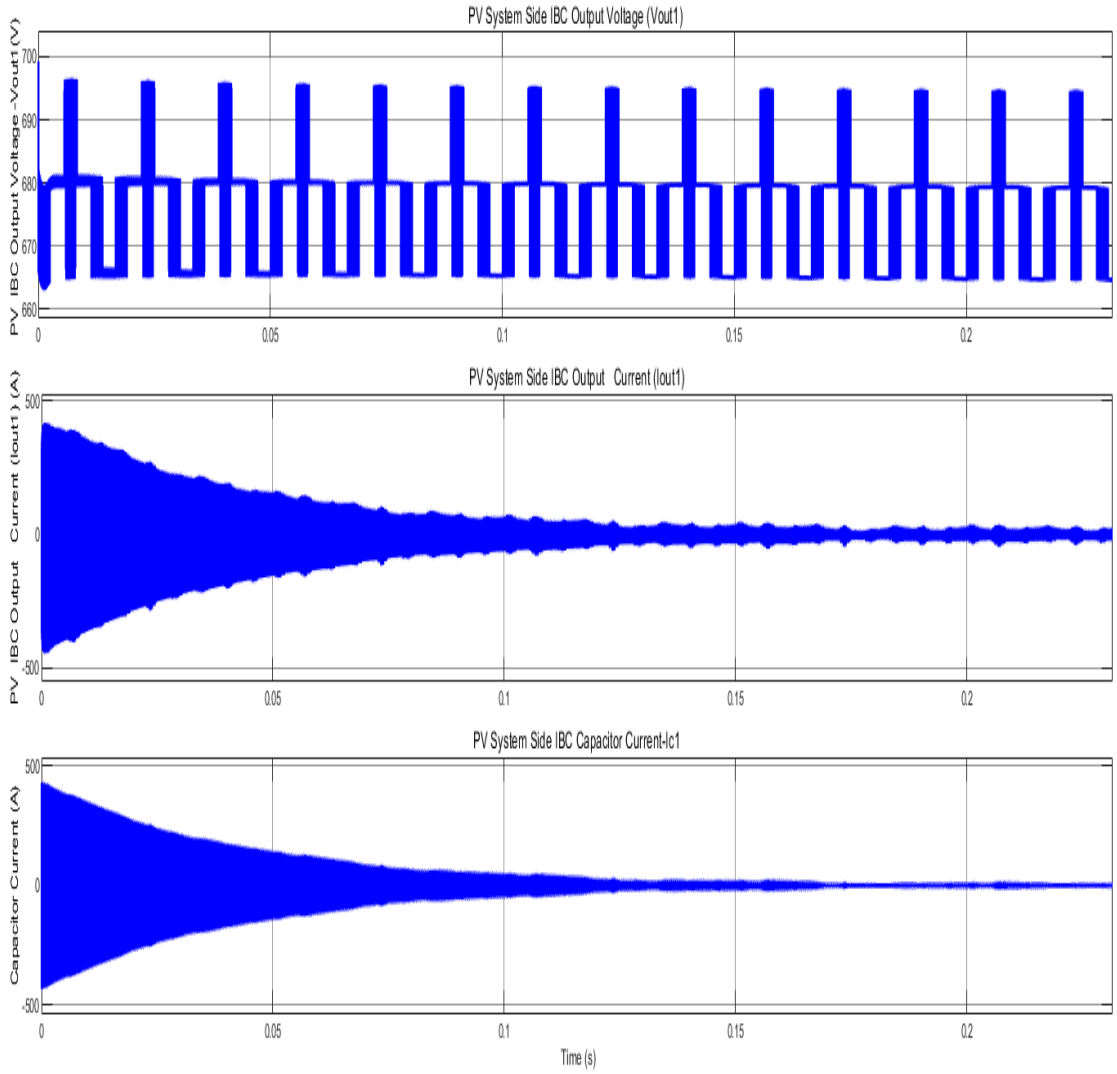

Figure 4.14: PV System IBC Output Voltage (V_{in}) and Current (I_{in}) in the Proposed Microgrid with PID Controller

In Figure 4.14, the PV system side IBC output voltage depicts a maximum value of 695 V and a minimum voltage of 665 V, proving that the voltage levels have been significantly boosted. The nominal voltage stays at 680 $\pm$ 15 V representing a ripple content of 4.5% throughout the operation of the IBC in the PV microgrid system. The PV side IBC output current and inductor current experienced enhanced, initially oscillating outputs between $\pm$400 A to settle to within $\pm$20 A after 0.15 s.

4.1.5.3 PV BESS Output Voltage, SoC, and Current in the Proposed Microgrid

Figure 4.15 shows the PV BESS Output Voltage, SoC, and Current in the proposed Microgrid with PID Controller.

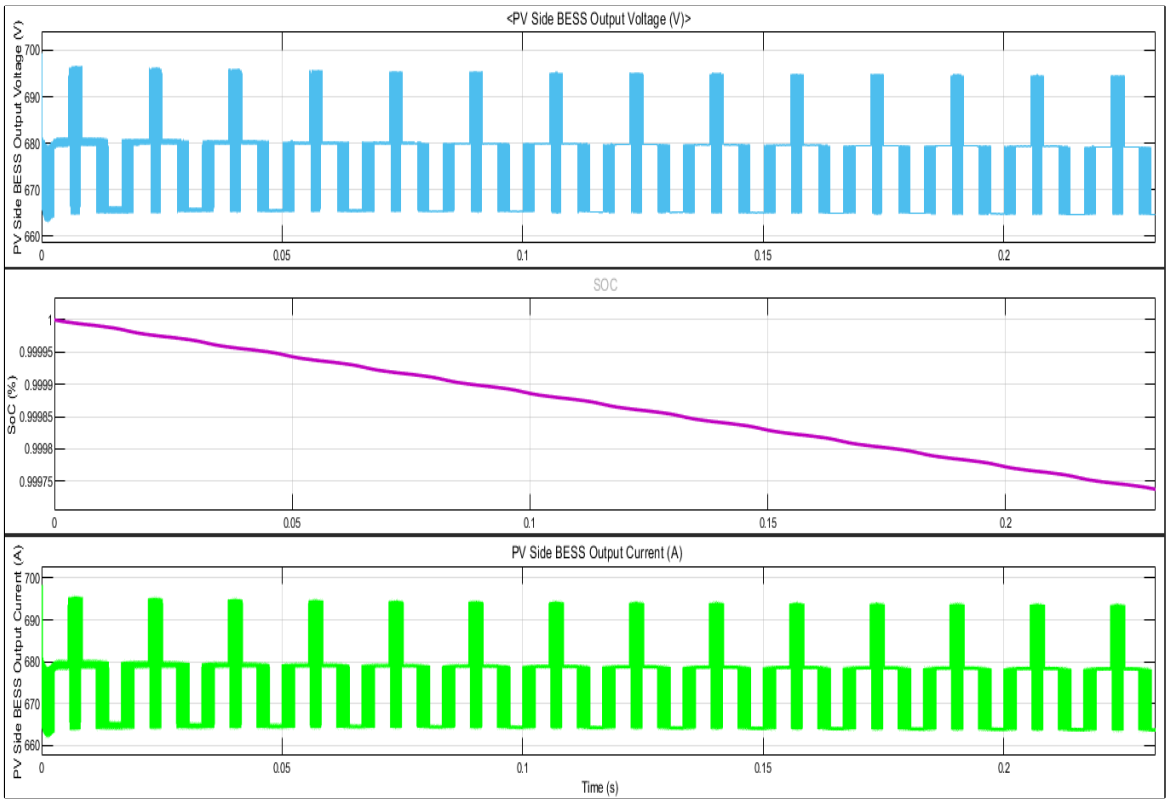

Figure 4.15: PV BESS Output Voltage, SoC, and Current in the Proposed Microgrid with PID Controller

From Figure 4.15, it was observed that the PV system side BESS output voltage depicted a maximum value of 697 V and a minimum voltage 665 V, proving the voltage levels of the IBC were nearly the same ones used to charge the BESS. The BESS charging and discharging was assumed to be identical and also the efficiency was assumed to be 95% . The SoC dropped from unity to about 0.95 in the simulated time period of 0.2 s. The PV BESS Output Current depicted a similar trend and profile to the PV BESS Output Voltage.

4.1.5.4 WT system Output Voltage and Current in the proposed Microgrid

Figure 4.16 shows the WT Stator Output parameters with PID Controller in the proposed microgrid in which the transients of the 3-phase AC current and the electromagnetic torque p.u. values are visible.

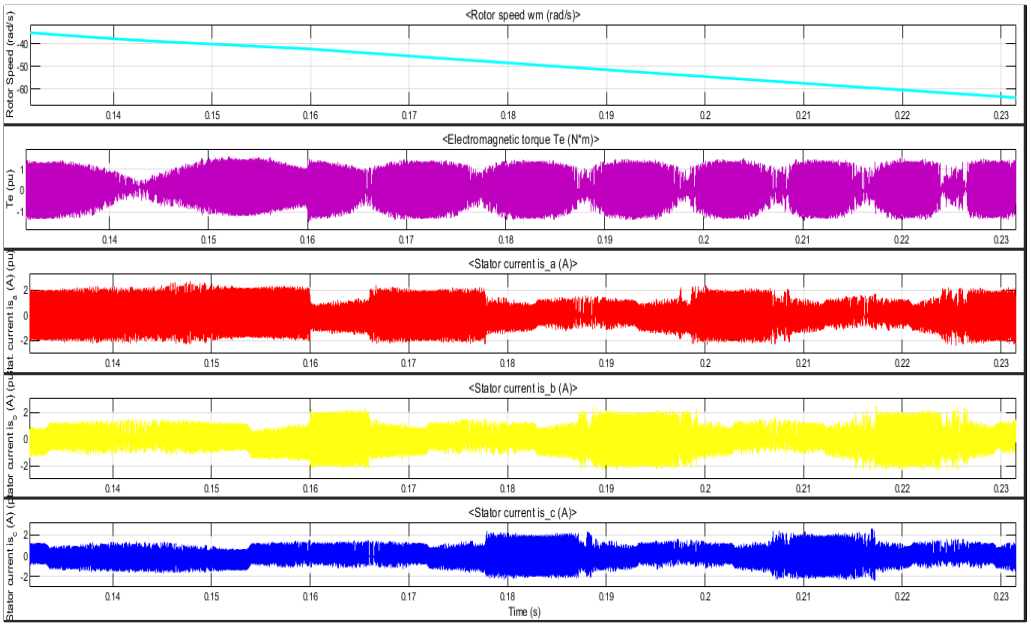

Figure 4.16: WT Stator Output Parameters with PID Controller

The stator currents experience similar disturbance levels but which are much more irregular than those suffered by the electromagnetic torque.

The WT Rectifier Input, Output Voltage, and Current profiles are depicted in Figure 4.17. Looking at the input and output voltage and current profiles of the WT at the rectifier output, the struggles of the PID controller with the non-linearities in the system are clearly evident with ripples and overshoots reaching to levels of 8% to 10%.

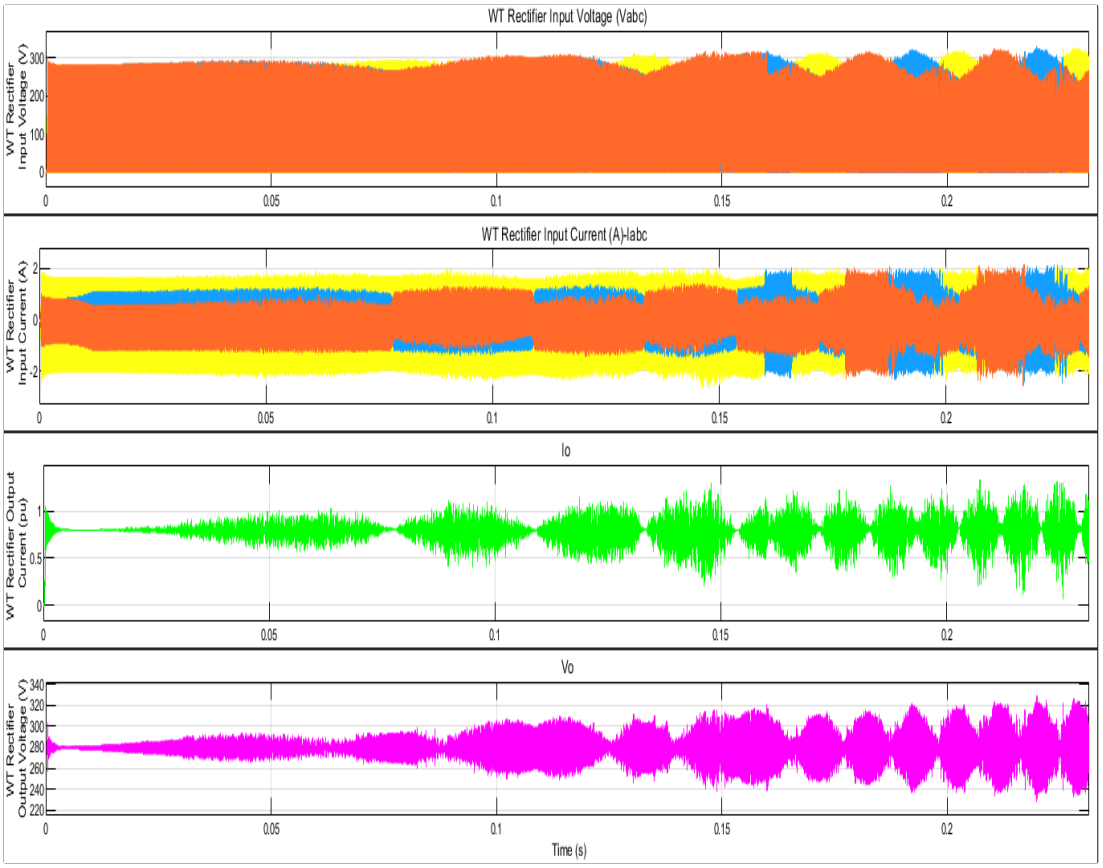

Figure 4.17: WT Rectifier Input and Output Voltage and Current with PID Controller

Figure 4.18 shows the WT Regulated Filtered Output Voltages (pu) in the proposed Microgrid. The effect of regulating the WT output voltages and the ability of the filter to clean or improve on the power quality output is clearly evident.

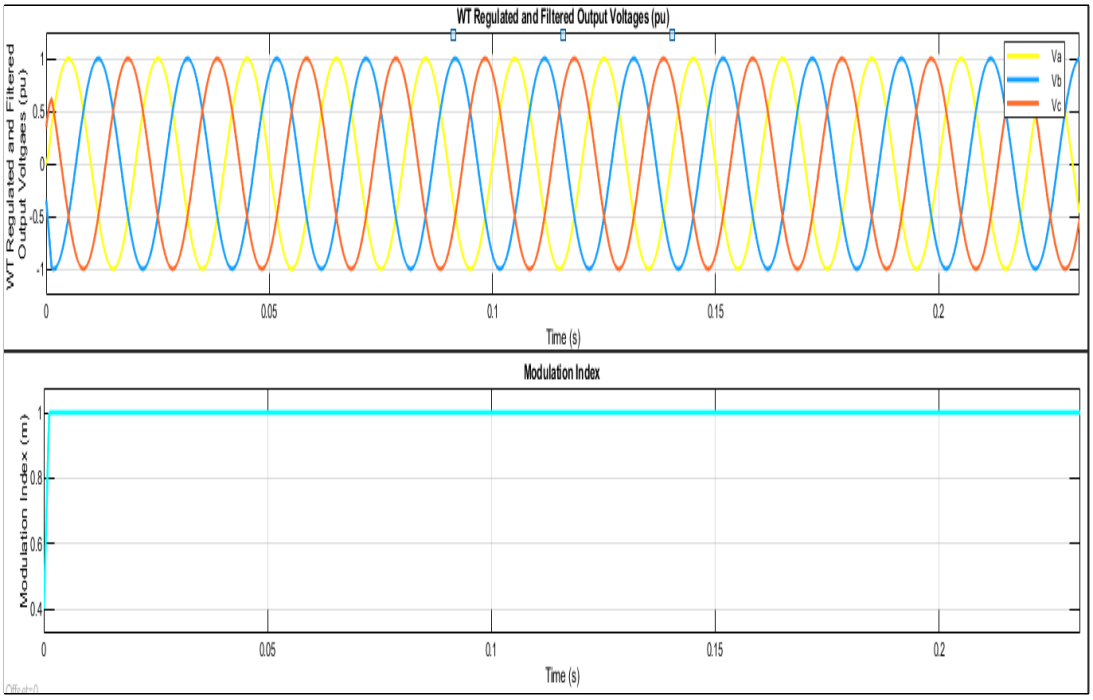

Figure 4.18: WT Regulated Filtered Output Voltage (pu) and Modulation Index with PID Controller

4.1.5.5 WT, BESS, and Inverter Output in the Proposed Microgrid

Figure 4.19 shows the WT BESS Outputs in the proposed Microgrid with the PID controller. Once again. the struggles of the PID controller with the non-linearities in the BESS system are clearly evident with ripples and overshoots reaching to levels of 8% to 10% especially in the current profile. The BESS voltage drops slightly by about $1V$ within $0.01\ s$ from $280.2\ V$ to $279.2\ V$.

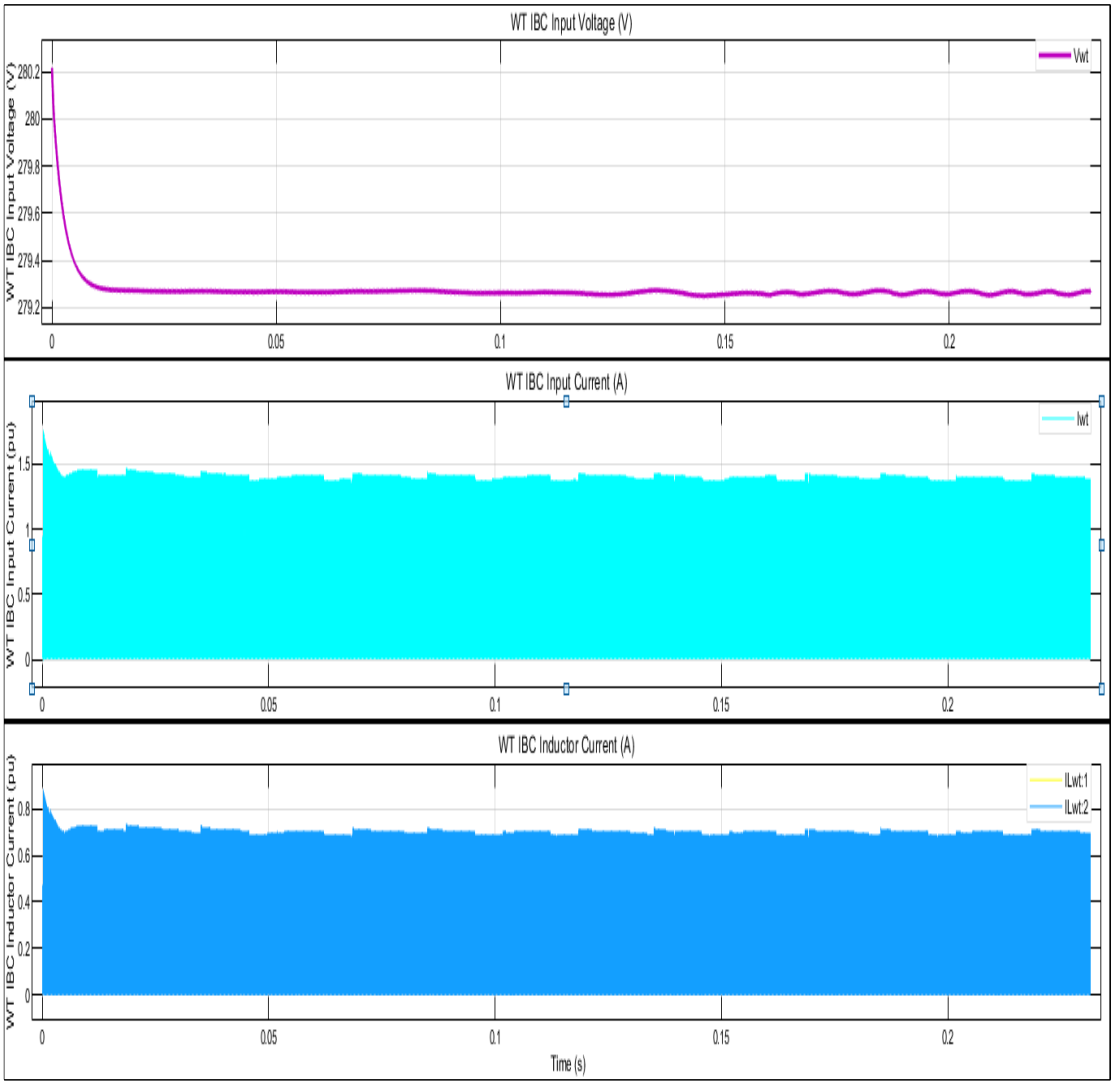

Figure 4.19: WT IBC Inputs in the Proposed Microgrid with PID Controller

Figure 4.20 shows the WT IBC Outputs in the proposed Microgrid with PID controller. From Figure 4.20, the WT system side IBC output voltage depicts a maximum value of $699\,V$ and a minimum voltage $688\,V$ with ripples and overshoot of about 1.5% throughout the operation of the WT IBC in the microgrid system. The WT side IBC output current and inductor current experienced enhanced, initially oscillating outputs between $\pm 250\,A$ to and $\pm 400\,A$, respectively. The WT IBC output current settled settle to within $\pm 25\,A$ after $0.15\,s$.

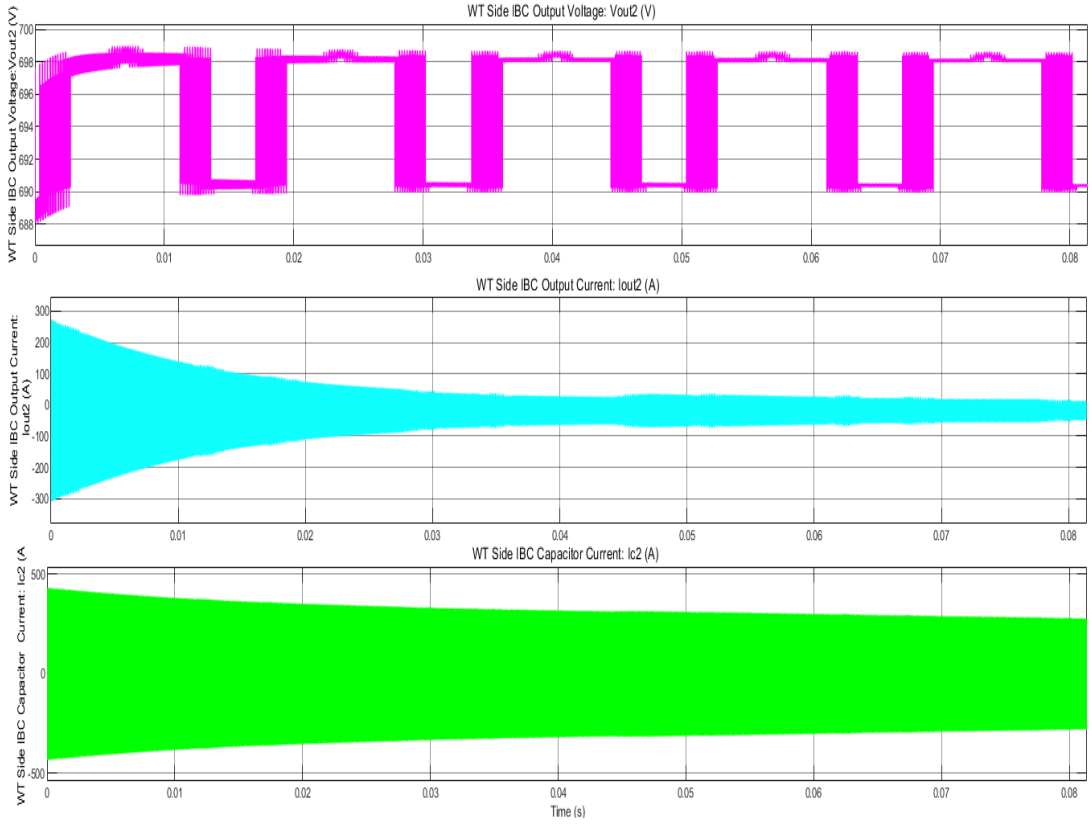

Figure 4.20: WT IBC Outputs in the Proposed Microgrid with PID Controller

Figure 4.21 shows the WT BESS Outputs in the proposed Microgrid with PID controller. From Figure 4.21, it was observed that the WT system side BESS output voltage depicted a maximum value of $699\,V$ and a minimum voltage $668\,V$, proving the voltage levels of the WT side IBC were nearly the same ones used to charge the WT BESS. The BESS charging and discharging was assumed to be identical and also the efficiency was assumed to be 95% . The SoC dropped from unity to about 0.95 in the simulated time period of $0.2\,s$. The PV BESS Output Current depicted a similar trend and profile to the PV BESS Output Voltage.

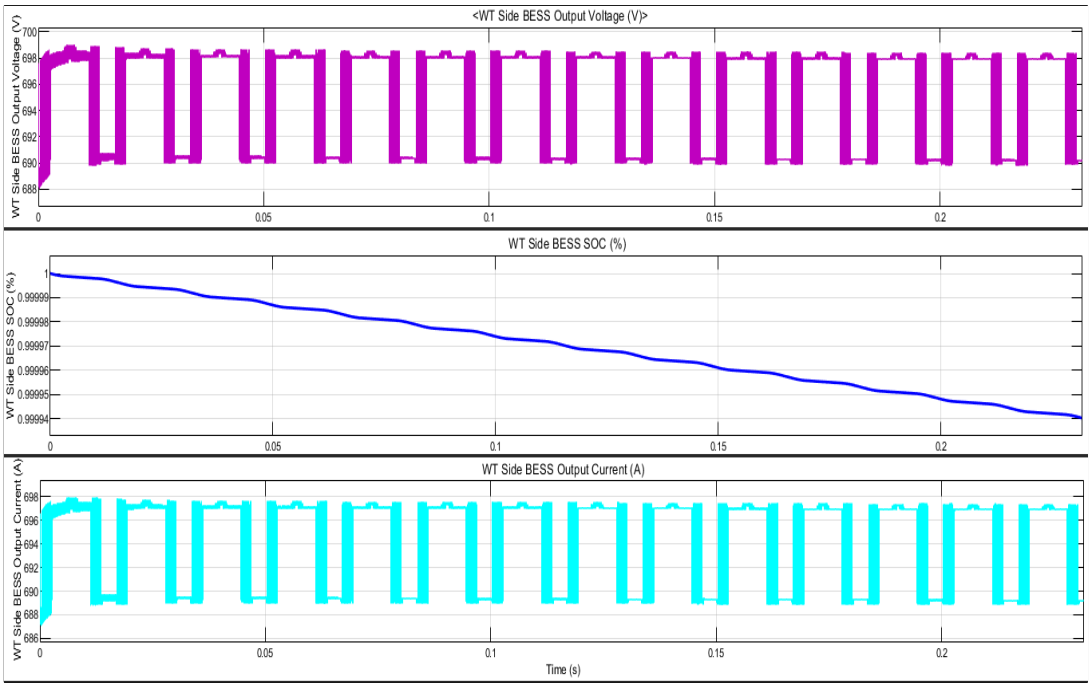

Figure 4.21: WT BESS Outputs in the Proposed Microgrid with PID Controller

4.1.5.6 Inverter Output and Power Output to Residential Loads

Figure 4.22 presents the PV side Inverter Outputs while Figure 4.23 shows WT side Inverter Outputs in the Microgrid under study with PID Controller.

From Figure 4.22 and Figure 4.23, the PV and WT inverter output voltage profiles are nearly identical ranging between a minimum of $630\ V$ and a maximum of $690\ V$. The ripple content and overshoot with the PID controller stood at 4.5% with the VSC inverter nominal output being at $660 \pm 30\ V$. The load voltage obtained from the inverter also had a similar profile on the PV and WT side being at $645 \pm 20\ V$. However, these presented a slightly different profile from those regarding the VSC outputs but this depends on the nature of the load connected to the inverter output terminals. From Figure 4.22 and Figure 4.23, the PV and WT inverter output voltage profiles are nearly identical and ranging between a minimum of $630\ V$ and a maximum of $690\ V$.

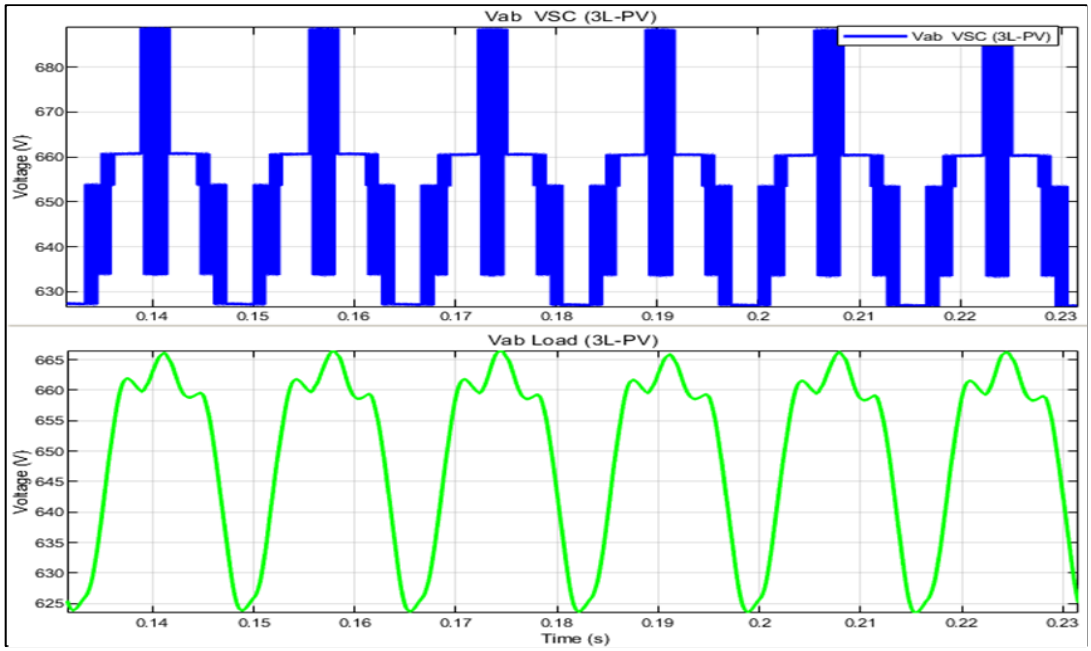

Figure 4.22: PV Side Inverter Outputs in the Proposed Microgrid with PID Controller

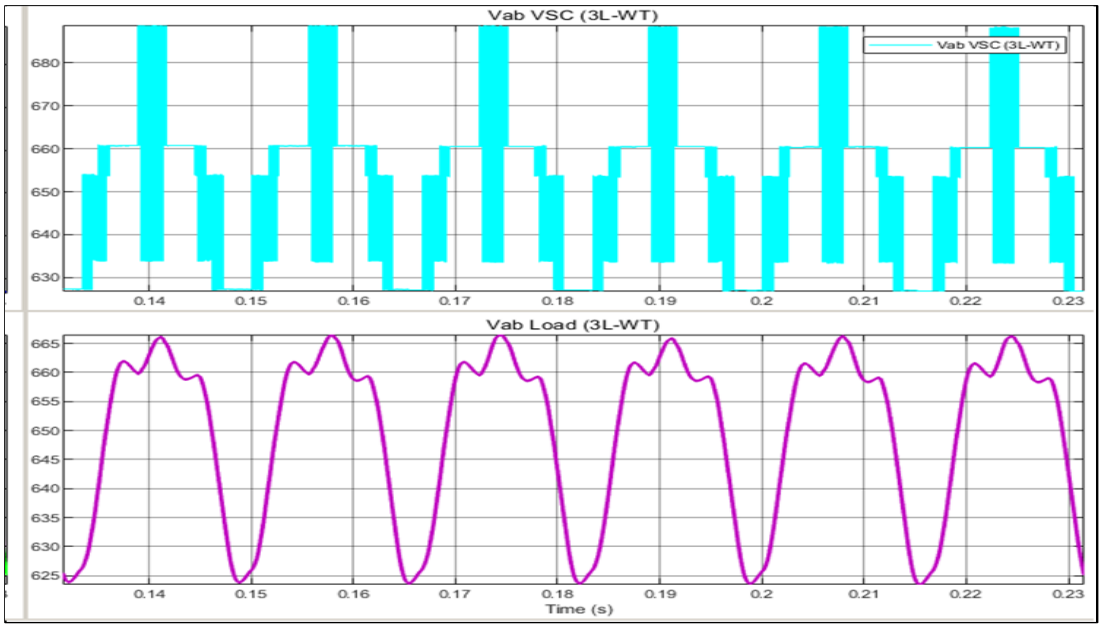

Figure 4.23: WT Side Inverter Outputs in the Proposed Microgrid with PID Controller

Figure 4.24 shows Power Output to Loads in the Microgrid under study with PID controller. It was observed that the active power of 6 kW depicted ripples of 10%. The reactive power was noted to be zero.

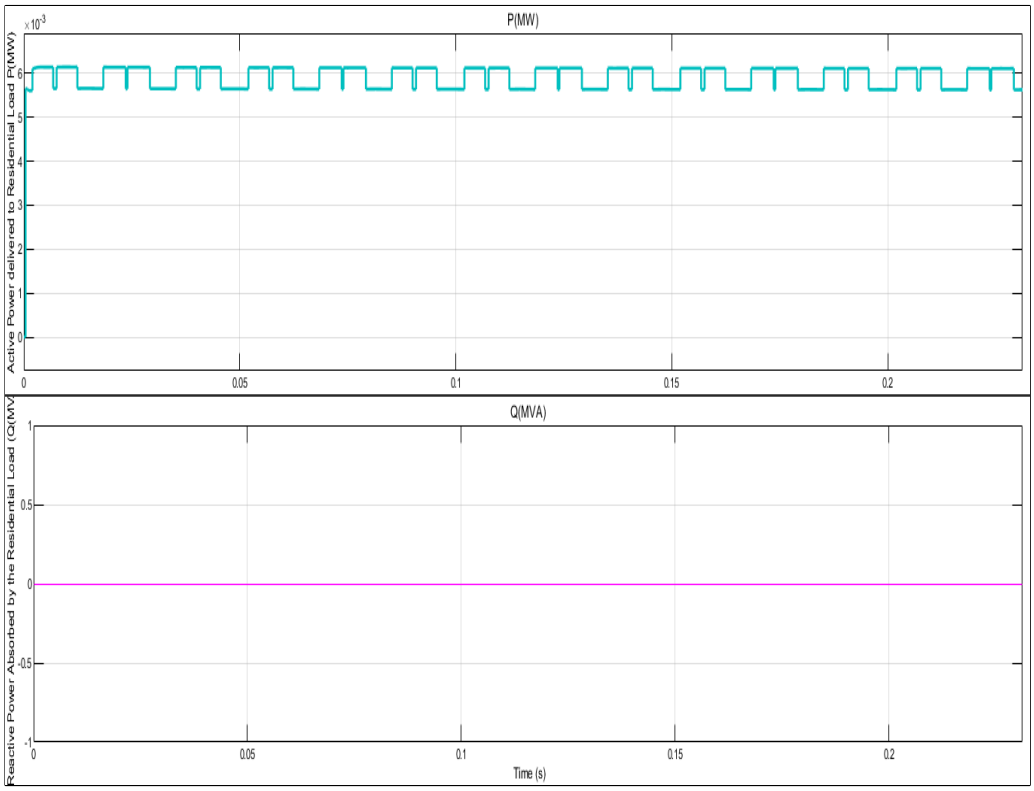

Figure 4.24: Power Outputs to Loads in the Proposed Microgrid

4.2 Performance of the GA-ANFIS-based Primary Microgrid Controller

This section corresponds to the specific objective number two and four. The results presented here have been obtained from the application of the designed Genetic Algorithm-Adaptive Neuro-Fuzzy Inference System (GA-ANFIS) controller in the regulation of microgrid voltage amid power generation variations. The performance of the GA-ANFIS algorithm has been compared with the Search Space Restricted-Perturb and Observe (SSR-P&O) and the Proportional-plus-Integral-plus-Derivative (PID) controllers using a simulation model built in MATLAB/SIMULINK.

4.2.1 Response of SSR-P&O, PID, ANFIS, and GA-ANFIS Controllers with the Microgrid TF Model

Figure 4.25 shows the response of SSR-P&O, PID, ANFIS, and GA-ANFIS controllers to the unit step change in voltage when applied to the Transfer Function (TF) model of the proposed PV-Wind hybrid microgrid.

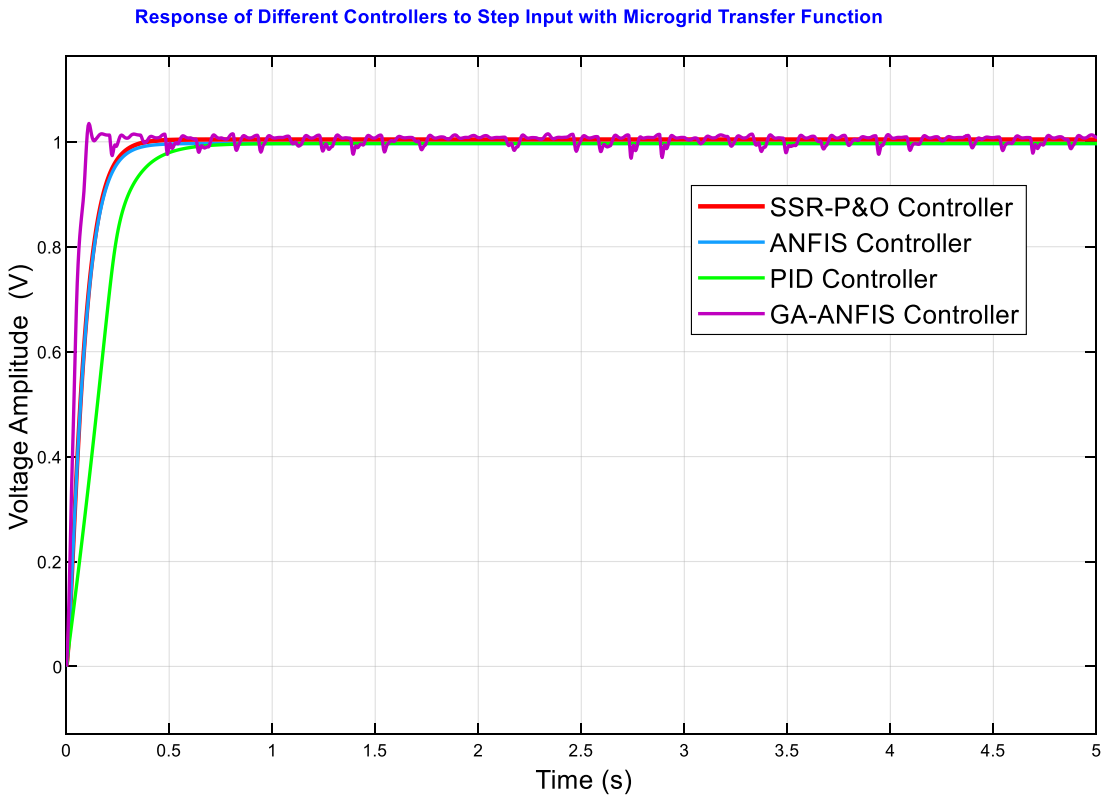

Figure 4.25: Response of Different Controllers to Step Change with the Microgrid TF Model

The performance of these algorithms was tested with other voltage changes, and the voltage regulation capabilities obtained were summarized in Table 4.1.

Table 4.1: SSR-P&O, PID, ANFIS, and GA-ANFIS Controllers with Various Voltage Changes

Step Input	SSR-P&O			PID			ANFIS			GA-ANFIS		
	t_r	t_s	M_p	t_r	t_s	M_p	t_r	t_s	M_p	t_r	t_s	M_p
(V)	(s)	(s)	(%)	(s)	(s)	(%)	(s)	(s)	(%)	(s)	(s)	(%)
1	0.3	0.4	0.0	0.3	0.8	0.0	0.2	0.4	0.0	0.1	0.2	3.5
2	0.3	0.4	0.0	0.4	0.7	0.0	0.3	0.4	0.0	0.1	0.2	3.5
3	0.2	0.5	0.0	0.3	0.8	0.0	0.2	0.4	0.0	0.1	0.1	3.6
4	0.2	0.4	0.0	0.4	0.7	0.0	0.2	0.4	0.0	0.1	0.2	3.5
5	0.3	0.5	0.0	0.4	0.8	0.0	0.2	0.5	0.0	0.1	0.1	3.5
Avg.	**0.26**	**0.44**	**0.00**	**0.36**	**0.76**	**0.00**	**0.22**	**0.42**	**0.00**	**0.10**	**0.16**	**3.52**

The results obtained with various voltage step inputs indicated that the GA-ANFIS responds with the fastest settling time (t_s) and shortest rise time (t_r). According to the average values in Table 4.1, GA-ANFIS recorded the best average performance. The rise time is 0.10 s for GA-ANFIS, 0.22 s for ANFIS, 0.26 s for SSR-P&O, and 0.36 s for the PID controller. The maximum overshoot (M_p) with GA-ANFIS is reduced up to 3.52% though there were no overshoots registered with the PID, SSR-P&O, and ANFIS controllers on the MPZC TF, which is a second-order plant. However, the PID, SSR-P&O, and ANFIS controllers depicted higher overshoots (M_p of 8.00%, 5.50%, and 5.00%, respectively) compared with the GA-ANFIS (M_p of 4.00%), when applied to the fourth-order microgrid TF without pole-zero cancellation. The settling time is 0.16 s for GA-ANFIS, 0.42 s for ANFIS, 0.44 s for the SSR-P&O, and 0.76 s for the PID. It is interpreted from these results that while using GA-ANFIS, the system tracks the new set voltage points in the fastest time (0.10 s) and with an acceptable overshoot of 3.52% (against IEEE-1547 and IEEE-519 standards voltage limits of $\pm 5\%$) as compared to SSR-P&O, ANFIS, and PID controllers.

The GA-ANFIS controller is also the most optimal controller with the best prediction, learning capability, and ability to cope with non-linearities associated with the microgrid.

However, this has been acquired at the expense of a 3.52% overshoot introduced in the steady state value, which is still well within the expected voltage limits. Despite showing zero overshoots, the SSR-P&O and PID controllers do not have the learning and prediction capability of the ANFIS and GA-ANFIS and struggle with nonlinearities in the microgrid.

4.2.2 Generator Outputs in the Proposed Microgrid with SSR-P&O and GA-ANFIS

Figure 4.26 shows the WT Stator Output parameters (rotor speed, electromagnetic torque, and three-phase stator currents) in the proposed Microgrid with SSR-P&O. The struggles of the SSR-P&O algorithm in the presence of nonlinear dynamics of the WT are evident. The performance of the SSR-P&O requires that the microgrid is operated solely under linear conditions. However, the practical microgrid system in addition to the WT, has the PV, BESS, and nonlinear loads present thus increasing the presence of non-linearities which cannot satisfactorily be dealt with by the SSR-P&O algorithm.

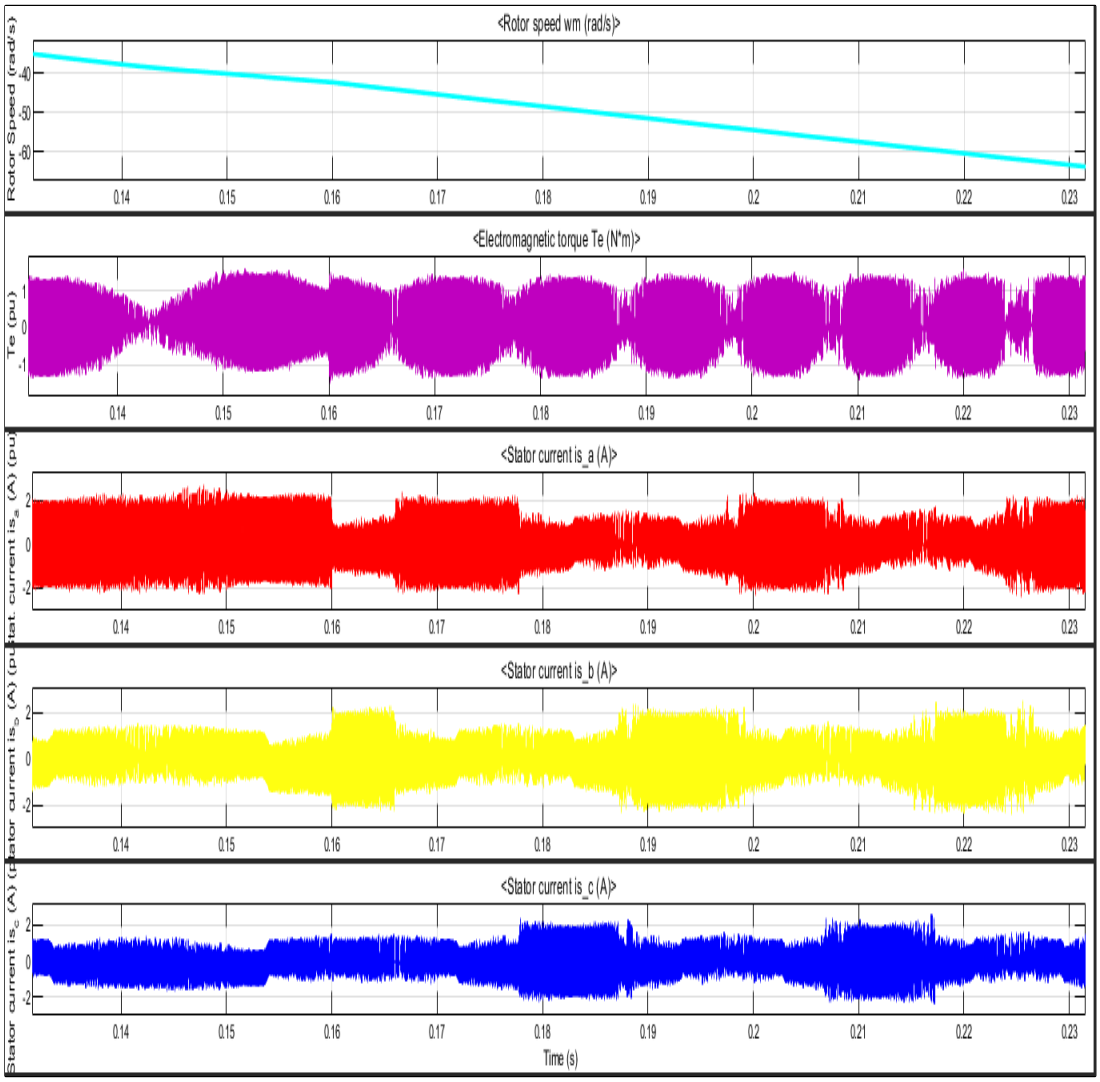

Figure 4.26: WT Stator Output Parameters in the Proposed Microgrid with SSR-P&O

In Figure 4.27, these generator output parameters are much refined owing to the ability of the GA-ANFIS controller to predict system conditions and deal with the nonlinearities. The three phase stator currents are almost perfect sinusoidal currents with the ripples minimized to within $\pm 3.5\%$. The rotor speed and the electromagnetic torque experience similar form of disturbance in which the GA-ANFIS stabilizes these two generator output quantities in a time frame of $0.08\ s$ with an overshoot of about $\pm 3.5\%$.

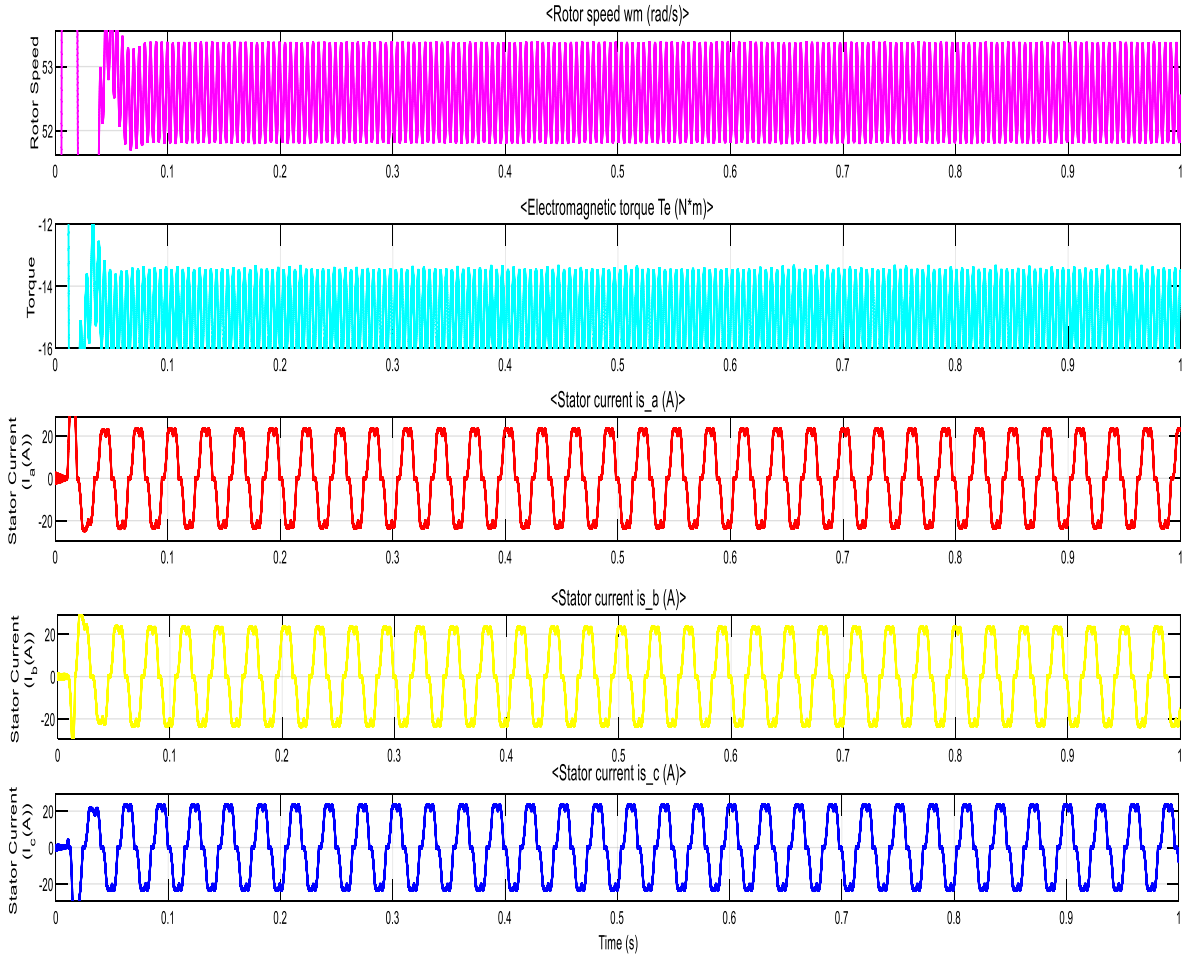

Figure 4.27: Generator Output Data with GA-ANFIS

4.2.3 Results from the IBC with SSR-P&O MPPT and GA-ANFIS Controller

The inputs to the proposed PV side IBC are voltage $V_{in} = 561\ V$ and current, $I_{in} = 26\ A$ whose profiles with SSR-P&O are shown in Figure 4.28. The first plot in Figure 4.28 indicates that the PV side IBC input voltage experiences considerable overshoot of $\pm 5.5\%$ representing a voltage deviation of $\pm 31\ V$ with the voltage maintaining some level of fluctuations of about $\pm 5\ V$, to be kept at $540 \pm 5\ V$ through ought. Further, from Figure 4.28, it was observed that the PV system IBC Input current and Inductor current experienced similar disturbances with the final currents falling to $30 \pm 5\ A$ and $15 \pm 5\ A$, respectively. The current plot with GA-ANFIS is shown in Figure 4.29, in which the GA-

ANFIS has been able to stabilize the PV side IBC input current to within $18 \pm 0.6\ A$ or $\pm 3.5\%$.

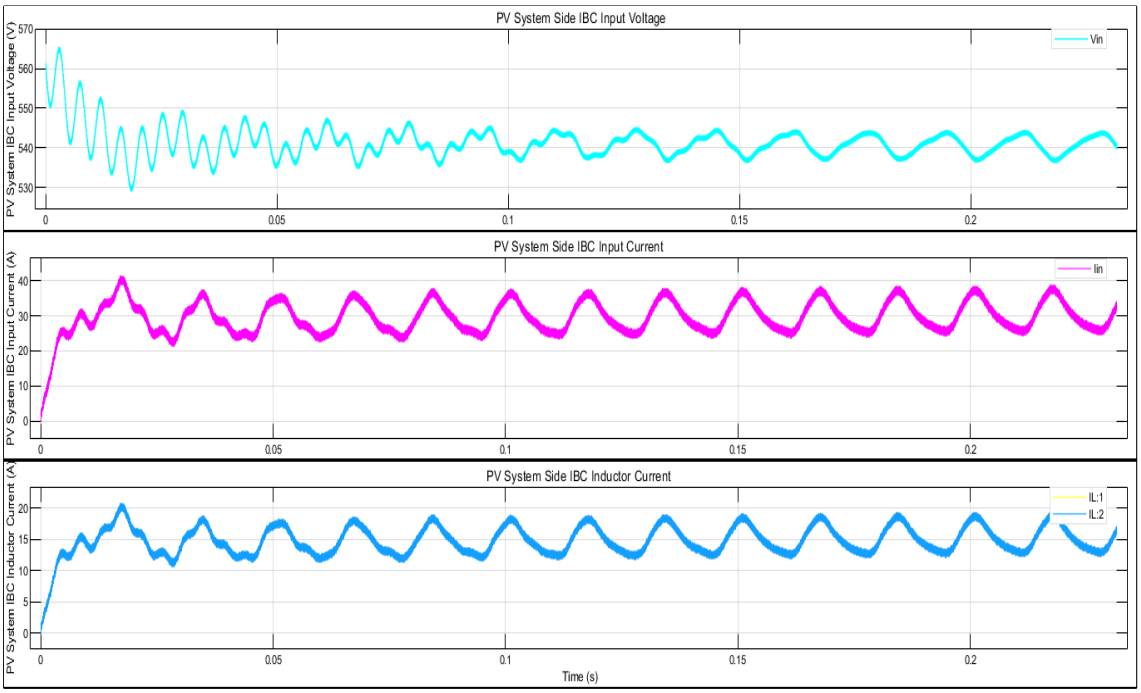

Figure 4.28: PV System IBC Input Voltage (V_{in}) and Current (I_{in}) in the Proposed Microgrid with SSR-P&O MPPT

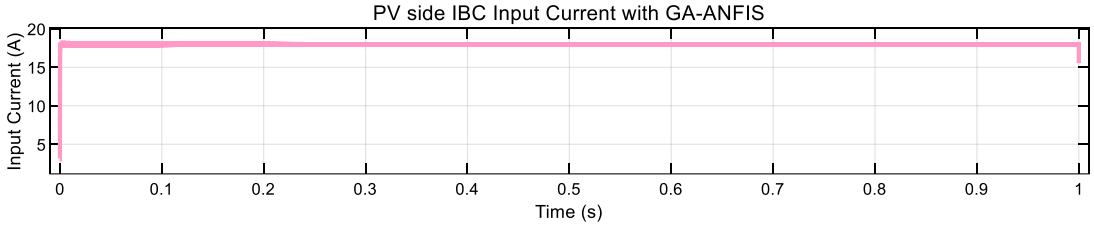

Figure 4.29: PV side IBC Input Current with GA-ANFIS

The IBC output voltage with SSR-P&O of $680\ V$ and current of $20.63\ A$ obtained at a switching frequency of $20\ kHz$ and the duty ratio of $D = 0.1928$ are presented in Figure 4.30. The SSR-P&O MPPT technology indicated a rise time of $0.25\ s$, a settling time of

0.40 s and an overshoot of 7.50% and an efficiency of 96.5% compared to one obtained in literature of 96.1% (Prabhakaran & Agarwal, 2020) and the conventional P&O which is 80 to 84%.

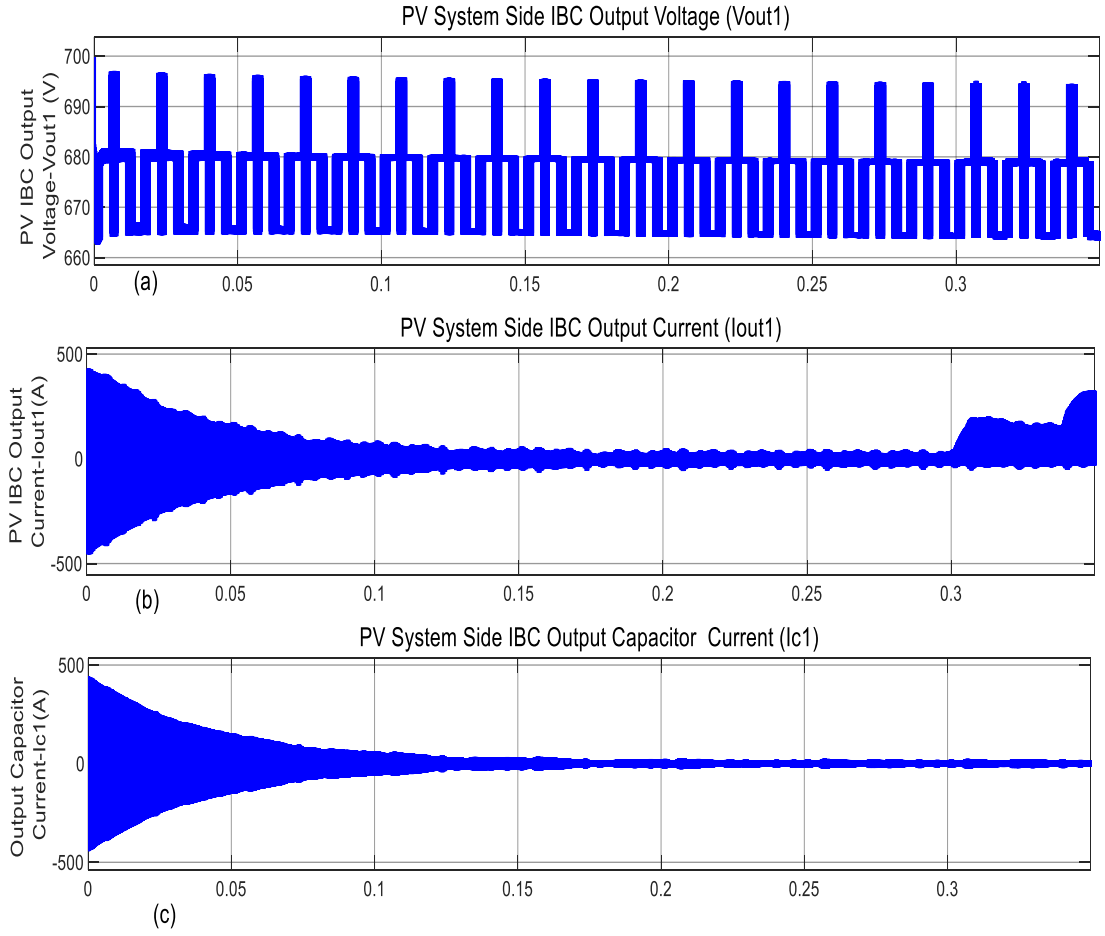

Figure 4.30: PV Side IBC Output Voltage and Current with P&O-SSR in Case Study Model

Figure 4.31 shows the PV Side IBC Output voltage and Current with GA-ANFIS in Case Study Model when the generated PV power varies. The GA-ANFIS regulated the IBC output voltage to within $\pm 2.21\%$ of the nominal $680V$, i.e., $680 \pm 15\,V$ which is well within the required $\pm 5\%$. The rise time and settling time of the GA-ANFIS were 0.10 s and 0.15 s, respectively, giving a better voltage profile than SSR-P&O.

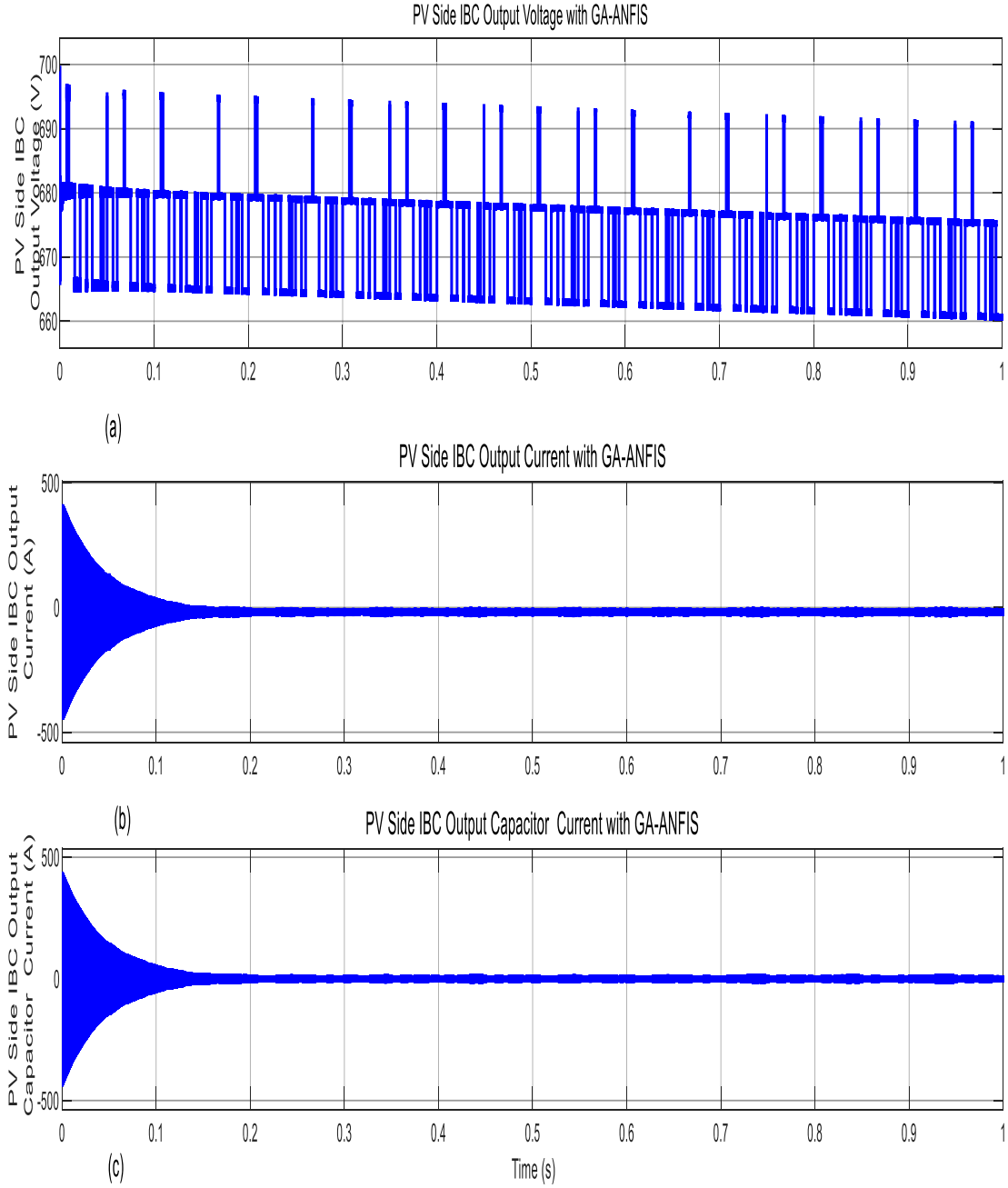

Figure 4.31: PV Side IBC Output Voltage and Current with GA-ANFIS in Case Study Model

Figure 4.32 and Figure 4.33 show the WT IBC Inputs and outputs with SSR-P&O in the proposed microgrid. The distortions in the voltage and current profiles depict the inability of the SSR-P&O algorithm to tackle the nonlinear dynamics of the microgrid system.

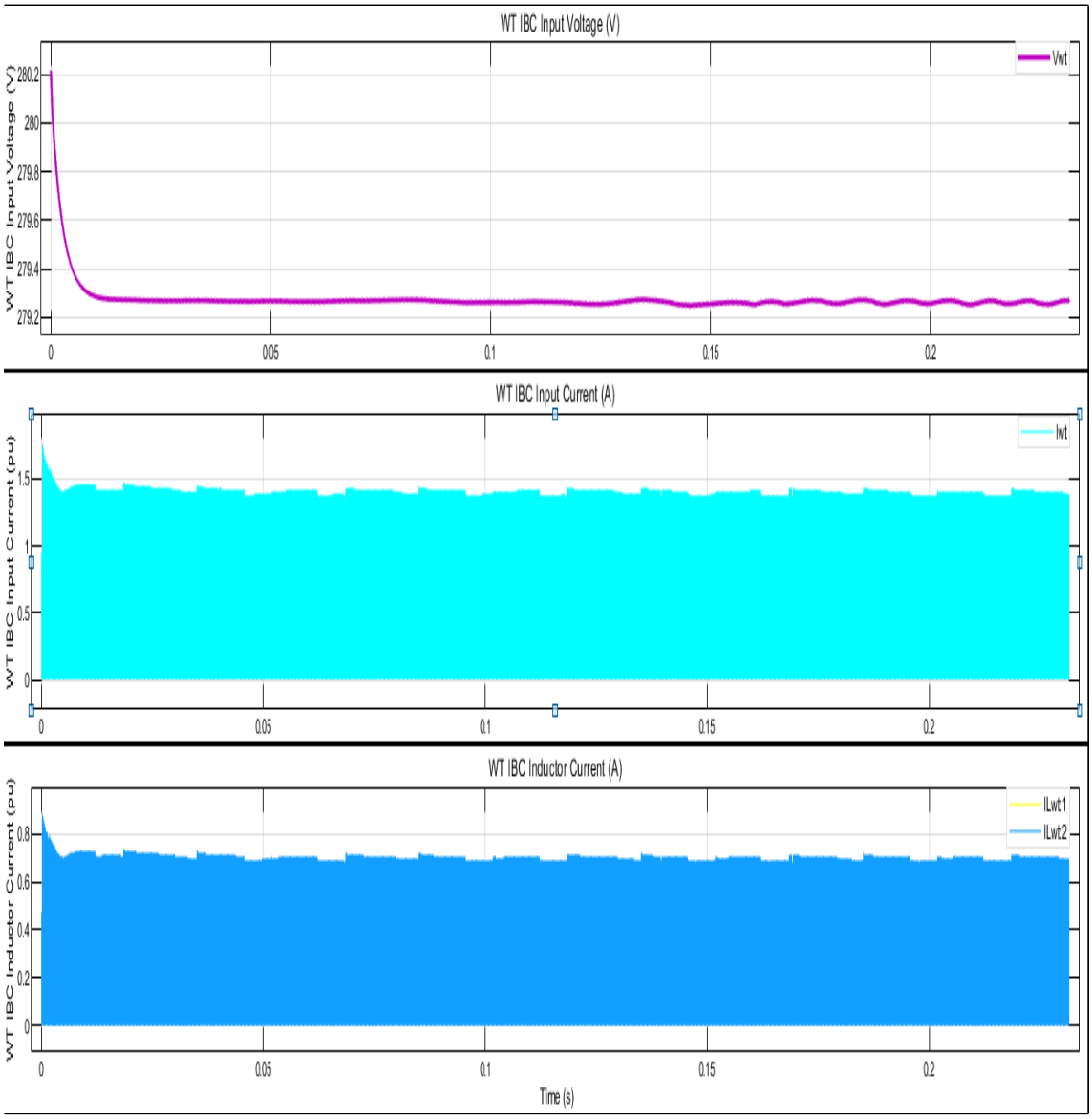

Figure 4.32: WT IBC Inputs in the Proposed Microgrid with SSR-P&O in Case Study Model

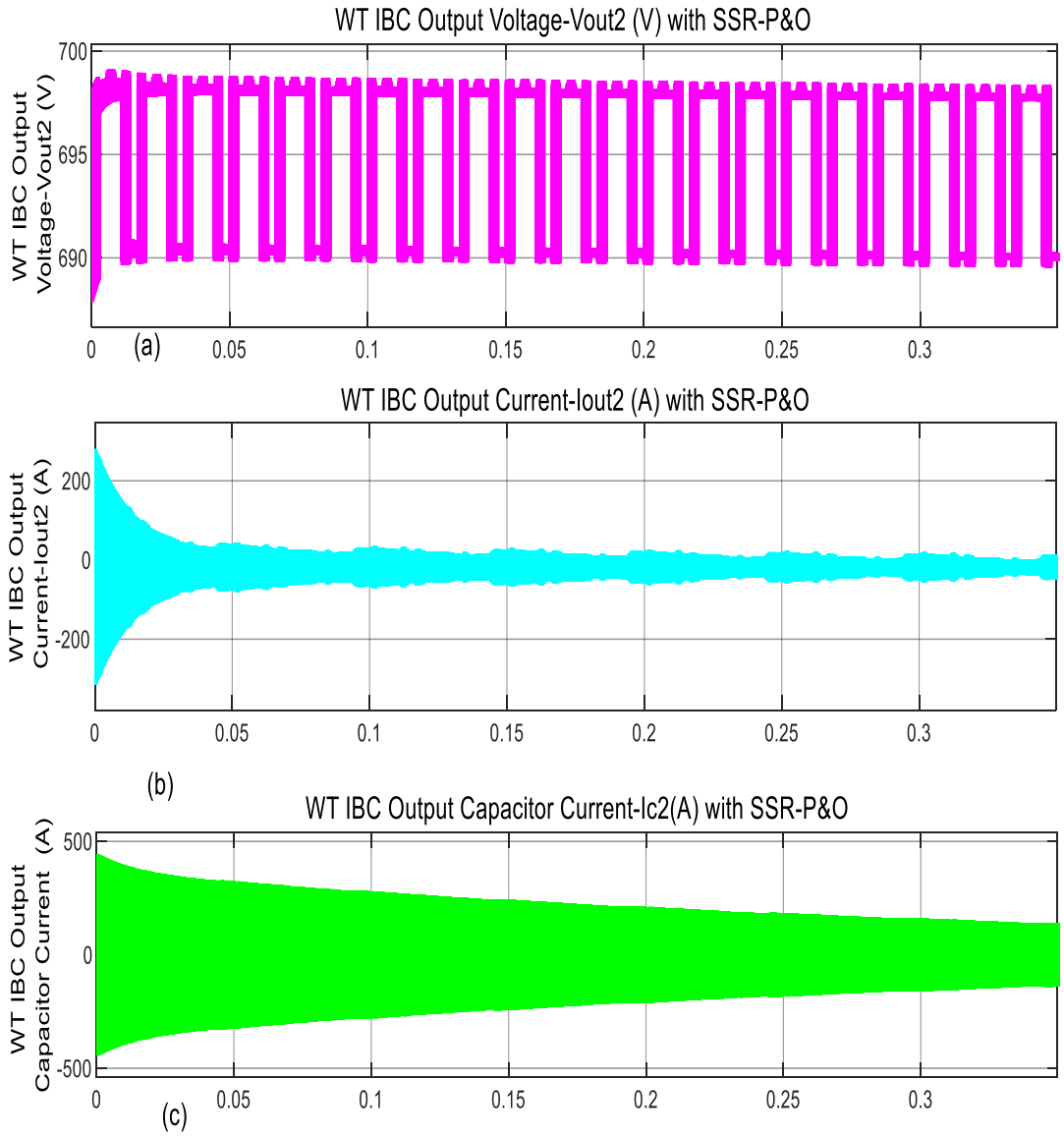

Figure 4.33: WT IBC Outputs with SSR-P&O in Case Study Model

When the SSR-P&O controller is replaced with the GA-ANFIS, the voltage, and current transient profiles are much refined, as shown in Figure 4.34 and Figure 4.35. This validates the ability of GA-ANFIS algorithm to tackle the nonlinear dynamics of the microgrid system.

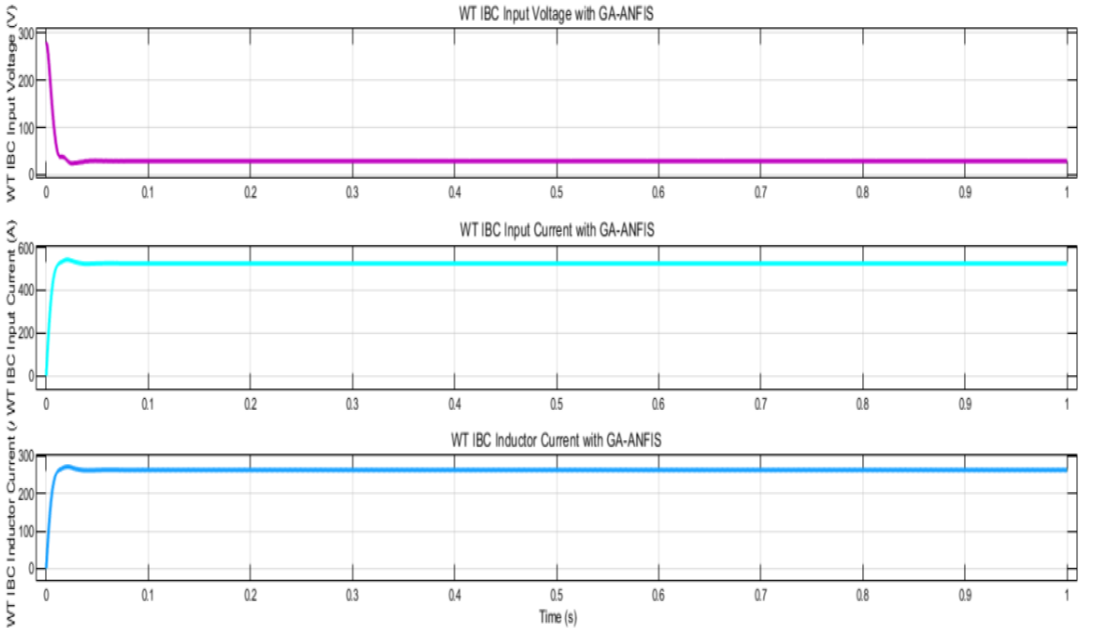

Figure 4.34: WT IBC Inputs in the Proposed Microgrid with GA-ANFIS in Case Study Model

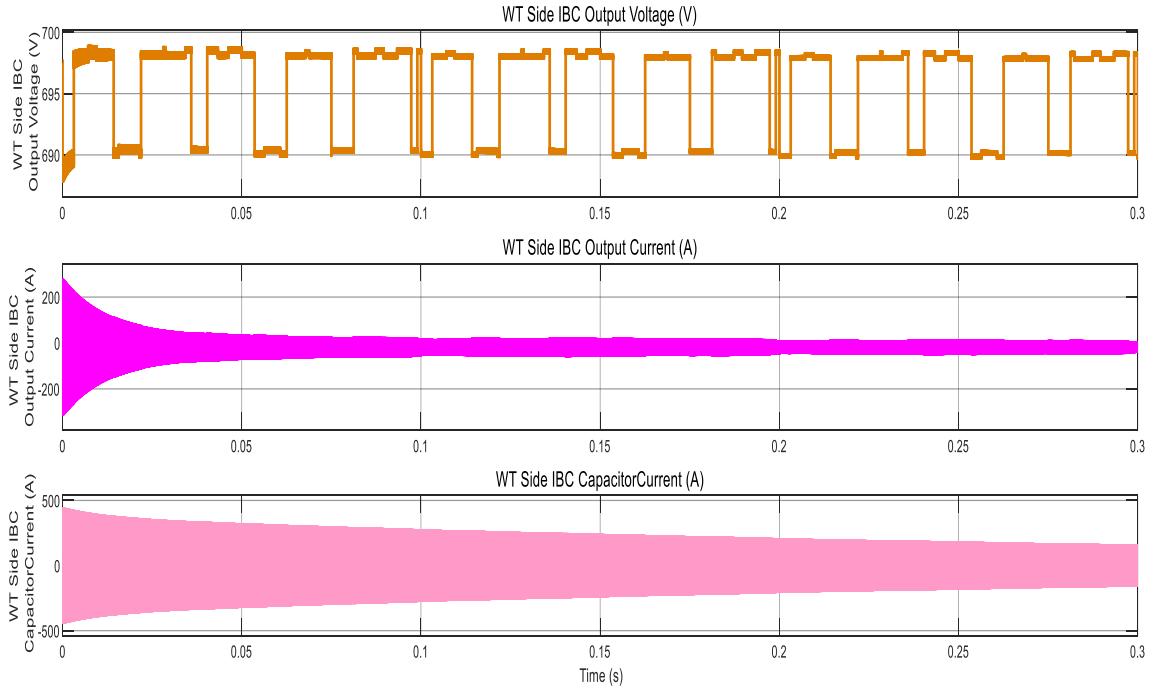

Figure 4.35: WT IBC Outputs with GA-ANFIS in Case Study Model

4.2.4 PV BESS Output Voltage, SoC, and Current in the Proposed Microgrid

The study used interleaving/paralleling technique in which two IBC converters have been used, one on the PV and the other on the Wind Turbine side. For uniformity, the study used two BESS systems one for the PV and the other for the PV but the two have been interconnected. The same applies to the inverters. Figure 4.36 and Figure 4.37 show the PV side BESS and WT side BESS Output Voltage, SoC, and Current with SSR-P&O in the proposed microgrid. The voltage is regulated to within $680 \pm 15\ V$ for PV side BESS and $695 \pm 5\ V$ for WT BESS but with notable distortions at about 8%.

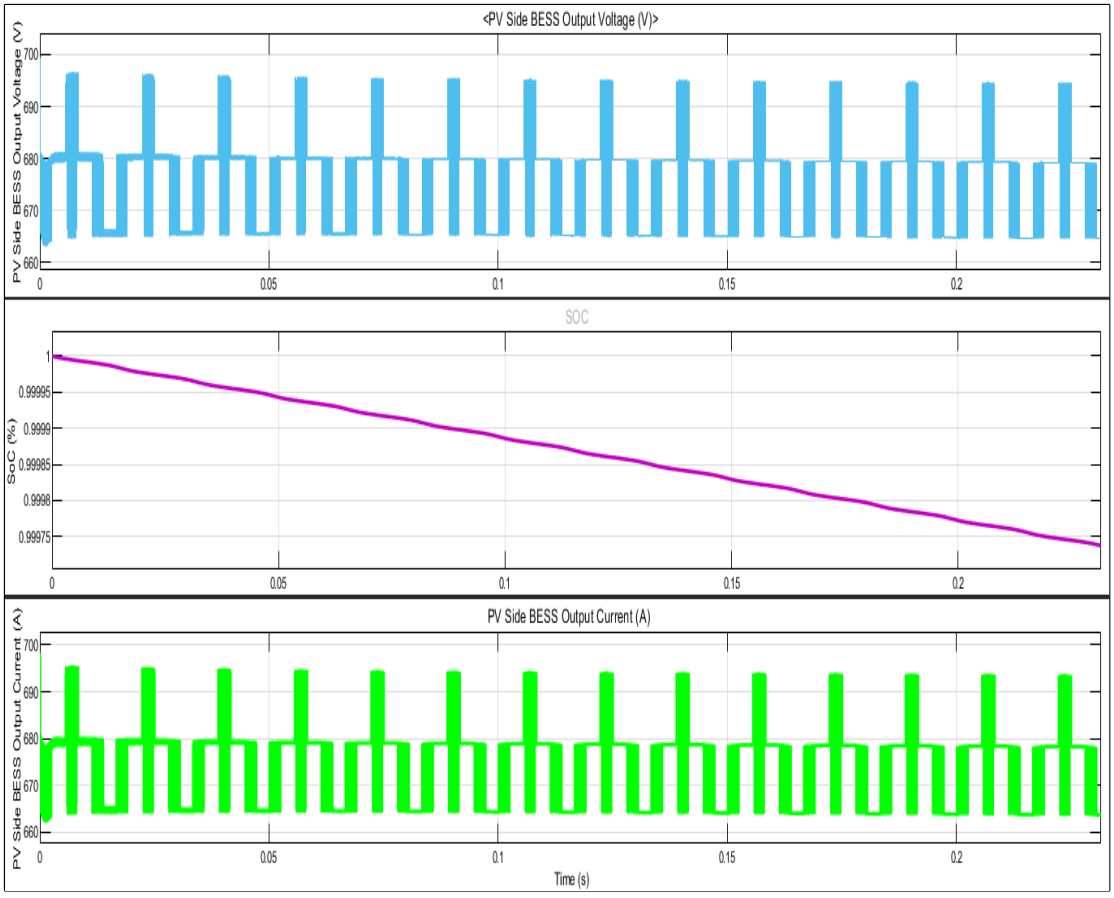

Figure 4.36: PV BESS Outputs with SSR-P&O in Case Study Model

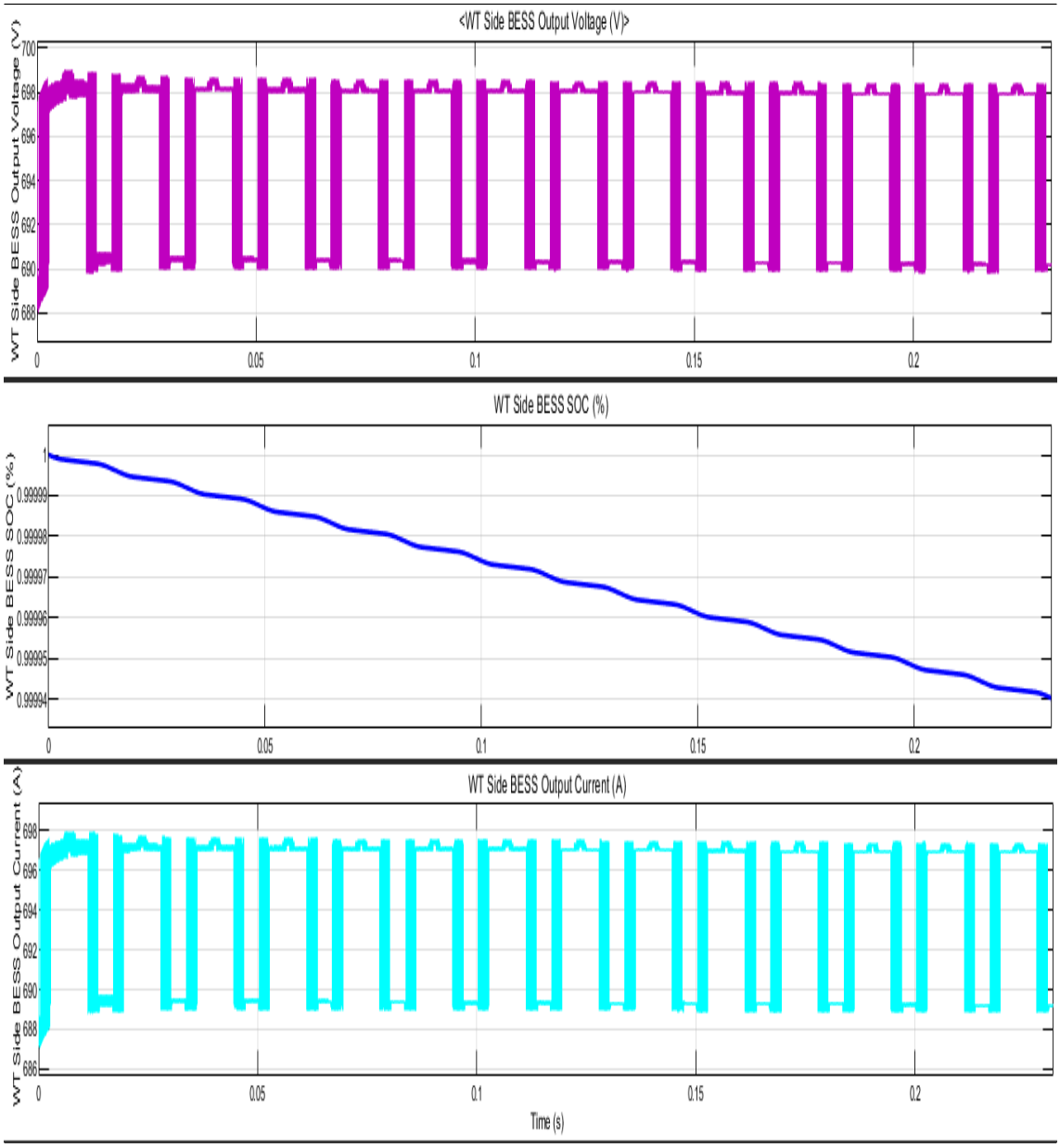

Figure 4.37: WT BESS Outputs with SSR -P&O in Case Study Model

Figure 4.38 and Figure 4.39 depict the PV side BESS and WT side BESS Output Voltage, SoC, and Current with the GA-ANFIS controller in the proposed Microgrid. The voltage is regulated to within $680 \pm 15\ V$ for PV side BESS and $695 \pm 5\ V$ for WT BESS with fewer distortions, faster rise times, and settling times.

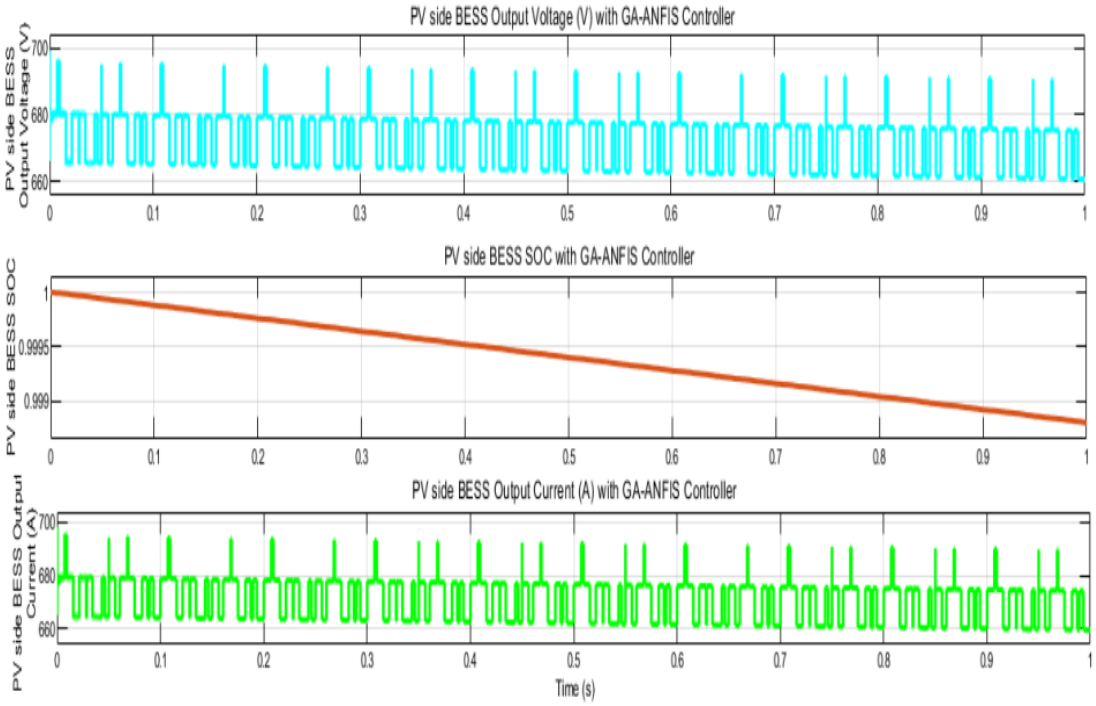

Figure 4.38: PV Side BESS Outputs with GA-ANFIS

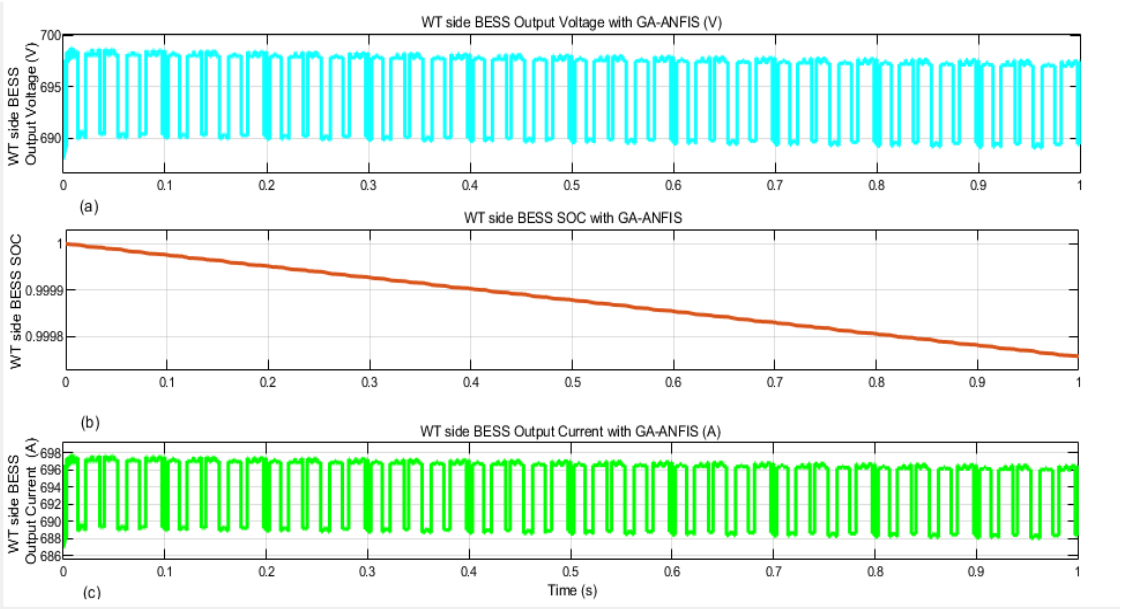

Figure 4.39: WT Side BESS Outputs with GA-ANFIS

4.2.5 Inverter Output and Power Output to Residential Loads in the Proposed Microgrid

Figure 4.40 and Figure 4.41 present the filtered three-phase voltage outputs of the proposed inverter on the PV and Wind Turbine sides, respectively, with the SSR-P&O algorithm. The voltage profiles in Figure 4.40 and Figure 4.41 (a) and (b) depicted a similar form with the SSR-P&O MPPT for both the PV side and WT side inverters and were kept at about $450 \pm 25\ V$ with ripples of 5.5%.

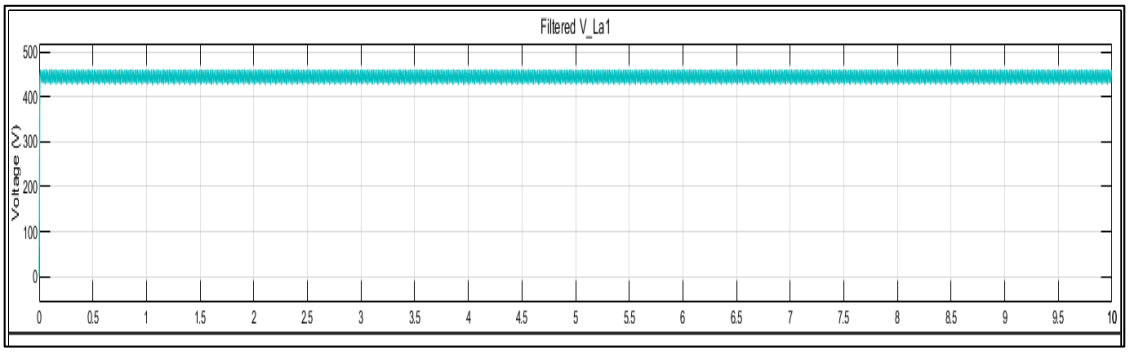

(a)

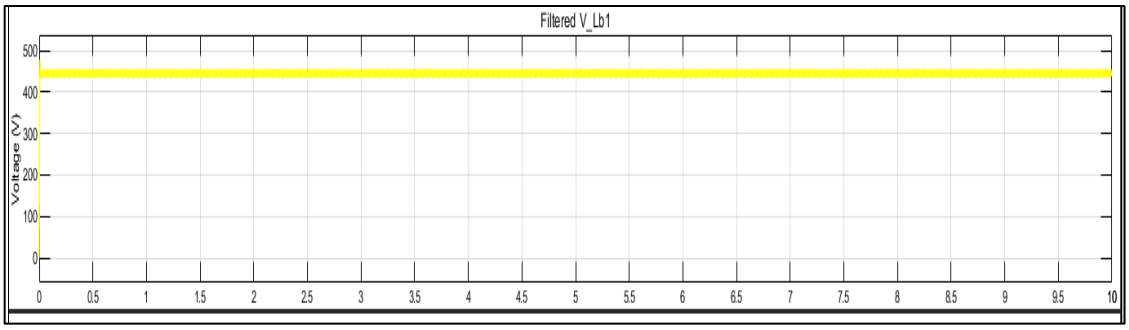

(b)

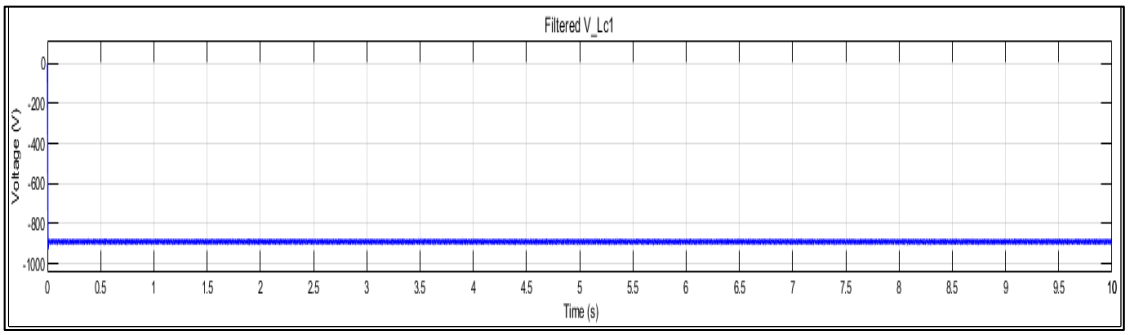

(c)

Figure 4.40: PV Side Inverter 1 Output Line Voltages with SSR-P&O

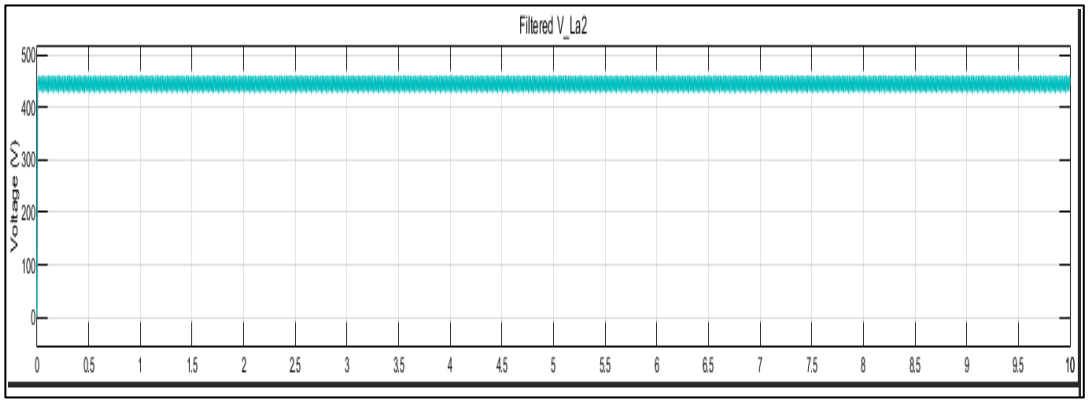

(a)

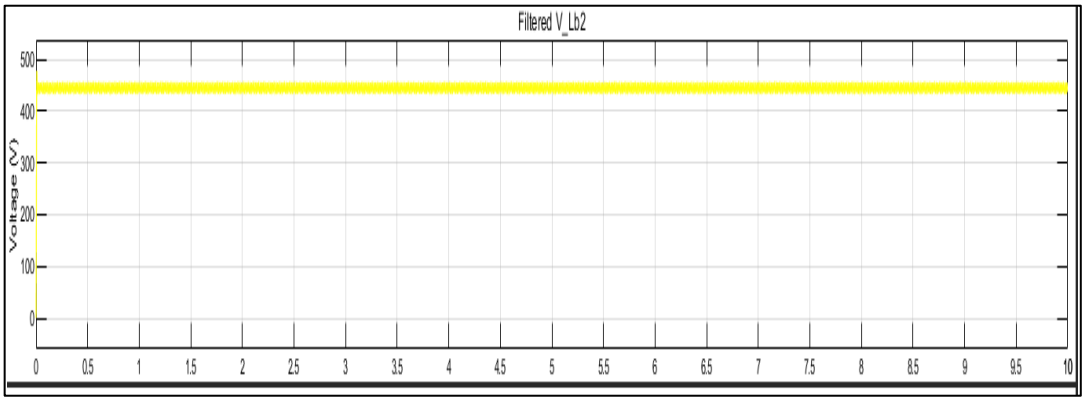

(b)

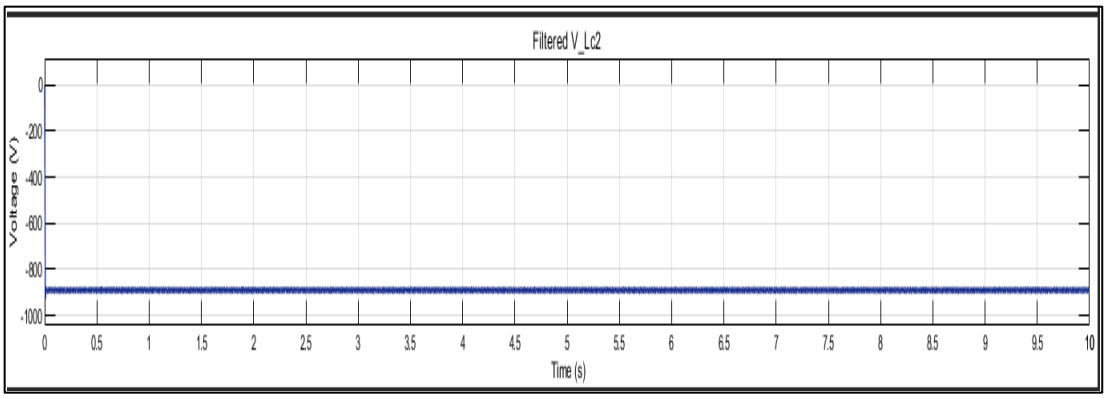

(c)

Figure 4.41: Wind Turbine Side Inverter 2 Output Line Voltages with SSR-P&O: (a) Red Phase; (b) Yellow Phase; (c) Blue Phase

The voltage recorded in part (c) in both cases turned out to be negative and larger than the rest at $-900 \pm 25\ V$ with a ripple content of 3.0%.

The GA-ANFIS controller plots are shown in Figure 4.42 and Figure 4.43, which depict better transient responses in terms of reduced settling time, rise time, and overshoots compared to the SSR-P&O algorithm.

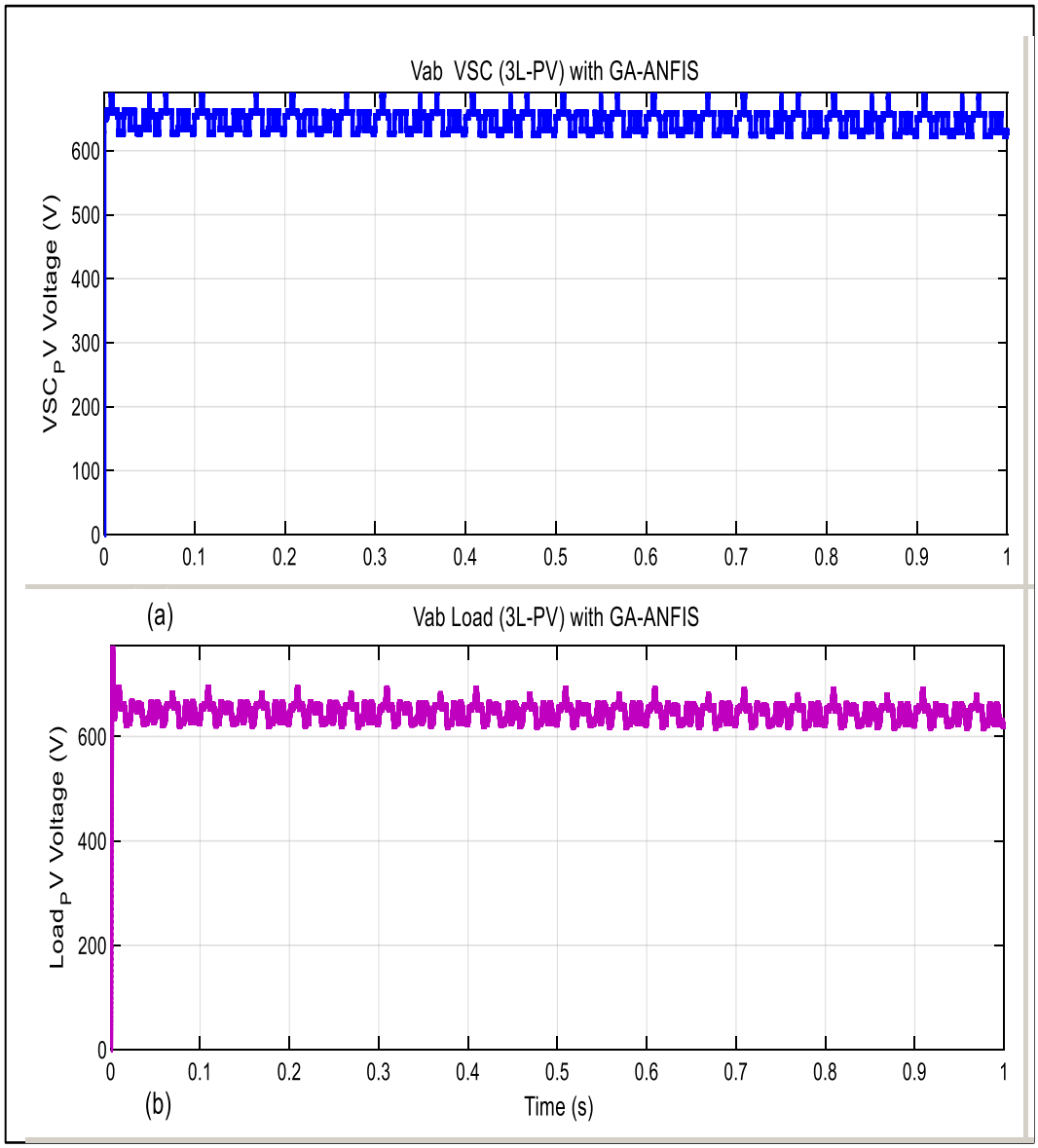

Figure 4.42: PV Side Inverter 1 Performance with GA-ANFIS: (a) VSC Output Line Voltage; (b) Load voltage

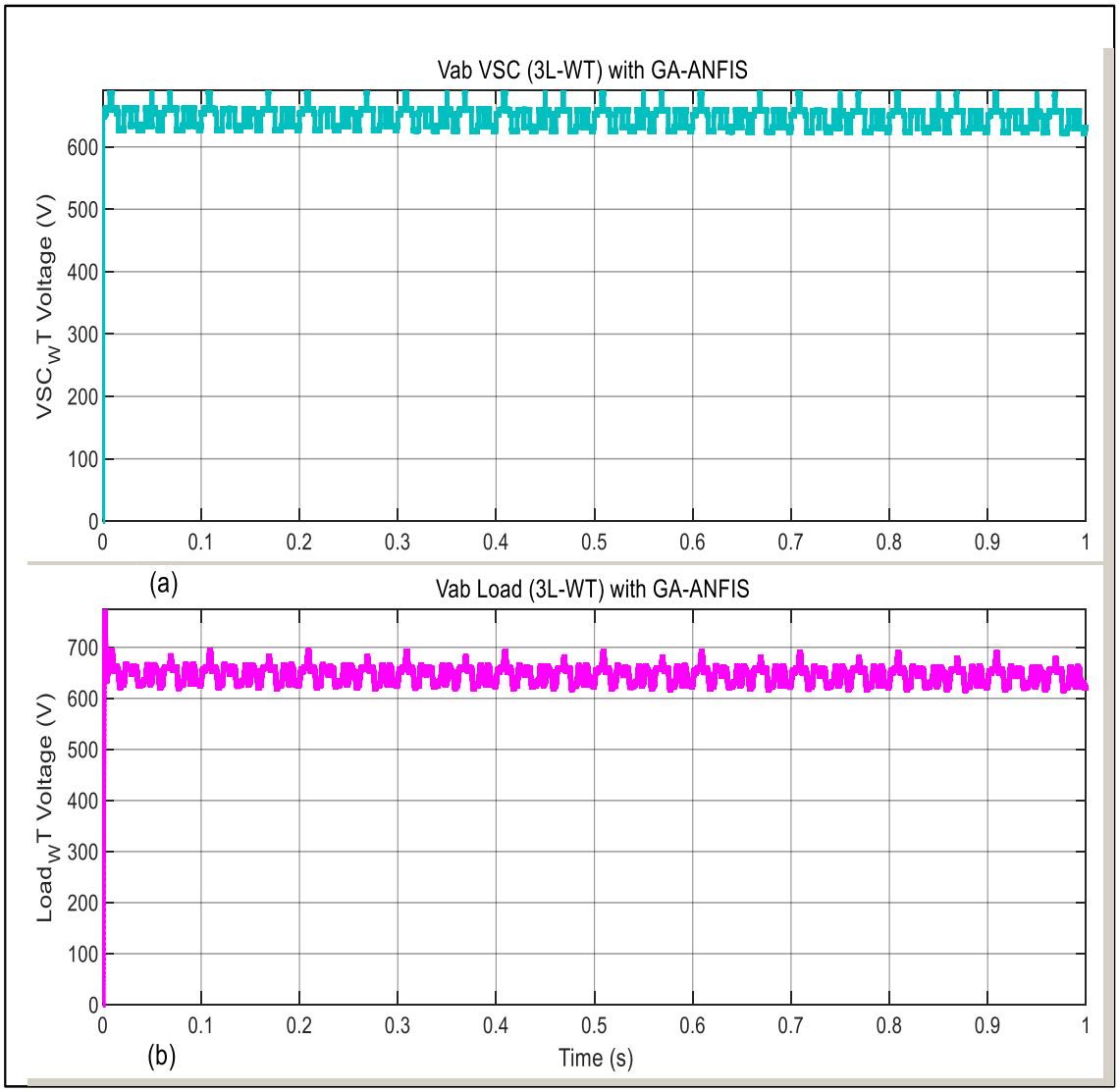

Figure 4.43: WT side Inverter 2 Performance with GA-ANFIS: (a) VSC Output Line Voltage; (b) Load Voltage

Figure 4.44 shows the power output to loads in the proposed microgrid with the GA-ANFIS controller, which confirms the generation and supply of well-regulated voltage that meet the transient voltage response requirements. The BESS power is close to the total power at about $4.5 \times 10^5\ W$ with the wind power experiencing some disturbance before stabilizing at about $0.2 \times 10^5\ W$ while the Solar power is at about $0.1 \times 10^5\ W$.

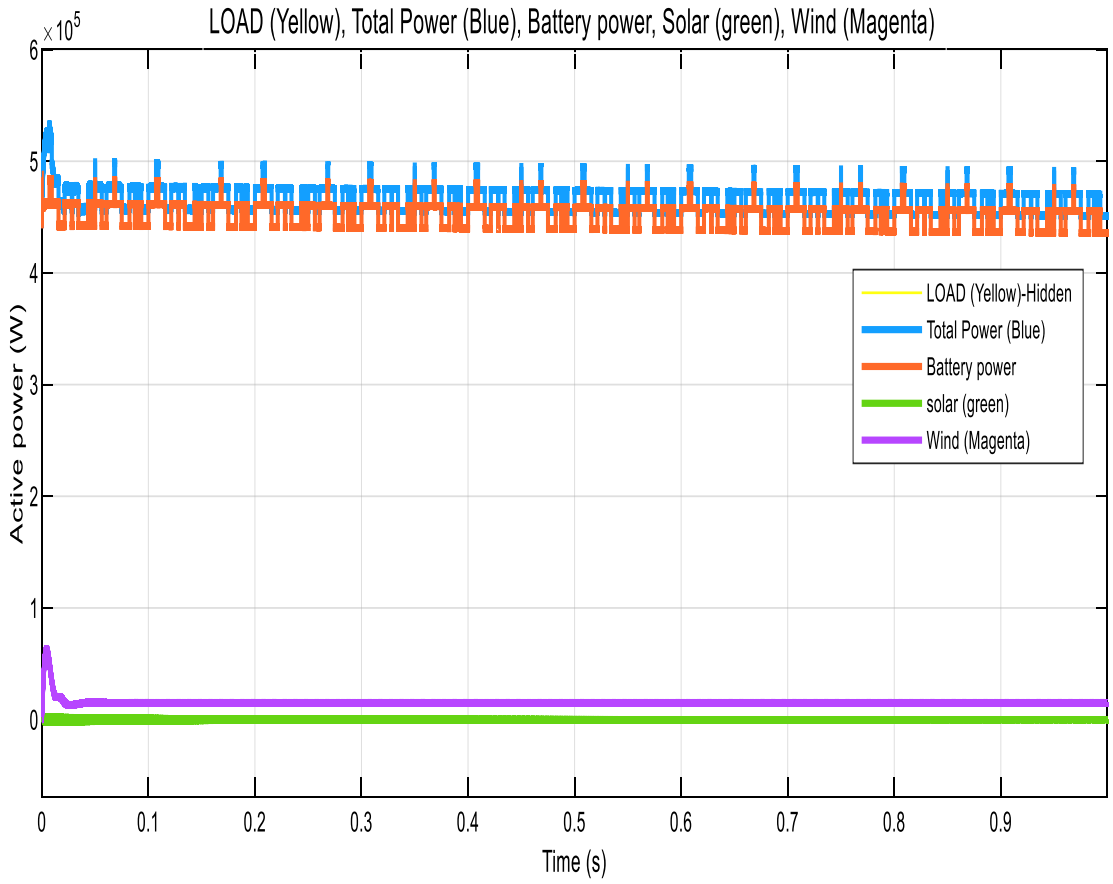

Figure 4.44: Power Outputs to Loads with GA-ANFIS

4.3 Performance of the Model Predictive Controller (MPC)

This section corresponds to the specific objective number three and four presents the results obtained from the experiments run with the MPC algorithm for BESS charging and discharging and voltage regulation in the microgrid.

4.3.1 BESS Microgrid Plant Inputs and Outputs with MPC Controller

Figure 4.45 shows the normalized BESS Microgrid Plant inputs with MPC Controller viewed in terms of the Manipulated Variable (MV), Measured Disturbance (MD) and Unmeasured Disturbance (UD).

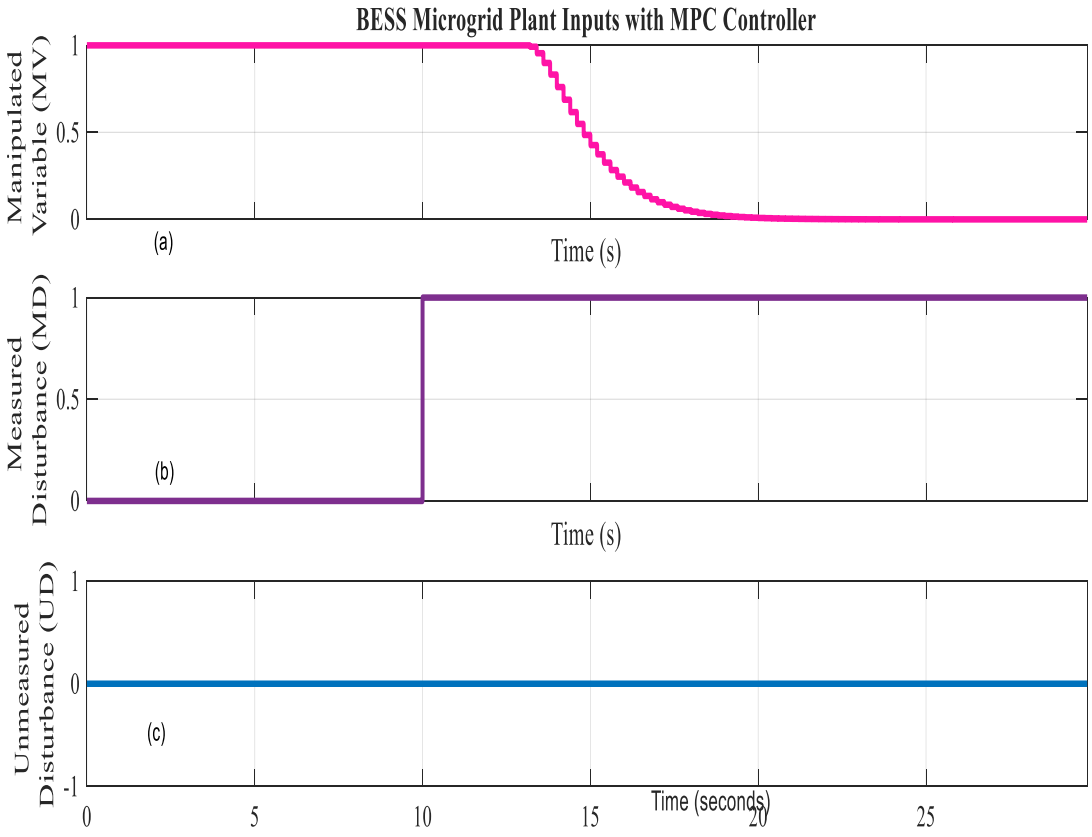

Figure 4.45: BESS Microgrid Plant Inputs with MPC Controller: (a) MV), (b) MD) and (c) UD

From Figure 4.45, it is observed that the Unmeasured Disturbance (UD) has been kept at zero since at this point in the MPC controller design, it is not necessary to specify any unmeasured disturbance, usually represented by noise. The introduction of the Measured Disturbance (MD) at time $t = 10s$ since the MPC controller started operating causes the MPC controller to respond by reducing the Manipulated Variable (MV), to a minimum

(zero) in a time period of $5s$. This is necessary so that the MPC controller can reject the disturbance and allow the microgrid plant output voltage to remain or track the reference point (voltage). The non-normalized values of MV and MD applied in the microgrid Case Study model have been updated using values adapted in simulation.

Figure 4.46 depicts the MPC controller voltage tracking performance when tested with the unit step input voltage considered to represent the BESS Microgrid plant output at the initial controller design stage.

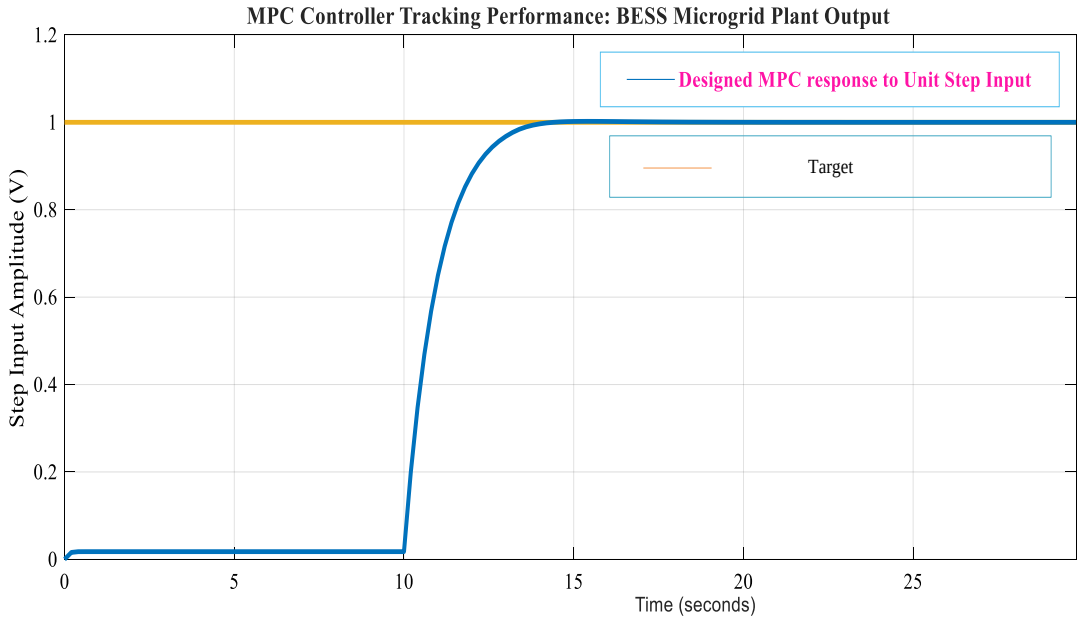

Figure 4.46: BESS Microgrid Plant Output with MPC Controller

Figure 4.46 shows that when the Measured Disturbance (representing a change in the voltage or generated power levels in the microgrid) occurs at time $t = 10s$, the MPC controller quickly tracks the BESS output charging/discharging voltage. This is done with the following transient response outcome: a rise time of $t_r = 2.5s$, settling time of $t_s = 3.5s$ and percentage overshoot, $M_p = 0\%$.

4.3.2 MPC Controller Performance with Variations from the PV Side

The performance of the designed MPC controller was also tested on the PV-Wind microgrid model amid voltage variations caused by the intermittency in the PV output, and the results are shown in Figure 4.47.

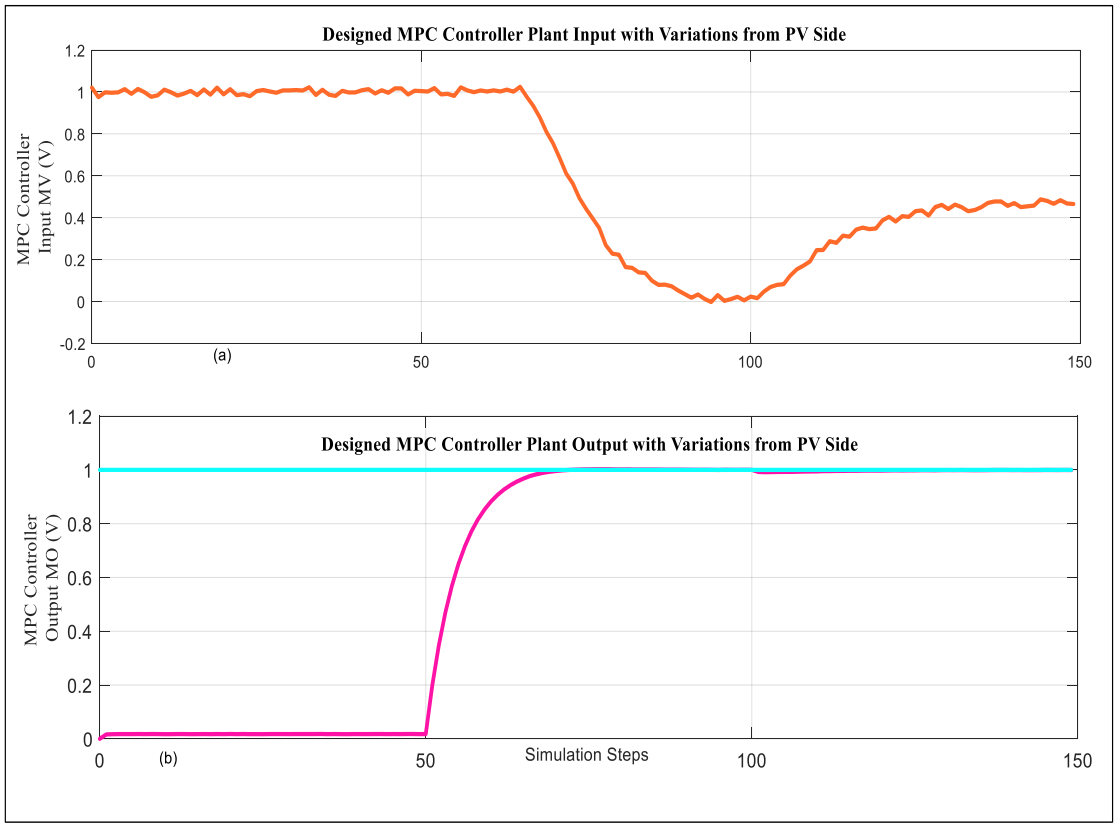

Figure 4.47: The Designed MPC Controller Combined Performance with Variations from the PV Side (a) Inputs and (b) Outputs

Figure 4.47 shows that when a drop in the unit step input voltage occurs around the 75th simulation step, representing a drop in the microgrid voltage from the PV side, the transient response of the MPC controller is as desired. As before, the MPC controller quickly tracks the desired reference voltage, which is set at the unit step for testing the controller's transient performance. The MPC controller in this case registered a transient response outcome with a rise time of $t_r = 3s$, settling time of $t_s = 4s$ and percentage

overshoot, $M_p = 0\%$. The change in PV input represents a change in the microgrid model at the 75th simulation step. Still, owing to its prediction capability, the MPC controller starts its action at the 50th simulation step in anticipation of a change in the model. One simulation step was assumed to translate into a time period of one second.

4.3.3 MPC Controller Performance with Variations from the WT Side

Figure 4.48 shows the MPC Controller Performance with variations from the WT Side. As noted in Figure 4.48, the MPC controller step input drops drastically to near zero at about 12 simulation steps, representing a sudden decrease in the WT voltage and power due to variations in wind. The MPC controller, at this point, responds quickly to this disturbance, achieving the desired step output of $1V$ with a transient response profile having a rise time of $t_r = 3.5s$, settling time of $t_s = 4.5s$ and percentage overshoot, $M_p = 0\%$. In addition, when a sudden drop in the unit step input voltage (to zero) occurred around the 50th simulation step, followed by a quick gain in the value (to about 80% of the final value), the MPC controller still recovered as required. However, this time, an overshoot of $M_p = 25\%$ has been registered before the controller attained the final value again within $t_s = 4s$. When the perturbations are repeated at around the 100th simulation step but now starting with a sudden rise in voltage followed by a sudden drop, the MPC controller recorded an undershoot of about $M_p = -20\%$. These perturbations are reminiscent of the sporadic changes in the WT voltage due to variations in wind speed. The MPC controller performs very well in rejecting such disturbances, always returning the controlled variable, the desired microgrid voltage, to the set operating point. This proves the voltage tracking performance of the designed MPC controller.

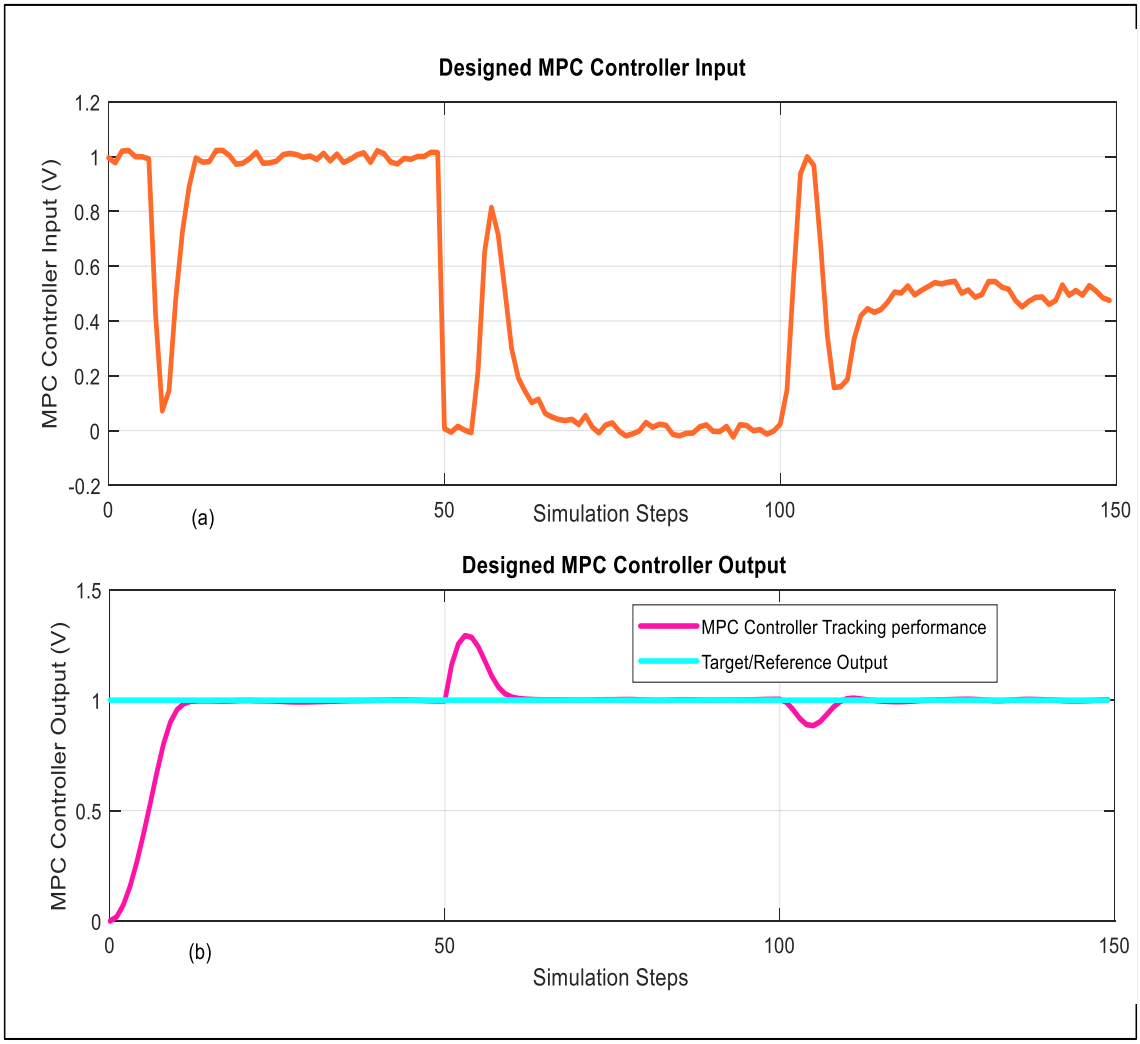

Figure 4.48: The Designed MPC Controller Combined Performance with Variations from WT Side (a) Inputs and (b) Outputs

4.3.4 MPC Controller Performance in the Microgrid Transfer Function

Figure 4.49 shows the response of the MPC Controller in comparison with the PID and GA-ANFIS in the Microgrid TF Model (MTFM). The MPC controller performance with the Microgrid Dynamic State Space Model (MDSSM) is also shown. The performance of the MPC, PID, and GA-ANFIS controllers on the Microgrid TF Model (MTFM) and

Microgrid Dynamic State Space Model (MDSSM) was tested with other voltage changes, and the voltage regulation capabilities obtained were as summarized in Table 4.2.

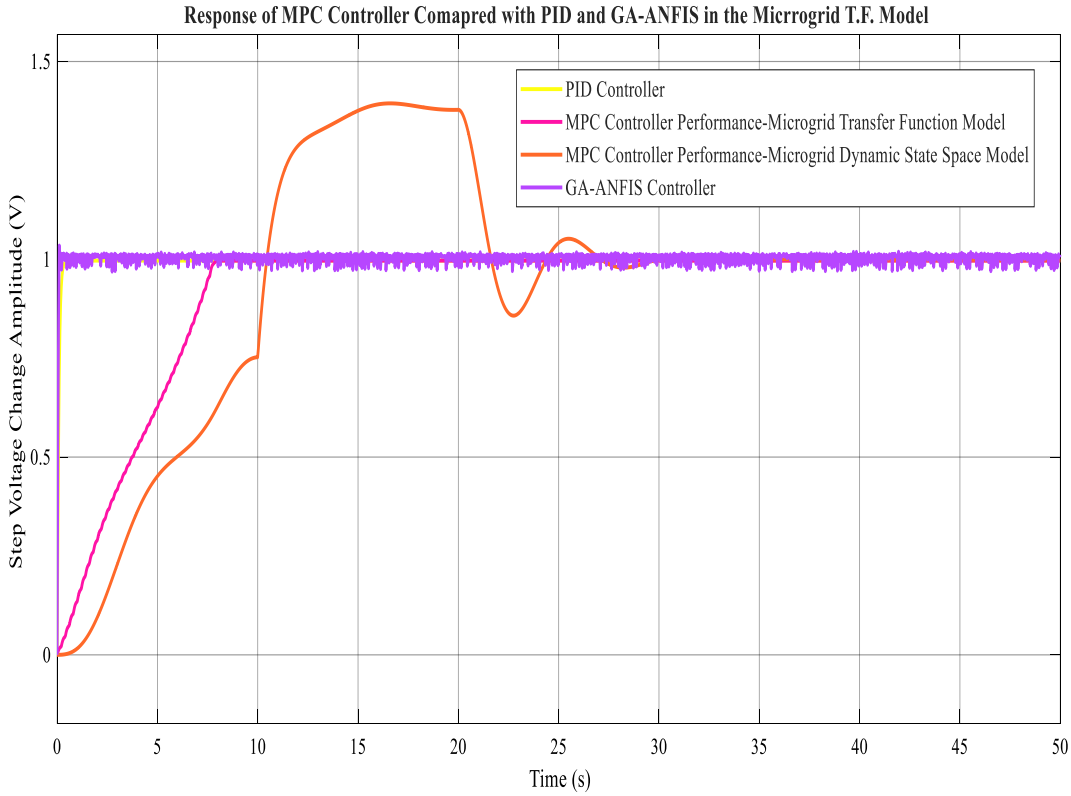

Figure 4.49: Response of MPC Controller Compared with PID and GA-ANFIS in the Microgrid TF Model

From Table 4.2, the MPC controller based on the Microgrid Transfer Function Model (MTFM) recorded a rise time of 6.40 s, settling time of 7.00 s, and overshoot of 0.00% compared to the 0.36 s, 0.76 s, and 0.00%, respectively, realized with the PID controller. At the same time, the GA-ANFIS controller registered a rise time of 0.10 s, settling time of 0.16 s, and overshoot of 3.52% compared to the 10.20 s, 30.00 s, and 36.00%, respectively, realized with the MPC controller based on the Microgrid Dynamic State Space Model (MDSSM). The increased computation time of the MPC controller is evident in terms of a higher rise time and settling times than both the PID controller and the GA-ANFIS controller.

Table 4.2: Summary of Simulink Case Study Model Results with Voltage Variations

Step Input	PID			GA-ANFIS			MPC (MDSSM)			MPC (MTFM)		
	t_r	t_s	M_p	t_r	t_s	M_p	t_r	t_s	M_p	t_r	t_s	M_p
(V)	(s)	(s)	$(\%)$	(s)	(s)	$(\%)$	(s)	(s)	$(\%)$	(s)	(s)	$(\%)$
1	0.3	0.8	0.0	0.1	0.2	3.5	10.0	30.0	35.0	6.0	7.0	0.0
2	0.4	0.7	0.0	0.1	0.2	3.5	9.5	30.5	36.0	6.5	6.8	0.0
3	0.3	0.8	0.0	0.1	0.1	3.6	11.0	28.5	37.0	7.0	7.2	0.0
4	0.4	0.7	0.0	0.1	0.2	3.5	10.0	30.0	36.5	6.0	7.1	0.0
5	0.4	0.8	0.0	0.1	0.1	3.5	10.5	31.0	35.5	6.5	7.0	0.0
Avg.	**0.36**	**0.76**	**0.00**	**0.10**	**0.16**	**3.52**	**10.20**	**30.00**	**36.00**	**6.40**	**7.00**	**0.00**

The MPC controller based on the MDSSM recorded the worst performance, proving that an MPC controller's tuning has to be done separately for both the MDSSM and the MTFM. Based on this, the MPC controller tuning parameters obtained with the MTFM have been utilized as a basis for the MPC controller applied to the simulated SIMULINK model case study.

The MPC controller using the MTFM responds better than the GA-ANFIS controller regarding zero overshoot in voltage regulation. However, the GA-ANFIS controller responds better than the MPC controller regarding reduced rise and settling times. The GA-ANFIS controller has been optimized using the renewable energy power generation data-driven approach, giving it prediction capabilities based on artificial intelligence. On the other hand, the MPC controller utilizes the model-based prediction dependent on the chosen prediction horizon, control horizon, model horizon, and the dynamic behavior of the microgrid system.

4.3.5 PV Side and WT Side IBC Outputs with the MPC Controller in the Case Study

Figure 4.50 shows the PV Side IBC Output voltage and Current with the MPC controller in the Case Study Model when the generated PV power varies.

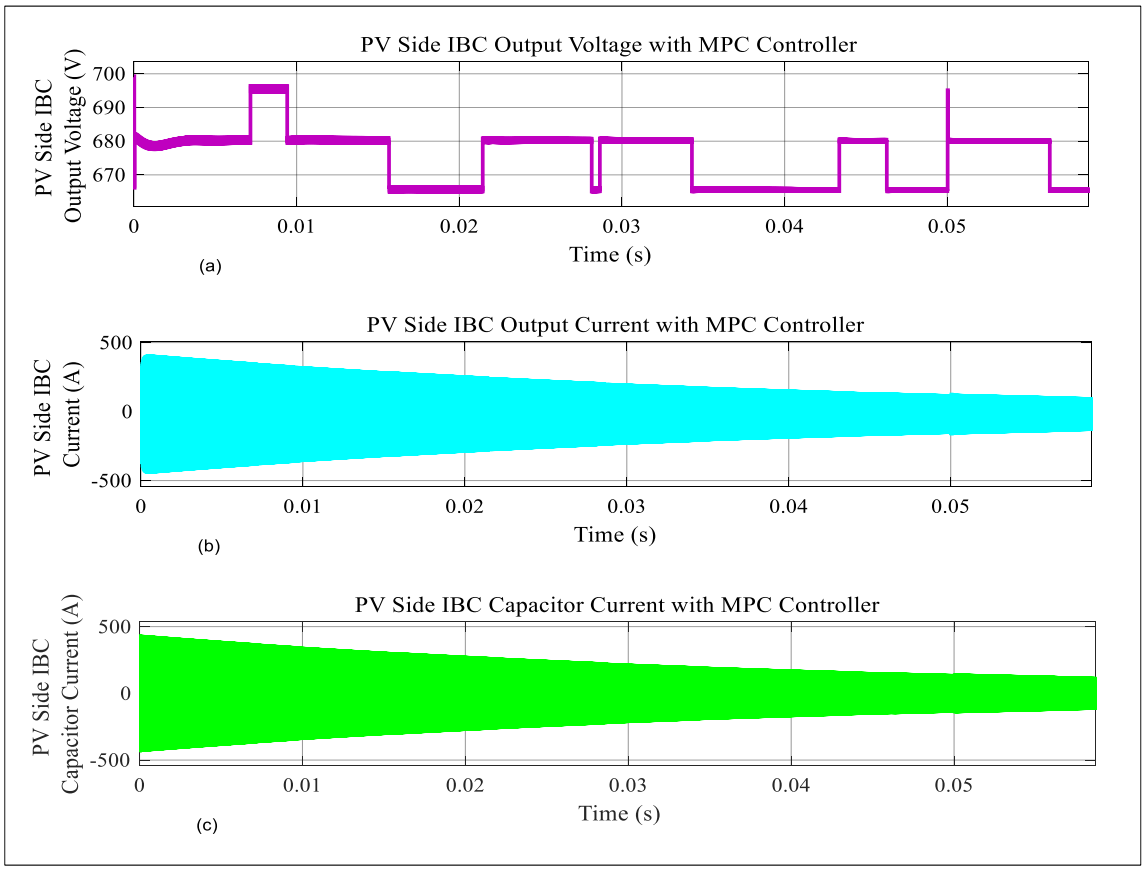

Figure 4.50: PV Side IBC Output Voltage and Current with MPC Controller in Case Study Model: (a) Output Voltage, (b) Output current and (c) Capacitor Output current

From Figure 4.50, The MPC controller regulated the IBC output voltage to within $\pm 2.35\%$ of the nominal $680V$, i.e., $680 \pm 16\,V$ (compared with $\pm 2.21\%$, i.e., $680 \pm 15\,V$ obtained with GA-ANFIS and $\pm 8.00\%$ with PID controller). The performance of the MPC controller in regulating PV side IBC voltage is well within the required $\pm 5\%$. The rise time and settling time of the MPC controller were $6.00\,s$ and $7.00\,s$, respectively, giving a better voltage profile than the PID controller. Despite zero overshoot on the linearized MTFM, the PID controller depicted deteriorated performance with an overshoot of 8.00% when applied to the simulated microgrid case study, where it couldn't cope with

the non-linearities. However, the MPC controller depicted an increased computation time compared with the GA-ANFIS and PID controllers.

Figure 4.51 depicts the WT side IBC Output Voltage and Current with the MPC controller in the proposed Microgrid.

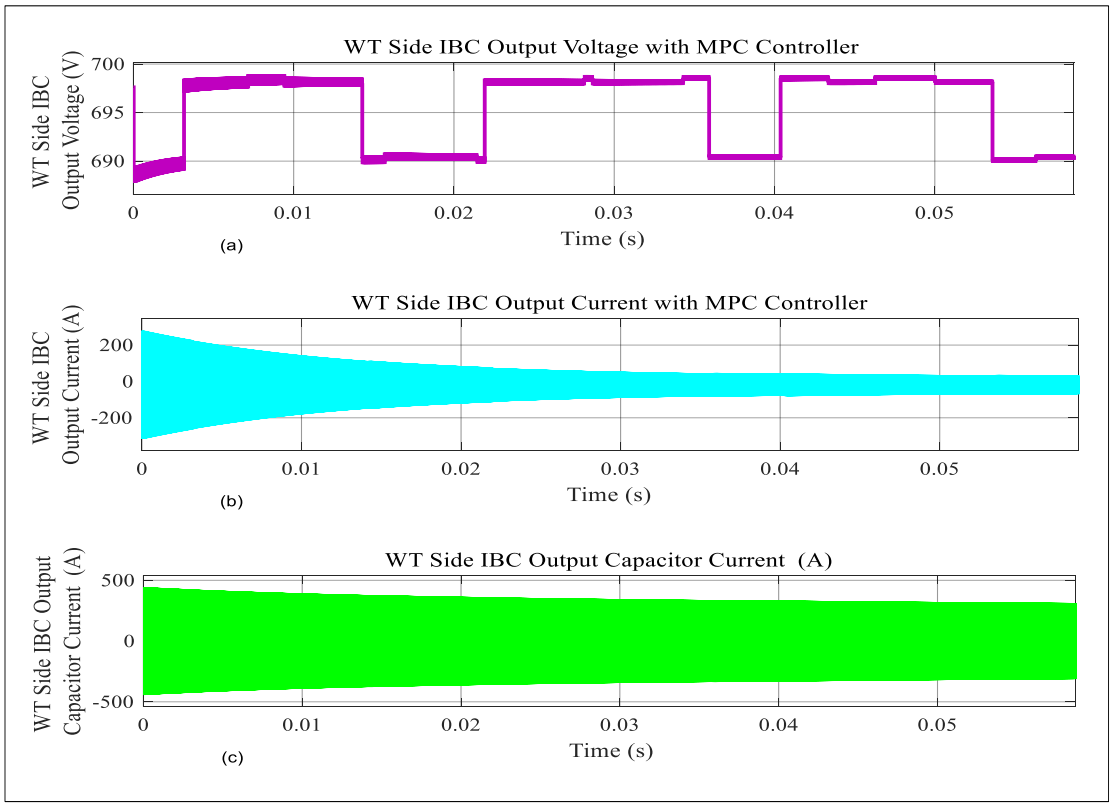

Figure 4.51: WT Side IBC Output Voltage and Current with MPC Controller in Case Study Model: (a) Output voltage, (b) Output Current and (c) Capacitor Output current

The voltage is regulated to within $\pm 2.35\%$ of the nominal $680V$, i.e., $680 \pm 17\,V$ (compared with $\pm 2.21\%$ i.e., $680 \pm 15\,V$ obtained with GA-ANFIS and $\pm 8.00\%$ with PID controller).

4.3.6 PV Side and WT Side BESS Response with the MPC Controller in the Case Study

Figure 4.52 and Figure 4.53 depict the PV side BESS and WT side BESS Output Voltage, SoC, and Current with the MPC controller in the proposed Microgrid.

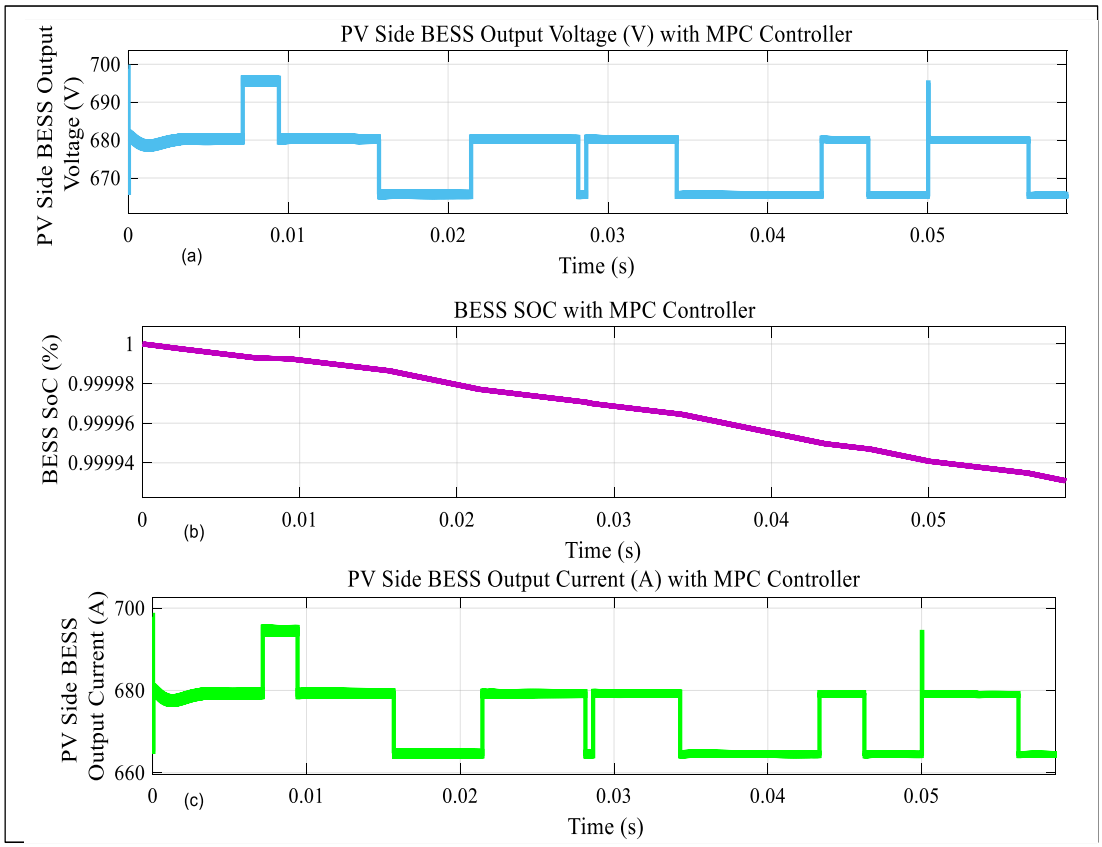

Figure 4.52: PV Side BESS Response with MPC Controller (a) Output Voltage (b) SoC and (c) Output Current

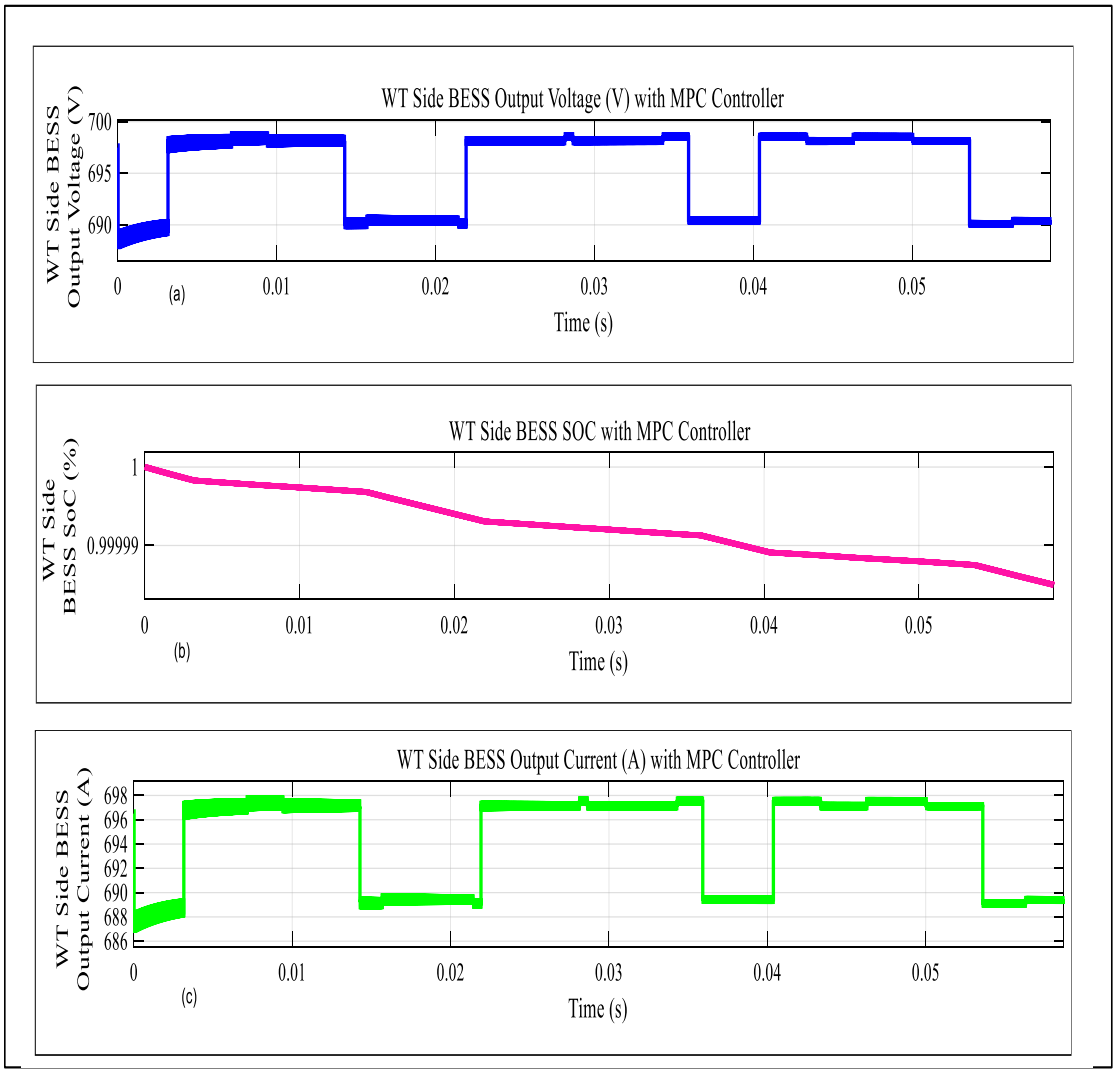

Figure 4.53: WT Side BESS Response with MPC Controller (a) Output Voltage (b) SoC and (c) Output Current

The voltage is regulated to within $680 \pm 16\ V$ for PV side BESS and $680 \pm 17\ V$ for WT BESS w, with fewer distortion but increased rise times and settling times than the PID or GA-ANFIS controller. This is because of the increased computation burden of the MPC controller. The MPC controller, therefore, is suitable for regulating BESS charging and discharging voltage to within $\pm 2.35\%$, which is well within the desired standard of $\pm 5.00\%$.

4.3.7 Inverter and Load Response with the MPC Controller in the Case Study

Figure 4.54 presents the inverter Output and Load voltage on the PV side with the MPC controller in the Microgrid under study.

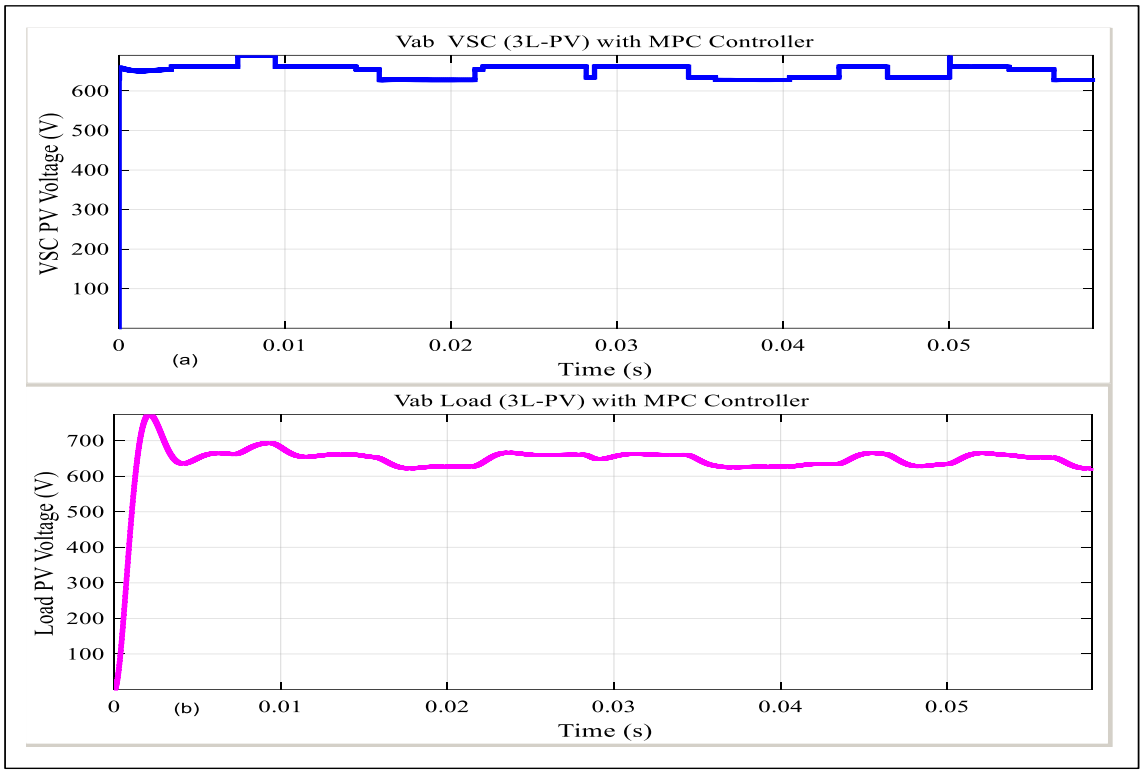

Figure 4.54: Inverter Output Voltage and Load Voltage on the PV Side with the MPC Controller in the Microgrid under Study: (a) VSC PV Inverter Output voltage (b) Load PV Voltage

The VSC PV voltage with the MPC controller are much more refined than those obtained with the SSR-P&O as well as the PID controller. The voltage rises almost in zero time to $650 \pm 25\ V$ representing a ripple content of about 3.8%. The load voltage with the MPC controller recorded an overshoot of about 15% and settled to $600 \pm 20\ V$ within $0.01\ s$.

Figure 4.55 presents the Inverter Output voltage and Load voltage on the WT side with the MPC controller in the Microgrid under study. These plots depicted similar patterns to those obtained with the VSC on the PV side.

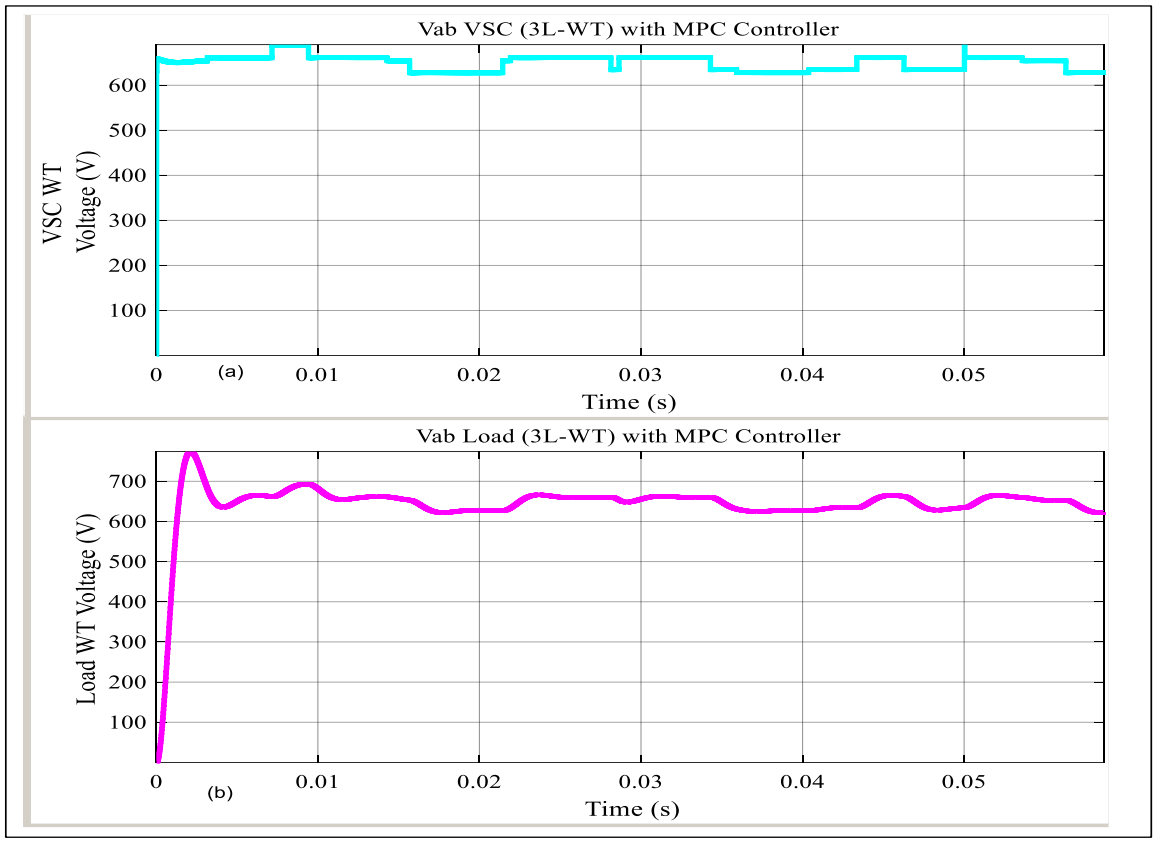

Figure 4.55: Inverter Output Voltage and Load Voltage on the WT Side with the MPC Controller in the Microgrid under Study: (a) VSC WT Inverter Output Voltage (b) Load WT Voltage

The voltage profiles are much more refined than those obtained with the PID or SSR-P&O controllers due to the ability of the MPC controller to handle the BESS charging and discharging dynamics.

Figure 4.56 shows the active power supplied to the loads by the BESS in the proposed microgrid with the MPC controller, which confirms the delivery of well-regulated voltage that meets the transient voltage response requirements.

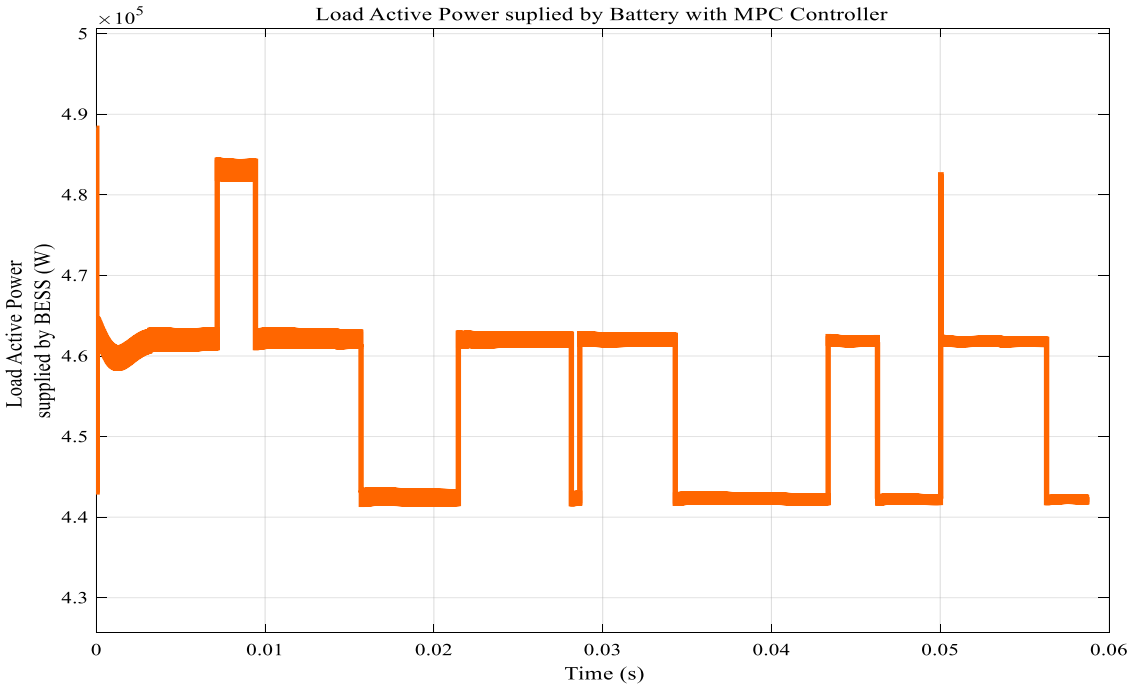

Figure 4.56: Active Power Supplied to the Loads by the BESS in the Proposed Microgrid with the MPC Controller

4.4. Discussions

4.4.1 Computation Time of the GA-ANFIS and MPC Controllers

The GA-ANFIS and MPC controllers depicted increased computation time when applied to the microgrid voltage regulation problem. The MPC controller designed presented computation time and computation burden that is about ten times that the PI(D) controller presented in the microgrid. Also, compared with the GA-ANFIS controller, the MPC

controller computation time is about five times higher. The complexity of the microgrid model, the non-linear dynamics associated with the PV and Wind generation sources, and the BESS contributed significantly to the increased computation time of both the GA-ANFIS and MPC controllers. For the GA-ANFIS controller, the size of the data set used in training, the optimization of ANFIS by the GA, and the training by the hybrid algorithm (combined back propagation and gradient descent) further contributed to increased computation time and burden. The increased computation time of the GA-ANFIS controller was addressed by performing dimension reduction on the data set used, designing some aspects of the GA-ANFIS controller offline before deploying on the model, and carefully selecting epochs and desired error limits.

In the case of the MPC controller, the following factors contributed to increased computation time and computation burden:

1. The microgrid control problem considered in this study is quite complex, involving the regulation of microgrid voltage and battery charging and discharging voltage.
2. The optimization algorithm chosen based on the quadratic programming and the complex objective function proved computationally intensive.
3. The increased size of the PV-Wind microgrid system also contributed to increased computation time due to increased model complexity.
4. The prediction horizon and control horizon lengths selected also added to the MPC controller's increased computation time and burden.
5. The sampling time of the microgrid system and the MPC controller also contributed to the increased computation.
6. The hardware and software computation platform also influence the computation time of the MPC controller.

The increased computational time of the MPC controller has been addressed through the following techniques:

1. Careful selection and trade-off in the final values of prediction horizon and control horizon lengths.
2. Proper selection of Solver options available in MATLAB & SIMULINK (used the quadratic solver).
3. Reduction in model complexity via pole-zero cancellation in the TF modeling and by carefully selecting the operating points in the SIMULINK case study.
4. Careful sampling time selection for the system and the MPC controller.
5. Simulations were carried out using a computer with core i7 7^{th} generation processors that allowed for parallel computing and processing.

4.4.2 Criteria for Selection of Simulation Time

The simulation time used in the simulations conducted ranged between $0.0\ s$ and $10\ s$. The exact simulation time slots used for the microgrid case study model and transfer functions simulations were selected based on a combination of factors. These include: microgrid design parameters, optimization of the microgrid system components, solver requirements, sampling time selection for the microgrid system, real-time simulation requirements and the modifications to the existing simulation environment. The choice of simulation time was also guided by the type of simulation, the trends noted in the literature and the industry standards.

On the type of simulation in MATLAB/SIMULINK, a choice can be made from any of the following: Normal, Accelerator, Rapid accelerator, Software in the loop (SIL), Processor in the loop (PIL) and External. All the simulations conducted were under the type of simulation designated as Normal which agreed with the selected simulation time to yield quick and valid results. For the solver selection, the Variable-step mode was selected instead of the Fixed-step with the maximum solver step size set to $0.04\ s$. This provided for greater flexibility and improved results in the simulations. The solver used was the ode23tb (Stiff/TR-BDF2) instead of discrete which does not allow for continuous states or the automatic solver selection (auto) which does not give the designer the opportunity to choose their own preferred solver.

4.4.3 Discussion of the Case Study Model Results with Voltage Variations

The results presented in sections 4.2 and 4.3 addressed the fourth specific objective. In these sections, the designed GA-ANFIS-MPC-based multilevel MCS has been split into two parts and applied to the off-grid Photovoltaic-Wind Hybrid generation microgrid system case study. The first part is the GA-ANFIS primary controller used mainly as a microgrid voltage regulator concerning controlling microgrid voltage amid variations introduced by the PV and WT generation sources.

The second controller is a secondary MPC controller whose main function is to regulate the microgrid's voltage to ensure safe BESS charging and discharging. The performance of the GA-ANFIS-MPC controller has been evaluated compared to the SSSR-P&O and Proportional plus Integral (PI) and or Proportional plus Integral plus Derivative (PID) control method. Table 4.3 shows a numerical summary of Simulink case study model results obtained with the SSR-P&O, GA-ANFIS, and MPC controllers amid voltage variations in the microgrid.

From Table 4.3, the GA-ANFIS controller recorded the best performance, followed by the MPC controller. The GA-ANFIS controller has a rise time of $0.10\ s$, settling time of $0.14\ s$, and overshoot of 3.54% compared to the $0.26\ s$, $0.46\ s$, and 7.6%, respectively, realized with the SSR-P&O controller.

Table 4.3: Summary of Simulink Case Study Model Results with Voltage Variations

Voltage Variation	SSR-P&O			PID			GA-ANFIS			MPC		
	t_r	t_s	M_p	t_r	t_s	M_p	t_r	t_s	M_p	t_r	t_s	M_p
(V)	(s)	(s)	(%)	(s)	(s)	(%)	(s)	(s)	(%)	(s)	(s)	(%)
1	0.2	0.4	7.5	0.3	0.8	0.0	0.1	0.2	3.5	6.0	7.0	0.0
5	0.3	0.5	7.0	0.4	0.7	0.0	0.1	0.2	3.5	6.5	6.8	0.0
10	0.3	0.5	8.0	0.3	0.8	0.0	0.1	0.1	3.6	7.0	7.2	0.0
15	0.2	0.4	7.5	0.4	0.7	0.0	0.1	0.1	3.5	6.0	7.1	0.0
20	0.3	0.5	8.0	0.4	0.8	0.0	0.1	0.1	3.6	6.5	7.0	0.0
Avg.	**0.26**	**0.46**	**7.60**	**0.36**	**0.76**	**0.00**	**0.10**	**0.14**	**3.54**	**6.40**	**7.00**	**0.00**

The MPC controller recorded a rise time of $6.40\ s$, settling time of $7.00\ s$, and overshoot of 0.00% compared to the $0.36\ s$, $0.76\ s$, and 0.00%, respectively, realized with the PID controller. However, the increased computation time of the MPC controller is notable in terms of a higher rise time and settling times than both the PID controller and the GA-ANFIS controller. The MPC controller responds better than the GA-ANFIS controller regarding reduced overshoot in voltage regulation. However, the GA-ANFIS controller responds better than the MPC controller regarding reduced rise and settling times.

The results obtained in this study with GA-ANFIS were also compared to those published in literature by Sibtain et al. (Sibtain et al., 2021), who proposed a Genetic Algorithm optimized fractional order PID (GA-FOPID) controller for PV-wind grid-connected system. The PV-wind modeling used a multi-control approach to obtain a $100\ kW$ grid-tied power system contrary to this study, which is specific to a $10\ kW$ off-grid PV-wind microgrid. In one of the operating points reported, the GA-FOPID recorded power tracking performance with a settling time of $0.034\ s$ and overshoot of 0.0% and voltage tracking performance with a rise time of $0.025\ s$, settling time of $0.05\ s$ and overshoot of 8.0%. The results proved the positive contributions of the GA algorithm.

By comparing the results obtained between the Transfer Function model and the Simulink case study model using the developed control algorithms, it was observed that even with changes in the plant model, there was no significant impact on the control system performance of the GA-ANFIS and the MPC controller. However, the SSR-P&O controller depicted degraded transient performance due to its struggles in handling nonlinearities. The GA-ANFIS's superior performance is attributed to the training of the ANFIS and its optimization with GA, which injected the right level of intelligence to the controller, thereby improving its time domain transient response characteristics and tolerance to changes in microgrid plant nonlinear dynamics.

The MPC controller utilizes the model-based prediction over the prediction horizon. In addition, it utilizes the Kalman state estimator to act as an observer to estimate any non-measurable states of the microgrid system during the dynamic behavior of the microgrid system. Therefore, the ability of GA-ANFIS and MPC to work for the voltage regulation and BESS charging/discharging control in the microgrid system despite non-linearities and other dynamic changes in its operating conditions has been verified. However, the MPC controller requires an accurate mathematical model of the microgrid, contrary to the GA-ANFIS controller, which can substitute model inefficacies with the accuracy and dependability of the training and testing data.

4.4.4 Impact of Implementation of the Designed GA-ANFIS-MPC Controller on a Practical Microgrid

The results obtained with the Simulink case study model using the developed control algorithms have been taken to emulate a practical microgrid. The practical case study model successfully proved the positive contributions of the GA algorithm to the ANFIS to create the GA-ANFIS hybrid controller. The GA-ANFIS controller introduces some levels of overshoot and increased computation time in a practical microgrid compared with the conventional controllers like the SSR-P&O and PID controllers. However, the GA-ANFIS controller compensates the challenges of a practical microgrid such as power quality issues in terms of voltage variations and other disturbances/inefficacies with the

accuracy, dependability and the intelligence. This is owing to its ability to learn from the PV-Wind generation data and other data sets generated from the simulations conducted.

The results also proved the strength of the MPC controller in dealing with the microgrid BESS charging/discharging dynamics. The main impacts of deploying the designed MPC controller in a practical microgrid are the increased computation time and burden, the need for linear conditions to prevail in the microgrid, and its lack of learning ability. Both GA-ANFIS and MPC controllers also require more powerful computers and hardware for execution, leading to increased complexity and cost of the microgrid system.

CHAPTER FIVE

CONCLUSIONS AND RECOMMENDATIONS

This Chapter presents the main conclusions drawn from the study undertaken alongside the recommendations entailing technical and industrial extensions of the work. The first section 5.1 concludes that the first objective of developing a PV-wind microgrid was successfully achieved as was the case with the second objective of designing the primary GA-ANFIS. It also confirms that the third objective of designing the secondary MPC controller and the fourth objective of validating the GA-ANFIS-MPC controller were successfully achieved. The last section 5.2 outlines the recommendations stemming from the study undertaken.

5.1 Conclusions

5.1.1. Conclusion from the Performance of the Baseline Controllers

The PID controller and SSR-P&O controller were used to validate the performance of the GA-ANFIS and MPC controllers on a TF microgrid model and the SIMULINK case study model by tracking the desired voltage outputs. This research section has found that the GA-ANFIS approach and the MPC controller provided the best performance in terms of rise time, settling time and overshoot compared to the conventional PID and SSR-P&O controller. The SSR-P&O and the PID controllers depicted serious struggles in the presence of non-linearities which led to increased settling times and overshoots compared with the GA-ANFIS and the MPC controllers.

5.1.2 Conclusions from the GA-ANFIS primary Controller Performance

From the comparison made between the performance of the GA-ANFIS approach to that of the SSR-P&O and PID, it has been concluded that the GA-ANFIS is better than the SSR-P&O and PID. The conclusion is corroborated by the fact that the GA-ANFIS

controller recorded a lower rise time, settling time and overshoot compared with the SSR-P&O and PID controller.

For instance, the GA-ANFIS registered a settling time of $0.15\,s$, and overshoot of 3.5% compared to the $0.45\,s$ and 7.5% for the SSR-P&O controller and, $0.76\,s$ and 8.0% for the PID controller respectively. The GA-ANFIS controller also significantly reduced the microgrid's voltage and current distortions. The results verified the functionality of the hybrid PV-Wind interleaved model and the GA-ANFIS controller as meeting all the specifications of the voltage regulation in the microgrid system.

5.1.3 Conclusion from the Results Obtained with the MPC Controller

The MPC controller turned out to be a successful secondary controller to the designed microgrid. The ability of the MPC controller to provide improved BESS charging and discharging has been proven according to the results and the performance obtained. For example, the MPC controller when applied to microgird case study for BESS charging/discharging, has been able to achieve a rise time of $6.00\,s$ and overshoot of 2.35% compared to the $0.36s$ and 8.00%, respectively, obtained with the PID controller.

At the same time, the increased computation time of the MPC controller is prevalent in terms of a higher rise time and settling times than both the SSR-P&O and PID controller. This notwithstanding, the MPC controller has been suggested as a complementary secondary controller in the microgrid. It helps to regulate the microgrid voltage during utilization of the BESS by dealing with the dynamics of BESS charging/discharging.

5.1.4 Overall Conclusions from the Deployment of the Designed GA-ANFIS-MPC Controller

The first specific objective of developing a microgrid model produced a working model that allowed for testing the designed GA-ANFIS-MPC controller. The second specific objective of designing the GA-ANFIS primary controller was successfully achieved as

has been proven from the performance of the GA-ANFIS controller. The GA-ANFIS controller while regulating the generation voltage, recorded the best performance compared with the SSR-P&O and the PID controllers, the baseline controllers. The SSR-P&O and PID controllers depicted degraded transient performance due to their struggles in handling nonlinearities. The GA-ANFIS's superior performance is attributed to the training of the ANFIS and its optimization with GA, which injected the right level of intelligence into the controller.

The MPC controller utilizes the model-based prediction to anticipate changes in the microgrid dynamic conditions and regulate the voltage accordingly. The MPC controller on the other hand emerged as the best controller compared with the SSR-P&O and the PID controllers to tackle the BESS charging and discharging, which is a highly non-linear process with challenging dynamics. However, the MPC controller showed an increased computation time and a higher rise time and settling times than the PID controller and the GA-ANFIS controller. The MPC controller is seen to have a better response than the GA-ANFIS controller regarding reduced overshoot in voltage regulation. However, the GA-ANFIS controller responds better than the MPC controller regarding reduced rise and settling times. The results obtained with the Transfer Function model and the Simulink case study model using the developed control algorithms proved the positive contributions of the GA algorithm to the ANFIS to create the GA-ANFIS hybrid controller. In addition, the results also proved the strength of the MPC controller in dealing with the microgrid BESS charging/discharging dynamics. The main shortcomings of the MPC controller are the increased computation time and burden, the need for an accurate mathematical model of the microgrid, and the lack of learning ability.

On the contrary, the GA-ANFIS controller substituted model inefficacies with the accuracy and dependability of the training and testing data used in the study. The GA-ANFIS controller also injected the intelligence into the Multi-level Microgrid Control System (MMCS) owing to its ability to learn from the PV-Wind generation data and other data sets generated from the simulations conducted.

Lastly, the GA-ANFIS controller does not need an accurate mathematical model and works comfortably in a non-linearity presence. Thus, the overall objective of this study to develop an MMCS for a Photovoltaic-Wind Hybrid generation system based on the GA-ANFIS-MPC controller has been achieved. Therefore, this study has proven the ability of the GA-ANFIS and MPC controller, called the GA-ANFIS-MPC MCS controller, to work for the voltage regulation and BESS charging/discharging control in the microgrid system.

5.2 Recommendations

This study has developed a $10kW$ Photovoltaic-Wind microgrid system in MATLAB/SIMULINK environment and incorporated the designed GA-ANFIS-MPC MCS to solve voltage regulation problems in a microgrid. In general, power quality in a microgrid is calculated in terms of the disturbances, i.e., transients, voltage sags and swells, over-voltages and under-voltages, outage, harmonic distortion, voltage notching, flicker, and electrical noise. This study used the microgrid voltage to measure power quality and was regulated, tracked, and kept within the specified limits using the designed GA-ANFIS-MPC controller. The study's limitations are that the GA-ANFIS-MPC controller was applied to an off-grid microgrid and that no micro-hydroelectric power sources were incorporated into the microgrid model. Thus, the impact of the connection of the microgrid to the grid or the addition of micro-hydroelectric power sources on the controller performance has not been investigated.

Moreover, the Transfer Function microgrid model is limited to the small-signal-based pole-zero cancellation to simulate a nearly linear microgrid. Although frequency influences the microgrid's performance, it is beyond the scope of the study undertaken. It has been assumed to have been regulated by the inverter at 50Hz on the AC side. Frequency regulation and the extension of the controller to other power grids such as mini-grids, is proposed as future work since the controller specifications will have to be adjusted or scaled accordingly. The deployment of the developed GA-ANFIS-MPC controller on an actual microgrid in real-time is also recommended as future work.

REFERENCES

Alwal, L., K. Kihato, P., & I. Kamau, S. (2016). Design of Neuro-Fuzzy System Controller for DC ServomotorBased Satellite Tracking System. IOSR Journal of Electrical and Electronics Engineering, 11(04), 89–102. https://doi.org/10.9790/1676-11040389102

ABB Power. (2015). Microgrids and renewable energy integration ABB solution and offering overview Global energy challenges Significant forecasted demand in emerging economies. 1–44. http://new.abb.com/docs/librariesprovider78/documentos-peru/presentaciones-primeras-jornadas-tecnicas-abb-peru/ps/peru-exibition-microgrids-and-pv-ebop-alfredo-diez.pdf?sfvrsn=2

Abdel-Rahim, O. (2020). A New High Gain DC-DC Converter With Model-Predictive-Control Based MPPT Technique for Photovoltaic Systems. CPSS Transactions on Power Electronics and Applications, 5(2), 191–200. https://doi.org/10.24295/cpsstpea.2020.00016

Ahmed, M. N., Hojabri, M., Humada, A. M., Daniyal, H. Bin, & Fahad Frayyeh, H. (2015). An Overview on Microgrid Control Strategies. International Journal of Engineering and Advanced Technology (IJEAT), 5, 2249–8958.

Akpolat, A. N., Habibi, M. R., Baghaee, H. R., Dursun, E., Kuzucuoglu, A. E., Yang, Y., Dragicevic, T., & Blaabjerg, F. (2022). Dynamic Stabilization of DC Microgrids Using ANN-Based Model Predictive Control. IEEE Transactions on Energy Conversion, 37(2), 999–1010. https://doi.org/10.1109/TEC.2021.3118664

Ali, M., Kotb, H., Aboras, K. M., & Abbasy, N. H. (2021). Design of cascaded pi-fractional order PID controller for improving the frequency response of hybrid microgrid system using gorilla troops optimizer. IEEE Access, 9, 150715–150732. https://doi.org/10.1109/ACCESS.2021.3125317

Ali, S. U., Waqar, A., Aamir, M., Qaisar, S. M., & Iqbal, J. (2023). Model predictive control of consensus-based energy management system for DC microgrid. In PLoS ONE (Vol. 18, Issue 1 January). https://doi.org/10.1371/journal.pone.0278110

Aloo, L. A., Kihato, P. K., Kamau, S. I., & Orenge, R. S. (n.d.). Model Predictive Control-Adaptive Neuro-Fuzzy Inference System Control Strategies for Photovoltaic-Wind Microgrid: Feasibility Review. 2020 IEEE PES/IAS PowerAfrica, PowerAfrica 2020, 2–6. https://doi.org/10.1109/PowerAfrica49420.2020.9219853

Aloo, L. A., Kihato, P. K., Kamau, S. I., & Orenge, R. S. (2023). Modeling and control of a photovoltaic-wind hybrid microgrid system using GA-ANFIS. Heliyon, 9(4), e14678. https://doi.org/10.1016/j.heliyon.2023.e14678

Alzahrani, A., Ferdowsi, M., Shamsi, P., & Dagli, C. H. (2017). Modeling and Simulation of Microgrid. Procedia Computer Science, 114, 392–400. https://doi.org/10.1016/j.procs.2017.09.053

Amara, S., Toumi, S., & Ben Salah, C. (2020). Modeling and Simulation of Hybrid Renewable Microgrid System. Proceedings of the 17th International Multi-Conference on Systems, Signals and Devices, SSD 2020, 20-23 July,Monastir, Tunisia, July, 1074–1079. https://doi.org/10.1109/SSD49366.2020.9364193

Aminu, M., & Solomon, K. (2016). A Review of Control Strategies for Microgrids. Advances in Research, 7(3), 1–9. https://doi.org/10.9734/air/2016/25722

Anvari-Moghaddam, A., Hamdi, A., Behnam, M.-I., & Nikos, H. (2021). Microgrids: Advances in Operation, Control, and Protection. In Power Systems. Springer. https://doi.org/10.1007/978-3-030-59750-4_5

Anwar, I. B. N., Mohd Hussain, M. N., Mohammad Noor, S. Z., Dahalan, N. Y., Onn, M. S., Tumian, A., Dey, A., Khatana, V., Mani, A., & Salapaka, M. V. (2024). Guaranteeing Service in Connected Microgrids: Storage Planning and Optimal

Power Sharing Policy. E3S Web of Conferences, 473, 1–8. https://doi.org/10.1051/e3sconf/202447302001

Badwawi, R. Al, Abusara, M., & Mallick, T. (2015). A Review of Hybrid Solar PV and Wind Energy System. Smart Science, 3(3), 127–138. https://doi.org/10.1080/23080477.2015.11665647

Banguero, E., Correcher, A., Pérez-Navarro, Á., Morant, F., & Aristizabal, A. (2018). A review on battery charging and discharging control strategies: Application to renewable energy systems. Energies, 11(4), 1–15. https://doi.org/10.3390/en11041021

Basantes, J. A., Paredes, D. E., Llanos, J. R., Ortiz, D. E., & Burgos, C. D. (2023). Energy Management System (EMS) Based on Model Predictive Control (MPC) for an Isolated DC Microgrid. Energies, 16(6), 1–22. https://doi.org/10.3390/en16062912

Bemporad, A., N. Lawrence Ricker, & Morari, M. (2019). Model Predictive Control Toolbox ™ Reference How to Contact MathWorks - R2019b. 994.

Bidram, A., Nasirian, V., Davoudi, A., & Lewis, F. L. (2017). Cooperative Synchronization in Distributed Microgrid Control. In Intelligent Microgrid Management and EV Control Under Uncertainties in Smart Grid (Vol. 1, Issue April). http://link.springer.com/10.1007/978-3-319-50808-5

Bilgundi, S. K., Sachin, R., Pradeepa, H., Nagesh, H. B., & Kumar, M. V. L. (2022). Grid power quality enhancement using an ANFIS optimized PI controller for DG. Protection and Control of Modern Power Systems, 2. https://doi.org/10.1186/s41601-022-00225-2

Blair, N., Diorio, N., Freeman, J., Gilman, P., Janzou, S., Neises, T. W., & Wagner, M. J. (2018). System Advisor Model (SAM) General Description. NREL/TP-6A20-70414. https://www.nrel.gov/docs/fy18osti/70414.pdf

Bogaraj, T., & Kanakaraj, J. (2016). A Novel Energy Management Scheme using ANFIS for Independent Microgrid. International Journal of Renewable Energy Research, 6(3).

Borazjani, P., Wahab, N. I. A., Hizam, H. B., & Soh, A. B. C. (2014). A review on microgrid control techniques. 2014 IEEE Innovative Smart Grid Technologies - Asia, ISGT ASIA 2014, May, 749–753. https://doi.org/10.1109/ISGT-Asia.2014.6873886

Borges, N., Soares, J., & Vale, Z. (2017). A Robust Optimization for Day-ahead Microgrid Dispatch Considering Uncertainties. IFAC-PapersOnLine, 50(1), 3350–3355. https://doi.org/10.1016/j.ifacol.2017.08.521

C, S., Yammani, C., & Maheswarapu, S. (2019). Load Frequency Control of Multi-microgrid System considering Renewable Energy Sources Using Grey Wolf Optimization. Smart Science, 7(3), 198–217. https://doi.org/10.1080/23080477.2019.1630057

Chatzigeorgiou, N. G., Theocharides, S., Makrides, G., & Georghiou, G. E. (2024). A review on battery energy storage systems: Applications, developments, and research trends of hybrid installations in the end-user sector. Journal of Energy Storage, 86(PA), 111192. https://doi.org/10.1016/j.est.2024.111192

Chen, M. R., Zeng, G. Q., Dai, Y. X., Lu, K. Di, & Bi, D. Q. (2019). Fractional-order model predictive frequency control of an islanded microgrid. Energies, 12(1). https://doi.org/10.3390/en12010084

Chen, Z., Wang, K., Li, Z., & Zheng, T. (2017). A review on control strategies of AC/DC micro grid. Conference Proceedings - 2017 17th IEEE International Conference on Environment and Electrical Engineering and 2017 1st IEEE Industrial and Commercial Power Systems Europe, EEEIC / I and CPS Europe 2017,06-09 June, 2017, Milan, Italy. https://doi.org/10.1109/EEEIC.2017.7977807

Dongol, D., Feldmann, T., & Bollin, E. (2018). A model predictive control based peak shaving application for a grid connected household with photovoltaic and battery storage. SMARTGREENS 2018 - Proceedings of the 7th International Conference on Smart Cities and Green ICT Systems,16-18 March 2018, Funchal, Madeira, Portugal, 2018-March(Smartgreens 2018), 54–63. https://doi.org/10.5220/0006685300540063

Du, Y., Pei, W., Chen, N., Ge, X., & Xiao, H. (2017). Real-time microgrid economic dispatch based on model predictive control strategy. Journal of Modern Power Systems and Clean Energy, 5(5), 787–796. https://doi.org/10.1007/s40565-017-0265-4

Elbeji, O., Hamed, M. Ben, & Sbita, L. (2014). PMSG Wind Energy Conversion System: Modeling and Control. International Journal of Modern Nonlinear Theory and Application, 03(03), 88–97. https://doi.org/10.4236/ijmnta.2014.33011

Elmouatamid, A., Ouladsine, R., Bakhouya, M., El Kamoun, N., Zine-Dine, K., & Khaidar, M. (2019). A Model Predictive Control Approach for Energy Management in Micro-Grid Systems. SEST 2019 - 2nd International Conference on Smart Energy Systems and Technologies, 1–6. https://doi.org/10.1109/SEST.2019.8848995

Elsisi, M., Tran, M., & Vu, L. T. (2021). Adaptive Energy Management in Microgrid based on New Training Strategy for ANFIS Adaptive Energy Management in Microgrid based on New Training Strategy for ANFIS. Advances in Engineering Research and Application, Springer International Publishing, December.

Faraj, K., & Hussain, J. (2020a). Analysis and comparison of DC-DC boost converter and interleaved DC-DC boost converter. Engineering and Technology Journal, 38(5), 622–635. https://doi.org/10.30684/etj.v38i5A.291

Faraj, K., & Hussain, J. (2020b). Analysis and Comparison of DC-DC Boost Converter and Interleaved DC-DC Boost Converter. Engineering and Technology Journal,

38(5), 622–635. https://doi.org/10.30684/etj.v38i5a.291

Félix Garcia-Torres, Carlos Bordons, M. A. R. (2020). Model Predictive Control of Microgrids, Advances in Industrial Control Carlos.

Fouad, M. A., Badr, M. A., & Ibrahim, M. M. (2017). Modeling of Micro-grid System Components using Matlab/Simulink. Global Scientific Journals, 5(5), 163–177. www.globalscientificjournal.com/researchpaper

Gamage, D., Zhang, X., Ukil, A., Wanigasekara, C., & Swain, A. (2021). Design of ANFIS Controller for a DC Microgrid. 3rd International Conference on Energy, Power and Environment: Towards Clean Energy Technologies, ICEPE 2020. https://doi.org/10.1109/ICEPE50861.2021.9404439

GE Digital Energy. (2012). Grid IQ Microgrid Control System. In Imagination at work.

Ghiasi, M., Niknam, T., Dehghani, M., Baghaee, H. R., Wang, Z., Ghanbarian, M. M., Blaabjerg, F., & Dragicevic, T. (2022). Multipurpose FCS Model Predictive Control of VSC-Based Microgrids for Islanded and Grid-Connected Operation Modes. IEEE Systems Journal. https://doi.org/10.1109/JSYST.2022.3215437

Ghorashi Khalil Abadi, S. A., Habibi, S. I., Khalili, T., & Bidram, A. (2022). A Model Predictive Control Strategy for Performance Improvement of Hybrid Energy Storage Systems in DC Microgrids. IEEE Access, 10, 25400–25421. https://doi.org/10.1109/ACCESS.2022.3155668

Grzegorz Ma´slak and Przemysław Orłowski. (2022). Microgrid Operation Optimization Using Hybrid System Modeling and Switched Model Predictive Control. Energies, 15, 833. https://doi.org/https:// doi.org/10.3390/en15030833

Hannan, M. A., Wali, S. B., Ker, P. J., Rahman, M. S. A., Mansor, M., Ramachandaramurthy, V. K., Muttaqi, K. M., Mahlia, T. M. I., Dong, Z. Y., Sterjova,

M., Minovski, D., & Sarac, V. (2021). BATTERY ENERGY STORAGE SYSTEMS AND TECHNOLOGIES: A REVIEW Прва меѓународна конференција ЕТИМА First International Conference Etima Battery Energy Storage Systems And Technologies: A Review. Journal of Energy Storage, 42(October), 103023. https://doi.org/10.1016/j.est.2021.103023

Hisar, C. (2020). Three-Phase Parallel Interleaved Boost Converters. MATLAB Central File Exchange. https://www.mathworks.com/matlabcentral/fileexchange/72749-three-phase-parallel-interleaved-boost-converters

Hizam, H. (2022). Artificial Neural Networks , PID , and Fuzzy Logic Controllers.

Hossain, M. A., Pota, H. R., Issa, W., & Hossain, M. J. (2017). Overview of AC microgrid controls with inverter-interfaced generations. Energies, 10(9), 1–27. https://doi.org/10.3390/en10091300

Huang, W., Lu, M., & Zhang, L. (2011). Survey on microgrid control strategies. Energy Procedia, 12, 206–212. https://doi.org/10.1016/j.egypro.2011.10.029

Jadav, K. A., Karkar, H. M., & Trivedi, I. N. (2017). A Review of Microgrid Architectures and Control Strategy. Journal of The Institution of Engineers (India): Series B, 98(6), 591–598. https://doi.org/10.1007/s40031-017-0287-3

Jain, R., & Arya, A. (2015). A comprehensive review on micro grid operation, challenges and control strategies. E-Energy 2015 - Proceedings of the 2015 ACM 6th International Conference on Future Energy Systems,14-15 July 2015,Bangalore, India, July, 295–300. https://doi.org/10.1145/2768510.2768514

Jang, J. S. R. (1993). ANFIS: Adaptive-Network-Based Fuzzy Inference System. IEEE Transactions on Systems, Man and Cybernetics, 23(3), 665–685. https://doi.org/10.1109/21.256541

Jayachandran, M., & Ravi, G. (2017). Design and Optimization of Hybrid Micro-Grid System. Energy Procedia, 117, 95–103. https://doi.org/10.1016/j.egypro.2017.05.111

Kamran, M., Mudassar, M., Fazal, M. R., Asghar, M. U., Bilal, M., & Asghar, R. (2020). Implementation of improved Perturb & Observe MPPT technique with confined search space for standalone photovoltaic system. Journal of King Saud University - Engineering Sciences, 32(7), 432–441. https://doi.org/10.1016/j.jksues.2018.04.006

Katiraei, F., Zamani, A., & Masiello, R. (2017). Microgrid control systems: A practical framework. IEEE Power and Energy Magazine, 15(4), 110–112. https://doi.org/10.1109/MPE.2017.2690528

Kerdphol, T., Rahman, F. S., Mitani, Y., Hongesombut, K., & Küfeoğlu, S. (2017). Virtual inertia control-based model predictive control for microgrid frequency stabilization considering high renewable energy integration. Sustainability (Switzerland), 9(5). https://doi.org/10.3390/su9050773

Khalil, A., Alfaitori, K. A., & Asheibi, A. (2016). Modeling and control of PV/wind microgrid. 2016 7th International Renewable Energy Congress (IREC), 22-24 March 2016, Hammamet, Tunisia, 1–6. https://doi.org/10.1109/IREC.2016.7478916

Kokate, A., Khandagale, H., George, J., Koli, A., & Nair, S. (2019). Modeling and simulation of standalone wind energy conversion system. Proceedings of the International Conference on Trends in Electronics and Informatics, ICOEI 2019, 23-25 April 2019, Tirunelveli,India, Icoei, 1295–1297. https://doi.org/10.1109/ICOEI.2019.8862682

Korjani, S., Facchini, A., Mureddu, M., & Damiano, A. (2017). A genetic algorithm approach for the identification of microgrids partitioning into distribution networks. Proceedings IECON 2017 - 43rd Annual Conference of the IEEE Industrial Electronics Society, 29th October, 2017-1st November 2017, Beijing, China, 2017-

Janua(October), 21–25. https://doi.org/10.1109/IECON.2017.8216008

Krishnan, J. R. (2021). PV and Battery system. MATLAB Central File Exchange. https://www.mathworks.com/matlabcentral/fileexchange/69064-pv-and-battery-system

Kumar, D., Mathur, H. D., Bhanot, S., & Bansal, R. C. (2020). Modeling and frequency control of community micro-grids under stochastic solar and wind sources. Engineering Science and Technology, an International Journal, 23(5), 1084–1099. https://doi.org/10.1016/j.jestch.2020.02.005

Lavanya, V., & Senthil Kumar, N. (2018). A review: Control strategies for power quality improvement in microgrid. International Journal of Renewable Energy Research, 8(1), 150–165. https://doi.org/10.20508/ijrer.v8i1.6643.g7290

Lei, M., Yang, Z., Wang, Y., Xu, H., Meng, L., Vasquez, J. C., & Guerrero, J. M. (2016). Design of energy storage control strategy to improve the PV system power quality. IECON Proceedings (Industrial Electronics Conference), 23-26 October 2016,Italy, 2022–2027. https://doi.org/10.1109/IECON.2016.7794071

Li, S., & Ke, B. (2011). Study of battery modeling using mathematical and circuit oriented approaches. IEEE Power and Energy Society General Meeting, 1–8. https://doi.org/10.1109/PES.2011.6039230

LI, Y., & NEJABATKHAH, F. (2014). Overview of control, integration and energy management of microgrids. Journal of Modern Power Systems and Clean Energy, 2(3), 212–222. https://doi.org/10.1007/s40565-014-0063-1

Mathew, P., Madichetty, S., & Mishra, S. (2019). A Multi-Level Control and Optimization Scheme for Islanded PV Based Microgrid: A Control Frame Work. IEEE Journal of Photovoltaics, 9(3), 822–831. https://doi.org/10.1109/JPHOTOV.2019.2897579

Meng, J., Luo, G., Ricco, M., Swierczynski, M., Stroe, D. I., & Teodorescu, R. (2018). Overview of Lithium-Ion battery modeling methods for state-of-charge estimation in electrical vehicles. Applied Sciences (Switzerland), 8(5). https://doi.org/10.3390/app8050659

Meng, L., Shafiee, Q., Trecate, G. F., Karimi, H., Fulwani, D., Lu, X., & Guerrero, J. M. (2017). Review on Control of DC Microgrids and Multiple Microgrid Clusters. IEEE Journal of Emerging and Selected Topics in Power Electronics, 5(3), 928–948. https://doi.org/10.1109/JESTPE.2017.2690219

Minchala-Avila, L. I., Garza-Castañón, L. E., Vargas-Martínez, A., & Zhang, Y. (2015). A review of optimal control techniques applied to the energy management and control of microgrids. Procedia Computer Science, 52(1), 780–787. https://doi.org/10.1016/j.procs.2015.05.133

Mohamed, S. A., & Abd El Sattar, M. (2019). A comparative study of P&O and INC maximum power point tracking techniques for grid-connected PV systems. SN Applied Sciences, 1(2), 1–13. https://doi.org/10.1007/s42452-018-0134-4

Mohanty, A., Viswavandya, M., Mishra, D. K., Ray, P. K., & Pragyan, S. (2017). Modelling & Simulation of a PV Based Micro Grid for Enhanced Stability. Energy Procedia, 109, 94–101. https://doi.org/10.1016/j.egypro.2017.03.060

Morstyn, T., Hredzak, B., Aguilera, R. P., & Agelidis, V. G. (2018). Model Predictive Control for Distributed Microgrid Battery Energy Storage Systems. IEEE Transactions on Control Systems Technology, 26(3), 1107–1114. https://doi.org/10.1109/ TCST.2017.2699159

Nanda, A. K., Panda, B., Panigrahi, C. K., Pradhan, A., & Hannoon, N. (2021). Trends in Microgrid Control. Microgrids: Design, Challenges, and Prospects, 5(4), 119–135. https://doi.org/10.1201/9781003121626-6

Nguyen, T. T., Yoo, H. J., & Kim, H. M. (2015). Application of model predictive control to bess for microgrid control. Energies, 8(8), 8798–8813. https://doi.org/10.3390/en8088798

Orłowski, G. M. and P. (2022). G. Ma'slak and P. Orłowski. Microgrid Operation Optimization Using Hybrid System Modeling and Switched Model Predictive Control,Energies 2022, 15, 833.

ÖZEL, K., & KARAARSLAN, A. (2020). the Design of Standalone Pv System Using P&O Algorithm for Maximum Power Point Tracking. Communications Faculty of Sciences University of Ankara Series A2-A3 Physical Sciences and Engineering, 62(1), 14–25. https://doi.org/10.33769/aupse.559971

Palizban, O., & Kauhaniemi, K. (n.d.). Microgrid control principles in island mode operation. 2013 IEEE Grenoble Conference PowerTech, POWERTECH 2013, 16-20th June, 2013,Grenoble, France, September 2014. https://doi.org/10.1109/PTC.2013.6652453

Pavan Kumar, Y. V., & Bhimasingu, R. (2021). Design of voltage and current controller parameters using small signal model-based pole-zero cancellation method for improved transient response in microgrids. SN Applied Sciences, 3(11). https://doi.org/10.1007/s42452-021-04815-x

Pawar, N., & Nema, P. (2020). ANFIS Based Forecast Model For Predicting PV Energy Generation System. 9(03).

Prabhakaran, P., & Agarwal, V. (2020). Novel Boost-SEPIC Type Interleaved DC-DC Converter for Mitigation of Voltage Imbalance in a Low-Voltage Bipolar DC Microgrid. IEEE Transactions on Industrial Electronics, 67(8), 6494–6504. https://doi.org/10.1109/TIE.2019.2939991

Priyadarshi, N., Padmanaban, S., Ionel, D. M., Mihet-Popa, L., & Azam, F. (2018). Hybrid

PV-Wind, micro-grid development using quasi-Z-source inverter modeling and control-experimental investigation. Energies, 11(9). https://doi.org/10.3390/en11092277

R.D Tayade & S., & Mopari, S. (2017). Comparative Analysis of Interleaved Boost Converter and CUK Converter for Solar Powered BLDC Motor. International Journal of Electrical and Electronics Engineering (IJEEE), 6(4), 1–12. http://www.iaset.us/view_archives.php?year=2017&jtype=2&id=15&details=archives

Reshma Mary Thomas, & Deepu Jose. (2015). Control Method for Parallel DC- DC Converters used in Standalone Photovoltaic Power System. International Journal of Engineering Research and, V4(08), 297–302. https://doi.org/10.17577/ijertv4is080706

S. A. Rahman Kashif. (2021). Three level three phase diode clamped SPWM inverter. MATLAB Central File Exchange. https://www.mathworks.com/matlabcentralfileexchange/27313-three-level-three-phase-diode-clamped-spwm-inverter

S. Kumar. (2022). Battery charging and discharging model. MathWorks 2022. https://www.mathworks.com/matlabcentral/fileexchange/ 38304-battery-charging-and-discharging-model

Sahin, P., Resmi, R., & Vanitha, V. (2017). PMSG based standalone wind electric conversion system with MPPT. Proceedings of IEEE International Conference on Emerging Technological Trends in Computing, Communications and Electrical Engineering, ICETT 2016, 21-22 October 2016, Kollam, India, November, 1–5. https://doi.org/10.1109/ICETT.2016.7873701

Samrat, N. H., Ahmad, N., Choudhury, I. A., & Taha, Z. (2015). Technical study of a standalone photovoltaic-wind energy based hybrid power supply systems for island electrification in Malaysia. PLoS ONE, 10(6), 1–35. https://doi.org/10.1371/journal

.pone.0130678

Sawle, Y., Gupta, S. C., & Bohre, A. K. (2016). PV-wind hybrid system: A review with case study. Cogent Engineering, 3(1). https://doi.org/10.1080/23311916.2016.1189305

Seborg E. Dale, E. F. T. and M. A. D. (2003). Process Dynamics and Control (2nd Editio). Wiley, Hoboken. https://doi.org/10.1201/9780203911501.ch5

Shen, Y. (2017). Microgrid Control Strategy Study and Controller Design Based on Model Predictive Control. 59. https://digitalcommons.du.edu/etd/1241

Sibtain, D., Murtaza, A. F., Ahmed, N., Sher, H. A., & Gulzar, M. M. (2021). Multi control adaptive fractional order PID control approach for PV/wind connected grid system. International Transactions on Electrical Energy Systems, 31(4). https://doi.org/10.1002/2050-7038.12809

Sumarmad, K. A. Al, Sulaiman, N., Wahab, N. I. A., & Hizam, H. (2022). Energy Management and Voltage Control in Microgrids Using Artificial Neural Networks, PID, and Fuzzy Logic Controllers. Energies, 15(1). https://doi.org/10.3390/en15010303

Sumathi, S., Ashok Kumar, L., & Surekha, P. (2015). Solar PV and Wind Energy Conversion Systems. In Green Energy and Technology. http://link.springer.com/10.1007/97 8-3-319-14941-7

Syed, M. A., & Khalid, M. (2023). An Intelligent Model Predictive Control Strategy for Stable Solar-Wind Renewable Power Dispatch Coupled with Hydrogen Electrolyzer and Battery Energy Storage. International Journal of Energy Research, 2023, 1–17. https://doi.org/10.1155/2023/4531054

Szeidert, I., Filip, I., & Prostean, O. (2016). Issues regarding the modelling and simulation

of hybrid micro grid systems. IOP Conference Series: Materials Science and Engineering, 106(1). https://doi.org/10.1088/1757-899X/106/1/012028

Tan, R. (2021). Battery Energy Storage System Model. MATLAB Central File Exchange. https://www.mathworks.com/matlabcentral/fileexchange/69512-battery-energy-storage-system-model

Ton, D., & Systems, P. (2015). Office of Electricity Delivery & Energy Reliability Microgrid Controls and Management Systems OE Mission.

Topa Gavilema, A. O., Gil, J. D., Álvarez Hervás, J. D., Torres Moreno, J. L., & García, M. P. (2023). Modeling and Energy Management of a Microgrid Based on Predictive Control Strategies. Solar, 3(1), 62–73. https://doi.org/10.3390/solar3010005

Tounsi, A., Abid, H., Kharrat, M., & Elleuch, K. (2018). MPPT algorithm for wind energy conversion system based on PMSG. 2017 18th International Conference on Sciences and Techniques of Automatic Control and Computer Engineering, STA 2017 - Proceedings, 2018-Janua(April 2018), 533–538. https://doi.org/10.1109/STA.2017.8314957

Truong, D. N., Ngo, V. T., Thi, M. S. N., & Hoang, A. Q. (2021). Application of An Adaptive Network-based Fuzzy Inference System to Control a Hybrid Solar and Wind Grid-Tie Inverter. Engineering, Technology & Applied Science Research, 11(5), 7673–7677. https://doi.org/10.48084/etasr.4413

Wang, C. N., Lin, W. C., & Le, X. K. (2014). Modelling of a PMSG wind turbine with autonomous control. Mathematical Problems in Engineering, 2014. https://doi.org/10.1155/2014/856173

Wang, L. (2016). Model Predictive Control System Design and Implementation Using MATLAB®. Springer London.

Wang, T., He, X., & Deng, T. (2019). Neural networks for power management optimal strategy in hybrid microgrid. Neural Computing and Applications, 31(7), 2635–2647. https://doi.org/10.1007/s00521-017-3219-x

Yahyaoui, I. (2018). Advances in renewable energies and power technologies: volume 1: solar and wind energies. Elsevier. https://doi.org/10.1016/C2016-0-04919-7

Zebraoui, O., & Bouzi, M. (2018). Comparative study of different MPPT methods for wind energy conversion system. IOP Conference Series: Earth and Environmental Science, 161(1). https://doi.org/10.1088/1755-1315/161/1/012023

Zhao, D., Sun, S., Mohammadzadeh, A., & Mosavi, A. (2022). Adaptive Intelligent Model Predictive Control for Microgrid Load Frequency. Sustainability (Switzerland), 14(18). https://doi.org/10.3390/su141811772

APPENDICES

Appendix I: Tuning PID Controller using the Ziegler-Nichols Method

The Ziegler-Nichols (ZN) method is a conventional PID tuning method widely accepted as the standard for the design of various controllers. Ziegler-Nichols presented two methods: The experimental step response method and the ultimate cycle method. This thesis used the ultimate cycle method in the PID controller tuning.

The procedure is as follows: First, the derivative time (T_D) is set to zero, and the integral time T_I set to infinity. This is used to obtain the initial gains of the PI(D) controller. The critical gain (K_u) and periodic oscillations (P_u) are determined using Routh-Hurwitz criteria. From the Routh-Hurwitz rows, K_u and P_u are determined by equating the rows containing "s" and "s^2" to zero, respectively. Next, the PID gains of K_P, K_I, and K_D are obtained using relations presented in Table A1.1, and the formulas K_P=0.6× K_u, $K_I = \frac{K_P}{T_I}$ and $K_D = K_P T_D$, with the critical period, $T_c = \frac{2\pi}{\omega}$. A proportional controller will have the effect of reducing the rise time and will reduce but never eliminate the steady-state error. An integral control will eliminate the steady-state error for a constant or step input but may make the transient response slower. A derivative control will increase the system stability, reducing the overshoot and improving the transient response.

Table A1.1: ZN PID Tuning Parameters

Control Type	K_P	T_I	T_D
P	$0.5K_u$	infinity	0
PI	$0.45K_u$	$(0.833T_c)$	0
PID	$0.6K_u$	0	$0.125T_c$

Appendix II: The Consolidated Microgrid Model

The Consolidated Microgrid Model (Figure A2.1) was obtained by integrating the individual models for the Solar PV system, Wind turbine system, IBCs, Two-parallel Inverters, the BESS, and the Load Model.

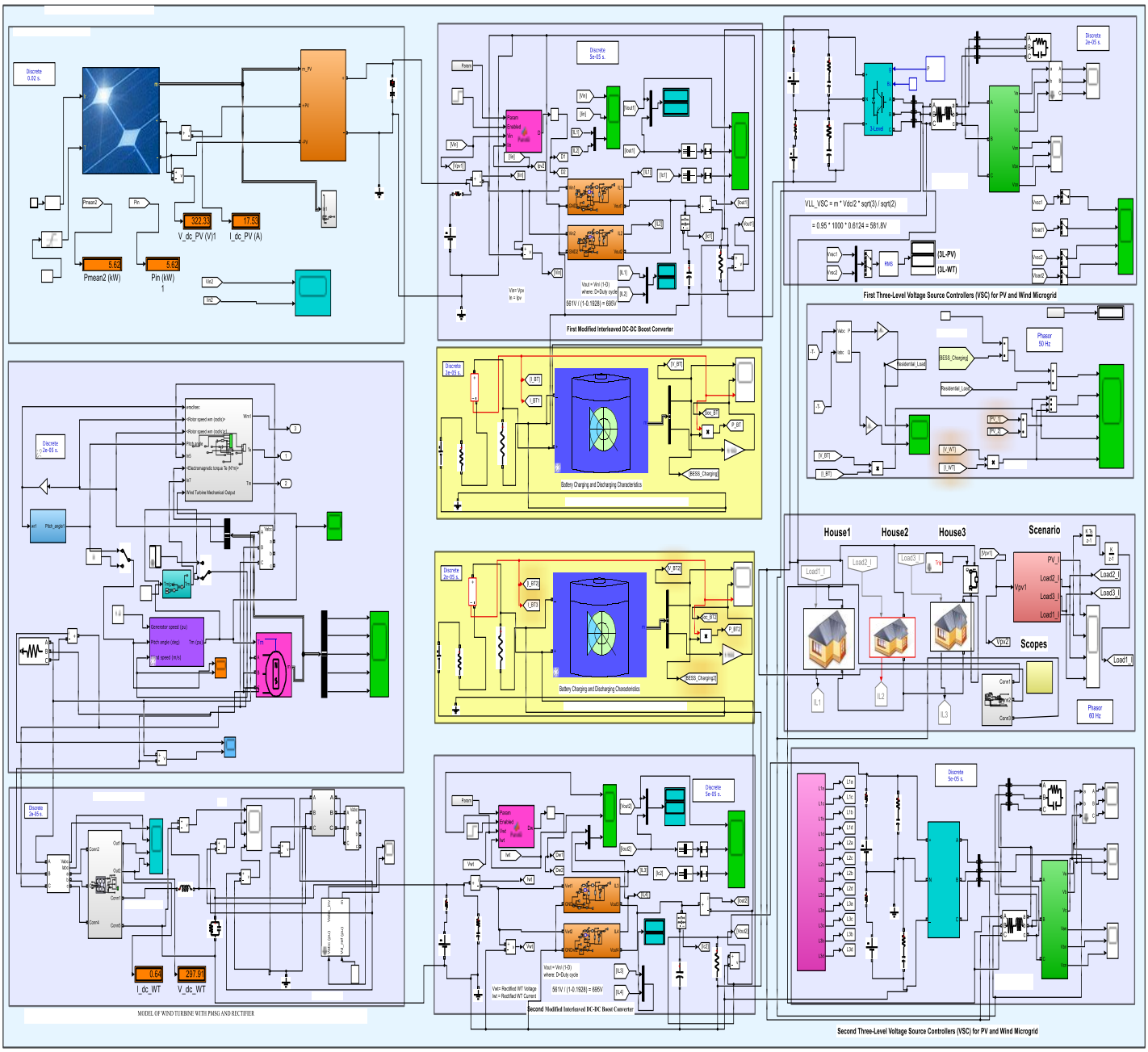

Figure A2.1: Combined Simulink Model of the Developed Microgrid with Case Study

Appendix III: Selected MATLAB Codes

Figure A3.1 shows the MATLAB functions and scripts code snippet that was used for transforming the continuous-time state space of the microgrid into the discrete-time state-space model based on a Zero-Order Hold (ZOH) with appropriate sample times as given in.

```
h = tf([1000, 56080], [1 163 5970 56080]); % define tf object without
delay

Ts = 0.2;% specify a sample time of 0.2 seconds

hd1 = c2d(h, Ts); % Obtain the discrete-time transfer function

h = tf([1000, 56080], [1 163 5970 56080], 'IODelay',0.25); % define tf
object with delay of □^−0.25□

hd2 = c2d(h, Ts); % Obtain the discrete time transfer function without
delay
```

Figure A3.1: Code for Continuous-Time State Space to Discrete-Time State Space Conversion

The discrete-time state-space model has been obtained directly from the continuous-time transfer function based on ZOH with a sample time, T_s of $0.2\,seconds$ and sampling instant k using the MATLAB script as given in Figure A3.2.

```
microgridplantTF = tf([1000, 56080], [1 163 5970 56080]) % define and
display tf object

microgridplantCSS = ss(microgridplantTF);% transfer function to
continuous state space

Ts = 0.2; % specify a sample time of 0.2 seconds

microgridplantDSS = c2d(microgridplantCSS,Ts)     % convert to discrete-
time state space, using ZOH
```

Figure A3.2: Code for Continuous-time TF to Discrete-time State Space Conversion

Appendix IV: Data Used in the Study

Table A4.1, A4.2 and A4.3, respectively, show part of the raw Typical Metrological Year (TMY) solar-wind data for the years 2017, 2018 and 2019 that was used to prepare the final GA-ANFIS data applied in the study.

Table A4.1: Part of the Raw TMY Solar-Wind Data for Year 2017

Source	Location	City	State	Country	Latitude	Longitude
NSRDB	1982496	-	-	-	-1.11	37.02
Year	Month	Day	Hour	Minute	Temperat	Wind Speed
2017	1	1	0	30	17.5	0.7
2017	1	1	1	30	17.3	0.7
2017	1	1	2	30	17.2	0.7
2017	1	1	3	30	16.2	1.9
2017	1	1	4	30	15.9	1.9
2017	1	1	5	30	15.7	1.9
2017	1	1	6	30	16.7	2.7
2017	1	1	7	30	19.1	3.9
2017	1	1	8	30	21.7	4.7
2017	1	1	9	30	23.8	5
2017	1	1	10	30	25.6	5.1
2017	1	1	11	30	26.9	5.1
2017	1	1	12	30	27.6	5.1
2017	1	1	13	30	27.8	5.1
2017	1	1	14	30	27.5	5
2017	1	1	15	30	26.7	4.9
2017	1	1	16	30	25.3	4.7
2017	1	1	17	30	23.4	4
2017	1	1	18	30	21.5	3.3
2017	1	1	19	30	20.4	3
2017	1	1	20	30	19.6	2.7
2017	1	1	21	30	19	2.4
2017	1	1	22	30	18.4	2.1
2017	1	1	23	30	17.9	1.7
2017	1	2	0	30	17.4	1.5
2017	1	2	1	30	17	1.5
2017	1	2	2	30	16.9	1.5
2017	1	2	3	30	16.3	1.5
2017	1	2	4	30	15.9	1.5
2017	1	2	5	30	15.7	1.6
2017	1	2	6	30	16.9	2.5
2017	1	2	7	30	19.5	4
2017	1	2	8	30	22	4.8
2017	1	2	9	30	24.1	5
2017	1	2	10	30	25.9	4.9
2017	1	2	11	30	27.4	4.9
2017	1	2	12	30	28.4	4.9
2017	1	2	13	30	28.6	4.9
2017	1	2	14	30	28.3	5
2017	1	2	15	30	27.5	4.9
2017	1	2	16	30	26.1	4.8
2017	1	2	17	30	24.1	4.1
2017	1	2	18	30	22	3.2
2017	1	2	19	30	20.6	3
2017	1	2	20	30	19.5	2.8
2017	1	2	21	30	18.4	2.3
2017	1	2	22	30	17.4	1.9
2017	1	2	23	30	16.6	1.6
2017	1	3	0	30	16	1.4
2017	1	3	1	30	15.5	1.4
2017	1	3	2	30	15.3	1.3
2017	1	3	3	30	14.7	1.4
2017	1	3	4	30	14.3	1.4
2017	1	3	5	30	14.1	1.5
2017	1	3	6	30	15.9	2.3
2017	1	3	7	30	19.4	3.9
2017	1	3	8	30	22.3	4.9

Table A4.2: Part of the Raw TMY Solar-Wind Data for Year 2018

Source	Location	City	State	Country	Latitude	Longitude
NSRDB	1982496	-	-	-	-1.11	37.02
Year	Month	Day	Hour	Minute	Temperat	Wind Speed
2018	1	1	0	30	17.3	2.6
2018	1	1	1	30	17	2.5
2018	1	1	2	30	16.9	2.5
2018	1	1	3	30	16.5	0.8
2018	1	1	4	30	16.1	0.9
2018	1	1	5	30	15.8	1
2018	1	1	6	30	17.3	1.1
2018	1	1	7	30	20.6	1.3
2018	1	1	8	30	23.6	1.5
2018	1	1	9	30	26.3	1.6
2018	1	1	10	30	28.6	1.6
2018	1	1	11	30	30.3	1.8
2018	1	1	12	30	31.4	2
2018	1	1	13	30	31.8	2.3
2018	1	1	14	30	31.5	2.6
2018	1	1	15	30	30.5	2.7
2018	1	1	16	30	28.7	2.7
2018	1	1	17	30	26.4	2.3
2018	1	1	18	30	24.2	2.1
2018	1	1	19	30	22.8	2.1
2018	1	1	20	30	21.7	1.6
2018	1	1	21	30	20.7	1.1
2018	1	1	22	30	19.6	1
2018	1	1	23	30	18.8	0.8
2018	1	2	0	30	18.3	0.8
2018	1	2	1	30	17.9	0.8
2018	1	2	2	30	17.7	0.8
2018	1	2	3	30	17	0.8
2018	1	2	4	30	16.6	0.8
2018	1	2	5	30	16.2	0.8
2018	1	2	6	30	17.4	0.9
2018	1	2	7	30	20.3	0.8
2018	1	2	8	30	23.2	0.7
2018	1	2	9	30	25.7	0.5
2018	1	2	10	30	27.6	0.4
2018	1	2	11	30	28.9	0.6
2018	1	2	12	30	29.7	0.7
2018	1	2	13	30	29.9	0.8
2018	1	2	14	30	29.2	0.8
2018	1	2	15	30	27.9	0.9
2018	1	2	16	30	26.3	0.8
2018	1	2	17	30	24.6	0.6
2018	1	2	18	30	23.2	0.5
2018	1	2	19	30	22.3	0.5
2018	1	2	20	30	21.6	0.6
2018	1	2	21	30	21	0.7
2018	1	2	22	30	20.4	0.8
2018	1	2	23	30	19.8	0.7
2018	1	3	0	30	19.3	0.6
2018	1	3	1	30	18.9	0.5
2018	1	3	2	30	18.6	0.4
2018	1	3	3	30	18.1	0.5
2018	1	3	4	30	17.9	0.5
2018	1	3	5	30	17.8	0.4
2018	1	3	6	30	18.2	0.5
2018	1	3	7	30	19.7	0.9
2018	1	3	8	30	21.7	1.4
2018	1	3	9	30	23.8	1.7
2018	1	3	10	30	25.7	1.8
2018	1	3	11	30	27.1	2
2018	1	3	12	30	27.7	2.2
2018	1	3	13	30	27.6	2.4
2018	1	3	14	30	27.2	2.5
2018	1	3	15	30	26.3	2.5
2018	1	3	16	30	25	2.3
2018	1	3	17	30	23.4	1.7
2018	1	3	18	30	21.9	1.2
2018	1	3	19	30	21	1.1
2018	1	3	20	30	20.2	1.2
2018	1	3	21	30	19.6	1.2
2018	1	3	22	30	19.1	1.2
2018	1	3	23	30	18.7	1.2

Table A4.3: Part of the Raw TMY Solar-Wind Data for Year 2019

Source	Location ID	City	State	Latitude	Longitude
NSRDB	1982496	-	-	-1.11	37.02
Year	Month	Day	Hour	Temperat	Wind Speed
2019	1	1	0	20.6125	3.016666667
				0.858854	0.125694444
	1	2		20.87917	2.8125
2019	1	3	0	16.3	1.4
2019	1	3	1	15.8	1.4
2019	1	3	2	15.6	1.4
2019	1	3	3	15.1	1.5
2019	1	3	4	14.7	1.5
2019	1	3	5	14.5	1.5
2019	1	3	6	16.3	2.2
2019	1	3	7	19.8	3.7
2019	1	3	8	22.5	4.7
2019	1	3	9	24.4	5
2019	1	3	10	25.9	4.9
2019	1	3	11	27.1	4.8
2019	1	3	12	27.8	4.9
2019	1	3	13	27.9	4.9
2019	1	3	14	27.4	4.9
2019	1	3	15	26.3	4.9
2019	1	3	16	24.8	4.7
2019	1	3	17	23	4.2
2019	1	3	18	21.4	3.6
2019	1	3	19	20.4	3.2
2019	1	3	20	19.8	2.8
2019	1	3	21	19.5	2.5
2019	1	3	22	19.3	2.3
2019	1	3	23	19.1	2.1

Table A4.4 shows part of the raw consolidated monthly TMY solar-wind data for the years 2017, 2018 and 2019 applied in the GA-ANFIS data set creation.

Table A4.4: Part of the Raw Typical Metrological Year (TMY) Solar-Wind Data

Variable	Time	Mean	Min	Max	Sum	St Dev	Avg Daily	Avg Daily Max
-1.123_37.0051_-1.123_37.0051_nsrdb-msg-v1-0-0-tmy_60_tmy.csv:Beam irradiance - DNI (W/m2)	Jan	297.423	0	1023	221283	405.381	0	932.613
	Feb	294.841	0	1031	198133	395.893	0	964.226
	Mar	270.216	0	1014	201041	374.424	0	943.936
	Apr	198.49	0	990	142913	327.4	0	850.871
	May	139.972	0	969	104139	278.157	0	725.161
	Jun	86.5764	0	937	62335	227.373	0	543.742
	Jul	77.4207	0	958	57601	206.493	0	568.3
	Aug	100.388	0	966	74689	245.07	0	604.355
	Sep	177.644	0	1018	127904	332.396	0	764
	Oct	161.21	0	1002	119940	311.25	0	796.871
	Nov	164.065	0	1010	118127	301.366	0	782.774
	Dec	255.055	0	1028	189761	377.355	0	928.193
	Total	184.688	0	1031	1.62E+06	329.853	0	778.745
-1.123_37.0051_-1.123_37.0051_nsrdb-msg-v1-0-0-tmy_60_tmy.csv:Diffuse irradiance - DHI (W/m2)	Jan	68.1855	0	543	50730	104.976	0	287.065
	Feb	80.619	0	573	54176	123.006	0	331.903
	Mar	84.332	0	553	62743	124.942	0	389.71
	Apr	97.2292	0	553	70005	144.909	0	431.935
	May	94.5806	0	509	70368	143.341	0	428.355
	Jun	102.504	0	510	73803	147.997	0	449.29
	Jul	99.5914	0	537	74096	146.124	0	436.935
	Aug	104.977	0	545	78103	156.838	0	482.419
	Sep	97.3569	0	556	70097	149.616	0	454.193
	Oct	99.2016	0	562	73806	147.333	0	454.645
	Nov	107.435	0	533	77353	160.029	0	454.871
	Dec	81.7742	0	549	60840	129.03	0	406.484
	Total	93.1644	0	573	816120	141.162	0	418.918
-1.123_37.0051_-1.123_37.0051_nsrdb-msg-v1-0-0-tmy_60_tmy.csv:Global irradiance - GHI (W/m2)	Jan	278.089	0	1079	206898	371.477	0	979.193
	Feb	298.85	0	1094	200827	389.335	0	1054.81
	Mar	292.2	0	1111	217397	384.27	0	1044.42
	Apr	249.696	0	1065	179781	343.688	0	948.516
	May	200.095	0	1014	148871	297.116	0	831.548
	Jun	166.865	0	951	120143	251.156	0	709
	Jul	155.563	0	958	115739	240.213	0	698.387
	Aug	182.796	0	1036	136000	280.119	0	806.548
	Sep	239.011	0	1097	172088	344.909	0	940.742
	Oct	228.915	0	1092	170313	335.363	0	931.548
	Nov	226.258	0	1040	162906	317.737	0	900.871
	Dec	259.816	0	1047	193303	350.099	0	959.161
	Total	231.081	0	1111	2.02E+06	331.586	0	898.658

The full dataset used in this study is freely and publicly available at https://nsrdb.nrel.gov/data-viewer as well as in the System Advisor Model (SAM) version

SAM 2018.11.11 provided freely by NREL (Blair et al., 2018). Figure A4.1 and Figure A4.2 show the monthly and annual solar data plots/profiles, year 2019 for the site Juja, Kiambu Kenya, whose data was used in influencing the GA-ANFIS training.

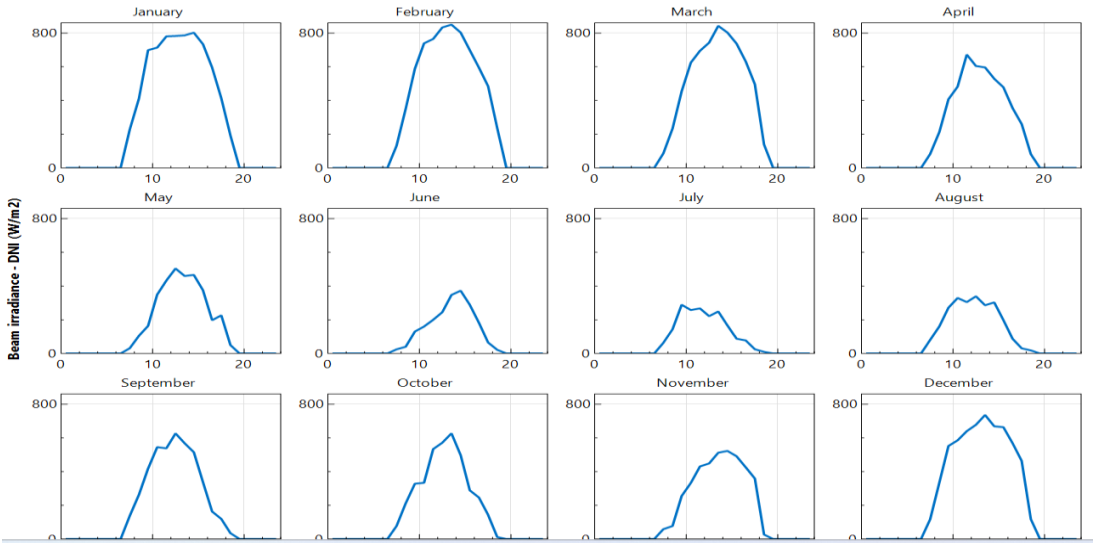

Figure A4.1: The Monthly/Annual Solar Data Plots/Profiles, Year 2019 for the Study

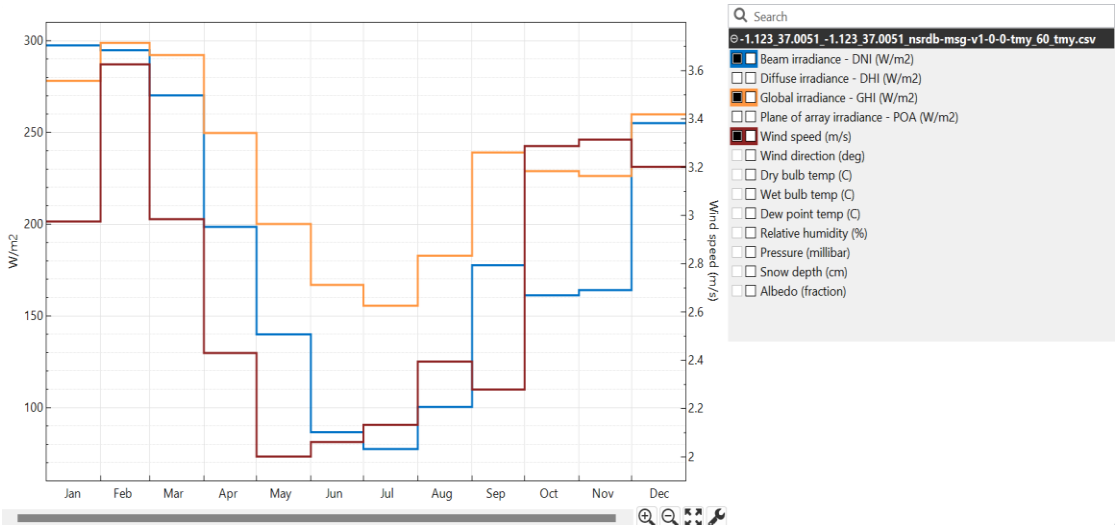

Figure A4.2: Consolidated Monthly/Annual Solar Data Profiles, Year 2019 for the Study

Table A4.5 shows a snapshot of the final data set that was used in training, testing and checking the GA-ANFIS training.

Table A4.5: A Snapshot of The Final Data Set for Training, Testing and Checking the GA-ANFIS Training

	Training Data Set			Checking Data Set-I		
S/No.	PV-Wind Power Generation Error	Change in Generation Error	GA-ANFIS Output	PV-Wind Power Generation Error	Change in Generation Error	GA-ANFIS Output
1	0.765840265	-8.952168833	1.063124915	0.111857821	-0.24210155	0.806681277
2	0.851444421	7.798540328	0.624705481	0.468462209	-0.284805082	1.029699145
3	0.119367607	-5.002801386	1.339107756	0.902159321	-4.30043564	1.120573642
4	0.858573305	0.756128091	0.879162222	0.319962583	10.60142693	0.652600106
5	0.594417691	-8.860308668	0.578699721	0.550151686	-3.4649603	0.60627047
6	0.091687981	2.702521447	1.549352577	0.210383223	-10.30312698	1.630170305
7	0.261788326	-6.28126096	1.445305639	0.706191036	7.426679811	0.062269129
8	0.514068628	4.08309611	0.907757966	0.239789409	-2.921920821	1.460527214
9	0.900056425	5.014184333	1.027083892	0.475599629	-6.845180923	1.506923266
10	0.906995223	6.57601721	0.968623762	0.657132119	-2.546328142	1.313703391
11	0.148156297	-1.31064764	0.342774783	0.837449057	-10.69395508	0.16287526
12	0.912357215	-11.02873348	0.497056445	0.90173394	-9.752707746	0.432087453
13	0.899736931	-7.182110329	0.777023525	0.514382598	11.71434066	0.553338786
14	0.45625311	10.95344008	0.380305464	0.130306976	12.08756532	1.12155112
15	0.752263641	-9.211982497	1.393109508	0.140336365	1.99302777	0.225312677
16	0.133373158	8.634149903	0.321361078	0.242057759	-11.66584211	1.190025373
17	0.396455606	1.016074534	0.372770939	0.790274221	-7.028332296	0.176157072
18	0.860791394	13.14756999	0.281668278	0.239025248	-3.891297863	1.078699625
19	0.74467489	-11.17834849	0.375646091	0.765427737	8.511642065	0.815386995
20	0.901922881	-1.519025851	0.718902829	0.228913471	-12.8418089	1.285435343
21	0.616396257	-10.42370159	0.513318773			
22	0.033568978	12.24029914	1.523576409	Testing Data Set-I		
23	0.798181548	-13.12719306	0.709842196	0.873507806	-12.10986926	1.179811179
24	0.877953653	7.285127315	0.304946928	0.32898474	-8.771764219	1.491138925
25	0.638011046	8.408535347	1.493053598	0.184799535	3.951560086	1.470022132
26	0.712275723	9.770409692	1.616584824	0.236018826	6.14064322	0.551369037
27	0.69854452	-11.01245009	0.724135456	0.579081996	3.915268023	1.152930623
28	0.368693398	-2.655759799	0.183346719	0.444891518	-1.30052178	0.326386214
29	0.616149217	-6.363434324	0.425806748	0.330559937	1.245735646	0.050392561
30	0.160915487	7.951814726	0.674387746	0.78097891	-5.397498651	1.22772253
31	0.663683323	-1.817533572	0.981578522	0.550148246	6.484359387	0.825037019
32	0.029922876	10.88216125	0.432649384	0.516740192	-8.242692102	0.791871533
33	0.260307606	-8.43105375	0.994691097	0.862162044	4.949548984	1.492791693
34	0.043401107	-6.259222712	1.173506038	0.268688678	-8.386954373	1.00627997
35	0.091303874	-9.39321702	0.365882111	0.711768215	-3.485158193	1.019149543
36	0.774050359	-9.644183194	0.193739124	0.708505349	3.328891859	1.418079804
37	0.653138906	9.786243502	0.489515191	0.357619096	7.426027032	1.32905755
38	0.298073511	2.112171565	0.525984198	0.533752342	-11.10016713	0.951590501
39	0.893208726	1.321295349	0.699875154	0.071303032	11.37872823	0.301822075
40	0.032379316	-9.408697847	0.83796617	0.050713112	7.306385983	0.395887817
41	0.412419698	9.35532462	0.141101065	0.4989497	-0.350021741	1.46274469
42	0.35866495	3.234460984	0.433095687	0.732417196	-1.699747403	0.047312352
43	0.719585781	-3.949761906	1.321674128	0.877970043	-1.41023064	0.808337291
44	0.747487907	0.351112806	0.048213458	0.276025077	-0.827329309	0.963088539
45	0.175660248	-2.602087106	1.53260933	0.679702677	-4.503455697	0.546805719
46	0.460378532	-11.23688267	1.205045924	0.655098004	4.027161099	0.521135831
47	0.418851029	-6.892221931	0.806204807	0.162611735	4.447871897	0.231594387
48	0.60753423	-9.982048227	0.954566351	0.118997682	-0.091359075	0.488897744
49	0.666802941	-8.376443611	0.391517907	Testing Data Set-II		
50	0.709405481	-6.89125807	0.757100566	0.122111836	-5.131738992	0.27707979
51	0.259463572	-2.192422669	1.58909609	0.534694241	0.225479368	1.614823072
52	0.638920516	-11.9341576	0.902229436	0.441227203	0.285446451	1.175945878
53	0.615792124	10.67197691	0.859874121	0.011187945	8.417134271	0.82577818
54	0.152855031	11.78686053	0.382130738	0.316895286	7.813032547	0.777295818

Appendix V: List of Journal Publications & Conference Papers

The following publications have resulted from this study:

Alwal, P.K. Kihato and S.I. Kamau, “A Review of Control Strategies for Microgrid with PV-Wind Hybrid Generation Systems", Proceedings of Sustainable Research and Innovation Conference, JKUAT Main Campus, Kenya, 2nd -4th May, 2018.

Linus A. Aloo, Peter K. Kihato, Stanley I. Kamau and Roy S. Orenge, "Model Predictive Control-Adaptive Neuro-Fuzzy Inference System Control Strategies for Photovoltaic-Wind Microgrid: Feasibility Review," 978-1-7281-6746-6/20/$31.00 ©2020 IEEE, DOI: 10.1109/PowerAfrica49420.2020.

Linus Alwal Aloo, Peter Kamita Kihato, Stanley Irungu Kamau, Roy Sam Orenge, “Interleaved boost converter voltage regulation using hybrid ANFIS-PID controller for off-grid microgrid,” Bulletin of Electrical Engineering and Informatics, Vol.12, Issue 4, pp. 2005-2016, Mar 2023.

Linus A. Aloo, Peter K. Kihato, Stanley I. Kamau, Roy S. Orenge, Modeling and control of a photovoltaic-wind hybrid microgrid system using GA-ANFIS, Heliyon, 2023, Volume 9, Issue 4, April 2023, e14678, ISSN 2405-8440, https://doi.org/10.1016/j.heliyon.2023.e14678.